Welding Procedure Specifications and Discontinuities Acceptance Criteria for Butt Welded Heavy Steel Sections Utilizing Submerged Arc Welding Process

By

Omar A. Ibrahim

Department of Civil Engineering and Applied Mechanics

McGill University

Montreal, Quebec, Canada

A thesis submitted to McGill University in partial fulfillment of the requirements of the degree of Doctor of Philosophy in Engineering

ACKNOWLEDGEMENT

I would like to express my profound gratitude to Professor Colin Rogers and Professor Dimitrios Lignos for their endless guidance, support, motivation and confidence in me. I also want to thank them for their support during experimental portion of my thesis. It has been a privilege working under their supervision.

This research would have not been possible without the financial support of the Natural Sciences and Engineering Research Council of Canada. I would also like to acknowledge ADF Group Inc. and DPHV Structural Consultants for their financial and technical support as well as allowing us to use their facilities to conduct a great portion of the experimental aspect of this research. Specifically I would like to thank Mr. Nicolas Roy for his assistance and advice with respect to technical aspects of welding.

I also recognize the Department of Mining and Materials Engineering, the Faculty of Engineering, McGill University for providing technical support and access to the Materials and Characterization Laboratories to conduct a portion of the materials testing.

I would like to express my sincere appreciations to my colleagues Ahmed Elkady and Sophie Lu for their invaluable help during the welding experiments. I would also like to thank my colleague Violetta Nikolaidou as well as the undergraduate students David Pizzuto and Andrea Iachetta for their help with the material testing. I am also thankful to my colleague Zaid Gouleh for sharing his experience with respect to material testing.

Last, but not least, I would like to express deepest gratitude to my father Abdelaziz and my mother Lubna for their constant support. I thank my wife Amal for her support, encouragement and understanding, without which I would not have been able complete my Ph.D.

ABSTRACT

Welding structural steel components is an essential stage in steel fabrication. Residual stresses and welding defects are often associated with the welding procedure. According to the fracture toughness of the material, the level of the residual stresses and the size of the discontinuities and flaws in the steel component being welded, cracks can initiate and repair will be required. In some cases, this repair will need to be repeated if additional cracks result from the weld repair procedure. As a result, welding and steel specifications contain limits as to the material fracture toughness and the size of discontinuities in the base metal. The origin of these limits is for the most part based on studies involving commonly used steel plates of less than 25 mm thickness. Nowadays, the use of heavy steel sections composed of plates or elements greater than 50mm in thickness has increased in construction because of current design specifications that require structures to withstand loads arising from blasts impact and large earthquakes, for example, which amplify the loading demands placed on the steel structure compared to what was considered for design in past decades. Available welding specifications and procedures have been employed in the fabrication of thick steel components; nonetheless, fabricators have reported unrepairable cracks that developed after the welding procedures were completed. The increase in thickness of the welded component results in greater restraint to the expansion and contraction induced by the welding procedure, which leads to an increase in the developed welding residual stresses. Moreover, the likelihood of discontinuities and flaws in thick steel is higher than that in found in thinner plates. In addition, the variability of the fracture toughness of a material increases as the thickness becomes larger. Accordingly, the welding of thick steel components requires separate welding specifications and acceptance criteria.

In this thesis, a comprehensive study is conducted based on a numerical and an experimental framework, with which the welding procedures of thick steel plates (greater than 50mm) using an automated submerged arc welding process is evaluated. A finite element simulation of the welding is developed and validated with measured results from a welding experiment. Material tensile and fracture toughness testing is conducted for thick steel plates to determine the variability in these properties. A probabilistic approach for assessing discontinuities is proposed based on fracture toughness tests, as well as a database compiled from previous and current research. The finite

element simulation and discontinuities assessment approach are used for the assessment of a parametric study of the main parameters of the welding procedure. According to the results of the parametric study, four submerged arc welding procedures are recommended for welding steel plates of thicknesses from 25 to 100mm. In addition, acceptance criteria are developed for discontinuities existing in the steel plates before welding based on a performance-based approach. Moreover, two experimental investigations are carried out; the first is to determine the effect of five submerged arc welding procedures on the weld quality and material properties of the heat affected zone. The results of the experiments are in agreement with the parametric study results. Based on the weld experiment results, two welding procedure specifications are recommended for welding thick steel plates. The second experiment aims to study the effect of multiple weld repairs on the heat affected zone of the base metal. The results of this study suggests using a maximum of three weld repairs at one location in steel fabrication.

RÉSUMÉ

Les éléments de soudure en charpente métallique est une étape essentielle dans la fabrication métallique. Les contraintes résiduelles et les défauts de soudure sont souvent associés aux procédures de soudage. Selon l'importance de la fracture du matériau, le niveau des contraintes résiduelles et la taille des discontinuités et des failles dans les éléments de l'acier déjà soudé, des chanfreins peuvent être faits et des réparations seront nécessaires. Dans certains cas, cette réparation devra être répétée si des fissures supplémentaires résultent de la réparation par les procédés de soudure. En conséquence, les procédés de soudage et des caractéristiques de l'acier peuvent imposer des limites quant à la fracture du matériau et la taille des discontinuités dans la base du métal. Ces limites sont justifiées en grande partie à partir des études impliquant des plaques d'acier d'une épaisseur inférieure à 25mm, couramment utilisées. De nos jours, l'utilisation de grands profilés d'acier composés de plaques ou d'éléments d'épaisseur supérieure à 50 mm, a augmenté dans la construction métallique. Et ceci en raison de hautes spécifications exigées dans la conception actuelle qui nécessitent des structures très résistantes pour supporter les charges découlant, par exemple, des explosions et des grands tremblements de terre. Surtout que les exigences de charges placées sur la structure métallique ont été amplifiées par rapport à ce qui était considéré au cours des dernières décennies. Les spécifications et les procédures de soudage disponibles ont été utilisées dans la fabrication des éléments en acier d'épaisseur plus importante; néanmoins, les fabricants ont déclaré irréparables des fissures apparues après que les procédures de soudage ont été achevées. L'augmentation de l'épaisseur des éléments soudés ont donné comme résultats une plus grande retenue à la dilatation et à la contraction induites par la procédure de soudage. Ce qui conduit à une augmentation des contraintes résiduelles développées par le soudage. De plus, la probabilité d'avoir des discontinuités et des défauts dans l'acier épais est supérieure à celle trouvée dans des plaques plus minces. En outre, la variabilité de la résistance à la rupture d'un matériau augmente à mesure que l'épaisseur devient plus grande. En conséquence, le soudage de composants en acier d'importante épaisseur nécessite des spécifications séparées des procédés de soudage et des critères d'acceptation.

Dans cette thèse, une étude détaillée est réalisée sur la base d'une numérique et expérimentale charpente métallique. Selon cette étude, les procédures de soudage de tôles d'acier d'épaisseur supérieure à 50 mm utilisant un soudage à l'arc automatique sont évaluées. Une simulation par éléments finis de soudage est développée et validée avec des résultats mesurés d'une expérience de soudage. Des tests sur la tension et la rupture des matériaux sont effectués sur des plaques d’acier épaisses pour déterminer la variabilité de ces propriétés. Une approche probabiliste des discontinuités évaluées est proposée sur la base des tests de dureté, ainsi qu'une base de données compilée à partir de recherches antérieures. La simulation par éléments finis et de l'approche d'évaluation des discontinuités sont utilisés pour l'évaluation d'une étude paramétrique des principaux paramètres de la procédure de soudage. Selon les résultats de l'étude paramétrique, quatre procédures de soudage à l'arc submergé sont recommandées pour souder les plaques d'épaisseurs de 25 à 100mm. En outre, les critères d'acceptation sont développés pour les discontinuités existantes dans les plaques d'acier avant le soudage. En outre, deux recherches expérimentales sont menées; la première consiste à déterminer l'effet de cinq procédures de soudage à l'arc sur les qualités de soudure et sur les propriétés des matériaux dans la zone affectée par la chaleur. Les résultats des expériences sont en accord avec les résultats de l'étude paramétrique. Sur la base des résultats des expériences de soudure, deux spécifications de procédures de soudage sont recommandées pour le soudage de tôles d'acier épaisses. La deuxième expérience a pour but d'étudier l'effet de multiples travaux de soudage sur la zone affectée par la chaleur du métal de base à souder. Les résultats de cette étude proposent d'utiliser un maximum de trois réparations de soudage en un seul endroit dans la construction de l'acier.

PREFACE

In accordance with the "Guidelines for Thesis Preparation", this thesis is presented in a manuscript-based format. Authorships of the five articles are explained below.

Chapter 3:

Ibrahim, O.A., Lignos, D.G and Rogers, C.A. Proposed Modeling Approach of Welding Procedures for Heavy Steel Plates. Submitted to Engineering Structures Journal on 22 November 2015.

- Mechanical testing, numerical study as well as writing of the manuscript were conducted by **O.A. Ibrahim**.
- D.G. Lignos and C.A. Rogers provided supervision of the research and editing of the manuscript.

Chapter 4:

Ibrahim, O.A., Lignos, D.G and Rogers, C.A. A Probabilistic Approach for Assessing Discontinuities in Structural Steel Components Based on Charpy-V-Notch Tests. Prepared for submission to Engineering Structures Journal.

- Literature research, mechanical testing, statistical analysis as well as writing of the manuscript were conducted by **O.A. Ibrahim**.
- D.G. Lignos and C.A. Rogers provided supervision of the research and editing of the manuscript.

Chapter 5:

Ibrahim, O.A., Lignos, D.G and Rogers, C.A. Recommendations for Improved Welding Procedures for Thick Steel Plates through Finite-Element Analysis. Prepared for submission.

- Literature research and numerical analysis as well as writing of the manuscript were conducted by **O.A. Ibrahim**.
- D.G. Lignos and C.A. Rogers provided supervision of the research and editing of the manuscript.

Chapter 6:

Ibrahim, O.A., Lignos, D.G and Rogers, C.A. Experimental Investigation in the Effect of Welding Procedure Specifications on Thick Steel Plates. Prepared for submission.

- Experimental design, work and analysis of the results as well as writing of the manuscript were conducted by **O.A. Ibrahim**.
- D.G. Lignos and C.A. Rogers provided assistance in the experimental work, supervision of the research and editing of the manuscript.

Chapter 7:

Ibrahim, O.A., Lignos, D.G and Rogers, C.A. Experimental Investigation in the Effect of Welding Repair on the Heat Affected Zone Toughness and Size. Prepared for submission.

- Experimental design, work and analysis of the results as well as writing of the manuscript were conducted by **O.A. Ibrahim**.
- D.G. Lignos and C.A. Rogers provided assistance in the experimental work, supervision of the research and editing of the manuscript.

TABLE OF CONTENTS

LIST OF FIGURES

LIST OF TABLES

Chapter 1 INTRODUCTION

1.1 Scope and Motivation

Welding became the main method for joining structural steel components during the 20th century. However, welding is accompanied with defects and residual stresses formed due to the expansion/contraction associated with the uneven heating and cooling of the welding procedure. Nowadays, structural design criteria include requirements for buildings to withstand blast and seismic loading. This, along with the tendency of constructing taller buildings and longer spans has resulted in an increased demand for thick steel sections (thickness of 50mm or more). As the thickness of the welded steel becomes larger, the required welding heat input increases, as do the constraints to expansion and contraction. The final result is the development of higher welding related tensile residual stresses than would occur in plates of common thickness. Also the likelihood of the occurrence of imperfections (discontinuities) in the base metal of thicker plates is greater; these imperfections represent potential crack initiation locations if subjected to high stress. Moreover, cracks have been reported in the base metal of thick plates after welding (Fisher and Pense, 1987, Blodgett and Miller, 1993). Welding guidelines were developed in order to decrease the accompanied defects and residual stresses in welded steel assemblies and increase the integrity of a welded connection. Available welding specifications and guidelines in North America (CWB/Gooderham-Centre, 2005, ANSI/AISC 360-10, 2010, AWS D1.1, 2010, CAN/CSA-W59, 2013) have detailed welding procedures and acceptance criteria for a range of steel assemblies as well as sub-assemblies; the intent is to ensure the quality of the welded connection. However, the available welding specifications and guidelines were developed for commonly used thicknesses of steel material, which were typically less than 25mm. Updated specifications for the welding processes of thick steel plates need to be developed.

Current welding design requirements (CWB/Gooderham-Centre, 2005, ANSI/AISC 360-10, 2010, AWS D1.1, 2010, CAN/CSA-W59, 2013, CAN/CSA-S16-14, 2014) do not include specific provisions for welding thick plates and shapes. However, AISC Design Guide 21 (Miller, 2006) and Miller (2010) do give general recommendations for decreasing the shrinkage stresses and reducing the restraints through the welding process for all plate thicknesses. Based on ANSI/AISC 360-10 (2010) and AWS D1.1 (2010) a base metal with a minimum Charpy-V-notch absorbed energy (CVN) of 27 Joules at a maximum temperature of 21°C is required of steel materials. In recent years, as the demand for thick steel plates has increased in modern steel designs, fabricators have been using available welding specifications and guidelines for the welding of thick steel plates. Potential losses are associated with welding thick steel plates either due to the development of cracks that require time-consuming repairs or scrapped steel due to the presence of unrepairable cracks after the welding procedure. An example, provided by one of the largest steel fabricators in North America, involves the welding of 75mm thick steel plates of a built-up box column using partial joint penetration (PJP) butt welds, through an automated submerged arc welding procedure (SAW). The fabricator was forced to scrap over 400 tons of thick steel plates that developed unrepairable cracks after welding, with total industry losses exceeding $1MM. The fabricator followed recommendations of AWS D1.1 (2010) for prequalified welding procedures as well as guidelines given by Miller (2006). Hence, the motivation for this research is the necessity to address the increasing demand on using heavy steel components in steel construction as well as associated industrial losses. Consequently this requires the development of separate welding specifications and acceptance criteria for welding heavy steel components.

1.2 Structural Welding Standards and Acceptance Criteria

The main standards for structural welding in North America are AWS D1.1 (2010), AWS D1.8 (2009), ANSI/AISC 360-10 (2010), ANSI/AISC 358-10 (2010), ANSI/AISC 341-10 (2010) ,CAN/CSA-S16-14 (2014) and CAN/CSA-W59 (2013). AWS D1.1 (2010) is a comprehensive welding code in the United States of America (USA) that governs the design, fabrication, inspection, repairs and erection of welded connections. It also provides the prequalified welding procedures specifications (WPS), which when used mean that the fabricator is exempt from carrying out connection qualification tests. Additionally, AWS D1.1 (2010) sets the acceptance criteria for base metals, filler metals, discontinuities and cracks. AWS D1.8 (2009) provides supplement specifications for seismic design. AISC 360-10 (2010) is the design standard for steel building construction in the USA. It also provides acceptable steel designation and filler metals, and defines locations where welded connections are required, in addition to setting the requirements for splices in heavy sections. AISC 358-10 (2010) provides specifications for prequalified connections in steel moment frames designed for seismic applications. These standards invoke all provisions of AWS D1.1 except as noted therein. AISC 341-10 (2010) contains seismic provisions for structural steel buildings and it invokes the provisions provided by AWS D1.8 except as noted therein. CAN/CSA-S16 (2014) is the primary design standard for steel building construction in the Canada. It also provides similar specification as AISC 360. Finally, CAN/CSA-W59 (2013) is the primary steel welding standard in Canada; it includes prequalified welding details for joint and welding processes, inspection procedures and acceptance criteria for the base metal and filler metal. The provisions of this standard work in conformity with the provisions of AWS D1.1.

Steel fabricators follow the requirements of these specifications along with guidelines provided by Miller (2006) and Miller (2010) for the welding of thick steel plates. The SAW procedure is recommended for welding assemblies requiring deep penetration; this is attributed to its high deposition rate. In such welding procedures the weld pass is submerged under a granular material called the flux that shields the weld arc and the molten metal from the surrounding atmosphere. Submerged arc welding is an automated welding procedure, suitable for long uninterrupted weldments. Current welding specifications (AWS D1.1, 2010, CAN/CSA-W59, 2013) provide the prequalified welding assemblies, dimensions and details; they also mandate 110^{o}C preheat and inter-pass temperatures for structural steel plates with thickness greater than 65mm, at a distance from the weld equal to the thickest welded part or 75mm. Inspection of the base metal and filler metal has to be performed before and after the welding procedure to ensure that imperfections, cracks and discontinuities are within acceptable limits. According to AWS D1.8 (2009) embedded discontinuities of length less than 6mm and at more than 3mm from the plate surface are acceptable. Other acceptance criteria are provided by AWS D1.1 according to the various methods of non-destructive testing (NDT). Fabricators also follow qualitative recommendations provided by the welding specifications (AWS D1.1, 2010, CAN/CSA-W59, 2013), as well as studies performed to determine and reduce the induced residual stresses and to limit the formation of cracks and discontinuities (Miller, 2010). It is worth mentioning that prequalified welding procedure specifications as well as discontinuities acceptance criteria provided by AWS D1.1 and CAN/CSA-W59, which are used in fabrication of welded thick steel plates, were qualified through tests conducted on plates of 25mm thickness according to feedback from industry. Most of the prequalified welding procedures provided by AWS D1.1 and CAN/CSA-W59 for 25mm thick steel plate are allowed to be used for plates of unlimited thickness. Special prequalified welding procedures and acceptance criteria are essential for the fabrication of welded thick steel assemblies. These procedures should be based on thorough tests on thick plate assemblies and may be separate from available procedures for thinner plate welds.

1.3 Review of Related Studies

Few studies have been conducted with the aim to develop separate acceptance criteria and welding procedures for thick steel plates. However, related studies were conducted to evaluate welding residual stresses in thick plates, as well as the effect of the welding parameters on the resulting residual stresses. Other efforts were carried out to suggest qualitative guidelines for fabricators to minimize the welding residual stresses in the base metal of thick plates and to reduce crack initiation after welding. Research has also been conducted to study other aspects of the welding procedure that may lead to crack development, such as repeated weld repairs that were conducted for stainless steel plates. Following is a brief review of these studies.

In 1969 the research project “Residual stresses in thick welded plates” was launched at Lehigh University. The aim of this research was to study the residual stress distribution in thick steel plates used in built-up H shaped sections, the effect of welding parameters on the residual stress distribution and the effect of the developed residual stresses on the column strength of the built-up section. Brozzetti et al. (1971) performed an experimental investigation of the effect of welding parameters, such as preheating, number of passes and welding speed, on the column strength of a built-up H shaped section of maximum plate thickness of 50mm. The main findings of this study were: (1) the variation in the through thickness residual stresses is only significant in the heat affected zone (HAZ), although it was substantially reduced at regions away from the welding area a distance more than 50mm; (2) the residual stresses at locations near the welding area were equal to the yield strength of the weld metal; (3) no significant improvement to the residual stress distribution is achieved by increasing the preheat temperature more than the normal temperature recommended by AWS D1.1 (2010); and (4) the number of passes have no effect on the column strength of welded built-up H shaped sections.

As part of the same project at Lehigh University, Bjorhovde et al. (1972) conducted experiments to determine the residual stresses in 20 steel plates with flame cut edges and 6 with as-rolled edges of thicknesses ranging from 40mm to 150mm. Some of the plates were tested in the as-manufactured condition, the others had weld beads at the centre or at the edges to simulate the welding locations for plates used in a built-up H shaped section. The main conclusions of these tests were: (1) for the as-manufactured plates with as-rolled edges, the residual stresses are in the shape of a parabola. The larger the thickness of the plate the larger the compressive stresses at the edges. Also as the thickness increases the likelihood of tensile residual stresses around the plate's centerline increases; (2) the heat input from the flame cutting procedure causes changes in the material properties at a narrow region adjacent to the edges. Additionally tensile residual stresses are developed at the plate's edges, these stresses may be higher than the yield strength of the plate material; and (3) the welding of heavy plates mainly affected the residual stresses in a relatively small region around the weld.

Bate et al. (1997) studied the residual stress distributions in different joints and their effect on the susceptibility of offshore structures to failure. The aim of this research was to identify representative residual stress distributions and classifications through data obtained from past experimental works. Additionally, Bate et al. studied the factors affecting the residual stress distribution such as the thickness of the base metal, the constraints and the heat input of the welding procedure. Through this investigation it was concluded that the residual stress distribution mainly depends on the applied constraints during the welding procedure; e.g. in a setup such as a flat butt welded plate in which the applied restraint is unknown the measured residual stress distribution varies and cannot be predicted. Moreover, upper bound residual stress profiles were suggested, for each joint type, to provide an estimate for residual stresses.

In more recent years Yang (2008) studied the effect of the welding current and travel speed of the SAW procedure on the physical and mechanical properties of ASTM A516 Gr.70 (2015) steel used in pressure vessels and ASTM A516 Gr.70 (2015) steel used in wind turbine towers, the maximum thickness of the plates used in this study was 17mm. The main conclusions of this investigation were that high welding travel speed and welding current result in severe undercuts. Low heat input caused lack of penetration defects. The fracture toughness of the heat affected zone (HAZ) increased with higher welding travel speed and current. Through his study of different combinations of the welding travel speed and current, Yang recommended using a welding current of 800 A and welding travel speed of 12.3 mm/s to achieve good weld quality and productivity, and to obtain mechanical properties of the HAZ that are similar to the base metal.

As the problems with welding thick steel plates became more pressing, Miller (2010) provided a set of recommendations, from practical and field proven examples, for fabricators to successfully weld heavy sections. According to Miller the problem of welding heavy sections is divided into four categories: high shrinkage strains, high restraint, cracks and/or crack-like stress raisers and reduced material resistance to fracture. Moreover, recommended fabrication procedures and principles were provided to overcome these welding related challenges. To lessen shrinkage strains Miller suggested to reduce the welding area where possible and to use the fewest number of passes to finish the weld. Additionally, he recommended limiting back gouging to only that which is required, applying higher preheat temperature, using weld metals with the lowest possible strength and utilizing post weld techniques (thermal relief and peening) that reduce these stresses. The second challenge was to reduce restraints. This can be achieved by welding small subassemblies then joining them into the final assembly, welding large and rigid components first, use of a welding sequence so that the shrinkage is balanced on opposite sides of the member, and to include gaps when welding tightly fit assemblies to allow movement of the member during welding. As to eliminate crack and/or crack-like stress raisers, it was recommended to use preheat, visually inspect thermally cut surfaces, grind thermally cut surfaces and use non-destructive testing, utilize mechanical cutting when possible and complete high restraint weldments without interruptions. Finally, to ensure minimum levels for fracture toughness, minimum fracture toughness requirements must be specified for both the base metal and the weld metal materials, and areas where low toughness is expected should be tested. As demonstrated, these recommendation are of a qualitative nature.

Deng and Kiyoshima (2011) studied the effects of welding parameters on the resulting residual stresses. In particular, they examined the effect of the weld deposition sequence and direction on the residual stresses at the weld start/end location for a weldment that was divided in length. Experiments and numerical evaluations were conducted on austenitic stainless steel plate of yield strength 276 MPa and 55mm thickness. The numerical simulation of the welding procedure was achieved through uncoupled thermo-mechanical finite element analysis; an independent simulation of the heat transfer through the steel plate was developed and the resultant temperature distributions were exported to a stress analysis model. The results indicated that the transverse residual stresses are more sensitive to the welding sequence than the longitudinal stresses.

Lin et al. (2012) conducted an experimental investigation into the effects of repeated weld repair on the microstructure and toughness of stainless steel plates. Two weld repair specimens were first fabricated using the gas tungsten arc welding (GTAW) process, and then the weld was repaired by back gouging and welding using the shielded metal arc welding (SMAW) process. The first specimen was repaired one time, and the other specimen was repaired five times. The results showed that there is no significant effect on the boundaries of the fusion zone. It was observed that the orientation of the texture of the HAZ had changed for the five times weld repair specimen. For the toughness tests there was no significant effect of the number of weld repairs on the fracture toughness values, however the fracture characteristics for the five times repaired specimens had changed such that the fracture occurred through the stainless steel grains implying a ductile fracture; whereas the energy is required to break the steel grains is less than that required to break the bonds between the grains. On the other hand, for the one time repaired specimen the fracture occurred between the stainless steel grains implying a brittle fracture whereas. In conclusion, increasing the number of weld repairs increases the energy between stainless steel grains.

Jiang et al. (2013) also performed an experimental study on the effect of multiple weld repairs on the microstructure, hardness and residual stresses of a stainless steel clad plate. The experiments included four specimens of one, two, three and four weld repairs. The flaws on the surface of the specimens were back gouged to a depth of 4mm and then welded using tungsten inert gas welding process. It was concluded that with the increase of weld repair number the fusion line thickness increases. Also the residual stresses and hardness at the HAZ increases with the increase in number of weld repairs. For stainless steel clad plates Jiang et al. (2013)recommended that the weld should not be repaired more than two times.

As demonstrated, past research has addressed the welding procedure and welding repair effects on steel plates and residual stress development. Studies that were conducted for the welding procedures of thick steel plates suggested qualitative recommendations to minimize residual stresses and cracks development. On the other hand, most of the available research concerned with this subject were established for stainless steel plates or structural steel plate of thickness less than

50mm. As such, quantitative recommendations are required along with qualitative principles available in the literature to ensure the successful welding of thick steel plates. Moreover, acceptance criteria for flaws and imperfections in the base metal of thick steel plates require improvement to avoid crack initiation triggered by the residual stresses induced by the welding procedure. Additionally, experimental studies that address the effect of weld repairs on the properties of the heat affected zone of structural steel plates are required due to the lack of relevant information.

1.4 Research Objectives

The main purpose of this thesis is to provide guidelines on how to assess the discontinuities observed in butt-welded ASTM A572 Gr.50 (2013) steel plates of thicknesses greater than 25mm comprising a partial joint penetration groove weld fabricated using the submerged arc welding procedure. Through the findings of this research a steel fabricator will have access to quantitative guidelines for welding thick steel plates, which can be followed to produce a suitable residual stress distribution in the base metal. Furthermore, by using these guidelines it will be possible to determine the likelihood of crack initiation through the base metal after the welding procedure. A second objective of this research is to experimentally study the effect of different welding procedures for thick steel plates, with different heat input values, on the heat-affected zone of the base metal, as well as the quality of the weld. The final objective of this research is to examine the effects of number of weld repairs on the base metal heat affected zone of A572 Gr. 50 steel through full-scale experiments.

1.5 Methodology

A methodology has been developed to achieve the main objectives of this thesis as stated in the previous section. The first challenge in providing welding guidelines for thick steel plates is to develop a validated numerical simulation for the welding procedure. This is achieved through the following:

- Developing detailed finite element models to simulate the welding procedures for heavy built-up box columns, using the nonlinear finite element (FE) package ABAQUS Dassault Systemes Simulia Corp. (2011). Two- and three-dimensional (2-D and 3-D) models are developed for this purpose. The simulation is divided into two separate models, one using heat transfer elements to determine the heat flow through base metal because of welding; the second model is a stress analysis model that incorporates the temperature distribution results from the first model and transforms them into strains and stresses. This technique has been used for weld modeling in previous research (Brickstad and Josefson, 1998, Pilipenko, 2001, Deng and Kiyoshima, 2011).

- Updating the material model of the welding simulation. This is obtained through material tests (tensile and Charpy-V-Notch (CVN) tests) for a case study of a welded heavy built-up box column that experienced cracks after welding, at different locations through the thickness. The built-up box columns are fabricated of 75mm thick ASTM A572 Gr.50 (2013) steel. Consequently, the results are compared with the requirements of Specifications ASTM A572 Gr.50 (2013), AWS D1.1 (2010) and CAN/CSA-W59 (2013). Furthermore, a welding experiment is performed using the same steel plates as the case study, for which temperature results are recorded during the welding procedure. These measurements are used for validation of the welding simulation procedure.
- A mesh sensitivity study is conducted for the 3-D model to determine the appropriate size of the finite element to provide accurate results from the welding simulation. Nominal values of the material properties are used for this preliminary model. Material properties such as the elastic modulus, yield stress, tensile strength, thermal expansion coefficient, thermal conductivity, specific heat and creep at elevated temperatures are considered.
- The developed welding procedure simulation is validated with the results from the temperature measurements from the welding experiment and observations from the case study box column.

The second challenge is to develop criteria to evaluate the potential for crack initiation under tensile stresses, which incorporate the uncertainty of the fracture toughness of the steel material under consideration. The following steps are employed:

- In addition to the eighty-eight CVN tests that are conducted as part of this thesis, CVN data are collected from the literature (Suwan, 2002).
- The CVN database is then classified to datasets according to the steel plate thickness, material and test temperature.

- For each dataset, statistical distributions are tested and fitted through logistic regression (Chatterjee and Hadi, 2006).
- By applying linear fracture mechanics; an expression is developed to determine the probability of a crack to initiate according to its stress intensity factor, plate thickness and temperature. Hence, the developed acceptance criteria of a crack or discontinuity depends on its size as well as the probability of it to initiate under the applied stresses.

Accordingly, after developing a validated numerical simulation for the welding procedure and acceptance criteria for cracks and discontinuities that take into account the uncertainty in fracture toughness, a parametric study of the welding procedure is performed. In this study the developed detailed finite element models are employed. The parametric study is established as follows:

- The parametric study is divided into two phases; the first phase contains parameters that are related to the heat input and cooling rate of the welding procedure, such as the welding temperature, welding travel speed and preheat and inter-pass temperatures. The second phase deals with parameters of the weld detail such as the base metal material, number of passes and plate thickness.
- Each parameter is assessed according to the resulting residual stress distribution after each welding pass, and the corresponding critical crack size according to a suggested acceptable probability of crack initiation of 5%.
- Through the parametric study the most effective parameters on the residual stress distribution and crack initiation are identified.
- These parameters are then used to recommend acceptance criteria for discontinuities in the base metal before welding according to the plate thickness and restraint condition.

To study the effect of different welding protocols on the HAZ and the weld quality of thick steel plates a welding experiment is conducted on two 75mm thick steel plates using five different welding protocols with different heat inputs. Weld qualification tests are conducted including, side bend, reduced section tension, all weld metal tension, CVN tests and microscopy, as well as chemical composition tests. The results are used to identify the heat input effects on the weld material properties, HAZ size and chemical composition. Another welding test is conducted to study the effect of the number of weld repairs on the base metal. Two 25mm ASTM A572 Gr.50

(2013) steel plates are welded using the SAW process, for which the length was divided into ten segments. Each segment is back gouged and repaired, using the flux core arc welding process (FCAW), one time more than the previous segment. This approach provides specimens having from one to nine weld repairs, in addition to a control specimen. The comparison of the results shows the effects of weld repairs on the material properties of the base metal.

1.6 Outline

Essential theoretical background related to welding procedures of steel plates and assemblies is discussed in Chapter 2. It involves a detailed description of the submerged arc welding technique and its parameters, inspection methods, weld repair and weld qualification tests. In addition, heat transfer theory and material properties required for its modeling are included. Also, the chapter comprises the steel material properties at elevated temperatures, as well as the steel creep properties at elevated temperatures. Linear fracture mechanics and crack initiation mechanism are discussed as well. Finally, relevant statistical operations are presented such as statistical distributions, goodness of fit test and logistic regression.

Chapter 3 focuses on the development and validation of the FE simulation for the welding procedure. A detailed description of the case study welded heavy built-up box column is included in this chapter as well as a description of the weld experiments conducted to measure temperature values for the validation of the FE simulation. Additionally, tensile and CVN test results from specimens extracted from different locations of the case study box-column are presented. A comprehensive description of the FE modeling approach utilized to simulate the welding procedure is provided. The effect of steel creep on the resulted residual stresses is studied. This chapter is concluded by comparing the temperature results from the FE simulation and the weld experiment and also integrating the residual stress results of the case study heavy built-up box column model with the material fracture toughness results to validate that crack initiation will occur as it did in the fabrication shop.

In Chapter 4 a probabilistic approach is introduced for developing acceptance criteria on how to assess discontinuities and cracks in steel plates. A CVN database is constructed based on collected data in addition to tests conducted on specimens from the case study box column. The CVN database is divided into datasets based on plate thickness, material type and test temperature. This chapter also contains a discussion of the statistical treatment of each dataset, including distributions, goodness of fit test and logistic regression. An expression is proposed to calculate the probability of crack initiation and tables of constants for each dataset are provided. This chapter also shows a study of the effect of different parameters on the probability of crack initiation.

In Chapter 5 the parametric study, conducted on the parameters of the welding procedure, is presented using the validated FE simulation and crack acceptance criteria introduced in Chapters 3 and 4, respectively. The chapter includes the two phases of the parametric study. The effect of each parameter on the resulting residual stresses and probability of crack initiation is likewise provided. Also in Chapter 5 the critical parameters of the welding procedure that can produce more suitable residual stress distributions than commonly used welding procedures are identified. In conclusion, the guidelines for welding thick steel plates using SAW and provides acceptance criteria for thick steel plates intended for welding in minimally restrained and highly restrained conditions are proposed in this chapter.

In Chapter 6 the welding experiments conducted to determine the effect of different welding procedures on the HAZ and the quality of the weld are discussed. The test setup and the properties of each welding procedure used in the test are presented. Additionally, the qualification tests conducted for each welding procedure are discussed. A comparison between the different welding procedures is also provided.

In Chapter 7 the welding experiments performed to determine the effect of the number of weld repairs on the base metal HAZ are presented. The experimental setup and the locations of the test specimens extracted from each segment are shown. A discussion of the results of the experiments is also provided.

Chapter 8 is a summary of the most significant findings of this research to provide quantitative guidelines for butt-welding thick steel plates using the SAW procedure

Chapter 2 LITERATURE REVIEW

2.1 Introduction

A presentation of the material that forms the essential background of the research documented in this thesis is provided herein. It includes a study of the properties of the welding procedure performed for thick steel plates as well as types of discontinuities associated with it and the methods utilized for inspection. Also the temperature effects on the steel metallurgy and behaviour of the steel material at elevated temperatures was investigated. In order to develop a numerical simulation of the welding process an investigation on the heat transfer mechanisms was performed. Moreover, a review of linear fracture mechanics and crack propagation mechanisms was conducted for the development of discontinuity and crack assessment criteria based on fracture toughness data.

2.2 Welding of Steel Plates

The most common welding practice in structural steel fabrication is arc welding. Arc welding utilizes an electric arc to produce heat to fuse metal parts. In most procedures of arc welding a filler (weld) metal is added to a previously prepared joint that accommodates the molten weld metal and the fusion is achieved through it. The challenge of welding metal parts through heating is that the resulting molten metal can dissolve large quantities of gases present in the atmosphere such as oxygen and nitrogen, as the molten metal cools these gases react with metallic atoms forming oxides and nitrides. Moreover, the gas bubbles exiting the molten metal as it solidifies leave surface cavities. In addition, some gasses such as nitrogen can be left within the solidified steel, which may result in embrittlement of the metal. Consequently, the molten metal has to be shielded from the ambient atmosphere; different arc welding processes are available with various methods to shield the molten metal from the atmospheric gases (AWS D1.1, 2010, CAN/CSA-W59, 2013). The choice of the welding process to be used depends mainly on the fabricator and the type of welding assembly (Miller, 2006). For thick steel plates the most common welding process used in fabrication is the submerged arc welding (SAW) process due to its high weld deposit rate as well as high productivity. Within Sections 2.2.1, 2.2.2, 2.2.3 and 2.2.4 a presentation of the SAW process, along with the welding defects and methods of inspection and the qualification tests for a welding procedure are found.

2.2.1 Submerged arc welding process

The submerged arc welding process has been successfully used for years in structural steel fabrication as well as for the pressure vessel and the ship building industries. In the SAW process, the molten metal is shielded by a blanket of a granular material, known as flux, which completely covers the welding area throughout the welding procedure. The filler metal is fed through the wire feeder with a controlled speed to adjust the deposition rate. The flux dispensed on the molten metal forms a glasslike slag that is less dense than the molten metal; so it floats on its surface and acts as a protective layer against the atmospheric gases. After finishing the welding pass, the unused granular flux layer is collected by a vacuum and recycled to be reused for the subsequent welding passes. Figure 2.1a shows the three main components of the SAW process; the welding electrodes, flux dispenser and vacuum. Figure 2.1b shows the flux covering the weld metal during the welding procedure of the SAW process.

The SAW process is either semi-automatic or automatic. In this process the arc welding sparks are shielded by the flux; hence it is relatively safe and comfortable for the welder to operate without the need of shields and guards to protect against arc flashes. Another advantage of this process is its high deposition rate, which enhances the welding speed and productivity. It also provides deep penetration that in some cases may eliminate the need of joint preparation (CWB/Gooderham-Centre, 2005). Furthermore, parallel electrode welding can be used such that two electrodes are fed with the arc controlled in only one electrode. Also multiple electrode welding (tandem arc welding) can be utilized where each electrode arc is controlled individually (Miller, 2006). Welds produced by the SAW process are of excellent spatter free appearance that rarely requires enhancements; this is significantly important for architecturally exposed structural steel (CWB/Gooderham-Centre, 2005, Miller, 2006). On the other hand, due to the granular nature of the flux, this welding process is limited to welds in the horizontal position. Another drawback is that the welder cannot see the weld puddle during the welding process, which requires an experienced operator to achieve the designed welding profile. SAW is a prequalified process in AWS D1.1 (2010) and CAN/CSA-W59 (2013), meaning that welding procedure specifications

(WPSs) using a SAW process can be qualified if they meet the requirement of the qualification tests and are available in AWS D1.1 (2010) and CAN/CSA-W59 (2013).

2.2.2 Welding defects

The defects resulting from the welding procedure include crack propagation, undercuts, lack of fusion, incomplete penetration as well as discontinuities such as porosity. Crack propagation is the most serious welding defect type of those considered not acceptable by current welding specifications in North America (AWS D1.1, 2010, CAN/CSA-W59, 2013). There are two types of weld cracking; hot cracking that occurs during the welding procedure and cold cracking that occurs while the metal cools after the welding procedure has been completed. Hot cracking is commonly developed in the weld but can also occur in the heat affected zone (HAZ). This type of crack is formed as a result of shrinkage strains during the solidification of the weld metal. Centerline cracking is the most common form of hot cracking; it is developed in the centerline of the welding bead as shown in Figure 2.2. According to Blodgett et al. (1999), a centerline crack can result for the following three reasons; first the segregation of the weld metal due to low melting point induced by contaminants from the base metal such as phosphorus and sulphur to portions of the weld metal, where the low melting point portion of the weld metal is forced to the center and solidifies last. This can be reduced by limiting the contaminants of the base metal or using a buttering layer of low energy weld on the surface of the base metal before welding. The second reason is due to the bead shape that is deep and narrow, SAW welding process is sensitive to this case when deep penetration is required, and in this case the solidifying grains intersect in the center of the bead with no fusion. A solution to this phenomena is to use weld beads with a width to depth ratio greater than 1 (Miller, 2006). Finally, a centerline crack can occur as a result of the weld surface profile, since a concave weld surface profile induces surface tension stresses due to the shrinkage of cooling weld metal. On the other hand a convex surface will overcome this condition.

Cold cracking develops in the HAZ due to high induced shrinkage stress, material sensitivity and hydrogen diffusion in steel and migration to dislocations. Lamellar tearing is a type of cold crack in which shrinkage stresses are perpendicular to the planes of weakness, and discontinuities in the base metal are excited to propagate. This type of cracking can be reduced by using preheat and post weld heat treatment of the steel. For steel types sensitive to hydrogen assisted cracking, such as quenched and tempered ASTM A514 and A517 Grade 100, AWS D1.1 (2010) requires that inspection to take place 48 hours after the completion of the welding process. Discontinuities located in the HAZ can also be triggered to propagate if the shrinkage stresses reach a critical level. Another type of cracking is transverse cracking (Figure 2.2); it is the least common crack type, which happens when using a weld metal of significantly over matching strength to the base metal.

Furthermore, other weld defects can occur that depend mainly on the welder and the employed welding procedure. Some defects have acceptable limits such as porosity, and some are not acceptable by the specifications (AWS D1.1, 2010, CAN/CSA-W59, 2013) and require repairs, such as lack of fusion. Figure 2.2 shows an illustration of the most common weld defects. An undercut occurs when a cavity is formed at the weld toe. Lack of fusion between the weld metal and the base metal may occur due to failure to choose a proper electrode type or welding procedure, also poor surface preparation can result in lack of fusion. Additionally, incomplete penetration may occur due to insufficient current density, improper joint detail and slow welding travel speed. The welding procedure is also susceptible to slag inclusion in the weld metal due to not completely removing slag from the surface of the previous welding pass, it can be minimized through proper joint design and choosing a suitable welding procedure. Porosity is the most common weld discontinuity type; it consists of small spherical or cylindrical particles of entrapped gases which result due to inadequate shielding during the welding procedure. Current specifications (AWS D1.1, 2010, CAN/CSA-W59, 2013) provide limitations for weld defects depending on type, size and distribution. For the SAW process as a result of the hidden weld bead under the flux one of the most common defects is centerline cracking due to improper width to depth ratio of the weld bead.

2.2.3 Welding inspection and repairs

The inspection of welds is divided into three categories; visual inspection, non-destructive tests (NDT) and destructive tests, all of which are used for the qualification of the employed welding procedure. The purpose of the inspection tests is to ensure the quality of the welded assembly and to determine the weld defects (Section 2.2.2) including their sizes and locations. These defects are then compared with the acceptance limits of the specifications (AWS D1.1, 2010, CAN/CSA-W59, 2013), hence it can be determined if a weld repair is required. This section discusses the visual inspection criteria as well as common non-destructive tests and weld repairs. Destructive tests are discussed in Section 2.2.4.

Visual inspection (VT) is considered the most efficient method of inspection as it does not need sophisticated equipment and can by itself improve the weld quality and prevent the development of weld defects (Blodgett et al., 1999). Visual inspection involves three stages; the first stage starts before welding and it includes a review of workshop drawings, checking the qualification of the welding procedure (prequalified or qualified by test), inspecting the compliance of the used equipment with the qualified welding procedure, checking for discontinuities in the base metal, welding joint alignment, preheat, ambient welding conditions and setting up a recording system for the inspection results (AWS D1.1, 2010, CAN/CSA-W59, 2013). The second stage of visual inspection takes place during the welding, according to AWS D1.1 (2010) and CAN/CSA W59 (2013) the inspection includes verifying the quality of the weld root bead, checking inter-pass temperatures, conformance of the welding procedure, inspection of the welding sequence, quality of each welding layer and the cleaning between each welding pass. The final stage of visual inspection takes place after the welding has finished, at this stage a welding inspector should inspect the final appearance of the weld (look for porosity, undercuts and other visible defects), inspect the final weld size and length, confirm the presence of all required welds and check for excessive distortions (AWS D1.1, 2010, CAN/CSA-W59, 2013).

An example of a non-destructive test is magnetic particle inspection (MT), which uses magnetic flux that is spread on the surface of the welded assembly. When a magnetic field occurs a change in the pattern is detected in the vicinity of a discontinuity in the tested piece. This method of inspection is effective in detecting discontinuities located at the surface and slightly subsurface (Blodgett et al., 1999). The magnetic particle test is normally utilized as an enhancer of visual inspection as it is able to reveal surface discontinuities. This method is characterized by its speed and efficiency in detecting surface and subsurface discontinuities (Blodgett et al., 1999).

A second example of a non-destructive test is radiographic inspection (RT), which utilizes X-rays and gamma rays that pass through the weld on to a photographic film on the other side of the joint (Blodgett et al., 1999). Precautions must be taken to protect the workers from exposure to radiation. As the radiation passes through the steel, part of it is absorbed by the material such that thin material absorbs less radiation than thick materials. As a result, more radiation will reach the photographic film on the other side of the joint in regions that have discontinuities than in regions with no discontinuities; hence, discontinuities appear as dark regions on the film. The radiographic test is mostly effective for discontinuities of volumetric nature such as slags and porosity, but less effective for cracks (can miss cracks that are parallel to the film plate). This method of inspection is suitable for complete joint penetration (CJP) groove welds and is not suitable for partial joint penetration (PJP) groove welds and fillet welds. Reading the results depends mostly on the skill of the technician. AWS D1.1 (2010) and CAN/CSA-W59 (2013) provide acceptance criteria for the reading of the RT inspection.

A final example of a non-destructive test is ultrasonic inspection (UT), which is established by applying high frequency sound waves through the material, which are reflected from the back surface of the material as shown in Figure 2.3, whereas a discontinuity-free metal will transmit all the applied sound waves to the receiver. If a discontinuity is present between the transmitter and the back surface of the material, a portion of the waves will be reflected back to the receiver and an intermediate signal will be received indicating the presence of a discontinuity. The magnitude of the reflected signal determines the size, type and orientation of the discontinuity. Comparing the reflected signal to the one reflected from the back wall determines the location of the discontinuity. This method is very sensitive to small discontinuities. It is most sensitive to planar discontinuities; for example cracks, laminations and planes of incomplete fusion (Blodgett et al., 1999). Spherical and cylindrical discontinuities can be missed using UT inspection. The ultrasonic test is most effective for CJP, and can also be used with PJP but the interpretation of the results may be difficult in this case. AWS D1.1 (2010) and CAN/CSA-W59 (2013) provide acceptance criteria for the reading of the UT inspection. Additionally AWS D1.8 (2009) provides limitations for discontinuities in the base metal detected by UT testing; such that no discontinuities are allowed within 3mm from the material surface and discontinuities of 6mm or less in length are allowed at depth more than 3mm from the material surface.

If inspection resulted in the detection of unacceptable welding defects, a weld repair is required. This procedure includes the removal of weld metal or portions of the base metal by machining, grinding, chipping or gouging. The unacceptable portions are removed and the surface cleaned thoroughly before welding again. The deposited weld metal must compensate for the absence of the weld removed to regain the designed weld size according to AWS D1.1 (2010) and CAN/CSA-W59 (2013). A weld repair may be repeated until the unacceptable defects are not present.

2.2.4 Welding procedures qualification

Current welding specifications (AWS D1.1, 2010, CAN/CSA-W59, 2013) provide a number of prequalified welding procedure specifications (WPSs) for a variety of welded joints that can be used by the fabricator without further testing. Submerged arc welding is an example of a prequalified welding procedure. These specifications comprise the base metal steel grade, welding electrode specifications, welding process, joint preparation geometry, base metal thickness, root opening size (for groove welds), welding position, weld size, minimum preheat/inter-pass temperatures and tolerances. If the engineer or fabricator chooses not to use a prequalified welding procedure for production welding, this selected procedure must pass qualification tests to ensure the weld integrity and quality. First a test plate is welded using the suggested WPS, then qualification tests are conducted. The type and number of qualification tests depend on the base metal thickness and the type of welding (for example complete joint penetration CJP), these tests are; visual inspection, non-destructive tests (NDT), side bend tests, reduced section tension, all-weld metal tension, Macroetch and Charpy-V-Notch test (CVN). If a specimen fails the requirements of AWS D1.1 (2010) and CAN/CSA-W59 (2013) two retests of the failed test are allowed. For thick materials (over 38mm) a failure of a specimen requires retesting specimens from two additional locations in the test specimen. Visual inspection and NDT are conducted as discussed in Section 2.2.3.

Side bend test specimens are taken from the welded test plate around the welded area; such that the centerline of the specimen coincides with the centerline of the weld as illustrated in Figure 2.4a. The specimen is placed in the bend test jig shown in Figure 2.4b with the weld and HAZ centered with the centerline of the plunger with the weld opening facing the die. The specimen is forced by the plunger into the die until the specimen is bent into a U-shape as shown in Figure 2.4c. Then the specimen is removed and inspected. According to AWS D1.1 (2010) and CAN/CSA-W59 (2013) the convex surface of the bent specimen shall be examined for discontinuities, where discontinuities greater than 1mm are not acceptable. Also if the sum of discontinuities between 1mm and 3mm in size is greater than 10mm, then the specimen will be rejected. A corner crack of 6mm is acceptable as long as it is not a result of a fusion defect such as slag inclusion.

The reduced section tension test is a traditional coupon tension test of a specimen taken from the welded test plate transverse to the weld direction and with the weld material at the center of the specimen. The specimen is then measured and pulled up to rupture. The tensile strength is obtained by dividing the maximum load achieved by the cross-sectional area of the specimen. According to AWS D1.1 (2010) and CAN/CSA-W59 (2013) a specimen is considered acceptable if its tensile strength is not less than the minimum specified tensile range of the base metal used in the test.

An all weld metal tension test is similar to the reduced section test, however the specimen is taken in a direction parallel to the weld direction and the material of the specimen is all of the weld metal. This test is conducted to confirm the properties of the weld metal and follows the requirement of a tensile coupon test in conformance with ASTM A370 (2014).

In a Macroetch test a specimen is cut comprising the weld and HAZ areas. The specimen is prepared and polished, then etched using a suitable solution to provide clear definition of the weld. For a specimen to be accepted by AWS D1.1 (2010) and CAN/CSA-W59 (2013) a PJP groove weld size has to be equal to or greater than the specified weld size, welds are required to have no cracks, fusion with adjacent layers of the weld metal, weld profile as specified by the detail with acceptable tolerances and no undercut exceeding 1mm is allowed.

The Charpy-V-Notch (CVN) test produces the energy required to break a notched specimen that is hit by a pendulum hammer. The CVN value derived from the difference in the height of the hammer before and after hitting the specimen, hence the difference is attributed to the energy absorbed by the specimen. Specimens are cut such that their longitudinal axis is perpendicular to the welding direction of the welded test plate. WPS qualification AWS D1.1 (2010) provides two options for testing; option A and B of three and five test specimens respectively. For option A two of the three specimens shall be equal or exceed the minimum average specified value (27J at specified temperature for base metal of yield strength $\leq$ 345 MPa), one specimen's CVN value can be lower than the minimum average specified value but not less than the minimum individual CVN value (20J). For option B the maximum and minimum CVN values are discarded while the other 3 are treated as per option A. this test is repeated three times; first the centerline of the notch of the CVN specimen is at the weld metal centerline, second is when the notch centerline is at 1mm from the fusion line at the HAZ, last is when the notch is at 5mm from the fusion line in the HAZ.

2.3 Structural Steel Metallurgy and Material Properties

The metallurgy of structural steel is one of the most important aspects required in the investigation of welding procedures for structural steel plates. High Strength Low Alloy steel (HSLA) is the commonly used type of steel in construction. This type of steel is of low carbon content (0.05 to 0.25 wt.%) and up to 2 wt.% of manganese and small additions of alloying elements such as niobium, aluminum, vanadium, titanium, molybdenum, copper, and zirconium (Jefferson and Woods, 1962, De Garmo et al., 2011). It is characterized by high yield strength, ductility and good weldability (Jefferson and Woods, 1962, CWB/Gooderham-Centre, 2005).

2.3.1 Heat treatment of structural steel

At room temperature HSLA steel is composed of two main crystalline structures; Ferrite and Pearlite. Ferrite is the crystalline structure of iron at room temperature and it is body centered cubic as shown in Figure 2.5a. Pearlite is a mixture with certain ratios of ferrite and iron carbide atoms which are called cementite. At high temperatures the HSLA steel crystalline structure is face centered cubic iron as shown in Figure 2.5b, with soluble carbon atoms, and is called Austenite. This structure has more room to accommodate carbon atoms than ferrite. A carbon content of 0.83 wt.% is the amount of carbon that saturates the body centered cubic iron atoms; therefore in this case at room temperature enough iron crystals are transformed to Cementite such that their ratio to Ferrite is that which makes the whole steel crystalline structure Pearlite. As the carbon content increases to more than 0.83 wt.% more iron crystals are transformed to Cementite and the mixture becomes that of Pearlite and Cementite (Jefferson and Woods, 1962) as illustrated in Figure 2.6. As for HSLA, the carbon content is less than 0.83 wt.%.

When applying heat to a steel component, the temperature of the steel increases gradually up to its melting point (1500^{o}C) and then the temperature stays constant as shown in Figure 2.7a until the entire component has melted. This is due to the absorption of energy required for the transformation of all the crystalline structure to Austenite. The mechanism of cooling is similar to that of applying heat; when slowly cooling a steel component from a liquid state it is noticed that the temperature flattens at certain temperatures, which is due to the elements changing from one phase to another, as illustrated in Figure 2.7b. As the temperature cools slowly from the melting point the Austenite starts transforming to Ferrite at a temperature between 910 and 723^{o}c according to the carbon content (see Figure 2.6). Carbon atoms are squeezed out of the face centered cubic crystals, the freed carbon atoms then unite with unsaturated Austenite that has not cooled, until it is saturated to form Cementite. At the temperature 723°C the mixture will be that of Pearlite and Ferrite. On the other hand, if the steel is cooled rapidly there is not enough time for the carbon atoms to diffuse out of the face centered cubic Austenite crystal to form Cementite. Instead, the austenite is transformed to a needle like structure of carbon saturated body centred tetragonal form of ferrite, which is called Martensite. This crystalline structure is characterized by having higher hardness and also by being more brittle than ordinary carbon steel at room temperature. In steel fabrication the procedure of rapidly cooling steel from high temperatures is called quenching. Figures 2.8a and 2.8b show a comparison between the formed Pearlite + Ferrite structure of the slowly cooled regions of a steel plate and the Martensite of the rapidly cooled region of the HAZ.

In the welding procedure the heat applied at the welding area is at the melting temperature of steel (formation of Austenite). The area of the base metal located next to the welding area (HAZ) experiences high temperatures and rapid cooling rate causing the formation of Martensite. Other areas far from the welding area are less affected by welding as their temperature has not been raised above the phase transformation temperature of 723°C (Figure 2.6) and the areas between the HAZ and the unaffected zone are relatively affected. Using preheat and inter-pass heating of steel through the welding procedure helps to decrease the cooling rate and the size of the HAZ. Other properties of steel that changes at elevated temperatures are discussed in the following sections.

2.3.2 Steel properties at elevated temperatures

In order to study the steel welding procedure and its effect on the base metal the changes in the base metal mechanical and thermal properties at elevated temperatures should be reviewed. These properties are; the modulus of elasticity, yield strength and ultimate strength, as well as the thermal conductivity, emissivity, heat transfer coefficient, thermal elongation and specific heat. Reduction factors for the mechanical properties of steel at elevated temperature are provided by ANSI/AISC 360-10 (2010) and CAN/CSA-S16-14 (2014). The reduction factors are similar to those measured by Hu et al. (2009) for ASTM A992 steel (ASTM A992 Gr.50, 2011) and Knobloch et al. (2013) for steel grade S355. Table 2.1 shows the reduction factors for the modulus of elasticity, yield strength and ultimate strength at different temperatures. Thermal material properties are important to understand for an accurate assessment of the welding procedure to take place. Following is a brief discussion of these properties.

The thermal conductivity k is the material property that describes the heat flow from one region to another through the same material (heat transfer by conduction) based on the temperature gradient between the two regions; hence, the flow direction is from high to low temperature, its unit is W/m˚C. The thermal conductivity of structural steel is approximately 54 W/m˚C at room temperature. Studies have been carried out to determine the values of steel thermal conductivity at elevated temperatures for other types of steel (Lie, 1992, Society of Fire Protection Engineers, 2008). Eurocode 3 Part 1-2 for structural fire design of steel (CEN, 2002) provides temperature dependant values for k of steel and can be calculated from equations 2.1 and 2.2.

$$k = 54 - 3.33x10^{-2}T, \qquad For\, 20^{o}C \leq T < 800^{o}C \tag{2.1}$$

$$k = 27.3, \qquad For\, 800^{o}C \leq T \leq 1200^{o}C \tag{2.2}$$

Where T is the steel temperature. The heat transfer coefficient α_c is a material property that describes the heat flow between the solid surface and the surrounding fluid (heat transfer by convection) depending on the temperature gradient; its units are W/m^2/°C. According to ANSI/AISC 360-10 (2010), CAN/CSA-S16-14 (2014), Eurocode 1 CEN (2002) and the Society of Fire Protection Engineers (2008), the heat transfer coefficient for a steel member at a uniform temperature that experiences a rise in temperature in a short period of time is 25 W/m^2/°C.

Emissivity ε_f is a surface property that describes the effectiveness of the surface to emit energy (heat transfer by radiation). Theoretically, it is the ratio of the thermal radiation emitted from a surface to that emitted from an ideal black surface at the same temperature as given by the Stefan–Boltzmann law. The ratio varies from 0 to 1. According to ANSI/AISC 360-10 (2010), CAN/CSA-S16-14 (2014), Eurocode 1 CEN (2002) and Society of Fire Protection Engineers (2008) for structural steel welding the surface emissivity should be in the range 0.5 to 0.7 .

Thermal elongation ε_{th} is the elongation in a member per unit increase temperature. Its unit is in/in/˚C or cm/cm/˚C. This property is responsible for the development of residual stresses; as any restraints on this change of volume result in internal stress. The thermal elongation of steel is 12.6

x 10^{-6} cm/cm/°C at 20°C. According to the ANSI/AISC 360-10 (2010) and CAN/CSA-S16-14 (2014) ε_{th} is constant at temperatures above 65°C and its value is 14x10^{-6} cm/cm/°C. Eurocode 3 (CEN, 2002) adopted formulas that were provided by Bletzacker (1966) who conducted tests on the thermal elongation of steel at elevated temperatures. Equations 2.3 to 2.5 shows the formulae used to calculate the thermal elongation of steel at elevated temperatures.

$$\varepsilon_{th} = \left(-2.416x10^{-4}\right) + \left(1.2x10^{-5}T\right) + \left(0.4x10^{-8}T^2\right), \quad For\, 20^oC \leq T < 750^oC \tag{2.3}$$

$$\varepsilon_{th} = 0.011, \qquad For\, 750^oC \leq T < 860^oC \tag{2.4}$$

$$\varepsilon_{th} = -0.0062 + \left(2x10^{-3}T\right), \qquad For\, 860^oC \leq T \leq 1200^oC \tag{2.5}$$

Specific heat C_p Is the amount of heat required to raise the temperature of unit mass of a material by one degree. Its unit is J/Kg.K or J/Kg.°C. C_p for steel varies at elevated temperatures. The Society of Fire Protection Engineers (2008) and Eurocode 3 CEN (2005) provide different equations to calculate the specific heat of steel with change in temperature, however the results are approximately the same. Equations 2.6 to 2.9 show the Eurocode 3 CEN (2005) approach to calculate the specific heat.

$$C_p = 425 + 0.773T + 1.69\times10^{-3}T^2 + 2.22\times10^{-6}T^3, \quad For\, 20^oC \leq T < 600^oC \tag{2.6}$$

$$C_p = 666 + \frac{13002}{738 - T}, \qquad For\, 600^oC \leq T < 735^oC \tag{2.7}$$

$$C_p = 545 + \frac{17820}{T - 731}, \qquad For\, 735^oC \leq T < 900^oC \tag{2.8}$$

$$C_p = 650, \qquad For\, 900^oC \leq T \leq 1200^oC \tag{2.9}$$

It can be concluded that elevated temperatures change the material properties as well as the crystalline structure of structural steel. The heat energy induced by the welding procedure subjects the base metal to high temperatures in the HAZ.

2.3.3 Steel creep and strain rate effects

Creep is the increase in strain with time under a constant tensile load. Studying creep is more common for concrete rather than steel structures; because of its significant effect on concrete at room temperature. Creep affects steel only at elevated temperatures. As such, creep is commonly studied for steel structures such as power plants and oil refineries; as stainless steel vessels are used and are subjected to stresses at relatively high temperatures (Society of Fire Protection Engineers, 2008). Consequently, the available test results are mostly for austenitic stainless steel. The temperature at which the creep becomes significant in steel is called the homologous temperature (Norton, 1929); it is when the ambient temperature is greater than 0.3 to 0.5 the absolute melting temperature of the material (Norton, 1929). The creep strain of steel becomes significant at ambient temperature greater than 400°C. Figure 2.9 illustrates the three stages where the strain increases through time at constant temperature and stress. Where ε_o is the initial creep due to the current loading. The primary creep is characterized by lasting a short period of time and that the rate of the strain is decreasing by time. The secondary creep has the longest period and has a constant strain rate (it is the minimum strain rate). In the tertiary stage the strain rate increases rapidly until fracture. There are two types of creep; uniaxial creep and multi-axial creep (Andrade, 1910). The basic standard creep test is uniaxial; such that the specimens are tested under a constant tension stress much less than the yield stress of the material, and at a constant temperature greater than the homologous temperature. The axial strain is plotted against time up to the end of the tertiary stage (creep rupture). A variety of information can be produced from this test, such as the shape of the creep curve and the duration of the creep stages, which depends strongly on the stress and temperature values.

Creep strain is always accompanied by two other properties; the creep strain recovery and the stress relaxation (Norton, 1929). The creep strain recovery takes place when the load is removed; first the elastic strain is recovered, then part of the creep strain is recovered leaving the permanent strain as shown in Figure 2.10a. Stress relaxation is the decrease of the stress with time under constant strain as shown in Figure 2.10b. For the effect of the loading type on the creep strain Faruque et al. (1996) conducted a study with the conclusion that for cyclic loading the creep strain curve is the same for all the creep stages as for static loading with a stress equal to the mean stress of the cyclic loading. However, for the cyclic loading, the creep rate is higher and the time to fracture is shorter.

Steel components are generally designed based on uniaxial creep data. However, components subjected to a welding procedure experience multi-axial stress state. In order to analyze such components; it is important to predict the creep strain of the component under multi-axial stress state. Notched specimens are widely used to study the effect of multi-axial state of stress on creep deformation and rupture behaviour of materials. The creep curve is geometrically the same as that of uniaxial creep. However, the creep rate is higher and is dependent on an equivalent stress value. The multi-axial creep was studied through creep tests (Boresi and Sidebottom, 1972, Goyal et al., 2013). According to Boresi and Sidebottom (1972) the equivalent stress is considered as a combination of Von Mises stress and the deviatoric stress. In the second approach the equivalent stress is a combination of the Von Mises stress and the maximum principal stress according to Goyal et al. (2013). Both studies are considered in this thesis for modeling the creep behaviour of steel through the welding procedure. Creep tests were conducted to evaluate the creep curves of A992 steel between the temperatures 400 and 1000 ˚C (Lee et al., 2012). The data from these tests were used to produce different formulae describing the creep strain of steel at different temperatures. Equations 2.10 and 2.11 show the two approaches of the equivalent stress value, according to the Von Mises stress and the deviatoric stress and according to the Von Mises stress and the maximum principal stress, respectively, utilizing constants developed by nonlinear regression of the tests conducted by Lee et al. (2012).

$$\varepsilon_{creep} = 2.125e-04 \times e^{\frac{-11111}{T}} \sigma_{vm}{}^{2} S_{dev} \times \Delta t \tag{2.10}$$

$$\varepsilon_{creep} = \frac{3}{2}(2.125) \times e-04 \times e^{\frac{-11111}{T}} (0.9\sigma_{vm} + 0.1\sigma_1)^3 \times \Delta t \tag{2.11}$$

In which, ε_{creep} is the creep strain, T is the temperature [˚C], σ_{vm} is the Von Mises stress [MPa], S_{dev} is the deviatoric stress [MPa], σ_1 is the maximum principal stress [MPa], and Δt is the time increment [sec]. For the welding procedure analysis, the temperature in the base metal exceeds the homologous temperature of the material only for a short period.

2.4 Heat Transfer Analysis

The main reason for the problems associated with the welding procedures of thick steel plates is the uneven heating and cooling of the welded assembly. Consequently, it is of great importance to understand the mechanism of heat flow through steel during and after the welding procedure. Heat flows when there is a difference in temperature between two adjacent systems or within the same system, from high temperature to low temperature. There are three main modes of heat transfer; conduction, convection and radiation. Heat transfer by conduction describes the flow of heat through a material if a temperature gradient is present. Heat transfer by convection describes the heat flow between a material and the ambient fluid adjacent to its surface depending also on the temperature gradient between them. Radiation is a phenomenon by which all bodies emit energy in the form of electromagnetic radiation depending of the temperature of the material and the nature of its surface. In most cases of heat transfer conduction and convection are present, however high temperatures must be involved for heat transfer by radiation to take place (Lienhard and Lienhard, 2011).

Heat transfer by conduction in solids occurs as molecules subjected to heat energy vibrate, and as such interact with neighbouring molecules transferring their kinetic and potential energies until the temperature becomes uniform with no bulk motion of the molecules (Lienhard and Lienhard, 2011). The heat energy that flows through a unit area of a material per unit time (heat flux (q)) is given by Fourier's law, such that the heat flux resulting from thermal conduction is proportional to the magnitude of the temperature gradient and opposite in direction to its sign. The proportionality constant is a material property and is called the thermal conductivity (k) (see Section 2.3.2). Equation 2.12 show Fourier's law of heat transfer by conduction in differential form.

$$\vec{q} = -k.\nabla T \tag{2.12}$$

Where $\vec{q}$ is the local heat flux (W.m^{-2}), k is the thermal conductivity (W.m^{-1}.^{o}C^{-1}) and ∇T is the temperature gradient (^{o}C.m^{-1}). The negative sign indicates that the heat flow is opposite in direction to the temperature gradient. This mechanism of heat transfer describes the heat transfer through the metal during the welding procedure.

Heat transfer by convection occurs between a solid surface and an adjacent fluid in motion. The faster the motion of the fluid the greater the heat transferred. There are two types of convection; natural convection where the movement in the fluid is caused by buoyancy forces induced by density difference due to temperature variation. The second type of convection is forced convection where the fluid is forced to move on the surface of the solid. The amount of heat transferred by convection is given by the steady state form of Newton's law of cooling shown in Equation 2.13 (Lienhard and Lienhard, 2011).

$$q = \bar{h}.(T_{surface} - T_{fluid}) \tag{2.13}$$

In which, $\bar{h}$ is the heat transfer coefficient (W.m^{-1}.^{o}C^{-1}) (see Section 2.3.2), $T_{surface}$ is the temperature of the solid surface (^{o}C) and T_{fluid} is the ambient temperature of the fluid (^{o}C). The heat transfer by convection explains the cooling of steel during and after the welding procedure.

The third mode of heat transfer is by thermal radiation. In this case heat energy is emitted from the surface; unlike conduction and convection radiation does not require a medium to occur. As a physical property at a given temperature a body will emit a unique distribution of energy (Lienhard and Lienhard, 2011). A black body has the highest value of energy emitted at any temperature. Therefore, the energy emitted by radiation from any material's surface is measured relative to the black body. Equation 2.14 shows the Stefan Boltzmann's formula for calculating the heat transferred by radiation; such that the thermal radiation of a black body multiplied by a coefficient ε that is called the emissivity (see Section 2.3.2) that relates any surface to that of a black body.

$$q = \varepsilon.\sigma.\Delta T_{abs}^{4} \tag{2.14}$$

In which, ε is the emissivity of the surface and it ranges from 0 to 1, σ is the Stefan Boltzmann constant (5.67 x 10^{-8} W.m^{-1}.^{o}C^{4}) and ΔT_{abs} is the absolute temperature (^{o}C). The heat transfer by radiation contributes to the cooling procedure of a welded assembly.

In summary, when applying heat to a material, there are three modes for the heat to flow. The heat conduction and convection requires a medium to transfer heat energy; conduction of heat is achieved through vibrations of molecules without any bulk motion, and convection is achieved through the motion of molecules. The heat transfer by radiation does not require a medium. The

First law of thermodynamics states that the rate of energy conducted in a material and that generated within is equivalent to the rate of energy conducted out of the material and that stored inside. From this law the three dimensional heat partial differential equation in is derived as shown in Equation 2.15 (Lienhard and Lienhard, 2011).

$$\frac{\partial T}{\partial t} = \frac{k}{\rho . C_p}\left(\frac{\partial^2 T}{\partial x^2} + \frac{\partial^2 T}{\partial y^2} + \frac{\partial^2 T}{\partial z^2}\right) + \frac{1}{\rho . C_p} q' \tag{2.15}$$

In which, ρ is the density of the material (kg/m^3), C_p is specific heat of the material (J/Kg.°C) and q' is the heat energy per unit volume. The heat transfer by convection and radiation can be added to this equation. This equation can be solved numerically to calculate the temperature at any location of the steel assembly being welded.

2.5 Simulation of the Welding Procedure

A simulation of the welding procedure has to comprise the heat source properties such as temperature, speed, size and location. Also the steel material heat transfer properties (see Section 2.4) as well as the changes in the steel material properties at elevated temperatures need to be included. The physical model of the welding procedure involves the application of heat and adding a new material to the model (welding pass), then the heat flows through the base metal and out of it according the heat transfer mechanisms discussed in Section 2.4. The heat flow results in expansion and contraction of the base metal according to temperature, which in turn develop residual strains and stresses. The simulation of this physical model is divided into two phases; the first phase is a simulation of the heat applied to the base metal during the welding of a pass, and that of the heat flow through the base metal and the interaction of the base metal surface with the ambient atmosphere. This phase results in temperature distributions in the base metal at all stages of the welding procedure. The second phase involves a stress analysis utilizing imported temperature distributions from the first phase every small increment of time; and according the temperature differences between the increments the amount of expansion or contraction strains is calculated and consequently the corresponding stresses at all stages of the welding procedure. This method of simulation is identified as an uncoupled thermo-mechanical simulation.

A summary of simulation of the welding procedure that were established are provided herein. Brickstad and Josefson (1998) developed a numerical simulation for the welding procedure of 40mm thick stainless steel nuclear piping systems to investigate the through thickness variation of axial and hoop stresses and to assess the growth of surface flaws at circumferential butt joints. An uncoupled thermo-mechanical simulation was utilized. The introduction of new welding passes as they are welded was simulated through a technique called "Birth and Death technique". In this technique the weld metal passes are introduced to the model from the start. Then the elements forming the weld passes are deactivated by multiplying their stiffness with a reduction factor of $1x10^{-6}$; so that they undergo all deformations induced during the welding procedure without experiencing significant stresses. Subsequently, after a pass is welded it is reactivated and starts contributing in the model. Acevedo et al. (2013) conducted a numerical assessment of residual stresses induced by welding at the region surrounding the toe of a tubular K-shaped joint using an uncoupled thermo-mechanical simulation. The residual stress results were verified with experimental measurements conducted through Neutron-diffraction of welded tubes of thicknesses 20mm and 8mm. Furthermore an uncoupled thermo-mechanical was utilized by Lee et al. (2015) to produce an assessment of the residual stresses of butt welded 25mm thick plates and to study the relaxation phenomena accompanied by post-welding cyclic loading. Also the results of the simulation were verified through experimental measurements.

2.6 Linear Fracture Mechanics

With the aim to update the discontinuity acceptance criteria for welded thick steel plates, the mechanism of crack propagation has to be emphasized. The study of fracture mechanics is a specialization in solid mechanics that considers the presence of a discontinuity in the material. The objective is to find quantitative relations between the crack length, material properties and applied stresses (Zehnder, 2012).

In general, when a crack grows in a solid the region of material adjacent to the free surfaces is unloaded and the strain energy is released. Additionally as the crack grows, energy is absorbed to create new surfaces as the bonds between molecules are broken. Figure 2.11a shows the released and absorbed energies as a crack is formed in a solid subjected to tension. The sum of energy associated with the crack growth is shown in Figure 2.11b. The point where the energy reaches its maximum value is called the critical crack length (a_c). Up to this point the crack will only grow if the stress is increased. If the length of the crack reaches a_c the crack growth will be spontaneous and catastrophic (Barsom and Rolfe, 1987, Zehnder, 2012). In ductile materials such as steel, energy is not absorbed by creating a new surface, but by energy dissipation due to plastic flow near the crack tip. In these materials, the critical point at which catastrophic fracture occurs is dependent on the plastic flow near the crack tip. A number of approaches have been suggested to describe the stress state at the crack tip; one of the most commonly used approaches is the stress intensity approach. This approach utilizes a stress intensity factor (K_I) that is directly proportional to the length of the yielded area from the crack tip (r). For this approach to be valid the plastic zone need not to be so large as to interact with the material's boundaries (Zehnder, 2012). The stress intensity factor depends on the crack type, location, size and the applied stress. Equations 2.16 to 2.20 gives the formulas to calculate the K_I according to Tada et al. (2000) and Murakami (1987).

$$K_I = \sigma\sqrt{\pi a}.\sqrt{\sec\left(\frac{\pi a}{2b}\right)}, \quad \textit{Through thickness crack in a finite plate} \tag{2.16}$$

$$K_I = \sigma\sqrt{\pi a}\ , \quad \textit{Through thickness crack in an infinite plate} \tag{2.17}$$

$$K_I = 1.12\sigma\sqrt{\pi a}.f\left(\frac{a}{b}\right), \quad \textit{Edge crack in a finite plate} \tag{2.18}$$

$$K_I = 1.12\sigma\sqrt{\pi a}\ , \quad \textit{Edge crack in an infinite plate} \tag{2.19}$$

$$K_I = 1.13\sigma\sqrt{a}\ , \quad \textit{Embedded circular crack} \tag{2.20}$$

Where a is equal to the crack length for edge cracks; half of the crack length for through thickness cracks; and the radius of the embedded circle for an embedded circular crack (mm), b is half of the thickness of the finite plate in the direction of the crack (mm), $f(a/b)$ is a factor depending on the relation between a and b, and σ is the applied stress level (MPa). A crack propagates if subjected to one of the three stress modes; the first mode of crack propagation is called Mode I and it occurs if the material is subjected to a tensile stress perpendicular to the crack plane as shown in Figure 2.12a, the second mode (Mode II) is when the material is subjected to in-plane shear forces as shown in Figure 2.12b and the third mode (Mode III) is when the material is subjected to out of plane shear forces (tearing) as illustrated in Figure 2.12c.

As the applied stress increases, the plastic zone size increases until it cannot grow any larger; at this point the crack is not constrained and an unstable crack propagation is induced and the stress intensity factor is at the critical value of the material which is called the fracture toughness of the material. The fracture toughness of a material is dependent on the temperature. The fracture toughness temperature relationship for metals is divided into three regions; the low shelf temperatures where the fracture toughness is at its lowest value, the high shelf temperatures where the fracture toughness of the material is at its highest value and the transition zone between the low and high shelf temperatures as illustrated in Figure 2.13. The fracture toughness is calculated from the CVN energy value (see Section 2.2.4) depending on the testing temperature and the material's elastic modulus. As a result of the dynamic nature of the CVN test, for lower shelf temperatures, the output is the dynamic fracture toughness. However, the static fracture toughness is of the same value but at a lower temperature (see Figure 2.13) computed from Equations 2.21 and 2.22 (Barsom and Rolfe, 1987).

$$T_s = 102 - 0.12\sigma_y, \qquad For\ 250 < \sigma_y \leq 965 \tag{2.21}$$

$$T_s = 0, \qquad For\ \sigma_y > 965 \tag{2.22}$$

Where T_s is the temperature shift (°C), σ_y is the yield stress of the material in MPa. For upper shelf temperatures there is no temperature shift required to transfer from the dynamic to the static fracture toughness (Barsom and Rolfe, 1987). The fracture toughness is given by Equations 2.23 and 2.24.

$$K_{Id} = \sqrt{0.64 \times CVN \times E}, \qquad For\ lower\ shelf\ temperatures \tag{2.23}$$

$$\left(\frac{K_{Ic}}{\sigma_y}\right)^2 = 0.646\left(\frac{CVN}{\sigma_y} - 0.0098\right), \qquad For\ upper\ shelf\ temperatures \tag{2.24}$$

In which, K_{Id} is the dynamic fracture toughness (KPa.√m), CVN is the absorbed energy from Charpy-V-Notch test (Joules), E is the modulus of elasticity of the material (KPa), and K_{Ic} is the static fracture toughness (MPa.√m). The stated fundamentals of linear fracture mechanics are utilized in this research for the assessment of crack propagation of discontinuities in the HAZ and weld area due to stresses induced by the welding procedure.

2.7 Summary

This chapter presents a summary of the theoretical background that was reviewed to carry out this research. Emphasis is made on literature related to the available welding procedures for thick steel plates as well as the associated defects and methods of inspection and repair. Also a review of the structural steel behaviour at elevated temperatures, including mechanical and thermal properties, is performed. Additionally, the mechanisms of heat transfer through solids was investigated to better understand the heating and cooling of steel assemblies during and after the welding procedure. Subsequently a survey on methods of simulating the welding procedure was conducted to be implemented in this research. Finally a review of methods of crack propagation was established to be employed in the assessment of the acceptance criteria of discontinuities.

Table 2.1: Reduction factors for mechanical properties of steel at elevated temperatures according to ANSI/AISC 360-10 (2010), CAN/CSA-S16-14 (2014).

Temp ^{o}C	K_E	K_p	K_y
20	1	1	1
93	1	1	1
204	0.9	0.8	1
316	0.78	0.58	1
399	0.7	0.42	1
427	0.67	0.4	0.94
538	0.49	0.29	0.66
649	0.22	0.13	0.35
760	0.11	0.06	0.16
871	0.07	0.04	0.07
982	0.05	0.03	0.04
1093	0.02	0.01	0.02
1204	0	0	0

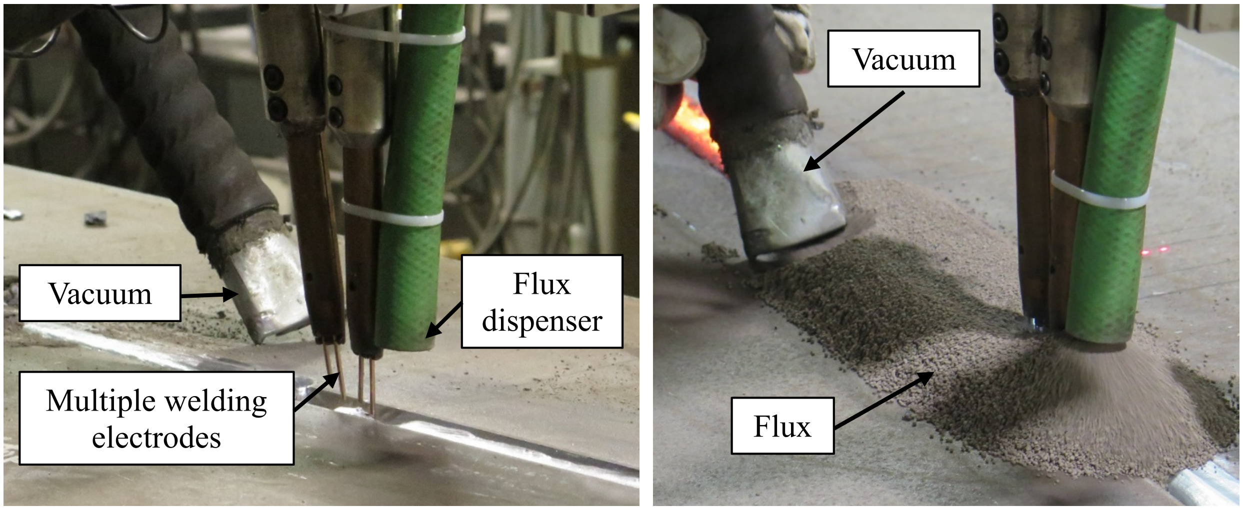

(a) (b)

Figure 2.1: Submerged arc welding process main components; a) before welding, b) during the welding procedure.

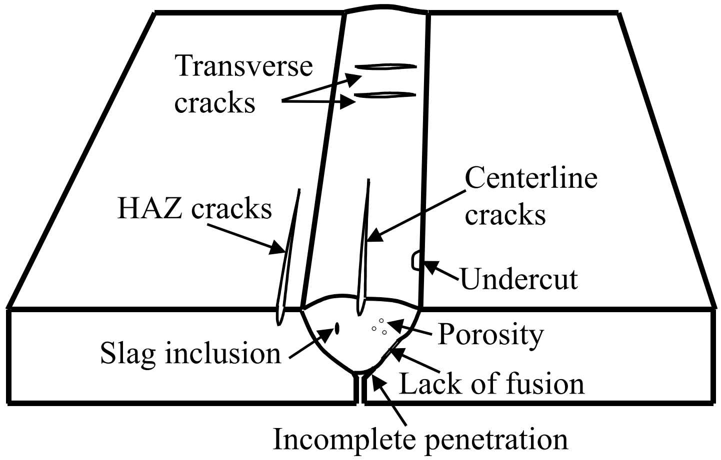

Figure 2.2: Illustration of defects and discontinuities induced by the welding procedure.

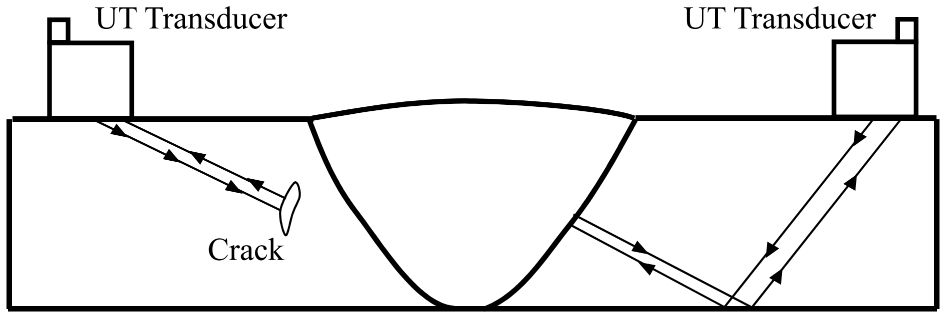

Figure 2.3: Ultrasonic inspection method.

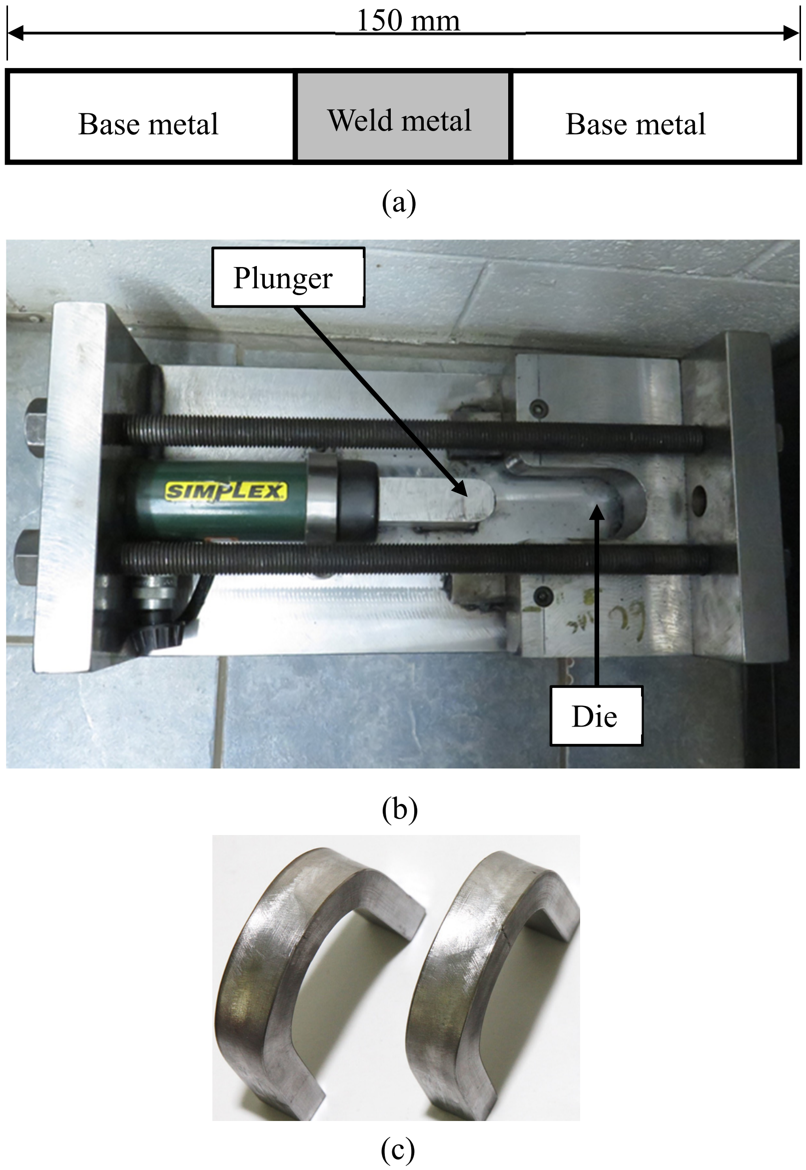

Figure 2.4: Side bend test; a) Specimen composition, b) Equipment required for test and c) Side bent specimens after the test.

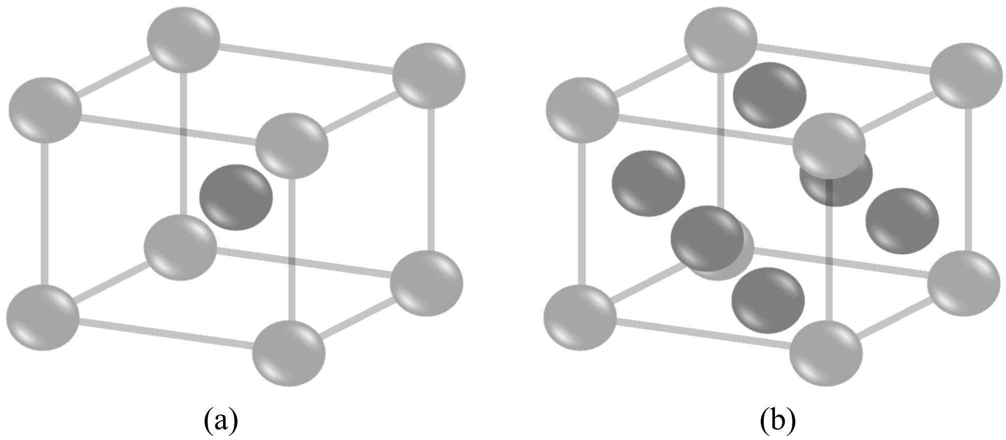

Figure 2.5: Crystalline structure of an iron element, a) body centered cubic structure at room temperature (Ferrite), b) face centered cubic structure at high temperatures (Austenite).

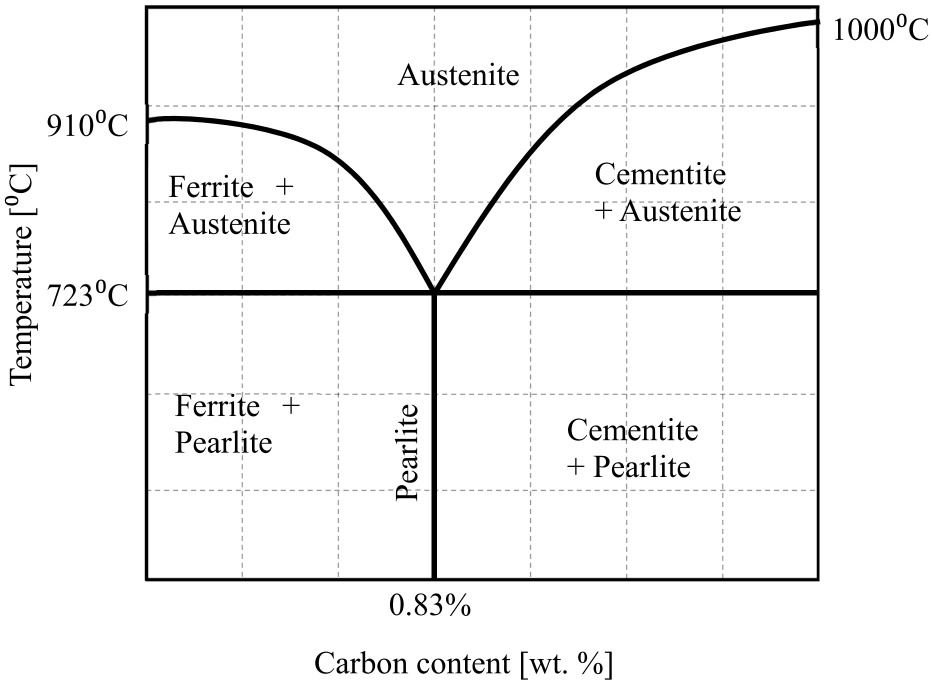

Figure 2.6: Phase changes of carbon steel with increase in temperature.

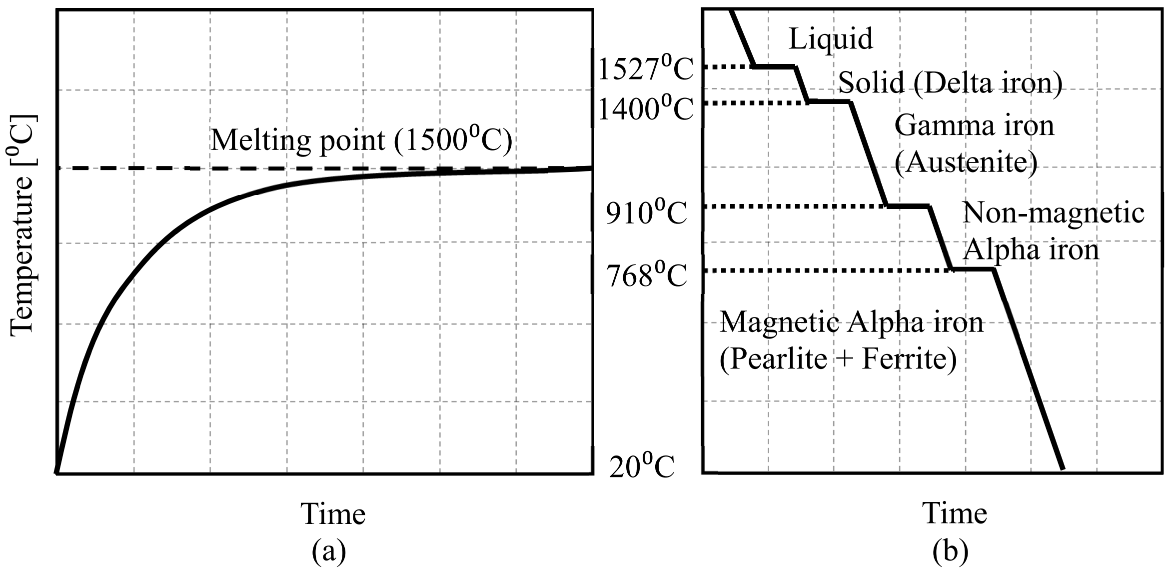

Figure 2.7: The behaviour of iron with temperature change; a) applying heat, b) slow cooling.

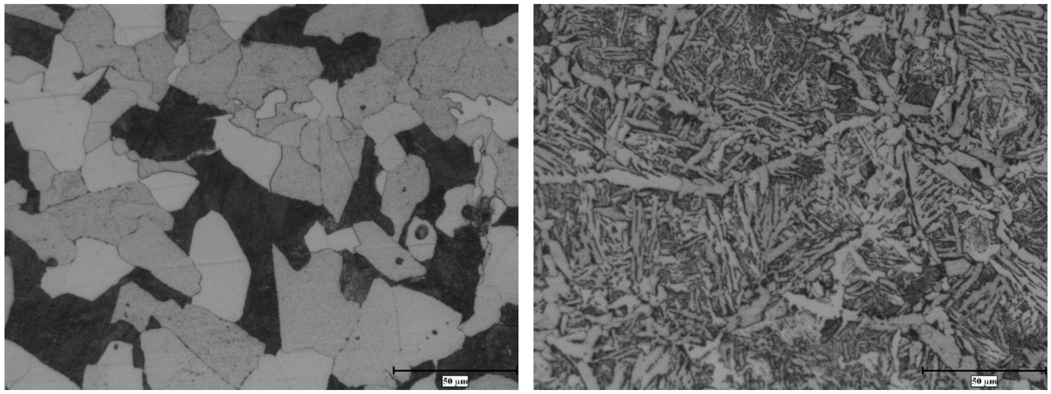

(a) (b)

Figure 2.8: Steel crystalline structure at 500x magnification; a) slowly cooled steel (Pearlite + Ferrite), b) rapidly cooled HAZ (Martensite).

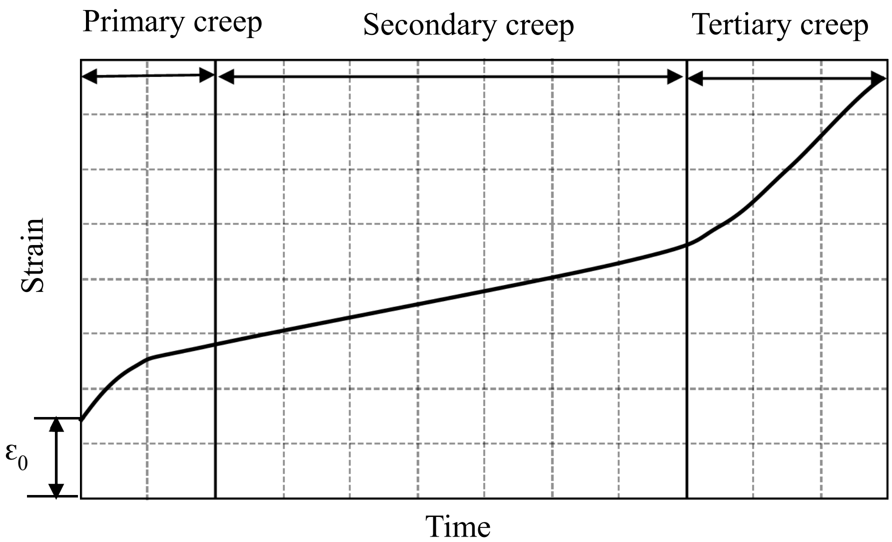

Figure 2.9: illustration of the 3 stages of creep for steel.

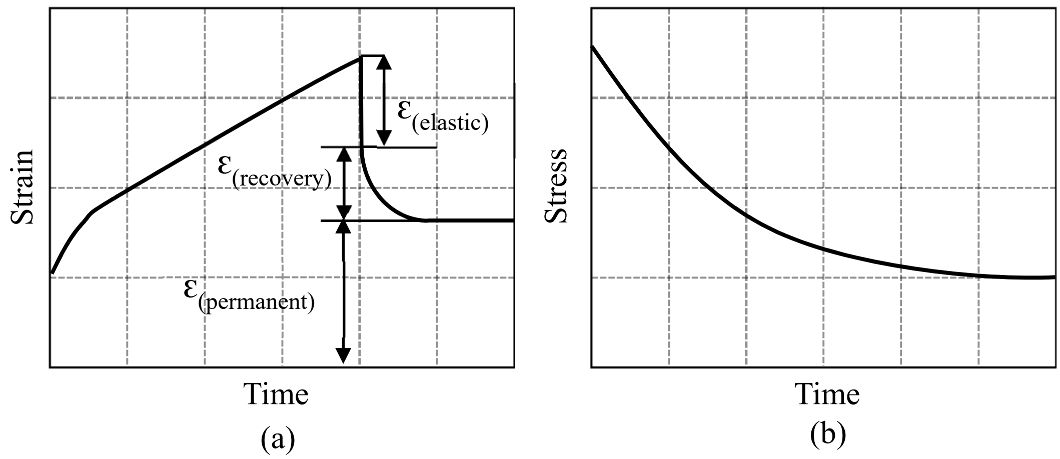

Figure 2.10: illustration of accompanying phenomena with creep; a) strain recovery, b) stress relaxation.

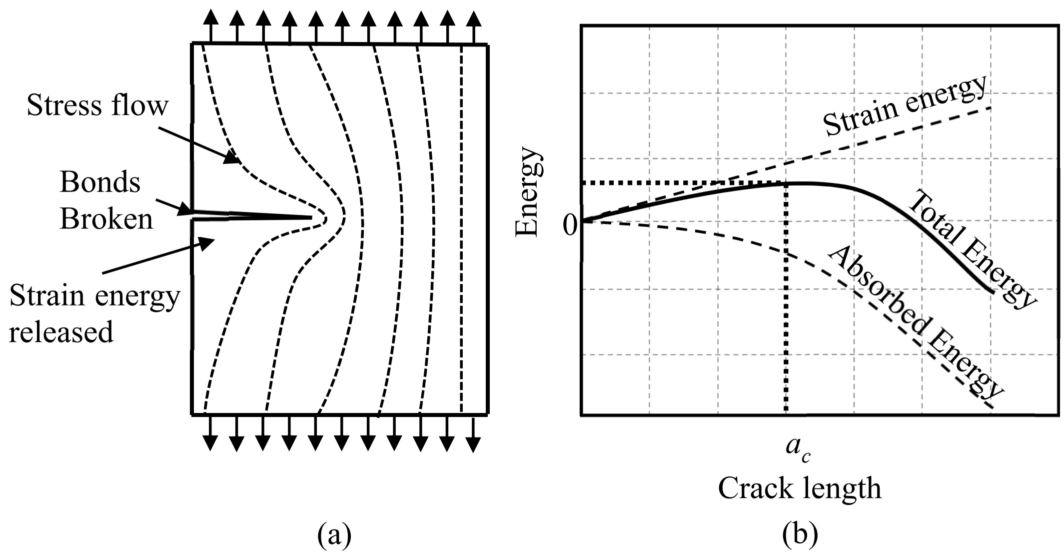

Figure 2.11: Crack growth mechanism; a) a cracked body under tensile stress, b) the total energy associated with crack growth.

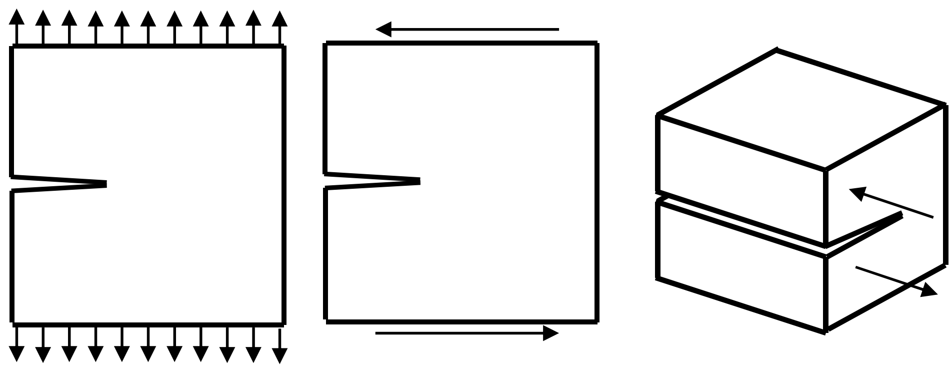

(a) (b) (c)

Figure 2.12: The three mode of fracture; a) Mode I tension, b) Mode II in plane shear, c) Mode III anti-plane shear (tearing).

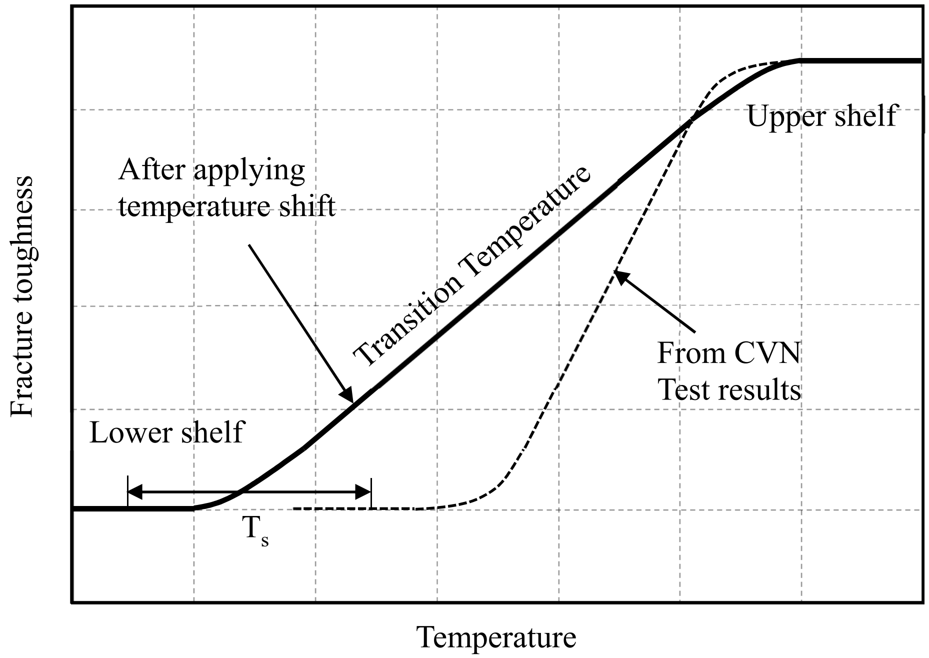

Figure 2.13: Fracture toughness and temperature relationship.

Chapter 3 MODELING APPROACH OF WELDING PROCEDURES FOR HEAVY STEEL PLATES

3.1 Introduction

Welding is a commonly used method for joining structural steel components. This is attributed to the reliability of the connection, its structural simplicity in terms of load transfer and its cost effectiveness. However, welding can also be problematic; a primary example is that the process is accompanied by residual stresses. These stresses develop in the plates being welded because of the uneven heat expansion and the subsequent contraction upon cooling, both of which are often constrained by the configuration of a structural member's or connection's cross-section. In recent years, the use of thicker built-up members and heavier steel shapes have been preferred for the construction of complicated structural systems having long spans, greater heights and larger loads due to more demanding design and performance requirements (American Society of Civil Engineers., 2013). The use of thick plates further exacerbates the development of weld related residual stresses because of the greater constraint to the steel's expansion and contraction; as a result, there is an increased likelihood of crack development originating from discontinuities and imperfections. Design codes and specifications (ANSI/AISC 360-10, 2010, AWS D1.1, 2010, CAN/CSA-W59, 2013, CAN/CSA-S16-14, 2014) provide guidance for the welding processes to ensure the integrity of the welded assembly. However, the available guidelines were developed based on commonly used less than 25mm thick structural steel plates. The relevant North American design specifications (ANSI/AISC 360-10, 2010, AWS D1.1, 2010, CAN/CSA-W59, 2013, CAN/CSA-S16-14, 2014) account for the aspects introduced by Miller (2010) to reduce the intensity of residual stresses induced by the welding procedure; however, these are mostly qualitative recommendations to reduce the restraint placed on the connection and to ensure that minimum material fracture toughness levels are met. Cases of structural failure have been reported due to failure in welded thick steel plates assemblies (Kaminetzky, 1991). Recently, based on feedback from one of the largest steel fabricators in North America; it was required to scrap over 400 tons of thick steel plates that developed unrepairable cracks after welding, with total industry losses exceeding \$1M. Given this current situation, the specifications for the welding procedures and the acceptance criteria for cracks and discontinuities for thick steel plates (greater than 25mm) (ANSI/AISC 360-10, 2010, AWS D1.1, 2010, CAN/CSA-W59, 2013, CAN/CSA-S16-14, 2014) are required to be updated. In order to do so, one of the first requirements is to develop a practical numerical approach from which one can examine the effect of different welding procedures on thick steel plates and the resulting residual stresses. It is necessary for this tool to comprise the features of the welding procedure, i.e. the welding temperature, the welding travel speed and the preheat/inter-pass temperatures, as well as the steel's time and temperature dependent material properties.

A summary of related laboratory and analytically based studies is provided herein. Bjorhovde et al. (1972) conducted an extensive testing program using the sectioning method to measure the residual stresses induced in 50mm ASTM A36 (2014) plates (f_y = 250 MPa) from rolling, flame cutting and welding. The results of these tests showed that the residual stress post fabrication near the welded area can be as high as the yield stress of the steel. Fisher and Pense (1987) detected cracks in a W360x1086 ASTM A572 Gr.50 (2013) section (f_y = 345 MPa) spliced with groove welds; the high residual stresses induced by the web groove welds initiated crack instability. The authors recommended using fillet welds instead of butt groove welds to avoid welding near the k-area of jumbo W-sections, which had revealed weak fracture toughness of 35 MPa.√m at 0°C compared to the AWS D1.1 (2010) specification limit of 58 MPa.√m at 0°C. In other research programs the investigation of the effects of the employed welding procedure on steel plates has also been conducted numerically. For example, Brickstad and Josefson (1998) developed a numerical simulation for the welding procedure of 40mm thick stainless steel nuclear piping systems, of 230 MPa yield stress, to investigate the through-thickness variation of axial and hoop stresses and to assess the growth of surface flaws at circumferential butt joints. Acevedo et al. (2013) conducted experimental and numerical assessment of residual stresses induced by welding at the region surrounding the toe of a tubular K-shaped joint. The residual stress measurements were conducted through Neutron-diffraction of welded tubes of thicknesses 20mm and 8mm. The numerical simulation comprised an uncoupled thermo-mechanical model, which was validated with the experimental data; analytical residual stress distribution equations were also developed. Nikolaidou et al. (2014) used an uncoupled thermo-mechanical model to investigate the cause of crack initiation after welding a 25mm doubler plate to the web of a W360x237 column of high strength ASTM A913 Gr.65 (2014) steel; the investigation proved that high residual stress induced by the welding procedure resulted in the detected cracks. Further, an uncoupled thermo-mechanical was developed by Lee et al. (2015) to produce an assessment of the residual stresses of butt welded 25mm thick plates and to study the relaxation phenomena accompanied by post-welding cyclic loading. The residual stress outputs from their model were validated by means of the results from a test program (Lee et al., 2010). The uncoupled thermo-mechanical model effectively predicted the residual stresses for the 25mm thick plates.

It is not practical to rely solely on an experimental study of the welding procedure of thick plates in order to improve current welding procedures of heavy assemblies due to the required large-scale weld tests and significant number of parameters to be investigated. Therefore the development and use of a numerical simulation of typical welding procedures for thick plates was justified. This Chapter describes a numerical uncoupled thermo-mechanical modeling approach which can be used to investigate the effect of the welding procedures on steel assemblies that utilize thick plates (> 50mm) and heavy cross-sections. The simulation was validated with a coordinated experimental program that consisted of three phases; the first phase included the validation of the temperature distribution results from the numerical model with the temperature measurements from the welding procedure of two 75mm thick ASTM A572 Gr.50 (2013) steel plates. The second phase was the validation of the resultant residual stress distribution with experimental results obtained by Chen and Chang (1993). The third phase included the application of the modeling approach to assess the influence of the employed welding procedure for a heavy built-up steel box column, fabricated from the same heat of steel plates studied in the first phase. Cracks were observed in this column after the welding procedure had been completed.

3.2 Proposed Modeling Approach for Welding Procedures

The aim of numerically simulating a welding procedure is to make it possible to use a practical approach to investigate the likelihood of crack propagation, as well as the influence of different welding procedures. A numerical simulation for the welding procedure has to comprise the effects of elevated temperatures on the steel plates and must provide the generated stress from the temperature change. The elevated temperatures change the crystalline structure of the steel material and, correspondingly, its properties (e.g., strength and stiffness). Because our interest is the magnitude of the generated residual stresses from the welding procedure, it is feasible to only include the changes of the mechanical properties of the steel material at elevated temperatures and to disregard the changes in the crystalline structure, since it is inherently incorporated in the strength change; this assumption has been also considered in previous research (Brickstad and Josefson, 1998, Acevedo et al., 2013, Nikolaidou et al., 2014, Lee et al., 2015). The proposed finite element (FE) approach is demonstrated through detailed modelling of the welding of a 75mm thick built-up box column and two 75mm thick steel plates, using ABAQUS 6.11 (Dassault Systemes Simulia Corp., 2011) for 3-dimensional (3-D) modeling. The FE simulation is divided into two phases. The first phase is a simulation of the heat transfer from the welding procedure through the base metal to obtain the temperature distribution over time. The second phase involves a stress analysis model (or a visco-plastic model to account for potential creep strain effects) to determine the stresses induced by the welding procedure. The two phases were then integrated to simulate the welding procedure.

The element "death and birth" technique, as described by Brickstad and Josefson (1998), was incorporated in the FE model. This technique is used to deactivate and reactivate the elements representing the welding beads to simulate the addition of new material to the connection during fabrication. As an example, Figures 3.1a-3.1b show the activation of only the first six passes at each corner of the built-up box column 3-D model shown in Figure 3.2a, while the remaining weld passes are deactivated. To achieve this, the "Model Change" interaction in ABAQUS 6.11 (Dassault Systemes Simulia Corp., 2011) was utilized such that prior to the deactivation step the forces/heat-fluxes that the region to be removed exerts on the surrounding nodes are ramped down to zero. Therefore, the effect of the removed region on the rest of the model is completely absent only at the end of the deactivation step. To reactivate a welding pass the same interaction is used with the "strain free" option in ABAQUS 6.11 (Dassault Systemes Simulia Corp., 2011) such that at the start of the weld pass it provides a zero strain contribution to the simulation. The two simulation phases are discussed in detail in Sections 3.2.1 and 3.2.2. The mesh sensitivity study and element selection of the FE models in the proposed approach are described in Section 3.2.3. Additionally, the effect of introducing creep strain properties on the residual stress results is discussed in detail in Section 3.2.4.

3.2.1 Heat transfer simulation

The heat transfer simulations for the built-up box column and the two steel plates were generated as illustrated in Figures 3.1a and 3.1c, respectively. The finite element mesh at the welding area as well as the welding passes for both cases are shown in Figures 3.1e-3.1f respectively. To achieve the resulting temperature distributions, the following steel material properties were considered: the thermal conductivity and the specific heat, as well as the effect of elevated temperatures on their values. The values of these properties were defined according to the "Society of Fire Protection Engineers" SFPE Society of Fire Protection Engineers (2008) as shown in Table 3.1. All the welding passes were explicitly created in the finite element model; however, they were deactivated at the first step of the analysis. Each pass was simulated in three steps; 1) heating of the welding area, for the considered pass, up to the welding temperature (1500°C), 2) activating the weld pass elements, and 3) cooling of the steel through natural convection until the preparation for welding of the next pass was finished. This was achieved by defining conduction and radiation contact surfaces between the steel and surrounding air of 20°C ambient temperature; considering a heat transfer coefficient of 25 W/m^{2}K (Society of Fire Protection Engineers, 2008) and an emissivity coefficient of 0.625 according to Eurocode 3 Part1.2:2001 (British Standards Institution., 2001), which is in the range specified by ANSI/AISC 360-10 (2010) for structural steel components (0.5 - 0.7). However, the heat transferred by radiation is negligible to that transferred by conduction and convection. The traveling heat source is simulated by dividing the traveling distance into a finite number of divisions, such that the heat is applied through a boundary condition of ramp heating from the preheat temperature to the welding temperature to each division according to the travel speed. The heating of each division starts at the end of heating of the previous division.

3.2.2 Stress analysis model

The stress analysis FE model imports the temperature distributions obtained from the heat transfer simulation at every increment during the heating and cooling of each weld pass. Using the thermal expansion coefficient, at the corresponding temperature, the change in temperature is transformed to strains, which are then transformed to the corresponding stresses as shown in Figures 3.1b and 3.1d. A multi-linear plasticity model and geometric nonlinearities are considered in the stress analysis model. The Von Mises yield surface is utilized in ABAQUS to simulate the isotropic metal plasticity. The material properties, at elevated temperatures, required for this analysis are the elastic modulus, the yield stress, the yield strain, the ultimate stress, the ultimate strain and the coefficient of thermal expansion. The welding procedure applies temperatures to the base metal as high as the melting point of steel (1500ºC). At such temperature the steel is at a liquid phase that has negligible stiffness and strength. As the steel temperature decreases the material transforms through different phases to reach its solid phase at room temperature; during these phase transformations the mechanical and thermal material properties of steel change gradually. Figure 3.3 illustrates the values for the material properties used in the stress analysis model.

The reduction factors for the material properties, due to elevated temperature, were set according to ANSI/AISC 360-10 (2010) and the SFPE Society of Fire Protection Engineers (2008). The chosen reduction factors were similar to those measured by Hu et al. (2009) for ASTM A992 Gr.50 (2011) steel. The weld metal properties were assumed as F7A4-EM12K according to A5.17 AWS D1.1 (2010), which is typically used for a SAW procedure. The base metal properties were obtained from tensile tests of the plate material, which are discussed in Section 3.3.1.1.

3.2.3 Mesh sensitivity study and selected finite element types

The solution of the proposed FE model is conducted using the ABAQUS implicit solver. The Euler backward method is utilized by ABAQUS for solving transient problems, which is unconditionally stable for linear finite elements (Dassault Systemes Simulia Corp., 2011). As such, linear elements were selected for the proposed FE model, specifically C3D8 elements for the 3-D model, which are 8-node linear isoparametric elements with full integration. A mesh sensitivity study was conducted for the proposed FE model to evaluate the optimum mesh size, in terms of accuracy and calculation speed, to be employed for the heat and stress analyses. As the ability of the finite element to transfer the applied heat and undergo deformation is required to be studied, this can be established regardless of the model size and plate thickness. A quarter section of a box configuration composed of 28 mm thick plates connected with a complete joint penetration (CJP) weld comprising 10 weld passes was utilized for the mesh sensitivity study. The mesh size varied from a maximum element dimension of 20mm to 5mm. Shear locking was avoided because the deformations in this analysis are very small compared to the size of the model; also, quadratic elements were tested and showed no significant difference in the results from using linear elements. Hour-glassing was avoided by using full integration and by comparing the results with those of models built with quadratic elements. From this study, the selected mesh for the 3-D model was of minimum element size 2mm and maximum 9mm, such that the difference between the maximum stresses of this mesh size and the denser mesh was less than 15%. Figure 3.4 shows the Von Mises stress distribution sensitivity to the mesh size and the mesh selected for this study.

3.2.4 Creep strain modeling

The effect of creep strain on the resulting residual stresses was investigated such that the welding simulation better accounts for the behaviour of the steel material. Creep is the increase in strain with time under a constant tensile load, as illustrated in Figure 3.5a. Creep effects on steel are only significant at elevated temperatures. The creep strain is divided into three stages; the primary, the secondary and tertiary creep (Andrade, 1910). The primary creep is for a short duration and is characterized by a decreasing strain rate. The secondary creep has the longest duration and has a constant strain rate (it is the minimum strain rate at a constant temperature and stress). In the tertiary stage the strain rate increases rapidly until fracture. Creep is commonly studied in steel structures such as nuclear power plants and oil refineries where stainless steel is used and high temperatures are experienced (Society of Fire Protection Engineers, 2008). Consequently, the available creep test results for steel are mostly for austenitic stainless steel. The temperature at which the creep becomes significant in steel is called the homologous temperature (Norton, 1929); it is when the ambient temperature is greater than 0.3 to 0.5 of the absolute melting temperature of the material (Norton, 1929). As such, the creep strain becomes significant for steel at ambient temperature greater than 400°C.

Creep strain is always accompanied by two other phenomena; the creep strain recovery and the stress relaxation (Norton, 1929). The creep strain recovery takes place when the load is removed; first the elastic strain is recovered, then part of the creep strain is recovered leaving the permanent strain as shown in Figure 3.5b. Stress relaxation is the decrease of the stress with time under constant strain as shown in Figure 3.5c. The loading type also has an effect on the creep strain according to Faruque et al. (1996). The temperature in the base metal exceeded the homologous temperature of the material only for a short period during the welding procedure simulations. As a result, the present study is only concerned with the primary and secondary creep stage. Creep tests were conducted by Lee et al. (2012) to evaluate the creep curves of ASTM A992 Gr.50 (2011) steel between the temperatures 400 and 1000 ˚C. The data from these tests were used to develop empirical equations describing the creep strain of the steel at different temperatures. The multi-axial creep was considered using two approaches. First according to Boresi and Sidebottom (1972), where the equivalent stress was considered as a combination of the Von Mises stress and the deviatoric stress (noted as "creep-1"). In the second approach the equivalent stress is a combination of the Von Mises stress and the maximum principal stress according to Goyal et al. (2013) (noted as "creep-2"). Equations 3.1 and 3.2 show the approaches developed in this research using constants developed by nonlinear regression of the test data obtained from Lee et al. (2012).

$$\varepsilon_{cr} = 2.125e-04 \times e^{\frac{-11111}{T}} \sigma_{vm}{}^{2} S_{dev} \times \Delta t \qquad \textit{For creep-1} \qquad (3.1)$$

$$\varepsilon_{cr} = \frac{3}{2}(2.125) \times e-04 \times e^{\frac{-11111}{T}} (0.9\sigma_{vm} + 0.1\sigma_{1})^{3} \times \Delta t \qquad \textit{For creep-2} \qquad (3.2)$$

Where, ε is the creep strain; T is the temperature [˚C]; σ_{vm} is the von Mises stress [MPa]; S_{dev} is the deviatoric stress [MPa]; σ_1 is the maximum principal stress [MPa]; and Δt is the time increment of the solution procedure [sec]. A FORTRAN subroutine was developed in ABAQUS (Dassault Systemes Simulia Corp., 2011) in order to incorporate the time dependent strain properties of steel in the proposed FE model. In this subroutine the two approaches stated above were implemented. Figure 3.6 shows a comparison of the resulting stresses from the welding procedure with and without creep strain considerations. The differences in the resulting maximum stresses are 4% and 8% for modeling approaches creep-1 and creep-2, respectively. The resulting maximum stresses considering the creep strain were always lower than those obtained without considering it. The reason for this is that the base metal did not experience temperatures above the homologous temperature of steel (400°C) for an adequate duration to develop creep strains. Moreover, in most of the results, stress relaxation took place, which was more significant than the stress change due to the creep strains. However, if a welding procedure utilizes a heat input that is much higher than the commonly used value (2 to 3 KJ/mm) the creep strain may become more influential.

In conclusion, considering the creep strains in the welding procedure simulation showed a very small change in the maximum stress results, neglecting the creep strains proved to be more conservative than incorporating them. Furthermore, the computational time required to analyze a FE model considering creep is more than double that required for a model without creep. For these reasons the creep strain properties were neglected from the final welding procedure simulations presented in this chapter. However, for welding procedures involving heat input higher than commonly used in practice, it is recommended to take into account the effect of creep strains on the resultant stresses.

3.3 Experimental Validation of the Proposed Modeling Approach for Welding Procedures

The proposed numerical modeling approach for welding procedures of heavy steel assemblies that utilize thick plates requires validation with relevant experimental data for both the heat transfer and stress analysis simulation phases. Three case studies were adopted for this validation. The first case study involved temperature measurements during the welding of two 75mm thick ASTM A572 Gr.50 (2013) (f_y = 345 MPa, f_u = 450 MPa) steel plates (Figure 3.7a); these measurements were used to validate the heat transfer simulation (Section 3.3.2). For the validation of the stress distribution results of the proposed modelling approach, the second case study involved the simulation of the welding simulation of a box section, of ASTM A572 Gr.50 (2013) steel, that underwent an experimental procedure to evaluate the residual stress distribution developed from the welding procedure by Chen and Chang (1993) (Section 3.3.3). The third case study was of a heavy built-up box column (Figure 3.2a) fabricated from 75mm thick steel plates of the same material (heat) as the first case study. This third case study is used to demonstrate how the proposed modeling approach can be incorporated in an assessment of the welding procedure (Section 3.3.4). The plates that were used for testing were originally intended for use in box columns that were eventually scrapped due to the development of cracks discovered during fabrication and, in particular, after welding. The scrapped plates were used for material tests to calibrate the FE model (Section 3.3.1).

3.3.1 Material tests for characterizing the properties of the built-up box columns

Tensile and Charpy-V-Notch (CVN) specimens were extracted from the box-column specimens retained by the fabricator to evaluate the material properties, and to determine the effect on these properties of the welding procedure at different stages. The measured material properties were also used to calibrate the corresponding FE model. This included a fully welded built-up box column (13 weld passes at each corner), a partially welded column (6 weld passes at each corner) and a non-welded plate as shown in Figure 3.8. A total of 74 tensile coupon and 100 CVN specimens were extracted from all the box-column and plate specimens at different locations within the thickness of the steel plates. The results were categorized into four groups regarding the location of the CVN and tensile coupon specimens; 1) near the weld and on the plate surface, 2) near the weld and through the plate thickness, 3) away from the weld and on the plate surface and 4) away from the weld and through the plate thickness. Figure 3.9 shows a sample of the different locations of the tensile and CVN specimens extracted from the fully welded column, the partially welded column and the non-welded plate.

3.3.1.1 Tensile coupon test results

The effect of the thickness of the welded plates and the welding procedure on the engineering stress-strain response of the steel material was assessed based on the tensile coupons that were extracted from the built-up box columns at the locations shown in Figures 3.9a-3.9c. The engineering stress-strain curves from the 74 tensile tests, carried out according to ASTM A370 (2014), are presented in Figure 3.10. A summary of the resulting mechanical properties of the steel material, according to the four classifications mentioned in Section 3.3.1, is shown in Table 3.2.

Based on Figure 3.10 and Table 3.2, the yield stress (f_y) and the ultimate stress (f_u) values were found to be greater than the nominal values according to the specifications for ASTM A572 Gr.50 (2013) steel. However, the welding procedure and plate thickness affected the engineering strain at fracture. In particular, for tensile coupons located through the thickness of the steel plate the average engineering strain at fracture was 0.16, and for the specimens near the weld it was 0.15. These values are lower than what is expected from ASTM A572 Gr. 50 steel; for which the minimum elongation is 0.18 (ASTM A572 Gr.50, 2013).

Specimens away from the weld and at the surface of the plate complied with the minimum elongation requirements per ASTM A572 Gr.50 (2013); the reason for this is that the area of steel from which these specimens were obtained was less affected by the welding and the lack of compactness of the steel grains from the rolling process that occurs at the through thickness regions of thick plates. Note that coupons extracted from the plate surface and away from the weld showed a low coefficient of variation (COV) for plastic strains compared to the ones that were extracted from the location through the plate thickness and near the weld.

3.3.1.2 Charpy-V-Notch test results

The CVN tests, conducted according to ASTM A370 (2014), provided values of the energy required to break a notched specimen. The fracture toughness of the steel material was computed from the CVN energy value depending on the testing temperature and the material's elastic modulus (Barsom and Rolfe, 1987). The 100 CVN specimens that were extracted from the box-columns were tested at temperatures of -60, -40, 0, 60 and 81˚C in order to develop the fracture toughness profile of the steel material. Specimens were taken from different locations through the thickness of the 75mm steel plates of the built-up box columns (Figures 3.9d-3.9f). The average CVN absorbed energy per location through the thickness of the respective steel plates is shown in Figure 3.11. A summary of the resulting absorbed energy values of the steel material, according to the four classifications, mentioned in Section 3.3.1, is summarized in Table 3.3. Figure 3.11 also shows the theoretical CVN-temperature curve based on the equivalent carbon content of the material according to Johnson and Storey (2008).

It is seen from Figure 3.11 that the average test results are very close to the theoretical CVN-temperature curve. The material's fracture toughness relation with temperature is divided into three portions; lower shelf values at low temperatures that are characterized by low fracture toughness values and small variations; upper shelf values at high temperatures that are characterized by high fracture toughness and small variations; and the transition zone values between the previous two portions, which are characterized by rapid linear variation in the fracture toughness values with temperature. The results are in agreement with the code requirements (ANSI/AISC 360-10, 2010, AWS D1.1, 2010, CAN/CSA-W59, 2013, CAN/CSA-S16-14, 2014), which state that a CVN value for ASTM A572 Gr. 50 steel should not be lower than 27 joules at 0°C.

However, the CVN results show a very high COV at lower shelf temperatures (Table 3.3), which reveals high variability in the obtained CVN values from the same location category and correspondingly, the fracture toughness of the material. Additionally, specimens near the weld and through the thickness showed low CVN values compared to specimens near the weld and at the plate surface at the same temperatures. This can be attributed to the fact that the through thickness grain sizes are greater than those at the surface (Jefferson and Woods, 1962), hence, the effect of the heat affected zone on the material toughness is greater at the through thickness region (Sundaram et al., 1987).

3.3.2 Case Study-1: Temperature measurements

In order to validate the results from the heat-transfer analysis of the proposed modeling approach discussed in Section 3.2 a testing program was established using two steel plates of the same material (heat) as the heavy built-up box column to perform temperature measurements during the welding procedure. The test layout is shown in Figures 3.7b-3.7c. The welding was conducted using an automatic submerged arc welding (SAW) procedure with average heat input of 3 KJ/mm, average current of 850 A and average voltage of 30 V. Each side was welded with a partial joint penetration (PJP) weld, with groove depth of 19mm and groove angle of 60°, consisting of 6 passes (Figure 3.7b). The electrodes and flux used for this procedure were F7A4-EM12K according to AWS D1.1 (2010) A5.17. Two electrodes were used with diameter 2.4mm and an 8mm gap. The average travel speed of the electrodes was 500 mm/min and the average wire feeding speed was 320 cm/min. The region to be welded and its surrounding area, at a distance equal to 75mm from both sides of the weld, measured from the edge of the weld, was pre-heated to 110 ˚C as specified by AWS D1.1 (2010) "Table 3.2". Once the welding passes had been completed on the first side (noted as "Side 1" in Figure 3.7b), the two plates were flipped and then the welding of the other side was completed (noted as "Side 2" in Figure 3.7b). During each welding pass temperature measurements were obtained at three locations (T1, T2 and T3) as illustrated in Figure 3.7c using an infrared radiation thermometer, with accuracy ±1% of reading and adjustable emissivity, at a 20 seconds time interval, the temperatures were also measured using a digital welding pyrometer with surface probe for validation of the results and it showed agreement with the results of the infrared thermometer. The closest measurements to the welding line were at 20mm due to the large amount of flux during the welding process. Figure 3.7d shows the final weld beads after completion of the welding procedure. Figure 3.12 shows the measured temperatures at T1 and T2 during the welding of passes 3 and 5 at side 1. The measured temperatures at location T1 were constant as the welding electrode approached this position. The temperature readings started to increase as the welding electrode passed T1. At location T2 the measured temperatures were largely constant through the welding procedure of each pass since it was away from the heat source by 40 mm. The temperature did, however, start to increase near the completion of the pass once the heat flow from welding was able to traverse this additional distance.

3.3.2.1 Validation of the heat-transfer simulation

In order to establish confidence in the results of the FE simulation for the welding procedure; temperature distributions were obtained from the 3-D FE model of case study-1 at the same locations that were extracted from the test. Figure 3.12 shows a comparison of the temperature results between the FE model and the measured temperatures at locations T1, T2 and T3 (Figure 3.7c) during the weld passes 3 and 5 at side 1 (Figure 3.7b). The comparison between the measured temperature results and the FE model results for all the other welding passes is shown in Appendix A. The welding simulation traced the temperature results of the weld experiments with a maximum absolute relative error of 20% at T1 and negligible for T2 and T3. This is in part attributed to the amount of the welding flux deposited on the steel plates from the SAW procedure, which made it a challenge to obtain precise temperature measurements at location T1 that was very close to the weld (Figure 3.7c).

3.3.3 Case study 2: Stress distribution validation

An experimental evaluation of the welding residual stresses was conducted for an ASTM A572 Gr.50 (2013) steel box-section of dimensions 500x500x1000x28 shown in Figure 3.13a by Chen and Chang (1993). Sectioning method was used at the mid-length of welded component to compute the residual strains using strain gauges of 250mm gauge length. A FE simulation of the welding procedure was developed utilizing a typical welding procedure for this complete joint penetration (CJP) assembly; such that the number of passes was 10, welding travel speed was 2.5mm/s and no preheat was performed. The material model in the simulation was updated according to the tensile test results conducted by Chen and Chang (1993) for the same box-section material. Figure 3.13b show the resultant residual stress distribution on the surface of the welded 28mm plate from the FE simulation. The stress distribution at the path at mid-length of the welded plate in the FE simulation, as shown in Figure 3.13b, is compared to the residual stress results from the sectioning test conducted by Chen and Chang (1993). A comparison of the residual stress distribution at the mid-length of the welded plate between the FE results and the experimental results is shown in Figure 3.13c. The proposed method for welding procedure simulation of thick steel plates traced the experimental peak tensile residual stress values with a maximum error of +8%.

3.3.4 Case study-3: heavy built-up box column

A simulation of the welding procedure for the second case study heavy built-up box column (Section 3) was also carried out. The fabricator followed the recommendations given by AWS D1.1 2010 “Clause 3 for prequalification of Welding Procedure Specifications (WPS)” for welding thick plates, however, extensive cracking still occurred after the completion of the welding procedure. The welding procedure was conducted on two corners of the built-up column simultaneously using an automatic SAW procedure with average heat input of 2.4 KJ/mm, average current of 700 A and average voltage of 30 V. Each corner was a PJP weld, with groove depth of 37.5mm and groove angle of 60°, consisting of 13 passes (Figure 3.2b). The electrodes and flux used for this procedure were F7A4-EM12K according to A5.17 AWS D1.1 (2010). Two electrodes were used at each corner with diameter 2.4mm and an 8mm gap. The average travel speed of the electrodes was 525 mm/min and the average wire feeding speed was 255 cm/min. For this case-study, the welding sequence according to the fabricator and the AISC welding guidelines by Miller (2006) for welding thick plates is summarized as follows: (a) weld one pass on one side (side-1) of the built-up box column; (b) flip the built-up box column and weld the other side (side-2) and complete weld passes 1 to 4; (c) flip again and weld side-1 and complete weld passes 2 to 7; (d) flip and weld the other side-2 and complete weld passes 5 to 7; (e) flip and weld the other side-1 and complete weld passes pass 8 to 13; (f) flip and weld the other side-2 and complete weld passes 8 to 13.

The region to be welded and its surrounding area, at a distance equal to 75mm from both sides of the weld, measured from the edge of the weld, was pre-heated to 110 ˚C as specified by AWS D1.1 (2010) “Table 3.2”. A weld pass was then completed with welding temperature of approximately 1500 ˚C. This weld was left at room temperature for about 20 minutes until the electrodes were returned to the start position and the weld surface was cleaned. The region surrounding the weld was heated again for the second pass. This pre-heating procedure was followed for all subsequent welds.

After the heavy built-up box columns had cooled to room temperature, they developed cracks near the weld in the direction parallel to the weld axis as illustrated in Figure 3.2c. These cracks occurred as a result of the high constraint provided by the thickness of the plates, the large amount of heat input required for welding such thickness and the non-homogenous nature of the grain structure of the steel. Additionally, as the plate thickness increases the likelihood of imperfections and defects resulting from the initial rolling process increases (Jefferson and Woods, 1962). Subsequently, these defects can easily propagate under the high residual stresses generated by the heating and cooling of the steel during welding.

3.3.4.1 Welding procedure assessment for case study-3

As an application of the FE simulation approach of the welding procedure an assessment was conducted for the case-study heavy built up box column through 3-D FE simulation. Based on feedback from the fabricator the 75mm plates used in the box-column underwent inspection according to AWS D1.1 (2010). Consequently, plates with discontinuities within 3mm from the plate surface and plates with discontinuities at the cut surface greater than 25mm and at more were rejected based on AWS D1.1 (2010) clause “5.15.1” for base metal preparation before welding. Applying principles of linear fracture mechanics, with an average upper shelf CVN value of 82 J for specimens taken near the welded area and through the thickness (Table 3.3), the corresponding fracture toughness of the steel at this area would be 105 MPa.√m according to the formula developed by Barsom and Rolfe (1987) shown in Equation 3.3. An application of the proposed welding simulation is to obtain residual transverse tensile stress values at the region near the weld and through the thickness; which are approximately 350 MPa. This stress level produces a stress intensity factor of 110 MPa.√m for an acceptable surface discontinuity of 25mm and for fracture mode I as shown in Equation 3.4 (Tada et al., 2000). The stress intensity factor is greater than 15% of the fracture toughness of the material at this location; as such, this discontinuity has a 50% chance of propagating as a result of the residual stresses produced from the welding procedure.

$$K_I = \sqrt{0.64 \times CVN \times E} = \sqrt{0.64 \times 82 \times 2.1 \times 10^8} = 105000\, KPa.\sqrt{m} = 105\, MPa.\sqrt{m}\,, \tag{3.3}$$

$$K = 1.12\sigma\sqrt{\pi a} = 1.12 \times 350 \times \sqrt{\pi \times 0.025} = 110\, MPa.\sqrt{m}\,, \tag{3.4}$$

Where K_I is the dynamic fracture toughness (KPa.√m), CVN is the absorbed energy measured from Charpy-V-Notch tests (Joules) from Table 3.3, E is the modulus of elasticity of the steel material (KPa) from Table 3.2, K is the stress intensity factor (MPa.√m), σ is the applied stress level for fracture modes I, II and III (MPa) and a is the crack length (m). Theoretically, by solving the stress intensity formula backward (Tada et al., 2000) and using the fracture toughness of the material as a stress intensity factor, the resulting discontinuity size becomes 20 mm. As such, for the built-up box column discussed herein any embedded crack of size greater than 20 mm had more than a 50% chance of propagating after the welding procedure has been concluded at the location near the welding area. It is worth mentioning that, according to AWS D1.1 (2010), for qualifying a welding procedure for unlimited thickness the test plates need only be 38mm thick. In addition, according to this study and a study conducted by Suwan (2002) on the CVN values for different thicknesses of ASTM A572 Gr.50 (2013) steel, the average upper shelf CVN value for plates in the thickness range 19-38mm is about double the value of plates with thickness range of 64-100mm. Accordingly, due to low fracture toughness expected for thick plates (greater than 50mm) as well as higher residual stresses due to welding (Miller, 2010), separate welding specifications and acceptance criteria for welding thick steel plates.

3.3.5 Summary of FE model results and validation

In summary, the FE model of the welding test, developed using the proposed modeling approach (Section 2), was able to predict the measured temperature values from case study 1 as well as the welding residual stress distribution in the 28mm thick box-section measured by Chen and Chang (1993) using sectioning method. Furthermore, the FE simulation of the welding procedure for the heavy built-up box column confirmed the propagation of cracks due to the employed welding procedure based on principles of linear elastic fracture mechanics. Hence, the proposed numerical modeling approach can be used for the assessment of welding procedures before they are conducted in order to develop acceptance criteria for the steel plates to be welded. Furthermore, this numerical modeling approach can be used to develop quantitative criteria for establishing better welding procedures and improving existing welding guidelines. The authors are currently working in this direction.

3.4 Limitations of the Proposed Modeling Approach for Welding Procedures

It is anticipated that the proposed numerical model would better replicate an automatic welding procedure compared with a manual procedure; this is attributed to the uncertainty in the values of welding parameters in the case of manual welding, such as the welding speed and the ability of a welder to complete the weld pass as straight as possible. Also, modeling the preheating process parameters, such as the temperature and the preheating period, has to be established as close as possible to their physical values to achieve the most accurate welding simulation. Consequently, welding procedures for which the preheating process is not strictly controlled cannot be simulated accurately at this stage based on the proposed numerical approach. The proposed model is not able to explicitly simulate potential crack propagation; only the residual stress output is provided. Fracture simulation can be introduced in the proposed simulation using the fracture modeling approach developed by Hillerborg et al. (1976). In this case, further validation will be required. Furthermore, the effects of the elevated temperature on the microstructure of steel is not explicitly modeled; to improve the proposed modeling approach the effect of the steel microstructure on the fracture behavior, as illustrated by Manigandan et al. (2014), should be considered. The proposed modeling approach is intended for arc welding procedures and cannot be used to simulate other welding procedures such as Oxy-fuel welding; which for example, is conducted by applying very high temperature up to 3500°C to develop a large pool of molten metal.

3.5 Summary and Conclusions

With the aim of improving guidelines for the welding of thick plates through a practice-oriented evaluation approach a numerical model of the welding procedure was proposed. This modeling approach incorporates a heat transfer analysis followed a stress analysis using the death and birth technique. A mesh sensitivity study was completed and the recommended element sizes are a minimum of 2mm and a maximum of 9mm apply for the 3-D model. The creep strain properties were introduced in the welding simulation. Two approaches were employed to define the time and temperature dependent strain. For a specific box-column case study, the difference in the stress distribution between the model that accounted for the creep strain properties and the one that did not account for creep was negligible. Tensile coupon and CVN material tests were completed using specimens obtained from different locations in the case-study box columns with the aim of calibrating the numerical model and studying the effect of the welding procedure on the welded plates. These tests demonstrated the extent of the effect of the plate thickness and the welding procedure on the properties of the steel material. The regions near the welded area and the regions through the plate thickness showed lower ductility and fracture toughness than the expected nominal values. In order to validate the results of the numerical model a welding test was carried out of two 75mm thick plates made of the same material as the case study box column. Temperature measurements were obtained during each weld pass at locations close to the welded area, and compared with the results of the numerical model at the same locations. The numerical model was able to predict the measured temperature values with maximum difference of 20% in the temperature values. The resulting residual stress distribution from the proposed method for welding simulation was also validated with experimental results conducted by Chen and Chang (1993). Moreover, based on the CVN test results and by applying the proposed numerical modeling approach on the box column discussed herein it was determined that any discontinuity greater than 0.8mm has more than a 50% chance to propagate under the residual stresses produced from the welding procedure. It can be concluded that the welding of thick plates requires a separate set of welding specifications to reduce residual stresses generated by welding and limit crack sizes and set minimum upper shelf CVN values near the welding area. The welding simulation can be used to test various automatic submerged arc welding procedures and techniques to determine quantitative guidelines for welding heavy assemblies that utilize thick steel plates.

Acknowledgments

The authors sincerely thank the ADF Group Inc. and DPHV Structural Consultants for their financial and technical support, for providing the tensile and CVN specimens and for carrying out the weld testing. The authors also acknowledge the financial support from the Natural Sciences and Engineering Research Council of Canada.

Table 3.1: Steel material properties at elevated temperatures for heat transfer simulation according to Society of Fire Protection Engineers (2008)

Required material properties for heat transfer		
T [ºC]	**Thermal Conductivity [W/m. ºC]**	**Specific heat [N.mm/Kg ºC]**
20	53.334	4.40E+08
100	50.67	4.88E+08
200	47.34	5.30E+08
300	44.01	5.65E+08
400	40.68	6.06E+08
500	37.35	6.67E+08
600	34.02	7.60E+08
700	30.69	1.01E+09
800	27.36	8.03E+08
900	27.3	6.50E+08
1000	27.3	6.50E+08
1100	27.3	6.50E+08
1200	27.3	6.50E+08

Table 3.2: Summary of the results of tensile coupon tests for ASTM A572 Gr.50 (2013) steel.

	Min	Max	Mean (μ)	St. dev. (σ)	COV
Specimens near the weld and at plate surface					
E [MPa]	198620	234790	211203	16438	8%
f_y **[MPa]**	355	425	391	39	10%
ε_y	0.0017	0.0021	0.0018	0.00017	9%
f_u **[MPa]**	589	651	609	25	4%
ε_u	0.0736	0.1384	0.1199	0.0263	22%
f_u/f_y	1.4246	1.6494	1.5497	0.0860	6%
ε_{max}	0.096	0.173	0.1494	0.0309	21%
Specimens near the weld and through the thickness					
E [MPa]	205220	213760	208747	4169	2%
f_y **[MPa]**	326	338	332	7	2%
ε_y	0.0015	0.0016	0.0015	0.00005	3%
f_u **[MPa]**	522	640	608	26	4%
ε_u	0.0543	0.1498	0.1253	0.0206	16%
f_u/f_y	1.3933	1.8253	1.6518	0.1152	7%
ε_{max}	0.0543	0.19	0.1520	0.0294	19%
Specimens away from the weld and at plate surface					
E [MPa]	195490	224690	209299	8744	4%
f_y **[MPa]**	375	411	396	13	3%
ε_y	0.0017	0.0020	0.0019	0.0001	6%
f_u **[MPa]**	576	640	614	16	3%
ε_u	0.1110	0.1570	0.1443	0.0110	8%
f_u/f_y	1.4291	1.7815	1.5731	0.1029	7%
ε_{max}	0.1610	0.2020	0.1855	0.0104	6%
Specimens away from the weld and through the thickness					
E [MPa]	192950	222870	202281	8248	4%
f_y **[MPa]**	344	387	365	14	4%
ε_y	0.0015	0.0019	0.0018	0.0001	7%
f_u **[MPa]**	518	634	595	34	6%
ε_u	0.0516	0.1660	0.1273	0.0226	18%
f_u/f_y	1.4066	1.7802	1.5986	0.1027	6%
ε_{max}	0.0592	0.1990	0.1645	0.0302	18%

Table 3.3: Summary of the CVN results for ASTM A572 Gr.50 (2013) steel.

Temperature [˚C]	Min [J]	Max [J]	Mean (μ) [J]	St. dev. (σ) [J]	COV
Specimens near the weld and at plate surface					
-40	41	44	42.5	2.1	5%
0	74	90	82	11.3	14%
60	135	143	139	5.7	4%
Specimens near the weld and through the thickness					
-60	4	20	12	8.1	67%
-40	14	20	16	3.2	21%
0	35	64	50	12.1	24%
60	98	128	112	8.7	9%
81	93	131	117	15.9	16%
Specimens away from the weld and at plate surface					
-60	13	45	31	16.5	53%
-40	22	79	32	21.6	68%
0	67	102	78	13	17%
60	117	157	135	10.6	8%
81	104	141	120	12.8	11%
Specimens away from the weld and through the thickness					
-60	4	12	8	4.1	51%
-40	14	101	33	34.8	105%
0	34	78	57	19.4	34%
60	87	159	109	21.3	20%
81	86	136	110	15.8	14%

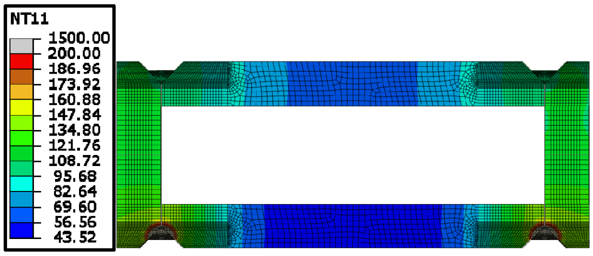

(a) Temperature distribution results from heat transfer simulation of built-up box column after the welding of the sixth pass

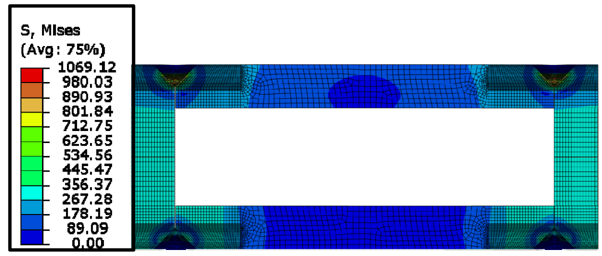

(b) Corresponding Von Mises stress from heat transfer simulation of built-up box column after the welding of the sixth pass

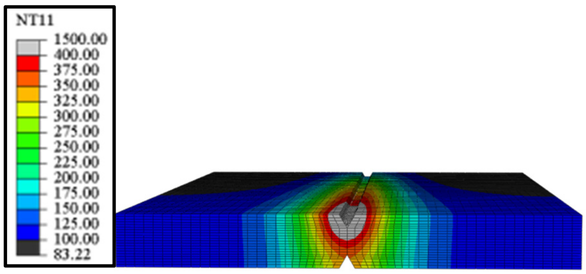

(c) Temperature distribution results from 3D heat transfer simulation of the temperature measuring test after the welding of the second pass

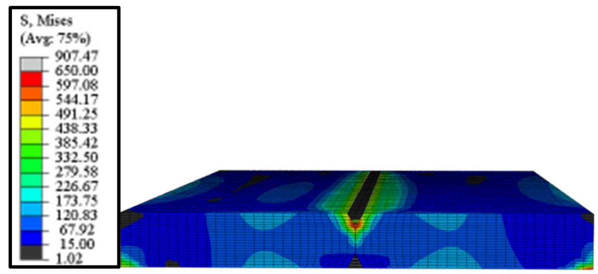

(d) Corresponding Von Mises stress from 3D heat transfer simulation of the temperature measuring test after the welding of the second pass

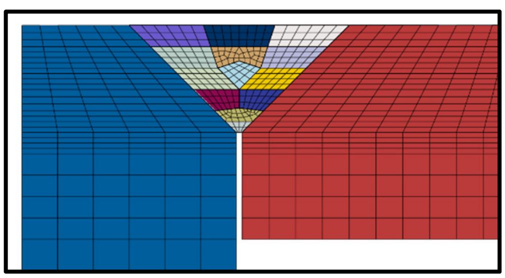

(e) Finite element mesh at the welding area for the 75mm thick built-up box column model

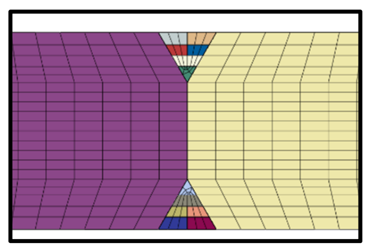

(f) Finite element mesh at the welding area for the flat welded 75mm thick plates

Figure 3.1: Finite element simulation of welding procedures in ABAQUS.

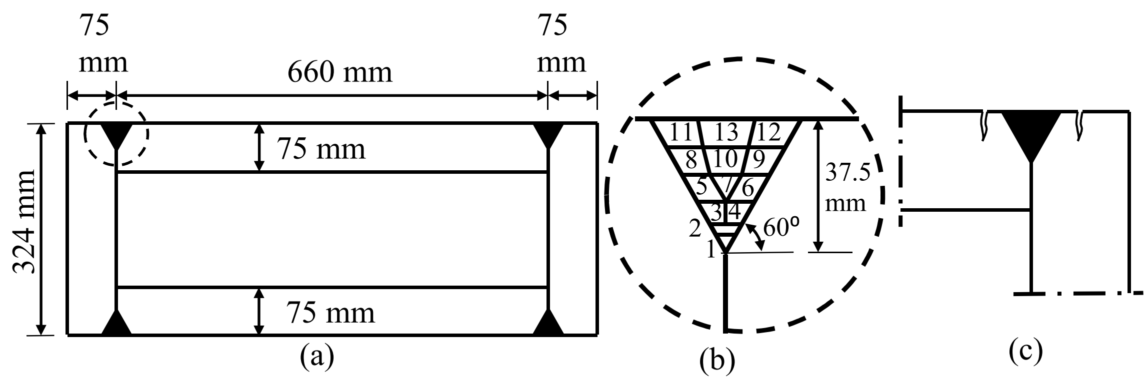

Figure 3.2: Schematic representation of the PJP welds on the built-up steel box column; a) cross-section dimensions of the built-up box column; b) profile of the welding passes at each partial penetration joint; c) illustration of the location of the cracks that occurred in the case study heavy box column.

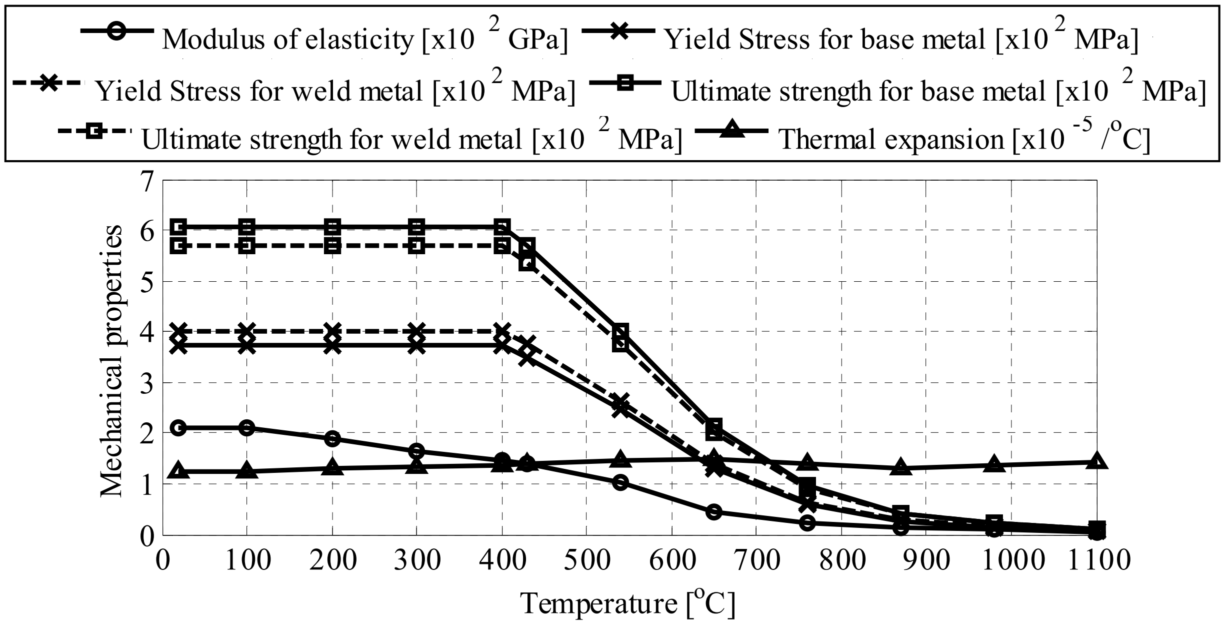

Figure 3.3: Material properties used in the stress analysis model at elevated temperatures based on ANSI/AISC 360-10 (2010) and Society of Fire Protection Engineers (2008).

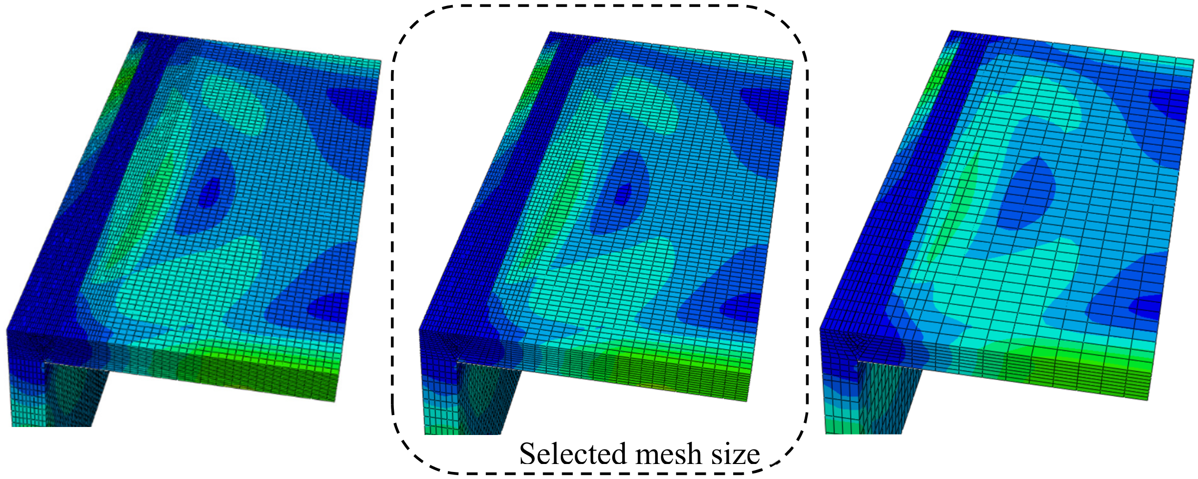

(a) (b) (c)

Figure 3.4: Employed mesh sizes for the FE welding simulation of the 3-D model. a) Maximum element dimension 1 to 5mm, b) Maximum element dimension 2 to 9mm, c) maximum element dimension 5 to 20mm.

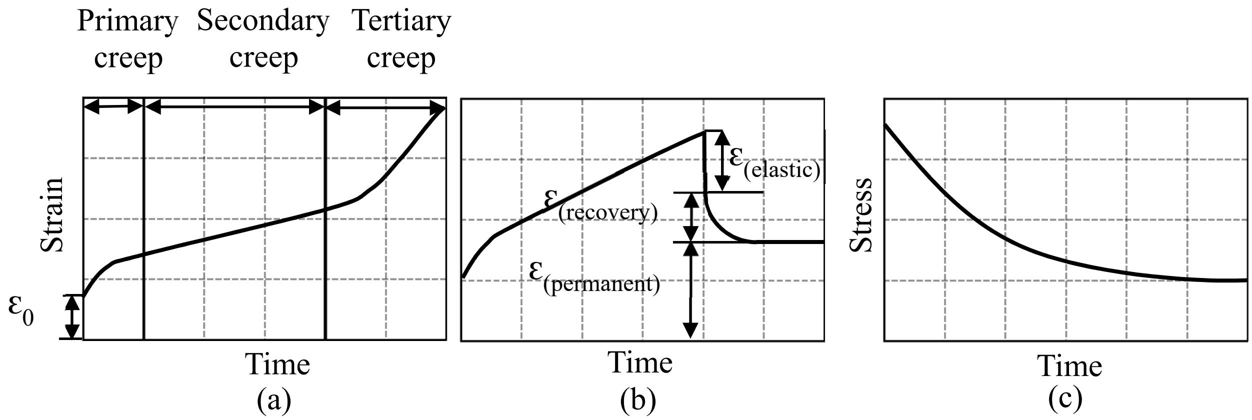

Figure 3.5: Consideration of creep effects on welding procedures of steel plates; (a) creep strain stages for constant stress and temperature; (b) creep strain recovery; (c) stress relaxation (adapted from Norton (1929)).

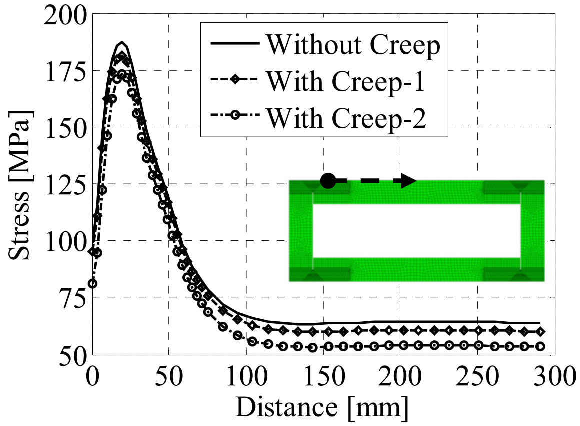

(a)

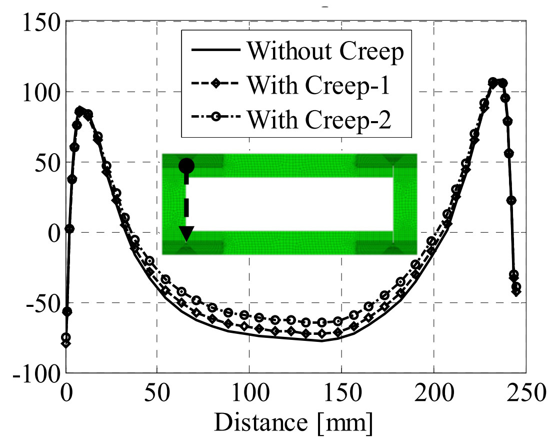

(b)

Figure 3.6: Creep strain effect on the resulting residual stress; (a) transverse stress comparison for creep at horizontal plate after pass number 26; (b) transverse stress comparison for creep at vertical plate after pass number 26.

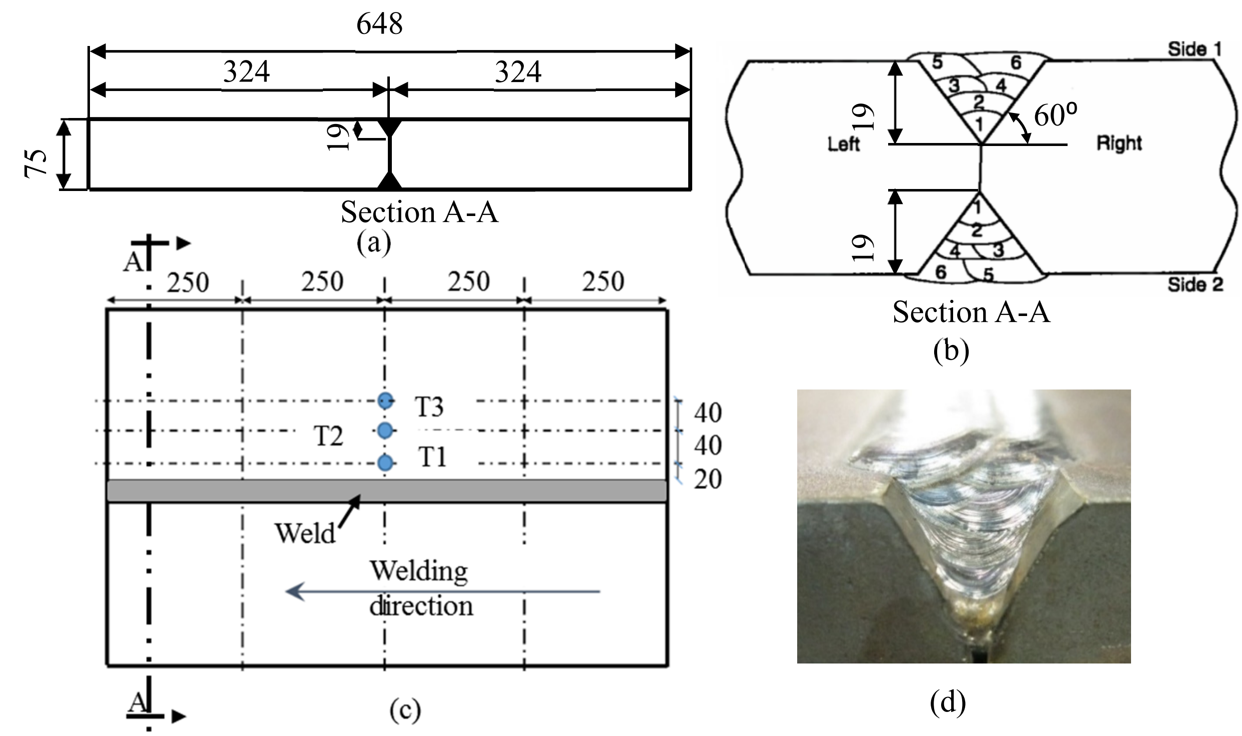

Figure 3.7: Weld test specimen (dimensions are in mm); (a) cross-section and dimensions of the welded plates; (b) welding sequence conducted for the test; (c) test layout and location of temperature measuring nodes; (d) welded passes after completing the welding process.

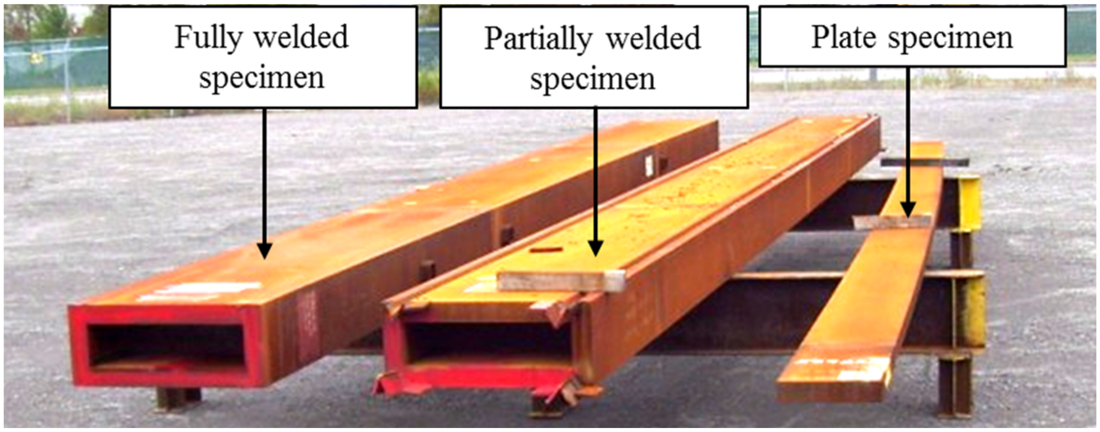

Figure 3.8: Specimens used for steel material characterization and FE model validation.

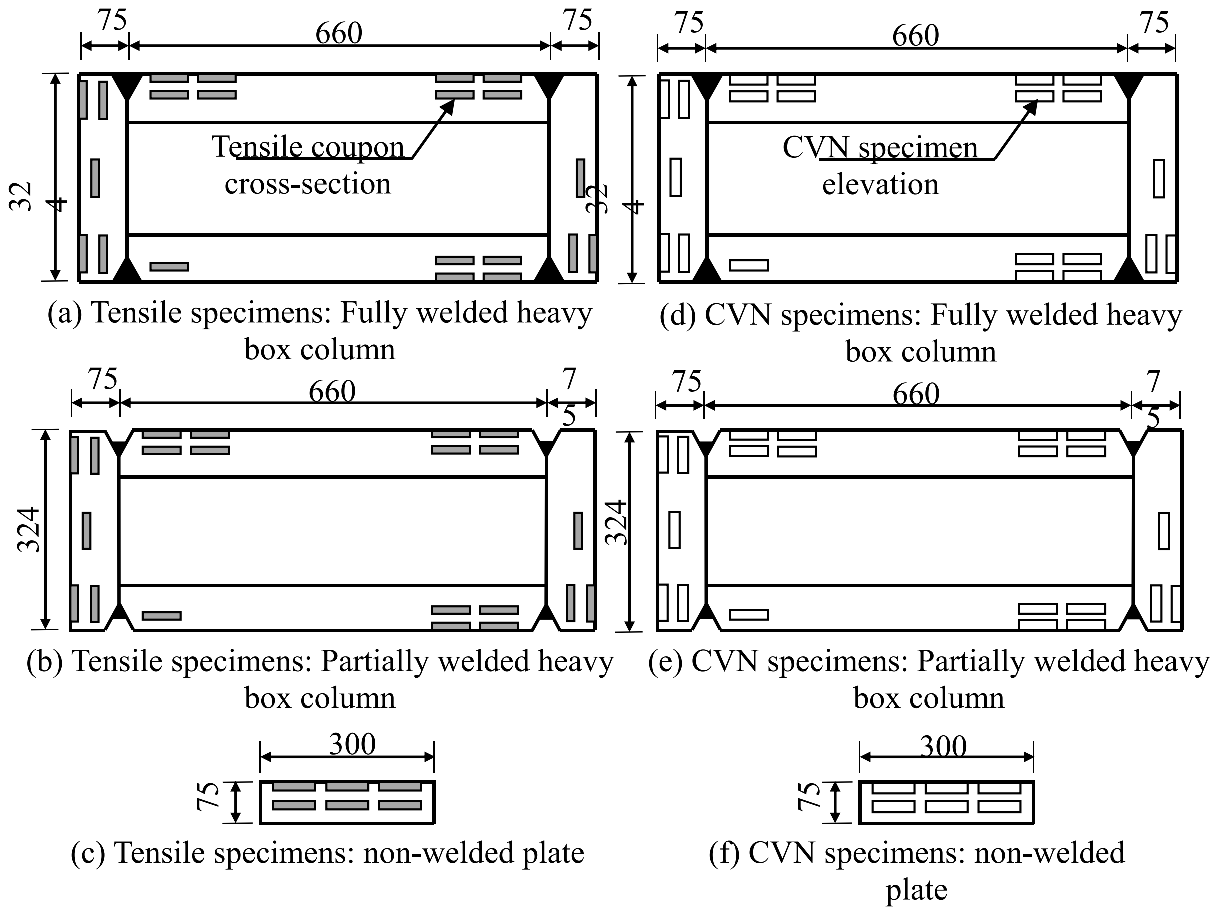

Figure 3.9: Locations of longitudinal tensile and transverse CVN specimens. (Dimensions are in mm).

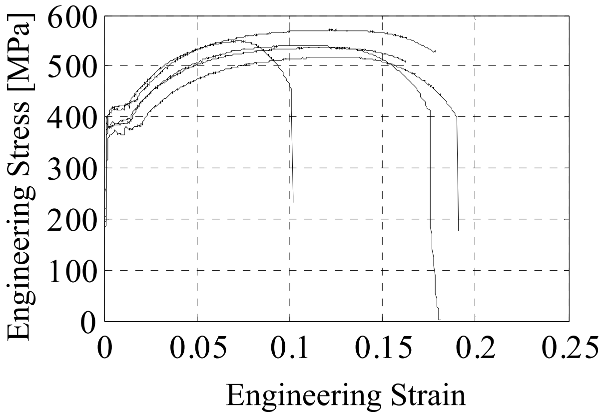

(a) Coupons at plate surface and near the weld

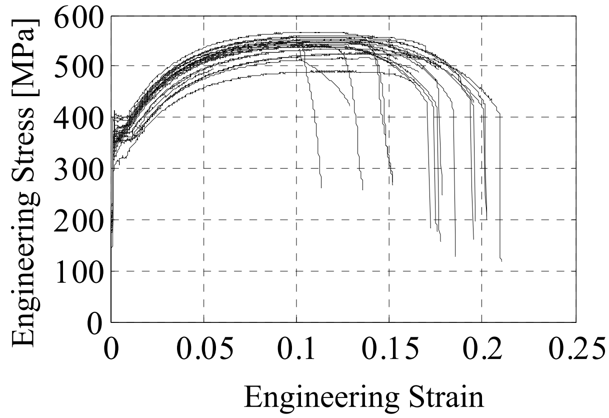

(b) Coupons through the thickness and near the weld

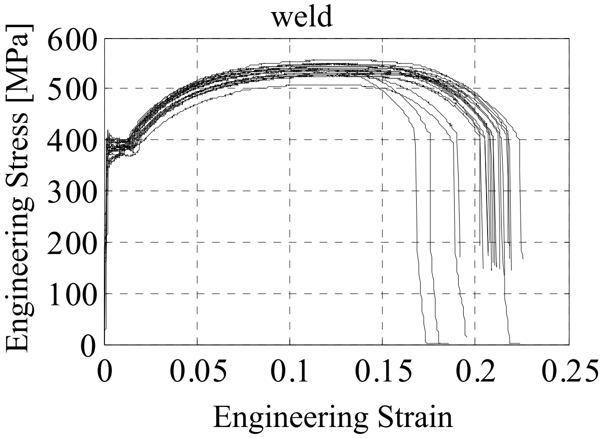

(c) Coupons at plate surface and away from the weld

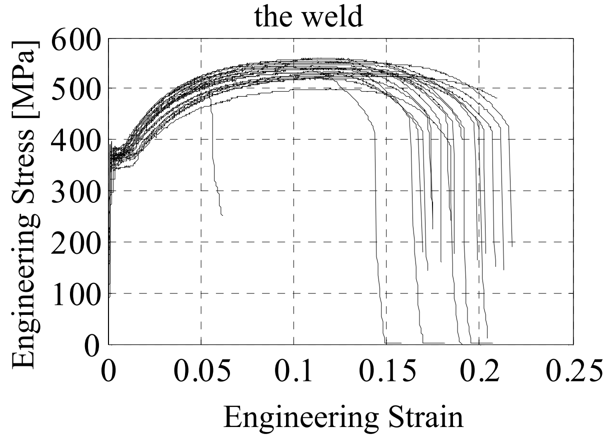

(d) Coupons through the thickness and away from the weld

Figure 3.10: Tensile coupon test results for case-study steel plate (t=75mm, ASTM A572 Gr. 50).

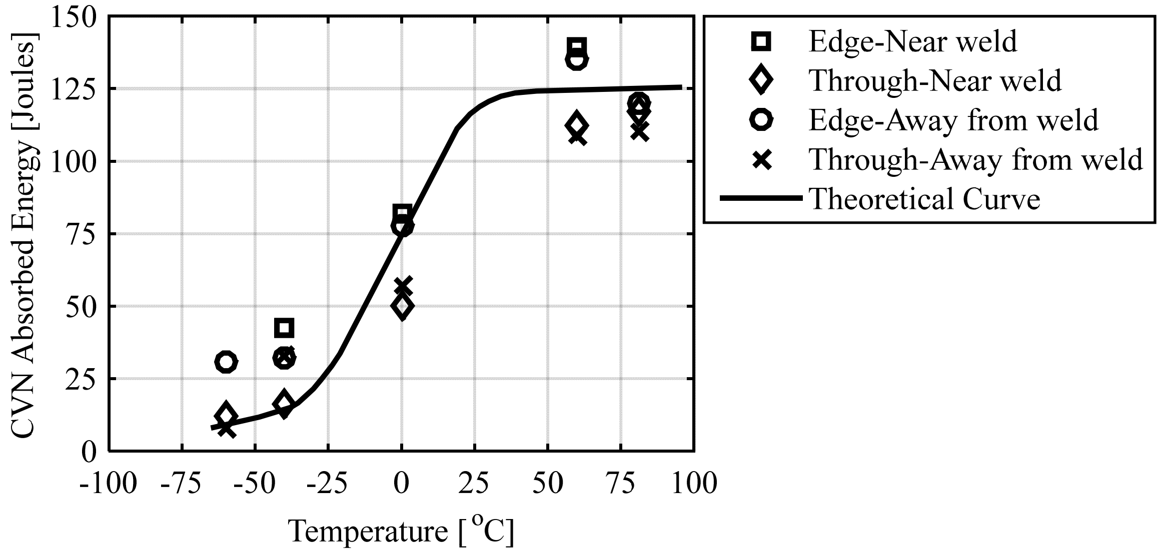

Figure 3.11: Average CVN absorbed energy values at tested temperatures for different locations in the case-study steel plate (t=75mm, ASTM A572 Gr. 50) and the theoretical CVN-temperature curve according to Johnson et al. (Johnson and Storey, 2008).

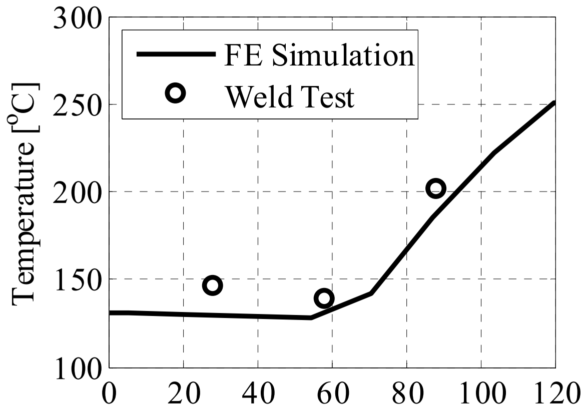

(a) Temperature at node T1 for pass number 3

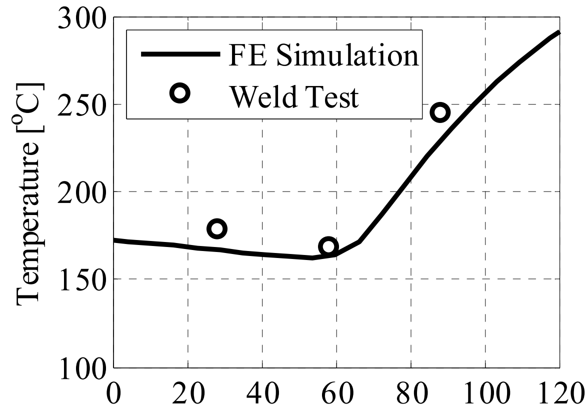

(b) Temperature at node T1 for pass number 5

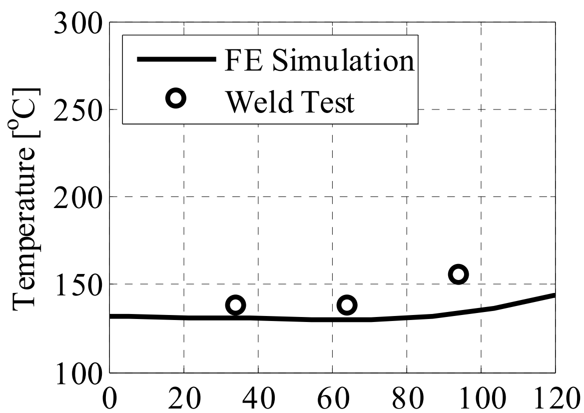

(c) Temperature at node T2 for pass number 3

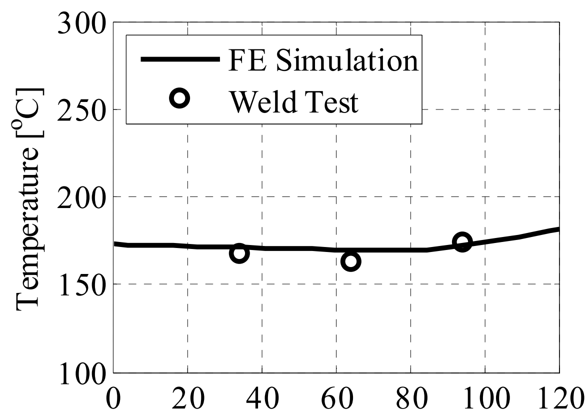

(d) Temperature at node T2 for pass number 5

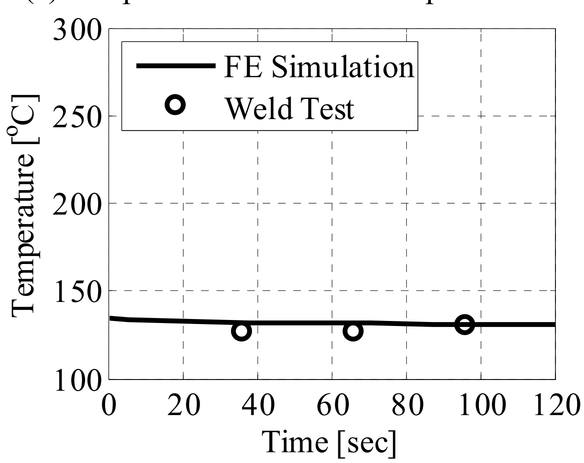

(c) Temperature at node T3 for pass number 3

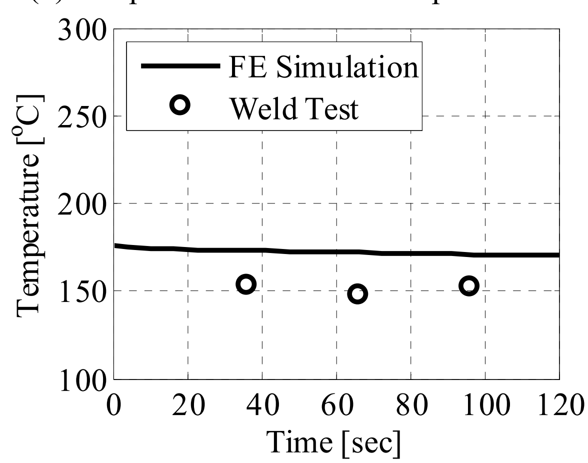

(d) Temperature at node T3 for pass number 5

Figure 3.12: Comparison of temperature results from the FE simulation and the weld test results.

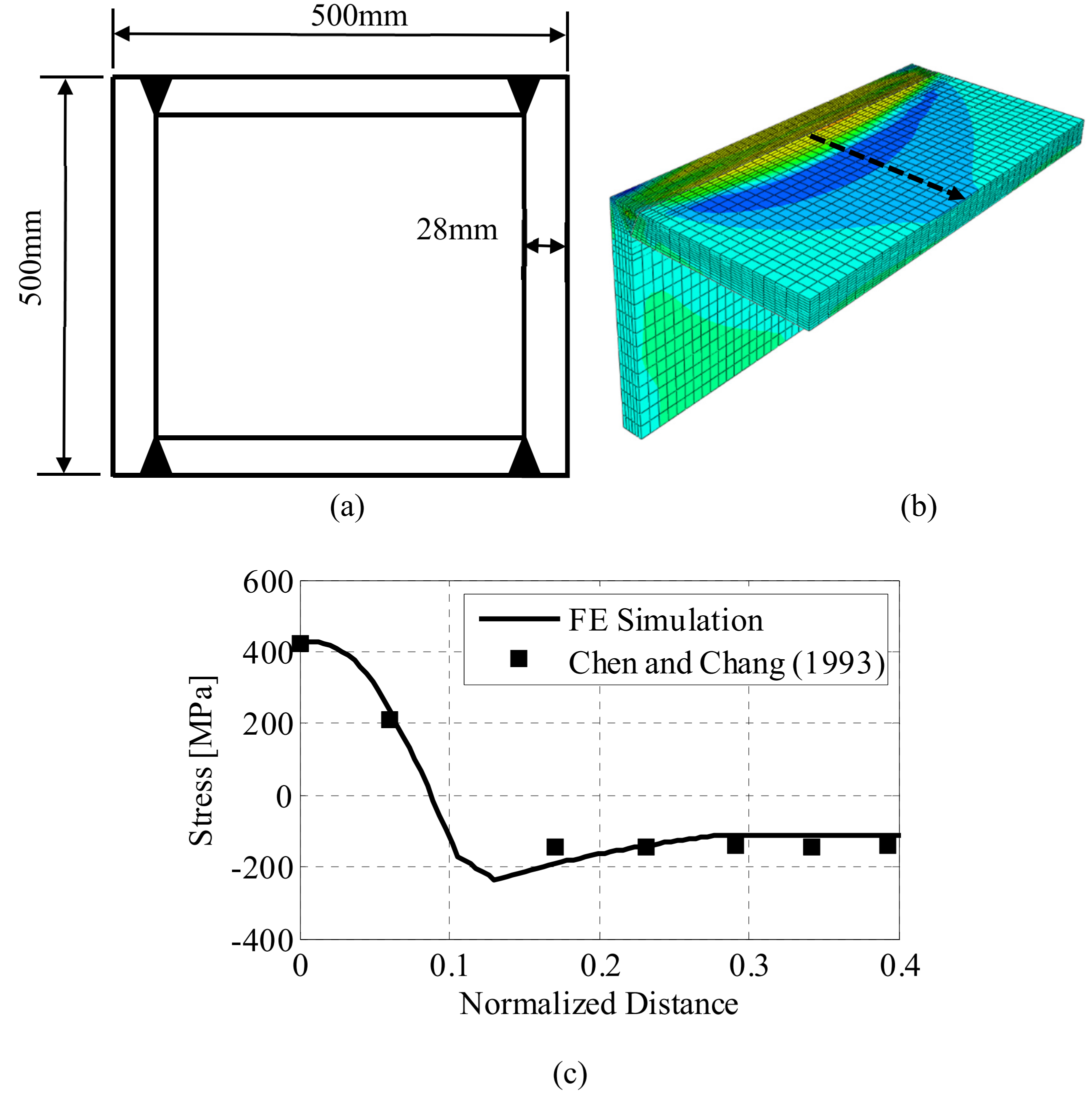

Figure 3.13: The validation of the residual stress distribution result of the FE simulation with the experimental results from Chen and Chang (1993); a) Dimensions of box section, b) Residual stress distribution from the FE simulation and studied path, c) A comparison between the FE stress distribution results and sectioning method results.

Chapter 4 ASSESSMENT OF DISCONTINUITIES IN STRUCTURAL STEEL COMPONENTS BASED ON CHARPY-V-NOTCH TESTS

4.1 Introduction

Welding is one of the most popular steel joining methods in North America. The combination of the tensile residual stresses associated with the welding procedures for steel assemblies and the discontinuities already present in the steel component prior to welding can lead to crack initiation. The crack initiation primarily depends on three parameters: the discontinuity size and type; the applied stress (welding residual stress level); and the fracture toughness of the steel material at the corresponding temperature (Zehnder, 2012). The fracture toughness of a material is often used to define its ability to withstand crack initiation; one of the most common methods of calculating fracture toughness is through the Charpy-V-Notch (CVN) absorbed energy value. Current assessment criteria for discontinuities in steel plates (ANSI/AISC 360-10, 2010, AWS D1.1, 2010, CAN/CSA-W59, 2013, CAN/CSA-S16-14, 2014) have been written such that only maximum allowable discontinuity sizes and minimum CVN values according to the steel grade are considered; the significance of other parameters such as the position and type of the discontinuity as well as the applied stress level are not addressed. Moreover, the fracture toughness of steel is not constant within a steel plate (Suwan, 2002, Ibrahim et al., 2015). This is another issue that is not addressed in today's specifications (ANSI/AISC 360-10, 2010, AWS D1.1, 2010, CAN/CSA-W59, 2013, CAN/CSA-S16-14, 2014).

In recent years, there is an increasing need for the use of thick steel plates in high-rise steel frame buildings as well as steel bridges. As the thickness of a steel plate increases its fracture toughness decreases, and the variation in the fracture toughness within the same component increases (Barsom and Rolfe, 1987, Suwan, 2002). It is understood that the uncertainty of the fracture toughness value through the thickness of a steel plate should be quantified, and as such should be considered by current welding and steel construction specifications. Furthermore, in the process of evaluating discontinuities, current specifications (ANSI/AISC 360-10, 2010, AWS D1.1, 2010, CAN/CSA-W59, 2013, CAN/CSA-S16-14, 2014) should take into account the importance of a steel component as part of a steel structure (i.e., fracture critical). The working load that a steel component experiences is also another important consideration (i.e., compressive only or compressive/tensile). For instance, in a building, exterior columns experience compressive as well as tensile stresses due to dynamic overturning effects during an earthquake. Interior columns are more likely to be subject to compressive stresses alone, or certainly much lower levels of tensile stresses than exterior columns. Accordingly, discontinuities at the butt-welded splices of exterior columns are more critical than at the same connections for interior columns; which requires distinction in the discontinuities acceptance criteria from non-critical components. Correspondingly, a reliable assessment of discontinuities in steel plates should incorporate the uncertainty in the steel fracture toughness value, the working stress level, the size, position and type of the discontinuity as well as the importance level of the steel component and assembly. This can be achieved through using an approach conceptually similar to that of performance-based building design.

In current North American code provisions (ANSI/AISC 360-10, 2010, AWS D1.1, 2010, CAN/CSA-W59, 2013, CAN/CSA-S16-14, 2014) the acceptance of a steel component to be used in construction depends on the steel grade and its CVN value. The latter is relied on to estimate the fracture toughness of the corresponding steel material. For instance, according to ANSI/AISC 360-10 (2010), CAN/CSA-S16-14 (2014), AWS D1.1 (2010) and CAN/CSA-W59 (2013) the CVN value for ASTM A572 Gr.50 (2013) steel (i.e., nominal yield stress f_y = 345MPa) and ASTM A913 Gr.65 (2014) steel (i.e., f_y = 450MPa) should not be less than 27 and 54 Joules at 21°C, respectively. These criteria are often used assuming the fracture toughness at a given temperature is consistent for all locations in the component, which may not be a valid approach (see Section 4.3). Furthermore, for cracks induced by the welding procedure, "Table 6.2" and Figures "(6.1-6.3)" of AWS D1.1.2010 (AWS D1.1, 2010) illustrate the acceptable crack sizes in a weld based on ultrasonic and radiographic tests, respectively. Based on linear fracture mechanics, a crack is likely to initiate if the stress intensity factor at the crack tip is greater than the fracture toughness of the steel material. The stress intensity factor depends on the crack shape and size as well as the applied stress (Murakami, 1987, Tada et al., 2000). The fracture toughness of the material is calculated from the CVN absorbed energy value of the material (Barsom and Rolfe, 1987). The accepted discontinuity size is 18mm for a 25mm weld size [see "Figure 6.1" in (AWS D1.1, 2010)]; considering a working tensile stress of 200MPa [60% of the yield stress of ASTM A572 Gr.50 (2013) Gr.50 steel] and a through thickness discontinuity, the corresponding stress intensity factor is 57MPa.√m (Murakami, 1987, Tada et al., 2000). However, acknowledging the CVN limit for ASTM A572 Gr. 50 (i.e., f_y = 345 MPa) steel, mentioned previously, the corresponding minimum fracture toughness limit is 56MPa.√m (Barsom and Rolfe, 1987). This means that although the discontinuity size is deemed acceptable according to the welding provisions in AWS D1.1 (2010) and the CVN limit is met (ANSI/AISC 360-10, 2010, CAN/CSA-S16-14, 2014), by employing basic concepts of linear fracture mechanics it can be demonstrated that a crack will most likely initiate along the weld. This simple example indicates that a more comprehensive approach is required to assess cracks and discontinuities present in a welded assembly. This approach should take into account the uncertainty in the fracture toughness value along with the influence of the parameters affecting the stress intensity factor. In addition, discontinuity tolerance limits should be set as a function of the probability of the discontinuity stress intensity factor to exceed the fracture toughness of the material. The same limits should be based on the importance as well as the working load of the structural steel component.

Proposed in this chapter is a practical approach for the assessment of discontinuities in steel plates to determine their critical sizes; taking into account the uncertainty in the value of the material fracture toughness. This was achieved in part through implementing statistical procedures to develop CVN fragility curves based on a database of CVN test results that includes: (a) various steel grades; (b) a range of temperatures; and (c) plates of different thickness. The CVN database was divided into subsets according to the material and testing conditions. A statistical treatment of the data subsets was also employed, accounting for various sources of epistemic uncertainty, to determine a statistical distribution that fits the assembled datasets. Fragility curves for crack initiation were then developed for each subset. Finally, using logistic regression (Chatterjee and Hadi, 2006) a predictive formula was developed to compute the probability of crack initiation given the stress intensity factor, temperature, material type and plate thickness. The impact of parameters such as the crack type, steel material grade, temperature, crack position and plate thickness, on the probability of the crack to initiate was investigated thoroughly. To the best of our knowledge there are no prior studies that utilize the uncertainty associated with the fracture toughness of a steel material and these parameters in order to develop a probabilistic approach for assessing cracks and discontinuities existing in a steel component.

4.2 Outline of the Proposed Methodology and Fragility Curves Development

The proposed methodology is based on a CVN database that was first developed as part of this study. This database, discussed in detail in Section 4.3, contains information regarding measured CVN values from different types of steel materials. Based on this database, in Section 4.4 fragility curves are developed for each steel type based on the maximum likelihood approach (Benjamin and Cornell, 1970, Chatterjee and Hadi, 2006). These curves are used to compute the probability of reaching or exceeding the CVN value given the thickness and temperature of the corresponding steel component. The epistemic uncertainty of the aforementioned fragility curves, induced by the test conditions, are also addressed. The corresponding fracture toughness of each subset is obtained from the CVN value. Through the use of logistic regression, predictive equations were proposed, with which one can compute the probability of crack initiation under a specified stress, crack size and type; this aspect of the methodology is discussed in Section 4.5.

4.3 CVN Database Development

The CVN database comprised tests conducted by Suwan (2002) for ASTM A572 Gr.50 (2013) steel (f_y = 345 MPa) and ASTM A588 Gr.B (2010) (f_y = 345 MPa); as these tests included different materials, thicknesses and test temperatures. Additional tests were conducted at McGill University for ASTM A572 Gr. 50 steel (f_y = 345 MPa) and ASTM A913 Gr. 65 steel (f_y = 450 MPa) (Nikolaidou et al., 2013, Ibrahim et al., 2015), to include additional test temperatures to those done by Suwan for A572 Gr.50 steel, and to add another steel grade that is also used in construction. The CVN tests conducted by Suwan according to ASTM A370 (2014) resulted in 672 absorbed energy values for ASTM A572 Gr. 50 steel and 777 for ASTM A588 Gr. B steel. The specimens, obtained from four different steel mills in the United States of America, were divided into four groups according to the corresponding steel plate thickness (<20mm, 20 to 40mm, 40 to 65mm and 65 to 100mm). The testing temperatures were -18, 4 and 21˚C. Each specimen was machined from a position parallel to the rolling direction of the parent plate.

The CVN dataset provided by Suwan (2002) was expanded through the inclusion of CVN tests conducted by Ibrahim et al. (2015) (see Chapter 3, Table 3.2) according to ASTM A370 (2014). The new dataset included 88 specimens made from ASTM A572 Gr. 50 steel plate from one mill in the USA at a temperature range of -60, -40, 0, 60 and 81 ˚C. All the specimens were taken from a position perpendicular to the rolling direction of the parent plate. Since the specimens were extracted from a 75 mm thick steel plate, these results were included in the thickness group ranging from 65 to 100mm. In addition, 114 specimens obtained from ASTM A913 Gr. 65 steel W360×237 wide flange sections by Nikolaidou et al. (2013) were incorporated as part of the study. A total of 56 of these specimens were taken from a position in the flanges parallel to the rolling direction of the W section, while the rest were obtained from a position in the flanges perpendicular to the rolling direction. Due to a nominal flange thickness of 30 mm this data subset was considered in the thickness group 20-40mm. These CVN specimens were tested at 0, 21, 48 and 69 ˚C. Tables 4.1 and 4.2 summarize the basic statistical quantities of the dissipated energy associated with the mean, μ, 5th and 95th mean percentiles (i.e., $\mu_{5\%}$, $\mu_{95\%}$) and the associated logarithmic standard deviations, β, of the CVN tests included in the database. The scatter in the reported CVN values for each dataset necessitates the use of a probabilistic approach for estimating the probability of reaching or exceeding each CVN value. From this database, it was possible to investigate the effects of temperature, the material type and the plate thickness on the fracture toughness of a steel component.

4.4 Statistical Treatment of the CVN Data

In order to compute the probability of crack initiation through a steel plate from the obtained CVN data, each subset was represented by a statistical distribution which was fitted following the rigorous goodness-of-fit approaches discussed in Section 4.4.1. Furthermore, the effect of epistemic uncertainty on the CVN results was considered with the approach discussed in Section 4.4.2.

4.4.1 Distribution fitting

The CVN values from each group discussed in Section 3 were evaluated using a Kolmogorov-Smirnov's (K-S) goodness-of-fit test (Benjamin and Cornell, 1970) to develop the optimal probabilistic distribution that fits the data; as the K-S test is independent of the function being tested and the sample size. Other statistical hypothesis test can also be used, such as the chi-square goodness-of-fit test (Phillips, 1972). However, the chi-square test requires a sufficient sample size in order for the results to be valid. The lognormal, the Weibull and the exponential probability distribution functions were employed to express the likelihood of reaching or exceeding a CVN value given a temperature and plate thickness. The parameters of these distributions were computed based on the method of maximum likelihood (Benjamin and Cornell, 1970). The maximum difference between the empirical distribution and each statistical distribution and the 5% significance level of the K-S test is shown in Table 4.3 for two different thicknesses (less than 20mm and 20-40mm) of the ASTM A572 Gr. 50 CVN tests conducted by Suwan (2002). The Weibull distribution has the least difference with the empirical results and the cumulative probability distribution of the CVN data. However, the lognormal distribution slightly exceeds the KS-test limit only for thicknesses less than 20mm at 4˚C. A lognormal distribution was ultimately employed because CVN values are always positive and most of the individual CVN data has a skewed distribution with a longer tail for upper values. A summary of the lognormal means (μ) and logarithmic standard deviations (β) of the energy values for all the subsets discussed in Section 3 are shown in Tables 4.1 and 4.2. The mean of a distribution increases with the increase of temperature as would be expected. Also, the standard deviations reflect how sensitive the CVN value is with respect to the location in the steel plate and the thickness of the steel plate from which the CVN coupon was taken.

Figures 4.1a and 4.1b show the fitted lognormal probability distributions (solid black line) of the empirical distribution CVN subsets of the A572 Gr. 50 steel at 0 and -40˚C, respectively. As anticipated, with the decrease in temperature the steel material becomes brittle and the probability of reaching or exceeding a specified CVN value decreases. For example, the probability of reaching or exceeding the CVN limit based on the current code provisions in North America (ANSI/AISC 360-10, 2010, AWS D1.1, 2010, CAN/CSA-W59, 2013, CAN/CSA-S16-14, 2014) at 0˚C is 99% and at -40˚C is 80%. Similarly, Figures 4.1c and 4.1d illustrate the lognormal probability distributions of the empirical distribution CVN subsets for ASTM A913 Gr. 65 steel at 0˚C in the positions parallel and perpendicular to the rolling direction, respectively. The probability of reaching or exceeding a specified CVN value for specimens oriented parallel to the rolling direction is larger than that for specimens located perpendicular to the rolling direction of the steel. As such, the probability of reaching or exceeding the CVN limit based on the current code provisions in North America (ANSI/AISC 360-10, 2010, AWS D1.1, 2010, CAN/CSA-W59, 2013, CAN/CSA-S16-14, 2014) for specimens parallel to the rolling direction is 68% and for specimens perpendicular to the rolling direction is 10%.

4.4.2 Incorporation of epistemic uncertainties in the fragility curves

The fragility curves presented in Section 4.1 only account for the specimen-to-specimen variability; it is possible to subsequently incorporate the effect of epistemic uncertainty into these developed fragility curves. One source of epistemic uncertainty arises from the finite sample of specimens included per group. Another source is the material variability; such that material properties are not the same for all the plates that were obtained from the same mill, in addition to the fact that the plates and wide flange sections, along with the corresponding CVN specimens, were from different mills. Another source of epistemic uncertainty is the difficulty to fully control the temperature conditions during each CVN test. In order to include the effect of these uncertainties on the CVN results, a 5% and 95% confidence interval was considered. The values of the shifted mean and standard deviations for the lognormally distributed data discussed earlier were estimated based on equations 4.1 and 4.2, respectively (Crow et al., 1960, Montgomery and Runger, 2014):

$$Shifted\ Means = \left(\overline{CVN} - \frac{\overline{\Delta}_{CVN}}{2} \right).\exp\left(\pm\ t_{\alpha/2}.\frac{\sigma_{CVN}}{\sqrt{n}} \right) \tag{4.1}$$

$$Shifted\ standard\ deviations = \left(\frac{(n-1).\sigma_{CVN}^2}{X_{\alpha/2,n-1}^2} \right)^{1/2} \quad and \quad \left(\frac{(n-1).\sigma_{CVN}^2}{X_{1-\alpha/2,n-1}^2} \right)^{1/2} \tag{4.2}$$

Where, $\overline{CVN}$ is the mean of the CVN subset under consideration, $\overline{\Delta}_{CVN}$ is the mean of the increment between the CVN values, σ_{CVN} is the standard deviation of the lognormal distribution, n is the number of specimens, $t_{\alpha/2}$ is the value of the student-*t*-distribution such that the probability of occurrence is $\alpha/2$ at number of specimens *n*; $X_{\alpha/2,n-1}^2$ is the value of the Chi-Squared-distribution such that the probability of occurrence is $\alpha/2$ at $n-1$ degrees of freedom; $X_{1-\alpha/2,n-1}^2$ is the value of the Chi-Squared-distribution such that the probability is $1-\alpha/2$ at $n-1$ degrees of freedom and α is the required confidence interval. Figure 4.1 shows an example of the shifted fragility boundaries for ASTM A572 Gr. 50 steel (Figures 4.1a and 4.1b) and ASTM A913 Gr. 65 steel (Figures 4.1c and 4.1d) with a 5% and 95% confidence interval. In the case of ASTM A913 steel for example, from Figure 4.1d the probablility of exceedance is 10% for an AISC [3] specified CVN value of 54 Joules, whereas if the epistemic uncertainty were accounted for the probability of exceedance would be in the range from 0 to 70%. This range indicates the sensitivity of CVN test data to testing conditions and that the probability of exceeding a specified CVN value may be better or worse as illustrated by the shifted distributions. Similar findings hold true for the rest of the subsets discussed in Section 4.3. Tables 4.1 and 4.2 show the corresponding shifted means ($\mu_{5\%}$ and $\mu_{95\%}$) and logarithmic standard deviations ($\beta_{5\%}$ and $\beta_{95\%}$) to compute the shifted boundaries for each group. Given the statistical distribution of each CVN subset the corresponding fracture toughness distribution can be developed. Subsequently, based on linear fracture mechanics one can compute the stress intensity factors for different crack sizes and at different tensile stress levels; thus the crack initiation fragility curves can be developed as discussed in Section 4.5.

4.5 Computation of Probability of Crack Initiation

A probabilistic approach to assess cracks and discontinuities based on the material fracture toughness uncertainty requires the development of crack initiation fragility curves. These curves are used to compute the probability of the material fracture toughness being less than the stress intensity factor of a crack, for a given crack size and a stress level. The same curves form the basis to establish expressions that may be used to compute the probability of crack initiation under a specified stress level and crack size (i.e., stress intensity factor). The first step for developing the crack initiation fragility curves is estimating the fracture toughness distribution for each subset from the obtained lognormal distributions for all the CVN subsets summarized in Tables 4.1 and 4.2. Knowing that the CVN test is essentially an impact test, the computed output from the CVN test corresponds to the dynamic fracture toughness (Barsom and Rolfe, 1987). For lower shelf temperatures, the static fracture toughness is of the same value but at a lower temperature such that the temperature shift is computed from Equation 4.3 (Barsom and Rolfe, 1987):

$$\begin{aligned} T_s &= 102 - 0.12 f_y, && for\ 250MPa < f_y \leq 965MPa \\ T_s &= 0, && for\ f_y > 965MPa \end{aligned} \tag{4.3}$$

Where T_s is the temperature shift (˚C) and f_y is the yield stress of the material in MPa. For upper shelf temperatures there is no temperature shift required to transfer from the dynamic to the static fracture toughness (Barsom and Rolfe, 1987); due to the increase in the material ductility at these temperatures. The fracture toughness is given by the following empirical equations,

$$K_{Id} = \sqrt{0.64 \times CVN \times E}\ , \qquad \textit{For lower shelf temperatures} \qquad (4.4)$$

$$\left(\frac{K_{Ic}}{f_y}\right)^2 = 0.646\left(\frac{CVN}{f_y} - 0.0098\right), \qquad \textit{For upper shelf temperatures} \qquad (4.5)$$

Where K_{Id} is the dynamic fracture toughness (KPa.√m), K_{Ic} is the static fracture toughness (MPa.√m), CVN is the absorbed energy measured from Charpy-V-Notch tests (Joules) and E is the modulus of elasticity of the steel material (KPa).

The statistical distribution of the static fracture toughness at 0 and 21°C was interpolated based on the ASTM A572 Gr. 50 steel subsets for the tests conducted at McGill University (Nikolaidou et al., 2013, Ibrahim et al., 2015). The values of the static fracture toughness at -60 and 60°C are at the start and end of the transition zone, respectively. According to the results of the tests conducted by Ibrahim et al. (2015) (Chapter 3 Table 3.2) it can be assumed that the relation between the static fracture toughness and the temperature is linear in the range from -60 and 60°C; therefore, the relationship between the fracture toughness and the probability of reaching or exceeding a given fracture toughness at any temperature between -60 and 60ºC can be linearly interpolated between the lognormal distributions at -60 and 60°C. From the developed lognormal distributions, the effect of the material type, plate thickness, temperature, and grain direction on the fracture toughness is considered. Moreover, for the estimation of the stress intensity factor, the fracture mode is considered to be "Mode I" (Zehnder, 2012). The stress intensity factor depends on the crack type and is computed according to the applied tensile stress (*σ)* and the crack size (*a)*. Five crack types are considered in this study: 1) through thickness crack in a finite plate; 2) through thickness crack in an infinite plate; 3) edge crack in a finite plate; 4) edge crack in an infinite plate; and 5) embedded circular crack. Figure 4.2 shows an illustration of these cracks, their shape and location on a steel plate. The stress intensity factor for each crack type can be calculated, in the same order for each crack type, according to Murakami and Tada et al. (Murakami, 1987, Tada et al., 2000) from the Equations 4.6 to 4.10:

$$K = \sigma\sqrt{\pi a}.\sqrt{\sec\left(\frac{\pi a}{2b}\right)},$$ *Through thickness crack in a finite plate* (4.6)

$$K = \sigma\sqrt{\pi a}\ ,$$ *Through thickness crack in an infinite plate* (4.7)

$$K = 1.12\sigma\sqrt{\pi a}.f\left(\frac{a}{b}\right),$$ *Edge crack in a finite plate* (4.8)

$$K = 1.12\sigma\sqrt{\pi a}\ ,$$ *Edge crack in an infinite plate* (4.9)

$$K = 1.13\sigma\sqrt{a}\ ,$$ *Embedded circular crack* (4.10)

in which, σ is the applied stress level for fracture modes I, II and III (MPa); a is equal to the crack length for edge cracks, half of the crack length for through thickness cracks and the radius of the embedded circle for an embedded circular crack (mm); b is half of the thickness of the finite plate in the direction of the crack (mm); and $f(a/b)$ is a factor depending on the relation between a and b. The stress intensity factor is calculated at different tensile stress levels and crack lengths for each crack type based on Equations 4.6 to 4.10. The probability of having a material fracture toughness less than or equal to the stress intensity factor of a crack, for a given crack size and a tensile stress level (crack initiation fragility curves) can be calculated from the statistical distribution of the fracture toughness.

Based on the developed crack initiation fragility curves of the subsets discussed in Section 4.3, mathematical expressions were developed based on logistic regression [11] to calculate the probability of crack initiation for each subset. These expressions give the relation between the probability of crack initiation through a material, at a given temperature, plate thickness and position, and the stress intensity factor of a given crack size and a tensile stress level. The logistic regression was conducted in MATLAB R2012b (Mathworks, 2012) in order to calculate the constants of Equation 4.11:

$$P(K_I < K \mid K = K_i) = \frac{e^{B_0 + B_1 K_i}}{1 + e^{B_0 + B_1 K_i}} \tag{4.11}$$

in which, K is the calculated stress intensity factor given the crack size and the applied stress level, K_I is the fracture toughness of the material and B_0 and B_1 are constants. Tables 4.4 – 4.6 summarize the values of B_0 and B_1 for each subset, and list the deviance and maximum residual for all the subsets. From Table 4.6, for the subset of ASTM A913 Gr. 65 steel, the deviance ranges from 0.14 at 69°C in the direction parallel to rolling to 8.21 at 0˚C in the perpendicular direction. As the deviance alone is not representative of the goodness-of-fit, the maximum residual for each set was also considered. The maximum residual ranges from 2.1% for the interpolated subset of ASTM A572 Gr. 50 steel at 21˚C to 9% for the subset of ASTM A572 Gr. 50 steel at -18˚C for thickness group (40-65mm). Figure 4.3 shows a comparison between the crack initiation fragility curves and Equation 4.11. According to Tables 4.4 – 4.6 the average deviances are 1.98, 1.14, 2.54 and 3.37, respectively, and the average maximum residuals are 0.05, 0.04, 0.06 and 0.07, respectively for all four material datasets.

Subsequently, the impact of the crack type, material type, the plate temperature, grain direction (a function of the rolling direction) and the plate thickness on the probability of crack initiation was evaluated through surface probability plots; in which the crack size and the applied stress level are on the horizontal axes and the probability of crack initiation on the vertical axis (Figure 4.3). The reason for using surface plots is to include the applied stress level in the graph and to examine its influence on the probability of a crack with a given size to initiate, as this parameter is also ignored by current specifications (ANSI/AISC 360-10, 2010, AWS D1.1, 2010, CAN/CSA-W59, 2013, CAN/CSA-S16-14, 2014). The stress intensity factor for the cracks in a finite plate depends on the ratio between the crack length and the material thickness *a/b* as shown in Equations 4.6 and 4.8; therefore, for each subset two surface plots were developed as an upper and lower bound of the probability of crack initiation. As an example, for the thickness group (20-40mm) *a/b* for the lower and upper bounds surface plots is *a/20* and *a/40* respectively. Figure 4.4 shows the upper and lower bounds of the probability of initiation of cracks in a finite plate for ASTM A572 Gr. 50 steel for thickness group (65-100mm). Sections 5.1 to 5.4 contain a discussion of the impact of each parameter on the probability of crack initiation of a crack type.

4.5.1 Impact of crack type

The probability of crack initiation is sensitive to the crack type (Figure 4.2). Figure 4.4 shows the difference in the probability of crack initiation between an edge crack (Figure 4.2b crack type 3) and a through thickness crack (Figure 4.2b crack type 1) for ASTM A572 Gr. 50 steel plates. An edge crack is more likely to initiate than a through thickness crack for the same stress level because a through thickness crack is confined by the steel material from both sides, while for an edge crack this is not the case. That is, an edge crack requires less energy to break the material bonds than that needed in a through thickness crack. After evaluating the other types of cracks in the same manner, the embedded circular crack type is the least sensitive to initiate under the same conditions compared to edge and through thickness cracks. It is implied that assessing a crack based on its size alone is not sufficient. This has direct implications into the current code provisions (ANSI/AISC 360-10, 2010, AWS D1.1, 2010, CAN/CSA-W59, 2013, CAN/CSA-S16-14, 2014) that specify the allowable crack size in welds without considering the crack type.

4.5.2 Impact of material type

The influence of the material type on the probability of crack initiation is described herein. Figure 4.5 shows surface probability plots for ASTM A572 Gr. 50 and ASTM A913 Gr. 65 steels for the same plate thickness, crack type and similar temperature. The probability of crack type 4 initiation for the A913 Gr. 65 material was higher than that of the A572 Gr. 50 material. This was attributed to the higher nominal yield stress of the A913 Gr. 65 steel. The current code provisions (ANSI/AISC 360-10, 2010, AWS D1.1, 2010, CAN/CSA-W59, 2013, CAN/CSA-S16-14, 2014) consider the material impact on the probability of crack initiation by specifying a higher CVN minimum requirement for ASTM A913 steel (Section 1). Furthermore, by converting the acceptance limits to the proposed probabilistic approach the maximum acceptable stress intensity factors calculated from the CVN minimum requirements would be 85 and 60 MPa.√m for ASTM A913 and A572 steels, respectively. By substituting these values in Equation 4.11, the probability of crack initiation is 29% and 0.7% for ASTM A913 and A572 steels, respectively. This means that current specification limits for ASTM A572 grade 50 steel (27J) correspond to a high probability of crack initiation according to the statistical distribution of the CVN values of this steel grade. While specification limits for ASTM A913 Gr. 65 steel (54J) correspond to a low probability of crack initiation according to the statistical distribution of the CVN values of this steel grade. Accordingly, there is no consistency between the CVN value acceptance limits for different steel grades in current specifications (ANSI/AISC 360-10, 2010, AWS D1.1, 2010, CAN/CSA-W59, 2013, CAN/CSA-S16-14, 2014). Figure 4.5 shows a comparison between the probabilities of crack initiation surface plots for both steel grades for an edge horizontal crack at 0°C. This illustrates that under the same conditions A913 grade 65 quenched steel has higher probability of crack initiation than A572 grade 50 steel.

4.5.3 Impact of temperature and grain direction

The effect of temperature and grain direction on the probability of crack initiation is presented given a stress level. Typically, with the decrease in temperature, the material becomes more brittle and the fracture toughness decreases (Zehnder, 2012). This decrease in the fracture toughness leads to an increase in the probability of crack initiation. Figure 4.6 shows the increase in the probability of the crack initiation with the decrease in temperature for ASTM A572 Gr. 50 steel. The CVN specimens for the ASTM A913 Gr. 65 material were milled from both the direction parallel and perpendicular to the rolling direction. It is assumed that the grain structure in the rolling direction is elongated, while in the perpendicular to rolling direction the grain structure is shortened. Figure 4.7 shows the probability of crack initiation at upper and lower shelf temperatures for ASTM A913 Gr. 65 steel in the directions parallel and perpendicular to the rolling direction (long and short grains directions respectively). The difference between the probability of crack initiation in the lower and upper shelf temperatures in the long grain direction is always higher than that in the short grain direction. This is attributed to the fact that the inter-grain connections in the long direction are stronger than those in the short direction (Jefferson and Woods, 1962). It is worth mentioning that current code provisions (ANSI/AISC 360-10, 2010, AWS D1.1, 2010, CAN/CSA-W59, 2013, CAN/CSA-S16-14, 2014) have no distinction for crack limitations in different directions; however, AWS D1.1 (2010) acknowledges that the rolling process causes the base metal to have different mechanical properties in the orthogonal directions. It is not clear if the provisions of the current specifications (ANSI/AISC 360-10, 2010, AWS D1.1, 2010, CAN/CSA-W59, 2013, CAN/CSA-S16-14, 2014) were established considering a lower bound or an upper bound of the CVN values; hence, the code provisions (ANSI/AISC 360-10, 2010, AWS D1.1, 2010, CAN/CSA-W59, 2013, CAN/CSA-S16-14, 2014) should include a distinction between the crack limitations in the long and short grain directions to avoid over or under estimating the CVN acceptance limits. One way to include these parameters in the assessment of discontinuities is through the approach proposed herein.

4.5.4 Impact of plate thickness

According to current North American steel and welding code provisions (ANSI/AISC 360-10, 2010, AWS D1.1, 2010, CAN/CSA-W59, 2013, CAN/CSA-S16-14, 2014) a material discontinuity is evaluated in the same way regardless of the steel plate thickness. However, it is generally known that when the steel plate thickness increases, the grain structure present through the steel plate thickness is not as effectively rolled as are the grains on the outer surface of the material (Jefferson and Woods, 1962). This can lead to an increase in the probability of crack initiation (Murakami, 1987, Tada et al., 2000). The proposed methodology for the evaluation of crack initiation given the stress level is able to consider this material variation; an important issue given the increasing use of thick steel plates in construction. Figure 4.8 shows the probability of crack initiation for the four different thickness groups that are summarized in **Error! Not a valid bookmark self-reference.** for ASTM A588 Gr. B steel. While the steel plate thickness increases, the probability of crack type 4 initiation increases. This indicates that the current provisions for acceptance criteria of discontinuities should be re-evaluated and a distinction based on steel plate thickness should be incorporated.

The proposed methodology for evaluating the likelihood of crack initiation includes consideration of the effect of the material type, the plate temperature, the grain direction and the plate thickness. In particular, Equation 4.11 and Tables 4.4 – 4.6 reflect these effects. Code provisions or a designer can define a probability limit in order to determine whether to accept a particular steel component given the size of its discontinuities. In the definition of this limit it is necessary to consider the importance of the structure or the steel assembly to be welded, as well as the stress level to which it will be subjected. As an example, the recommended probability of crack initiation limit should not be more than 5% based on the probability of exceeding the prescribed CVN limit (ANSI/AISC 360-10, 2010, AWS D1.1, 2010, CAN/CSA-W59, 2013, CAN/CSA-S16-14, 2014) for ASTM A572 Gr. 50 steel.

4.6 Summary and Conclusions

A new methodology is proposed to calculate the probability of a crack to initiate through a steel component accounting for the uncertainty in its fracture toughness. The development of this approach is based on a database of CVN values from steel plates and wide-flange sections of different thickness and grade, with specimens obtained from different locations with various grain directions and tested over a range of temperatures. The datasets have undergone rigorous statistical framework comprising the goodness-of-fit of the describing statistical distribution and the epistemic uncertainty from the testing procedure. Through logistic regression, expressions were developed to calculate the probability of a crack to initiate through a steel component. Consequently, the impact of the different parameters was investigated. From this assessment, the following conclusions hold true:

- An edge crack is more prone to initiate under a specified stress level than a through thickness crack, which in turn has a higher probability of initiation compared with an embedded circular crack. Therefore, present code provisions (ANSI/AISC 360-10, 2010, AWS D1.1, 2010, CAN/CSA-W59, 2013, CAN/CSA-S16-14, 2014) should assess a crack based on its type as well as its size.
- A high strength steel material has a higher probability of crack initiation than a low strength steel material. Present code provisions (ANSI/AISC 360-10, 2010, AWS D1.1, 2010, CAN/CSA-W59, 2013, CAN/CSA-S16-14, 2014) consider this issue. However, the uncertainty associated with the fracture toughness value, which increases with the respective steel strength, is currently neglected. This could lead to the acceptance of a material CVN value based on a test result, which may not be valid for specimens from a different location in the same material. Hence, this can be avoided by including the uncertainty of the CVN value of a material in the acceptance criteria.
- With an increase in temperature the probability of crack initiation decreases until the maximum fracture toughness of the steel material is reached. The difference between the probability of crack initiation in the lower and upper shelf temperatures in the direction parallel to rolling is always higher than that in the perpendicular direction.
- The greater the steel plate thickness the larger the scatter in the fracture toughness values of a steel component. This is attributed to the effectiveness of the rolling procedure from the plate surface to the centerline of its thickness.

The proposed approach can be employed to assess discontinuities and cracks in a steel component, which are often the result of welding and/or the fabrication process. The approach can be also used to assess the integrity of existing components that have developed cracks by computing the likelihood of crack initiation. The proposed approach can be expanded to other steel grades that are typically used in steel construction. Moreover, in line with Performance-Based Design, the code provisions should incorporate acceptable probabilities of crack initiation to evaluate discontinuities, which are established according to the objective of the building performance instead of a prescriptive fracture toughness value.

Table 4.1: Summary of the results of the lognormal distribution of energy for ASTM A572 Gr. 50 steel and ASTM A588 Gr. B steel for CVN tests conducted by Suwan (2002)

	Mean ($\mu_{5\%} - \mu - \mu_{95\%}$)	St. Dev. ($\beta_{5\%} - \beta - \beta_{95\%}$)	No. Specimens
	A572 Gr. 50 (f_y=345 MPa) Thickness Group: < 20mm		
-18˚C	138 – 67 – 35 J	0.83 – 0.94 – 1.07	91
4˚C	174 – 99 – 59 J	0.60 – 0.68 – 0.78	91
21˚C	199 – 130 – 86 J	0.44 – 0.49 – 0.56	91
	A572 Gr. 50 (f_y=345 MPa) Thickness Group: 20-40mm		
-18˚C	126 – 71 – 41 J	0.58 – 0.66 – 0.77	70
4˚C	172 – 119 – 83 J	0.34 – 0.39 – 0.45	70
21˚C	204 – 149 – 108 J	0.28 – 0.32 – 0.37	70
	A572 Gr. 50 (f_y=345 MPa) Thickness Group: 40-65mm		
-18˚C	109 – 3.81 – 21 J	0.90 – 1.03 – 1.21	63
4˚C	196 – 66 – 26 J	0.85 – 1.00 – 1.20	49
21˚C	383 – 126 – 48 J	0.63 – 0.75 – 0.94	35
	A572 Gr. 50 (f_y=345 MPa) Thickness Group: 65-100mm		
-18˚C	29 – 17 – 10 J	0.30 – 0.40 – 0.59	14
4˚C	63 – 29 – 14 J	0.37 – 0.48 – 0.71	14
21˚C	111 – 39 – 16 J	0.44 – 0.57 – 0.85	14
	A588 Gr. B (f_y=345 MPa) Thickness Group: < 20mm		
-18˚C	148 – 86 – 52 J	0.65 – 0.72 – 0.82	105
4˚C	193 – 127 – 85 J	0.47 – 0.52 – 0.59	105
21˚C	209 – 153 – 113 J	0.34 – 0.38 – 0.43	105
	A588 Gr. B (f_y=345 MPa) Thickness Group: 20-40mm		
-18˚C	217 – 125 – 74 J	0.58 – 0.65 – 0.74	91
4˚C	256 – 179 – 126 J	0.35 – 0.39 – 0.45	91
21˚C	254 – 197 – 152 J	0.25 – 0.28 – 0.32	91
	A588Gr. B (f_y=345 MPa) Thickness Group: 40-65mm		
-18˚C	98 – 41 – 19 J	0.80 – 0.93 – 1.12	49
4˚C	135 – 58 – 28 J	0.69 – 0.81 – 0.97	49
21˚C	169 – 79 – 40 J	0.59 – 0.69 – 0.83	49
	A588 Gr. B (f_y=345 MPa) Thickness Group: 65-100mm		
-18˚C	100 – 37 – 15 J	0.42 – 0.55 – 0.82	14
4˚C	151 – 65 – 29 J	0.32 – 0.42 – 0.62	14
21˚C	181 – 108 – 65 J	0.18 – 0.23 – 0.35	14

Table 4.2: Summary of the results of the lognormal distribution of energy for ASTM A572 steel Gr. 50 and ASTM A913 Gr. 65 steel for CVN tests conducted at McGill University (Nikolaidou et al., 2013, Ibrahim et al., 2015)

	Mean ($\mu_{5\%} - \mu - \mu_{95\%}$)	**St. Dev. ($\beta_{5\%} - \beta - \beta_{95\%}$)**	**No. Specimens**
		A572 Gr. 50 (f_y=345 MPa)	
-60˚C	28 – 11 – 5 J	0.43 – 0.60 – 1.02	9
-40˚C	90 – 37 – 17 J	0.32 – 0.43 – 0.69	11
0˚C	191 – 85 – 39 J	0.25 – 0.33 – 0.53	11
60˚C	208 – 164 – 128 J	0.12 – 0.15 – 0.19	28
81˚C	191 – 156 – 126 J	0.11 – 0.13 – 0.17	29
		A913 Gr. 65 (f_y=450 MPa) Long direction	
0˚C	914 – 84 – 15 J	0.81 – 1.05 – 1.50	16
21˚C	399 – 121 – 42 J	0.43 – 0.56 – 0.79	17
48˚C	420 – 150 – 58 J	0.31 – 0.40 – 0.61	13
69˚C	479 – 162 – 60 J	0.26 – 0.36 – 0.59	10
		A913 Gr. 65 (f_y=450 MPa) Short direction	
0˚C	64 – 33 – 17 J	0.31 – 0.40 – 0.60	14
21˚C	83 – 43 – 22 J	0.30 – 0.39 – 0.57	15
48˚C	52 – 40 – 31 J	0.11 – 0.15 – 0.22	14
69˚C	48 – 39 – 31 J	0.10 – 0.13 – 0.19	15

Table 4.3: Maximum difference in probability between empirical results and the distribution compared to the KS-test limit with 5% significance for ASTM A572 Gr. 50 steel tests by Suwan (2002)

Thickness Group: < 20mm				
Distribution	**Lognormal**	**Weibull**	**Exponential**	**Limit (5%)**
-18˚C	0.099	0.110	0.088	0.128
4˚C	0.132	0.099	0.209	0.128
21˚C	0.121	0.066	0.286	0.128
Thickness Group: 20-40mm				
Distribution	**Lognormal**	**Weibull**	**Exponential**	**Limit (5%)**
-18˚C	0.086	0.071	0.243	0.146
4˚C	0.114	0.071	0.343	0.146
21˚C	0.129	0.143	0.400	0.146

Table 4.4: Values of B_0 and B_1 and the deviance of the logistic regression for ASTM A572 Gr. 50 and ASTM A588 Gr. B steel according to tests conducted by Suwan (2002)

Thickness	Temperature	B_0	B_1	Deviance	Max. Residual
		A572 Gr. 50 (f_y=345 MPa)			
t<20mm	**-18°C (-79°C)***	-3.59	0.035	6.74	0.085
	4°C (-57°C)*	-5.16	0.043	3.92	0.070
	21°C (-40°C)*	-7.22	0.054	2.03	0.056
t=20-40mm	**-18°C (-79°C)***	-5.31	0.053	3.15	0.069
	4°C (-57°C)*	-9.29	0.074	1.07	0.047
	21°C (-40°C)*	-11.35	0.081	0.76	0.042
t=40-65mm	**-18°C (-79°C)***	-3.16	0.037	7.19	0.090
	4°C (-57°C)*	-3.35	0.033	7.47	0.088
	21°C (-40°C)*	-4.69	0.035	5.19	0.075
t=65-100mm	**-18°C (-79°C)***	-9.06	0.189	0.43	0.048
	4°C (-57°C)*	-7.42	0.119	0.89	0.055
	21°C (-40°C)*	-6.18	0.084	1.62	0.062
		A588 Gr. B (f_y=345 MPa)			
t<20mm	**-18°C (-79°C)***	-4.8	0.043	4.31	0.073
	4°C (-57°C)*	-6.79	0.051	2.32	0.058
	21°C (-40°C)*	-9.52	0.066	1.15	0.047
t=20-40mm	**-18°C (-79°C)***	-5.48	0.041	3.79	0.068
	4°C (-57°C)*	-9.14	0.059	1.36	0.048
	21°C (-40°C)*	-12.95	0.081	0.67	0.039
t=40-65mm	**-18°C (-79°C)***	-3.54	0.044	5.69	0.086
	4°C (-57°C)*	-4.21	0.045	4.77	0.079
	21°C (-40°C)*	-5.054	0.047	3.70	0.071
t=65-100mm	**-18°C (-79°C)***	-6.39	0.089	1.46	0.060
	4°C (-57°C)*	-8.57	0.092	0.95	0.050
	21°C (-40°C)*	-15.39	0.129	0.36	0.036

* The temperature between brackets is the shifted temperature for static loading

Table 4.5: Values of B_0 and B_1 and the deviance of the logistic regression for A572 Gr. 50 steel according to tests conducted at McGill University (Ibrahim et al., 2015)

Temperature	B0	B1	Deviance	Max. Residual
-60°C (-120°C)*	-5.90	0.148	0.98	0.051
-40°C (-100°C)*	-8.33	0.118	0.77	0.064
0°C (-60°C)*	-10.87	0.103	0.63	0.043
0°C (interpolated)	-15.84	0.108	2.75	0.023
21° C (interpolated)	-18.06	0.111	2.34	0.021
60°C	-24.14	0.127	0.27	0.030
81°C	-27.01	0.146	0.23	0.030

* The temperature between brackets is the shifted temperature for static loading

Table 4.6: Values of B_0 and B_1 and the deviance of the logistic regression for ASTM A913 Gr. 65 steel according to tests conducted at McGill University (Nikolaidou et al., 2013)

Position	Temperature	B0	B1	Deviance	Max. Residual
Parallel to rolling direction	0°C (-48°C)*	-3.26	0.028	8.21	0.089
	21°C (-27°C)*	-6.38	0.049	2.64	0.061
	48°C	-8.82	0.042	1.92	0.049
	69°C	-9.97	0.046	1.53	0.046
Perpendicular to rolling direction	0°C (-48°C)*	-8.96	0.134	0.61	0.049
	21°C (-27°C)*	-9.21	0.121	0.65	0.048
	48°C	-21.56	0.211	0.17	0.032
	69°C	-25.32	0.251	0.14	0.030

* The temperature between brackets is the shifted temperature for static loading

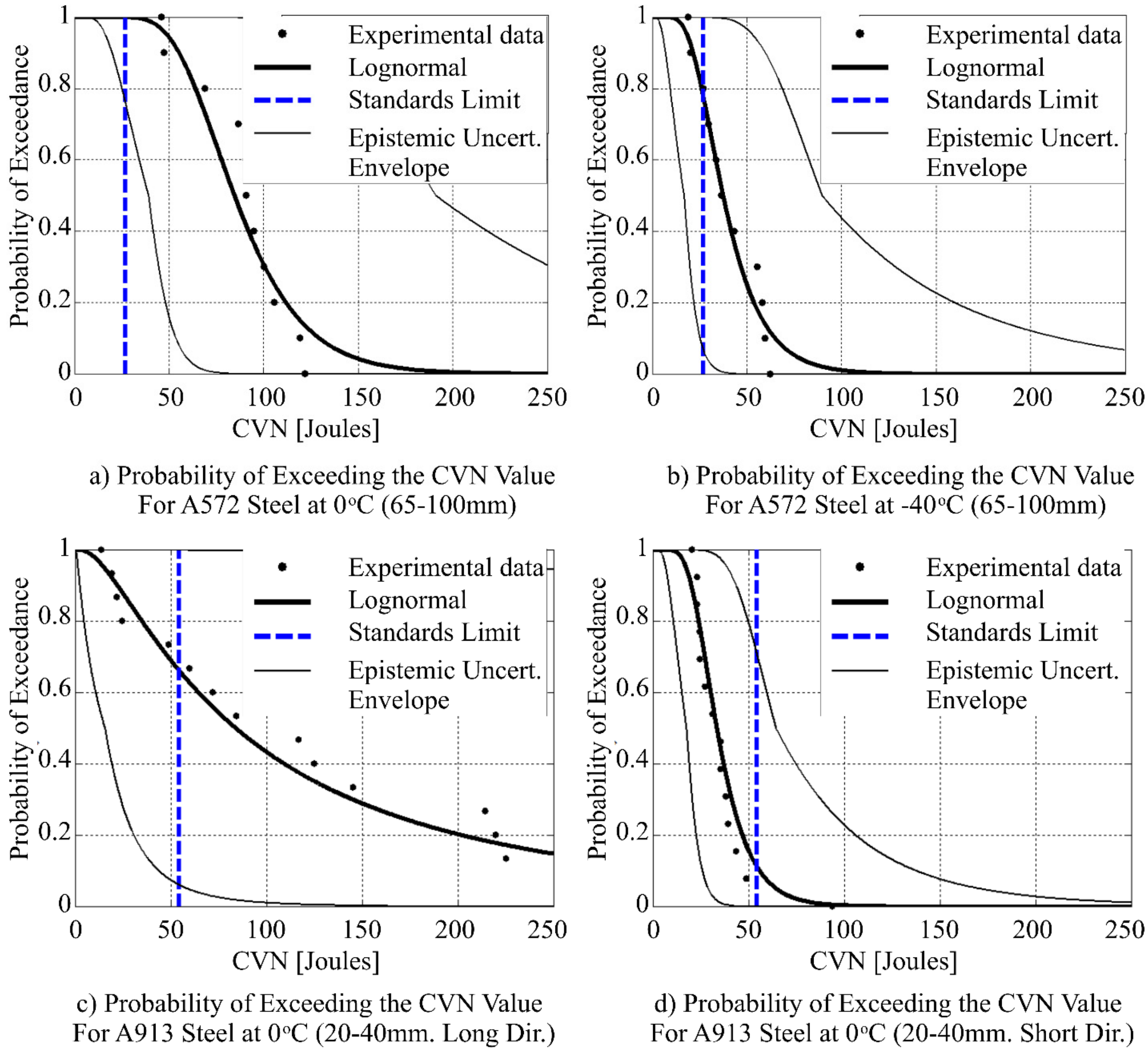

Figure 4.1: Epistemic uncertainty of CVN Data with 5% and 95% confidence interval (data from (Suwan, 2002, Nikolaidou et al., 2013, Ibrahim et al., 2015))

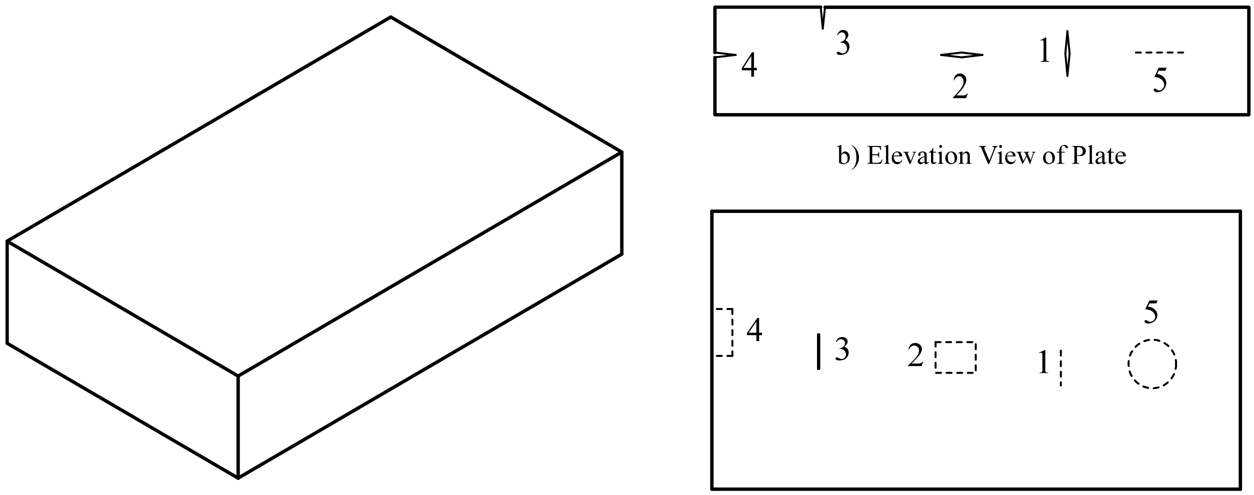

b) Elevation View of Plate

a) 3D View of Plate

c) Plan View of Plate

Figure 4.2: Illustration of considered crack types

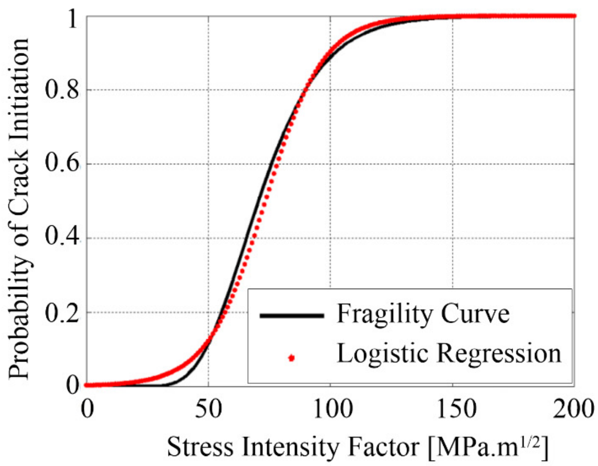

a) Comparison Between the Logistic Reg. Formula and the Crack Fragility Curve For A572 Steel at 21/-40°C (65-100mm)

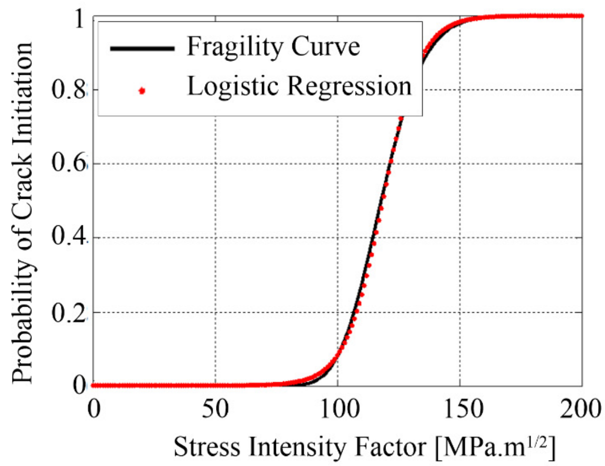

b) Comparison Between the Logistic Reg. Formula and the Crack Fragility Curve For A588 Steel at 21/-40°C (65-100mm)

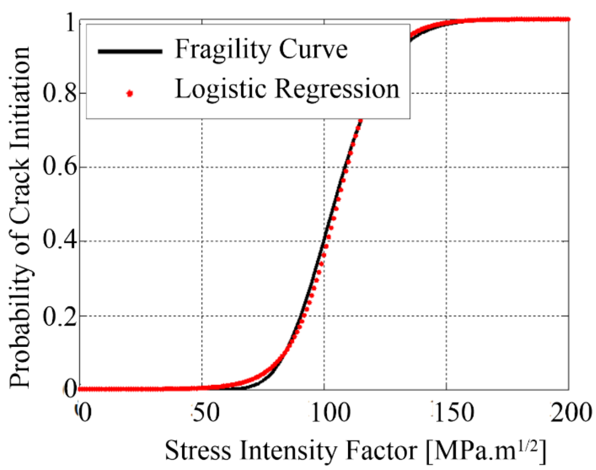

c) Comparison Between the Logistic Reg. Formula and the Crack Fragility Curve For A572 Steel at 0/-60°C (2013)

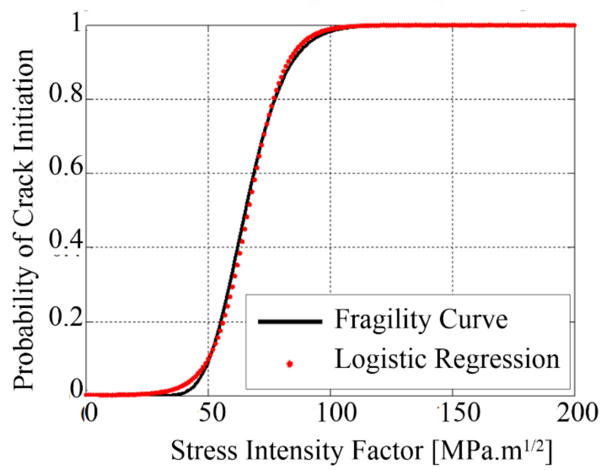

d) Comparison Between the Logistic Reg. Formula and the Crack Fragility Curve For A913 Steel at 0/-48°C (2013)

Figure 4.3: A comparison between the crack initiation fragility curves and the logistic regression formula

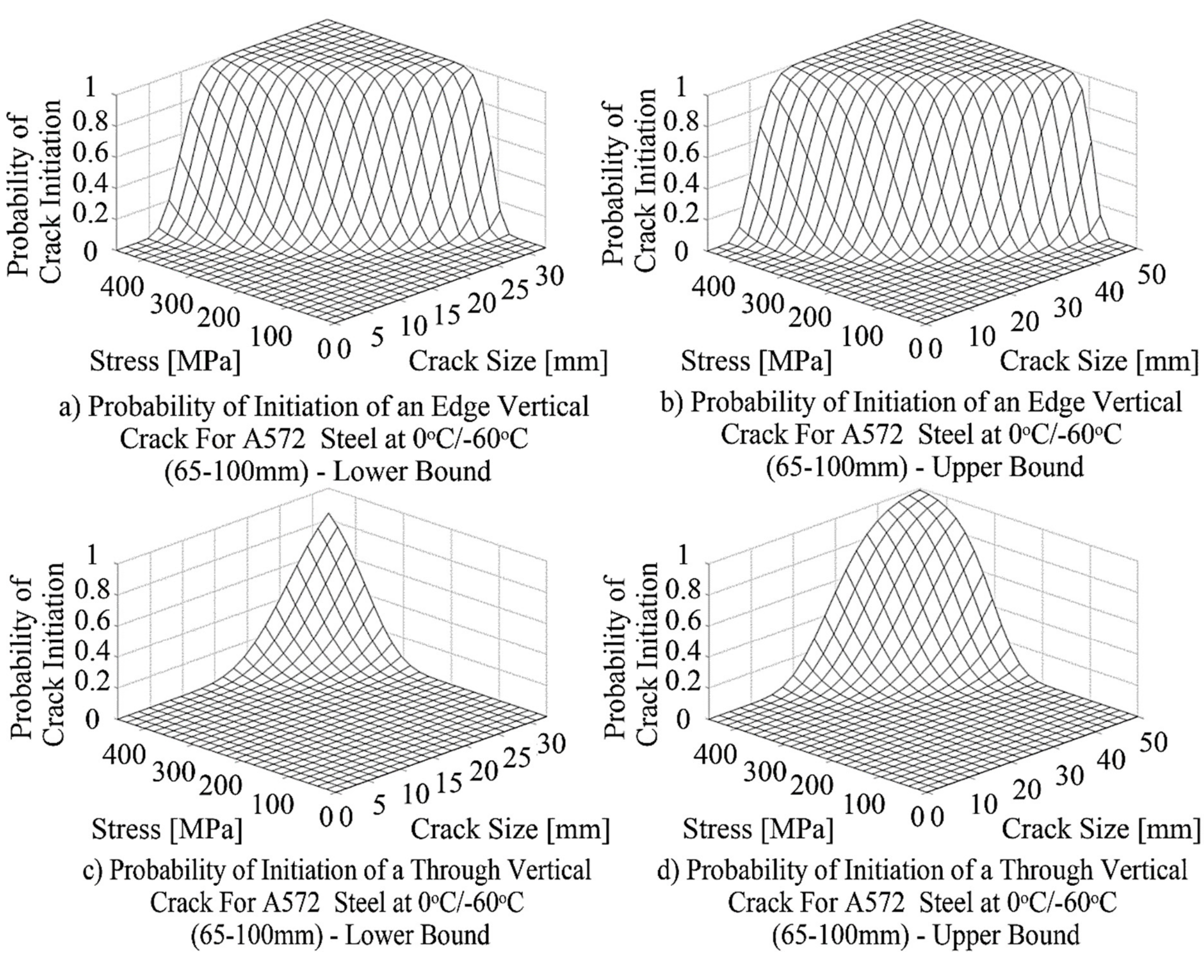

Figure 4.4: Impact of the crack type on the probability of crack initiation showing the upper and lower bound probabilities of crack types 1 and 3 for the ASTM A572 Gr. 50 steel (f_y=345 MPa) (dynamic/static temperatures) based on tests conducted at McGill University (Nikolaidou et al., 2013, Ibrahim et al., 2015)

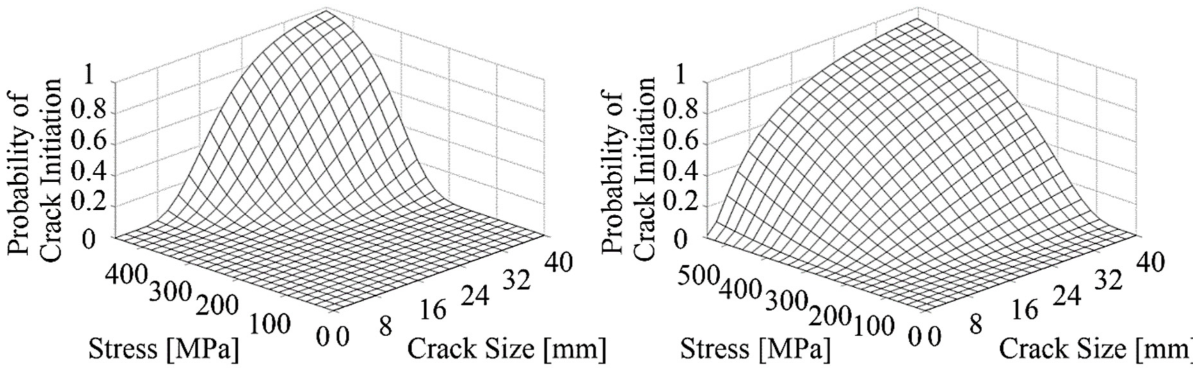

a) Probability of Initiation of an Edge Horizontal Crack For A572 Steel at 4°C/-57°C (20-40mm)

b) Probability of Initiation of an Edge Horizontal Crack For A913 Steel at 0°C/-48°C (20-40mm)

Figure 4.5: Impact of material type on the probability of crack type 4 initiation for the ASTM A572 Gr. 50 steel (f_y= 345 MPa) and ASTM A913 Gr. 65 steel (f_y= 450 MPa) (dynamic/static temperatures)

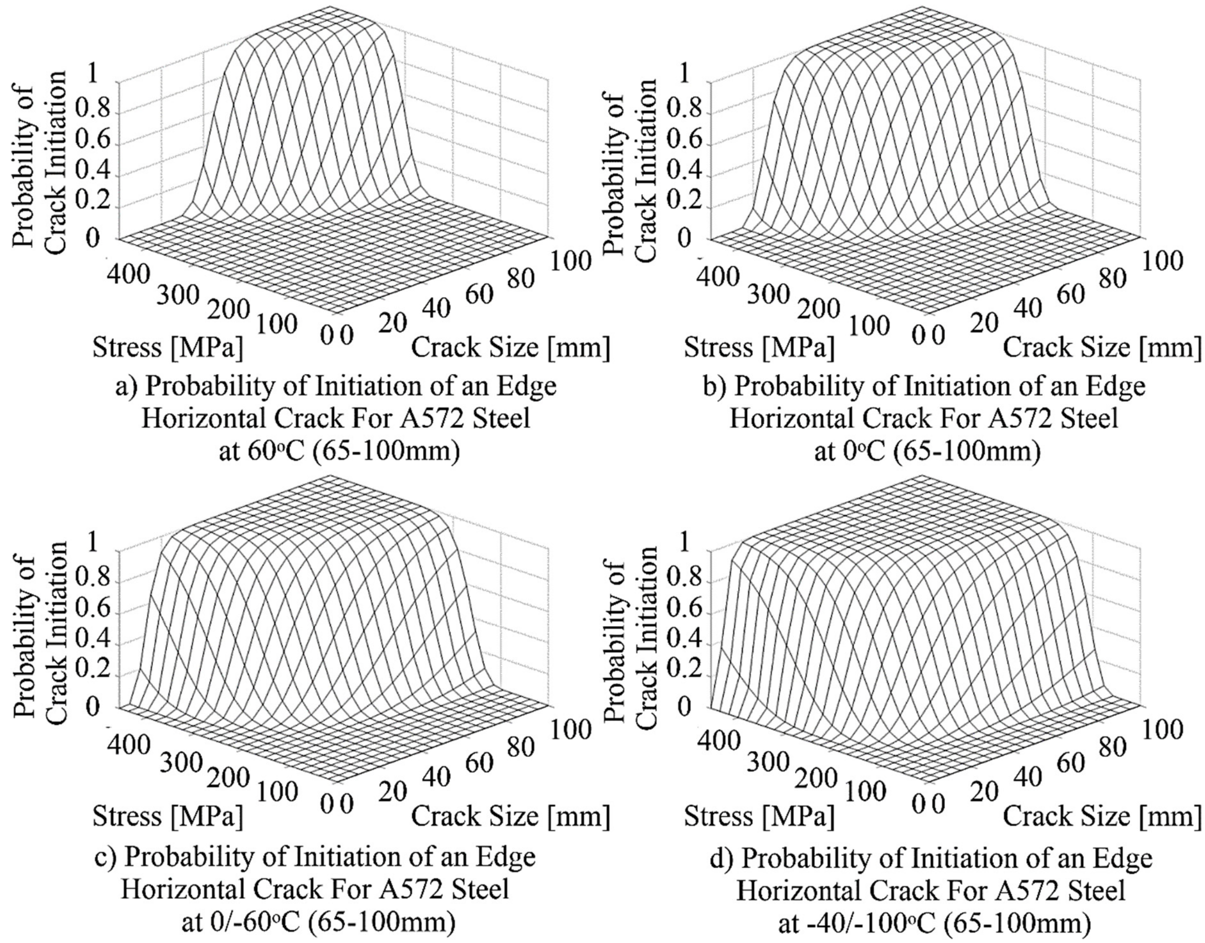

Figure 4.6: Impact of temperature on the probability of crack type 4 initiation for the ASTM A572 Gr. 50 steel (f_y= 345 MPa) (dynamic/static temperatures) based on tests conducted at McGill University (Nikolaidou et al., 2013, Ibrahim et al., 2015)

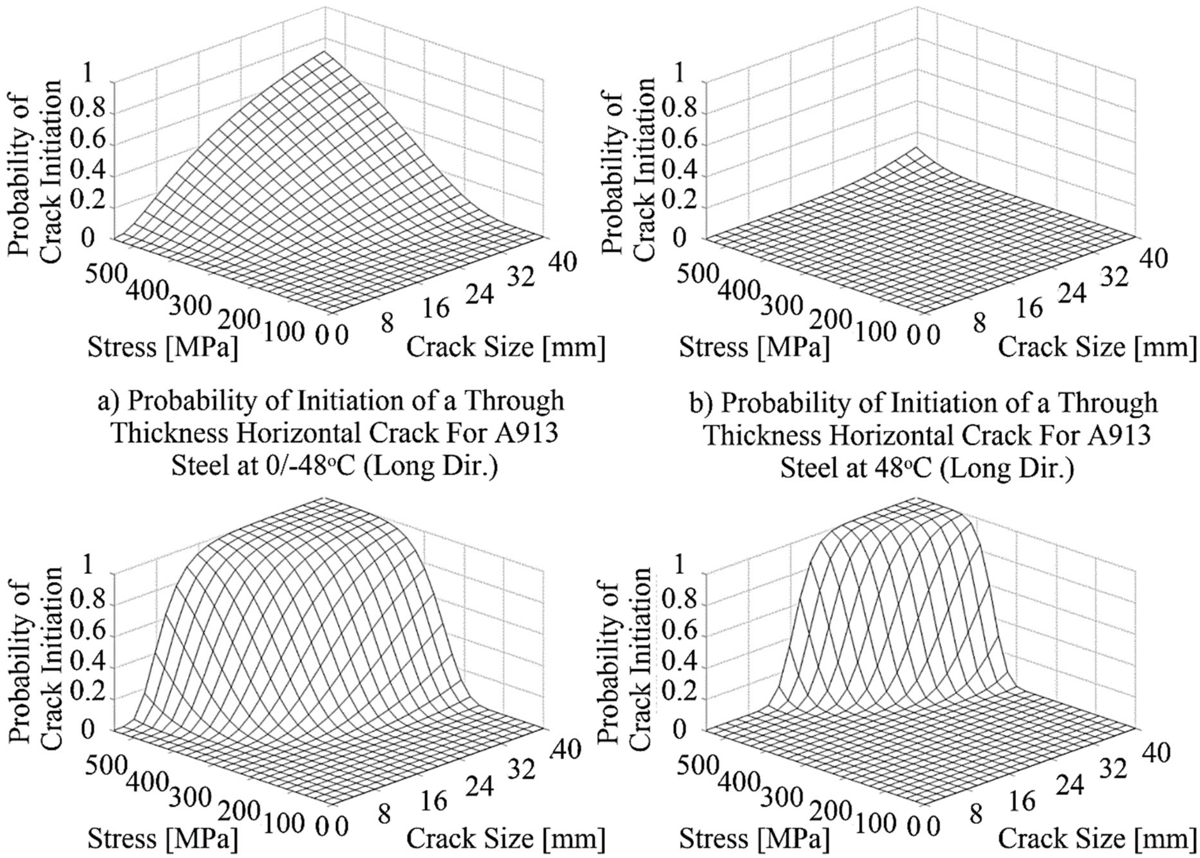

a) Probability of Initiation of a Through Thickness Horizontal Crack For A913 Steel at 0/-48°C (Long Dir.)

b) Probability of Initiation of a Through Thickness Horizontal Crack For A913 Steel at 48°C (Long Dir.)

c) Probability of Initiation of a Through Thickness Horizontal Crack For A913 Steel at 0/-48°C (Short Dir.)

d) Probability of Initiation of a Through Thickness Horizontal Crack For A913 Steel at 48°C (Short Dir.)

Figure 4.7: Impact of grain direction on the upper and lower shelf probabilities of initiation of crack type 2 for the ASTM A913 Gr. 65 steel (f_y= 450 MPa) in long and short grain directions (dynamic/static temperatures) according to tests conducted at McGill University (Nikolaidou et al., 2013, Ibrahim et al., 2015)

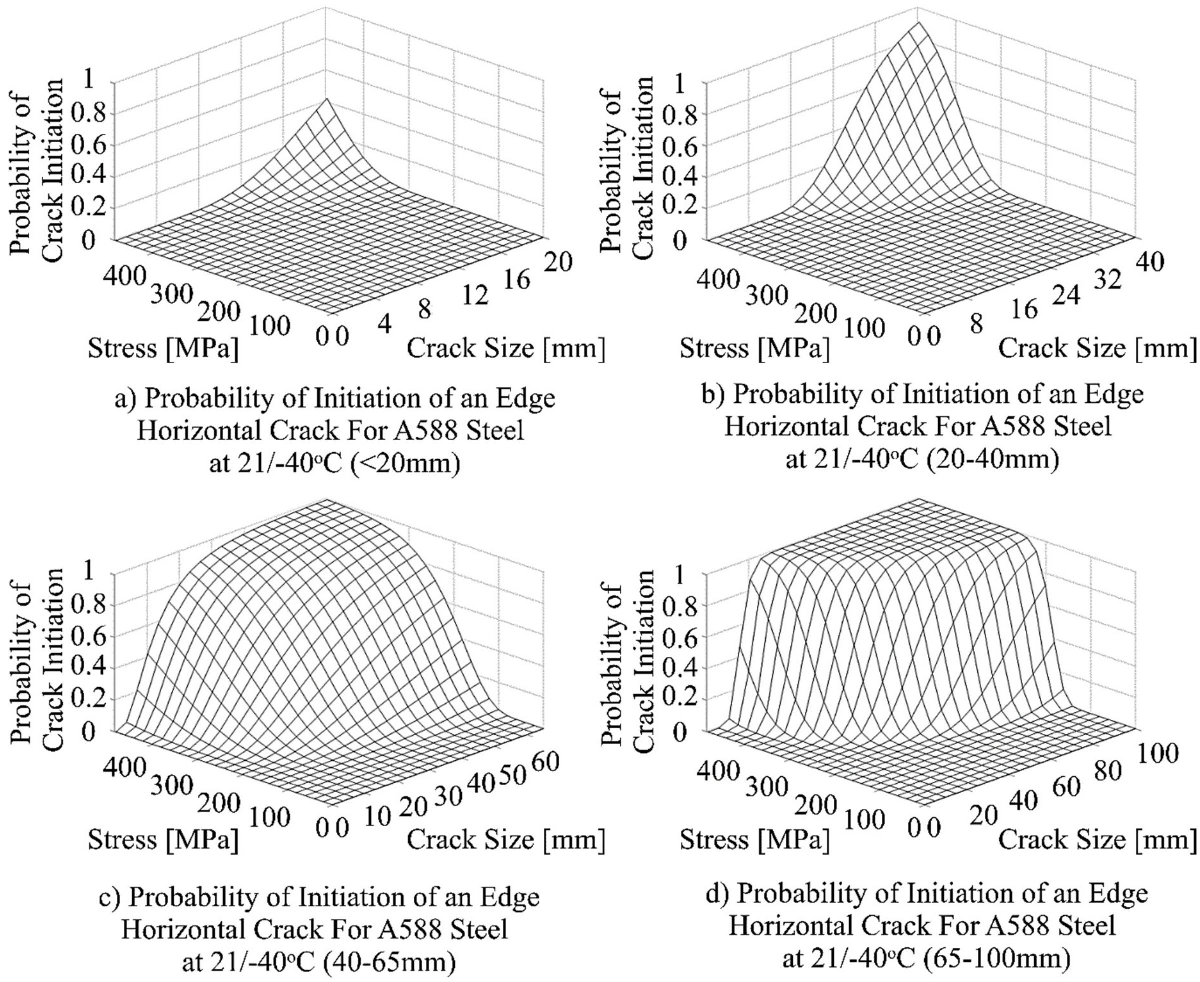

Figure 4.8: Impact of plate thickness on the probability of initiation of crack type 4 for ASTM A588 Gr. B steel (f_y= 345 MPa) (dynamic/static temperatures) according to tests conducted by Suwan (2002).

Chapter 5 RECOMMENDATIONS FOR WELDING PROCEDURES FOR THICK STEEL PLATES

5.1 Introduction

Connecting steel components through welding is always accompanied by residual stresses. The welding process involves concentrated heat input at the welding location causing the expansion of regions close to the heat source. This is then followed by heat convection due to exposure to an ambient medium of lower temperature, which causes the regions far from the welded area to cool faster than closer regions. The areas of steel near the weld that cool last experience contraction that is constrained by already contracted neighboring areas, resulting in tension residual stresses that remain in the plates after the completion of the welding procedure. With more stringent design criteria for seismic and blast loading steel plates with thickness 50mm and higher are becoming common in the steel construction industry to form heavy built-up sections that can resist the applied design loads. Welding such plates employs higher heat input than that required for commonly used 25mm thick plates. Additionally, the plate thickness provides substantial constraint to the contraction of the heated steel resulting in high tensile residual stresses that can lead to crack initiation (Fisher and Pense, 1987, Blodgett and Miller, 1993). One of the steps taken to address the developing problem of welding thick steel plates was first proposed by Miller (2010), who introduced recommendations to reduce shrinkage stresses and restraints, in addition to ensuring that minimum levels of fracture toughness be met. Although these recommendations are informative and provide fabricators with the knowledge to weld thick steel plates, they are of a qualitative nature. Furthermore, welding specifications (AWS D1.1, 2010, CAN/CSA-W59, 2013) have no special requirements for the welding of thick steel plates. According to AWS D1.1 "Table 3.2" (AWS D1.1, 2010); the required prequalified minimum preheat and inter-pass temperatures for the welding of steel plates increase according to the plate thickness. However, AWS D1.1 (AWS D1.1, 2010) also states in "Tables 4.2 and 4.3" that in order to qualify a welding procedure for unlimited thickness, it is permissible to use test plates of 25mm in thickness. Consequently, steel fabricators are using welding procedures qualified for thick plates that were tested on common 25mm plates. With the increasing demand to use thick plates, welding procedures should be revisited with the aim to develop quantitative welding recommendations for various applications (AWS D1.1, 2010, CAN/CSA-W59, 2013). To the best of our knowledge, there has not been a study to provide quantitative recommendations for the welding of thick steel plates.

Recently, studies addressing the effect of different parameters of the welding procedure on the resulting residual stresses have been carried out. Pilipenko (2001) utilized finite element modeling of the welding procedure to study two different mitigation techniques to reduce the resulting residual stresses; mechanical straightening and thermal tensioning. Both techniques showed a 35 - 45% decrease in peak tensile residual stresses. However, new residual stresses were generated in previously stress free regions. The ASTM A131 Gr. 50 steel plates (i.e., nominal f_y = 345 MPa) used in this study were of maximum thickness of 45mm. Yang (2008) conducted experiments to study the effect of submerged arc welding current and speed on the mechanical and physical properties of ASME SA516 Gr. 70 (i.e., nominal f_y = 480MPa) and ASTM A709 Gr. 50 (i.e., nominal f_y = 345MPa) steel. The dimensions of the welded sample plates were 915 x 122 x 17mm. According to the findings of this research high travel speed and welding current result in severe undercuts, and the toughness of both steel materials increased with increasing the welding current and speed. In addition, the percent elongation increased with travel speed but decreased with welding current. Deng and Kiyoshima (2011) studied the effect of weld deposition sequence and direction on residual stresses through experiments and numerical analyses of the weld start/end location. A 55mm thick austenitic stainless steel plate of yield stress 276 MPa was utilized in this research. The results indicated that the transverse residual stresses are more sensitive to the welding sequence than the longitudinal stresses.

With the aim of developing an improved submerged arc welding procedure for thick plates using a partial penetration butt joint, a study of the parameters affecting the resulting post welding residual stresses was completed. A case study of a heavy built-up box column that experienced unrepairable cracks after welding using a qualified welding procedure according to AWS D1.1 (AWS D1.1, 2010) is utilized in the present study. Additionally, a numerical simulation of the welding procedure for thick plates, validated with experimental results (Chapter 3) (Ibrahim et al., 2015), is used to study the effects of the welding parameters on the resulting residual stresses. The parametric study is divided into two phases; the first phase involves parameters directly related to the heat input and cooling rate. These parameters are; the welding temperature, the welding speed and the preheat and inter-pass temperatures. The second phase involves a set of general parameters; the material quality, the welded plate thickness, the number of passes, as well as the welding sequence. The assessment of each parameter is based on two criteria; first the stress profile during and after the welding procedure. Second, the minimum computed crack size according to the resulting residual stresses; based on conducted fracture toughness tests for the steel material (Ibrahim et al., 2016). The results of the parametric study are utilized to provide quantitative recommendations for the welding of thick steel plates that are currently used in the steel construction practice in North America.

5.2 Main Features of the Employed Numerical Model for Welding Simulation

Establishing a detailed parametric study for SAW procedures through experiments is time consuming and costly. A practical approach to conduct such a parametric study is through numerical simulation. A simulation of the welding procedure for thick steel plates was developed using an uncoupled thermo-mechanical finite element model proposed in Chapter 3 (Ibrahim et al., 2015). The simulation is divided into two models; a heat transfer model that produces temperature distributions at all stages of the welding procedure. The temperature distributions are then exported to a stress analysis model that calculates the corresponding strains and stresses, which have resulted from the temperature changes. The results of the numerical model were validated with a welding test, involving thick plates, described in Chapter 3 (Ibrahim et al., 2015). The validation was achieved by comparing temperature distribution results from the model with measured temperatures from the welding test at the same time and location for each welding pass. In this numerical simulation, the main parameters are the heat input, preheat and inter-pass temperatures, steel material properties, thickness of the welded plate, number of passes and welding sequence. The heat input is simulated through the welding temperature, pass size and the welding travel speed. Preheat and inter-pass temperatures are modeled by applying heat boundary conditions at the required area on the surface of the base metal until the required temperature is achieved.

A heavy built-up box column, that experienced cracks after welding, was adopted for this study. The box column is composed of two 660x75mm plates and two 324x75mm plates of ASTM A572 Gr.50 (2013) steel (f_y = 345 MPa, f_u = 450 MPa). The material properties of the numerical model were calibrated through tensile tests conducted for specimens obtained from different locations of the heavy built-up box column. Additional Charpy-V-Notch (CVN) tests were conducted to estimate the base metal and heat affected zone (HAZ) fracture toughness (Chapter 3) (Ibrahim et al., 2015). The welding procedure was conducted on two corners of the built-up column simultaneously using an automated SAW process with average heat input of 2.4 KJ/mm, average current of 700 A and average voltage of 30 V. Each corner was a partial joint penetration (PJP) weld, with groove depth of 37.5mm and groove angle of 60°, consisting of 13 passes. Due to symmetry, only half the built-up box is modeled, as shown in Figure 5.1a. The electrodes used for this procedure were F7A4-EM12K according to AWS D1.1 A5.17 (AWS D1.1, 2010) with suitable granular flux type (OK FLUX 10.71). Two electrodes were used at each corner with diameter 2.4mm and an 8mm gap. The average travel speed of the electrodes was 525 mm/min and the average wire feeding speed was 255 cm/min. For this case-study, the welding sequence according to the fabricator and the AISC welding guidelines by Miller (2006) for welding thick plates is summarized as follows: (a) weld one pass on one side (side-1) of the built-up box column; (b) flip the built-up box column and weld the other side (side-2) and complete weld passes 1 to 4; (c) flip again and weld side-1 and complete weld passes 2 to 7; (d) flip and weld the other side-2 and complete weld passes 5 to 7; (e) flip and weld the other side-1 and complete weld passes pass 8 to 13; (f) flip and weld the other side-2 and complete weld passes 8 to 13. Another model of the welding procedure is utilized in this study; it consists of two steel plates welded in the flat position with PJP welds as shown in Figure 5.1b. This model is used to simplify the study of parameters involving variation in the model geometry as the plate thickness and the number of passes changes. These two welding models are used to conduct a study of the main parameters of the welding procedure as an approach to produce quantitative guidelines for the welding of thick steel plates. Further details regarding the FE model are discussed in Chapter 3.

5.3 Description of the Methodology Employed for Welding of Thick Plates

The parametric study of the welding procedure for thick steel plates is divided into two phases. The first phase (Phase A) involves three parameters that directly affect the heat input and the cooling rate and does not require variations of the weld geometry or sequence. The product of this phase is the assessment of the main parameters of the welding process and the recommendations regarding the heat input including preheat and inter-pass temperatures. As the aim of Phase A is to compare the influence of different parameter values, the average base metal material properties are used through the thickness. In Phase B additional general parameters are introduced, including the variability of the material properties and the plate thickness. Additionally, in this phase the effect of the number of passes and the welding direction are included. The values of different parameters and the analysis models used in this study for Phases A and B are shown in Table 5.1. Each phase of the study is discussed in Sections 5.3.1 and 5.3.2, respectively. The assessment criteria for each parameter are summarized in Section 5.3.3.

5.3.1 Phase A: parameters affecting the heat input and cooling rate

The two main parameters in the heat transfer modeling are the amount of heat introduced in the welded plates (the heat input) and the rate of cooling of the plate from the welding temperature to the ambient temperature (the cooling rate). These parameters are represented in the model by the welding temperature, the speed of welding (electrode), preheat and inter-pass temperatures. Ten models were analyzed in this phase (Table 5.1) using the average base metal material properties based on seventy four tensile coupon test results that were conducted by the authors for the case study heavy box column (Table 3.2, Chapter 3) (Ibrahim et al., 2015). The welding temperature is that of the molten pool, and is a direct representation of the welding heat input. The welding temperature has to be higher than the steel melting temperature which is approximately 1450°C to achieve fusion between the weld metal and base metal (CWB/Gooderham-Centre, 2005, Miller, 2006); the common welding temperature is 1500°C. Relatively high welding temperatures, i.e. 2000 and 2500 °C, are used as well to study the effect of applying high heat input on the residual stress distribution. The welding temperature parameter is studied through Model 1 to 3 (Table 5.1). The heat input also depends on the travel speed of the electrode (Miller, 2006). In turn, this welding travel speed has a great effect on the weld penetration and the bead size. With slow welding speed the heat input increases, as does the penetration and the bead size. The disadvantages of slow welding travel speed are that it diminishes the control of the molten pool and increases the slag inclusion. The average welding travel speed of the submerged arc welding procedure is approximately 10 mm/s (Miller, 2006, AWS D1.1, 2010). Lower and higher values are used in the study to illustrate the effect of the welding travel speed on the heat input and on the residual stresses. The welding travel speeds of 2.5 and 25 mm/s were studied to emphasize the effect of travel speed on the welding residual stress. However, these welding travel speeds are not practical because the slow welding travel speed decreases the control of the molten weld metal and the fast welding travel speeds lead to low heat input, which affects the fusion between the weld metal and base metal. The welding travel speed parameter is studied using Model 1 and Models 4 to 7 (Table 5.1).

The cooling rate is the primary parameter that affects the shrinkage cracks that develop in welded plates. A slow cooling rate will decrease the shrinkage stress that leads to shrinkage cracks. According to Graville (1975) the cooling rate can be calculated from the heat input, the plate thickness and the preheat temperature. Preheat and inter-pass temperatures are the parameters that have the highest influence on the cooling rate. According to AWS D1.1 (2010), for ASTM A572 steel plates with thickness greater than 65mm, the preheat temperature is 110°C and the inter-pass temperature should not be lower than 110°C. Moreover, the preheated area should be at a distance from the weld equal to the thickness of the thicker plate and not less than 75mm. In the current study preheat and inter-pass temperatures vary from the case were no preheat or inter-pass temperatures are utilized (room temperature 20°C) to 400°C, and were studied through Model 1 and Models 8 to 10 (Table 5.1). This phase was conducted using the case study model of the built-up box column (Figure 5.1a).

5.3.2 Phase B: general parameters

This phase focuses on other general parameters, including those which affect indirectly the resulting residual stresses after completion of the welding procedure. Twelve models are included in this phase, in addition to Model 1 of Phase A (Table 5.1). The variability of the steel's mechanical properties through the thickness of thick steel plates may have an impact on the distribution of the residual stress induced by welding. To take this into account, tensile steel coupons from different locations in the steel plate were tested and the mechanical properties of the material through the thickness was developed. In the parametric study, the impact of the steel mechanical properties is assessed based on the mean and standard deviation values of the elastic modulus (E), the yield stress (f_y) and the ultimate strength (f_u). Three material profiles were based on 74 tensile coupon tests (46 through thickness specimens and 28 specimens from the plate surface) conducted in Chapter 3 (Ibrahim et al., 2015) for different locations in the case study heavy box-column; the average, the lower bound (LB) and the upper bound (UB) material properties, as shown in Table 5.2. The base metal material properties parameter is studied through the Models 1, 11 and 12 (Table 5.1) of the case study model of the built-up box column (Figure 5.1a).

A study of the impact of the plate thickness is also included in this modelling phase. The thicknesses used in the study are; those commonly used in current practice 25, 12, 19, 38mm, and thicker plates 50, 75 and 100mm. The thickness parameter is studied through Models 13 to 19 (Table 5.1). Another important parameter is the number of welding passes. Four welding procedures were studied, the first three are composed of 5, 13 and 20 welding passes. The fourth welding procedure utilizes 13 welding passes with unequal welding pass sizes; such that small welding pass sizes are used for the first 10 passes and larger welding pass sizes are used for the final welding layer. The number of welding passes parameter is studied through Model 18 and Models 20 to 22 (Table 5.1). Due to the variation in the model geometry for these two parameters, they were studied through the model of welding two steel plates in the flat position (Figure 5.1b).

5.3.3 Parameter assessment criteria

According to the preliminary results of the numerical simulation technique utilized in this study, which conform to the findings of previous research programs that involved numerical and experimental investigations (Bjorhovde et al., 1972, Pilipenko, 2001, Yang, 2008), the maximum residual tensile stresses from the welding procedure are located at the surface of the welded plates, and gradually decrease through the thickness until reaching the center of the steel plate. Consequently, the temperature and residual stress results of each of the 22 models discussed in Sections 5.3.1 and 5.3.2 (Table 5.1) were obtained at the plate surface after each welding pass at all the locations shown in Figures 5.2 and 5.3 in the transverse and longitudinal directions, respectively. These paths represent possible regions for the peak tensile residual stresses according to the stress distribution results and feedback from steel fabricators. Figure 5.4 shows an example of the residual stress distributions at the studied paths 1a, 4a, 5a and 6a, to illustrate the locations of the maximum tensile stresses at each surface. The assessment of the results from each parameter is based on two criteria; the first criterion is the effect of the parameter on the stress distribution and peak tensile stresses at the plate surface for all the paths mentioned in Figures 5.2 and 5.3, as well as through the plate thickness. The second criterion is the critical crack sizes at the plate surface, after each welding pass, for a probability of crack initiation of 5% based on the statistical assessment of the fracture toughness results achieved from the CVN tests documented in Chapter 4 (Ibrahim et al., 2016). Figure 5.5 shows the relation between the applied stress, the crack size and the probability of this crack to initiate at 21°C. In this example, if the probability limit of crack initiation is set to 5% and the applied stress is assumed as 600 MPa then the critical crack size will be 7mm. Through this assessment process the impact of each parameter on the output stress distribution and on the temperature distribution throughout the welding procedure has been taken into account.

5.4 Results and Discussion

The results of the stress and temperature distributions for each one of the 22 models (Table 5.1) of the parametric study were obtained at the studied locations (Figures 5.2 and 5.3). Each parameter was assessed according to Section 5.3.3. Sections 5.4.1 and 5.4.2 contain a discussion of the results of Phases A and B of the parametric study, respectively. Recommendations are provided for the welding procedures of thick steel plates (greater than 50mm thick) in Section 5.4.3, to improve the residual stress distribution and to reduce the probability of crack initiation.

5.4.1 Discussion for Phase A results

Phase A of the parametric study primarily focuses on the heat input and cooling rate of the welding procedure. The aim of this phase is to compare the commonly used values for the welding process parameters for thick steel plates with other values for the welding temperature, travel speed and preheat/inter-pass temperature.

5.4.1.1 Welding temperature

The welding temperature is a direct representation of the heat input in the numerical model; temperatures of 1500, 2000 and 2500°C were considered. Figures 5.6a and 5.6b show the transverse residual stresses through the Path-5a (Figure 5.2a) (in the direction perpendicular to the welding line) for the welding temperatures 1500°C and 2000°C, respectively; maximum residual stress values, from all studied paths, for the welding temperature parameter are presented in Appendix B. The graphs illustrate that the residual stress increases with each welding pass such that the maximum residual stress is that after the last welding pass. It can be concluded from the graphs that with a 500°C increase in welding temperature the residual transverse stress at the plate surface near the welding area increases by 20%. For a welding temperature of 2500°C the analysis stopped after the fifth welding pass due to numerical limitations given the high heat input, and as such a full set of results could not be presented. Figure 5.6c shows the critical longitudinal surface discontinuity size at the welded plate surface after each welding pass for a probability of crack initiation of 5% according to the resulting stress levels at all the studied paths (Figures 5.2a and 5.3a). For the early welding stages there is a significant difference in the allowed discontinuity size for the commonly used welding temperature (t_w=1500°C) and for the higher welding temperature (t_w=2000°C). For the final welding stages, there is no significant difference in the critical discontinuity sizes (30mm) between the welding temperatures used in the study. In conclusion, the residual tensile stress developed at the end of the welding procedure produce the smallest critical discontinuity size.

5.4.1.2 Welding travel speed

The heat input is inversely proportional to the welding (electrode) travel speed. Based on feedback from the steel industry, for the automated SAW process, the fastest practical welding travel speed is 15mm/s and the slowest is 5mm/s. In this study the models were run with welding speeds of 2.5, 5, 10, 15 and 25 mm/s. Figures 5.7a and 5.7b show the transverse residual stresses resulting from the fastest practical welding travel speed V_w=15mm/s and the slowest practical welding speed V_w=5mm/s along Path-1a (Figure 5.2a) as one of the studied paths; maximum residual stress values, from all studied paths, for the welding travel speed parameter are presented in Appendix B. The graphs show that the maximum residual stress distribution occurs after the welding of the last pass. Additionally, the graphs show that with an increase in the welding travel speed (decreasing the heat input), the transverse residual stresses have increased. However, the width of the area of the base metal subjected to high tensile stresses has decreased. Figure 5.7c demonstrates the critical longitudinal discontinuity sizes at the plate surface for each welding travel speed after each welding pass for a 5% probability of crack initiation according to the resulting stress levels at all the studied paths (Figures 5.2a and 5.3a). The critical discontinuity size at early welding stages is high for V_w=25mm/s compared to that of V_w=10mm/s and V_w=15mm/s. For the slowest welding travel speeds used in this study, i.e. V_w=5mm/s and V_w=2.5mm/s, the critical discontinuity size at the plate surface at early welding stages was the lowest. After the welding process had finished, the critical discontinuity sizes for all welding travel speeds used in the study was the same; equal to 30mm (Figure 5.7c). High welding travel speed such as V_w=25mm/s can result in lack of fusion (Miller, 2006). From these results it can be implied that using the fastest welding travel speed, at which fusion is still assured, provides the benefit of a narrow high tensile stressed area in the base metal which decreases the likelihood of the presence of a discontinuity in this area, while the slowest welding travel speed provides lower tensile stress values at a wider area in the base metal.

5.4.1.3 Preheat/inter-pass temperatures

The last parameter, which was investigated as part of Phase A is the preheat/inter-pass temperature. The base metal is preheated to a specified temperature in the vicinity of the welding area before the welding procedure starts. This temperature is maintained at these regions throughout the welding procedure. Figure 5.8 illustrates the transverse stress distribution, along Path-5a (Figure 5.2a) as one of the studied paths, for the case of no preheating (20°C) and then for a preheat/inter-pass temperatures (t_p) of 150°C, 225°C and 400°C; maximum residual stress values, from all studied paths, for the preheat/inter-pass temperature parameter are presented in Appendix B. The maximum stress distribution also occurs after the final welding pass. Using preheat/inter-pass temperature directly affects the stress distribution in the base metal, because it decreases the amplitude of the heating cycles through the welding process as well as the cooling rate. Preheat/inter-pass temperatures of 150°C, 225°C and 400°C resulted in a very close stress distribution as shown in Figure 5.8; the peak transverse stress decreased by 25% as a result of applying t_p. Figure 5.9 shows the critical discontinuity sizes in the transverse and longitudinal directions for the different preheat/inter-pass temperatures after each welding pass according to the resulting stress levels at all the studied paths (Figures 5.2a and 5.3a). By applying preheat and inter-pass temperatures, the critical crack sizes become longer. The difference between the critical crack sizes for t_p 150°C, 225°C and 400°C is not significant; therefore, the minimum preheat/inter-pass temperature of 150°C currently suggested by AWS D1.1 (2010) is sufficient to achieve the lowest stress distribution.

5.4.2 Discussion for Phase B results

In Phase B of the study, the general properties of the welded assembly are studied with the aim to detect the properties that have the most influential contribution to the residual stress distributions and the probability of crack initiation.

5.4.2.1 Mechanical properties of the base metal

Due to the variability of the mechanical properties of thick steel plates as illustrated by the tensile test results conducted by Ibrahim et al. (2015) (Table 3.2, Chapter 3); the material model was defined as having the average mechanical properties of the test results, the lower bound (LB) properties and the upper bound (UB) properties as shown in Table 5.2, throughout the material thickness. Figures 5.10a and 5.10b show the transverse stress distribution of the LB and the UB material models along Path-1a (Figure 5.2a) as one of the studied paths; maximum residual stress values, from all studied paths, for the base metal mechanical properties parameter are presented in Appendix B. The difference in stress distributions is not significant; the more ductile material based on specimens taken near the case study plate surface produced a slightly lower stress distribution than the brittle material property based on specimens taken through the thickness of the case study plate. Figure 5.10c shows the critical longitudinal crack size for a 5% probability of crack initiation according to the resulting stress levels at all the studied paths (Figures 5.2a and 5.3a). Similar observations hold true regardless of the employed material model. It can be concluded from this study that the mechanical properties of the base metal material, within the range considered, have a negligible impact on the residual stress distribution and probability of crack initiation. As such, it seems acceptable to neglect the variability of the mechanical properties through the thickness of a steel plate.

5.4.2.2 Base metal plate thickness

Furthermore, the impact of the plate thickness on the welding residual stresses and critical crack sizes is studied for the flat plate model. Figure 5.11 shows the transverse stress distributions for the plate thicknesses of 12, 25, 50 and 100mm along Path-1b (Figure 5.2b), as one of the studied paths maximum residual stress values, from all studied paths, for the plate thickness parameter are presented in Appendix B. The same welding procedure was applied for all plates with the same number of passes (13) but with a relative pass size based on the plate thicknesses ratio; such that all plate models experience the same number of heat cycles irrespective of thickness on the account of the heat input used for the welding procedure, being proportional to the plate thickness. Residual stresses and crack initiation are more critical for thick plates than thin plates due to the higher restraints provided by the plate thickness; for example, a 50mm thick steel plate has a maximum tensile residual stress of 200MPa after welding, while that of a 25mm thick plate is less than 100MPa, as shown in Figure 5.11. However, thin plates experience more deformation during the welding procedure than thick plates (Pilipenko, 2001) as shown in Figure 5.12.

The base metal plate thickness also has a direct effect on the steel plate through thickness stress distribution. Figure 5.13 shows the transverse and longitudinal stress distribution, after the welding procedure has been completed, through the thickness of the plates and at a distance from the welded area equal to 20% of the plate thickness (t). The transverse stress distributions demonstrate an increase in the stress variation through the plate thickness with the increase in thickness. For the 12mm thick plate the maximum transverse stress at the plate surface was 40MPa and the minimum stress through the thickness was -25MPa, while for the 100mm thick plate the maximum transverse stress was 240MPa and the minimum was -100MPa. The reason for this is that with the increase in thickness the heating and cooling process, associated with the welding procedure, becomes less uniform through the thickness of the plate. High variation in the longitudinal stresses through the thickness for thick plates was also detected (Figure 5.13c), while thinner plates exhibited a low variation in the longitudinal stresses but a higher average stress through the plate thickness. This is attributed to the more uniform through thickness expansion and contraction in the welding direction for thin plates than thick plates; such that the whole thickness of the plate contributes to restraining the hotter regions from contraction.

Figure 5.14a shows the critical longitudinal crack sizes for all the studied thicknesses at a probability of crack initiation of 5% according to the resulting stress levels at all the studied paths (Figures 5.2b and 5.3b). The critical crack size increases with the decrease in thickness due to the lower transverse stresses (Figure 5.11), as well as the higher average fracture toughness based on CVN tests (Chapter 4) (Ibrahim et al., 2016). Although the longitudinal stresses for thin plates were higher than those of the thick plates, the critical transverse crack sizes at 5% probability of crack initiation for thin plates (Figure 5.14b) were less than those of the thick plates. This is attributed to the greater average fracture toughness of the thin plates compared to that of the thick ones (Chapter 4) (Ibrahim et al., 2016).

5.4.2.3 Number of welding passes

The size and number of the welding passes required for the welding procedure also have an impact on the resulting residual stresses. The reason is that this parameter controls the amplitude and number of heating and cooling cycles applied to the base metal. Figure 5.15a shows the four studied cases for welding a 75mm thick plate; 5 welding passes (large size passes), 13 welding passes (commonly used number of passes according to feedback from the industry), 20 welding passes (small size passes) and the commonly used number of passes with unequal pass sizes. The weld assembly and overall size of the weld is the same for each case. The weld pass size can be made larger by increasing the number of electrodes, the heat input, the wire feeding speed or decreasing the welding travel speed or any combination of the above mentioned parameters. The welding travel speed is considered constant for each of the studied cases (Table 5.1). Figures 5.15b to 5.15e show the transverse stress distribution along Path-1b of the flat plate model (Figure 5.2b) for the four studied cases; maximum residual stress values, from all studied paths, for the number of welding passes parameter are presented in Appendix B. The graphs suggest that increasing the number of welding passes increases the peak value of the residual tensile stress near the welding area. Furthermore, using a small number of welding passes results in a wider area of tensile stress near the welding region (Figure 5.15b) compared with the case where a larger number of welding passes are used (Figure 5.15d); thus a wider heat affected zone (HAZ). This is due to the higher heat input required to complete the large size welding passes. Also, there is no significant difference between the final residual stress distribution for the modified 13 welding pass procedure (Figure 5.15e) and the 5 welding pass procedure (Figure 5.15b). As such, it has been demonstrated that the size of the final welding passes has a greater impact on the residual stress distribution than the size of the welding passes at the early stages of the welding procedure, regardless of the number of passes.

The through thickness stress distribution for each of the studied welding procedures was also obtained. Figure 5.16a shows the location of the through thickness studied path at the mid-span of the welded plates and at 15mm from the edge of the welding. Figures 5.16b and 5.16c show the transverse and longitudinal stress distributions, respectively. For the through thickness transverse stresses there is no significant difference between the results of the different welding procedures. Using only 5 welding passes resulted in the highest through thickness tensile longitudinal stresses, while using 20 welding passes resulted in the lowest tensile longitudinal stresses. The high heat input associated with using 5 welding passes results in more expansion strains than in the other welding cases. After cooling, higher tensile stresses are formed in the longitudinal direction than for the other welding cases constrained by the length of the welded plates. While in the transverse direction the high heat input causes higher expansion strains as well as a wider area of expansion; therefore decreasing the constraint levels in this direction in comparison with the other welding cases. Moreover, Figure 5.17 shows a comparison between the developed plastic strains after completing half the weld for the 5 and 20 welding pass cases (the weld metal elements were removed from the figure to emphasize the strains of the base metal); the 5-pass case shows a wider plastic strain area than the 20-pass case.

Figures 5.18a and 5.18b show the critical crack sizes in the longitudinal and transverse directions respectively for a probability of crack propagation of 5% according to the resulting stress levels at all the studied paths (Figures 5.2b and 5.3b). For the four studied cases there is no significant difference in the critical crack sizes at the end of each welding procedure. Although the critical crack size for the 20 welding pass case is smaller than that of the 5 welding pass case due to the higher residual stresses, the 5 welding pass case has a wider HAZ which increases the chance of imperfections being subjected to tensile stresses. Based on the stated results, the number of heating and cooling cycles induced by the welding procedure for thick steel plates is a critical parameter affecting the resulting residual stress distribution.

5.4.3 Recommendations for welding thick steel plates

Based on the results of the parametric study discussed in Sections 5.4.1 and 5.4.2, it can be concluded that the most critical parameters, that have the greatest impact on improving the resulting residual stress distribution and minimizing the probability of crack initiation, are the preheat/inter-pass temperatures, the welding travel speed and the number of welding passes. The preheat and inter-pass temperature of 110°C that is mandated by the welding specifications (AWS D1.1, 2010, CAN/CSA-W59, 2013) is essential and sufficient for the welding procedure of thick steel plates (thickness greater than 50mm). Moreover, using a fast welding travel speed of 15mm/s has the benefit of reducing the maximum tensile residual stress, however the HAZ size increases.

Another benefit of using a fast welding travel speed is increasing the production rate which is an important factor in steel fabrication. If the resulting wide area in the base metal subjected to tensile stress leads to the propagation of discontinuities present in the base metal, the fabricator may instead select a slower welding travel speed to provide a narrower tensile stressed area, however the maximum tensile stress is higher than that obtained with a fast welding travel speed. The number of welding passes has the same effect as welding travel speed on the tensile stress values and distribution. Using a small number of welding passes results in a wide area under tensile stress with low maximum tension stress value, while using a large number of welding passes leads to a narrow area of tensile stress with high maximum tensile stress value.

Accordingly, four welding procedures are recommended for PJP groove welding of thick steel plates. All four procedures utilize a preheat/inter-pass temperature of 110^{o}C. The first welding procedure provides the lowest tensile stress value and widest tensile stressed area and is a combination of a welding travel speed of 5mm/s and 5 welding passes. The second welding procedure provides the narrowest area subjected to high tension stresses and utilizes a welding travel speed of 15mm/s and 20 welding passes. The third welding procedure provides the highest fabrication rate using welding travel speed of 15mm/s and 5 welding passes. The fourth welding procedure provides the slowest production rate using a welding travel speed of 5mm/s and 20 welding passes. Figure 5.19 shows the residual stress distribution as well as the residual deformation (with a scale factor of 5) for the four recommended welding procedures assuming two 75mm thick steel plates were welded in a flat position (the weld metal was removed from the figure to clarify the comparison between the welding procedures). The results are in agreement with the parametric study results; such that the slow welding travel speed and small number of passes results in the lowest tensile residual stress distributed on the widest area, while the fastest welding travel speed and the largest number of passes resulted in the highest residual tensile stresses in the narrowest area. Furthermore, using a fast welding travel speed with a small number of passes resulted in the highest residual deformation due to high shrinkage strains, while using a slow welding travel speed with a large number of passes results in the least residual deformation (Figure 5.19).

A detailed analysis of the recommended welding procedures in combination with the crack assessment method based on fracture toughness tests developed in Chapter 4 (Ibrahim et al., 2016) was performed. In this analysis thick plates are divided into two categories according to the thickness ranges; 25 to 50mm and 50 to 100mm. The analysis was developed for minimally and highly restrained welding conditions. Consequently, for welding thick steel plates, the base metal has to be inspected before welding for discontinuities and the following recommendation shall apply for the four welding procedures;

- The corresponding critical probability of crack initiation, with respect to the specifications' (AWS D1.1, 2010, CAN/CSA-W59, 2013) limit of 27J at 0°C CVN value for ASTM A572 Gr.50 (2013) steel is 2% according to Chapter 4 (Ibrahim et al., 2016).
- Provided in Table 5.3: the minimum distance from the edge of the plate to be welded, for surface and through thickness discontinuities in the direction of the weld as well as in the transverse direction for each welding procedure. Such that the restraint to the deformation of the plates in the welding procedure is minimal for a probability of crack initiation of 2%.
- Provided in Table 5.4: the minimum distance from the edge of the plate to be welded for surface and through thickness discontinuities in the direction of the weld as well as in the transverse direction for each welding procedure. Such that the plates used in the welding procedure are fully restrained, for a probability of crack initiation of 2%.

It is worth mentioning that the AWS D1.1 (2010) acceptability limits for laminar discontinuities in cut surfaces is 25mm. According to the results of the present study this limit should not be applied for thick steel plates undergoing a welding procedure; instead, Tables 5.3 and 5.4 should be employed. In addition, according to the residual stress results in the weld metal, the limitations of porosity and fusion discontinuities in the weld metal for welded steel plates with thickness greater than 50mm should follow Clause 6.12.2.1 of AWS D1.1 (2010), which normally is for cyclically loaded non-tubular connections in tension, because of the maximum discontinuity length of 12mm.

5.5 Limitations of the Present Study

The parametric study and recommendations for the welding procedures of welding thick steel plates was established for plates with thickness greater than 25mm that are welded using the automated SAW process. This study is also limited to steel plates that are butt-welded using either complete joint penetration (CJP) or partial joint penetration (PJP). The crack assessment approach is based on fracture toughness data from ASTM A572 Gr.50 (2013) steel plates. The fracture toughness variability can be different for high strength steel grades and other types of steel; therefore further investigation is required for these cases.

5.6 Summary and Conclusions

In order to develop quantitative recommendations for the welding procedure of butt-welded thick steel plates using a SAW process, a parametric study was conducted for the welding procedure parameters. The study utilized a validated numerical simulation approach of the welding procedure for thick steel plates. The simulation was established for two assemblies; for a case study heavy built-up box column and two thick steel plates welded in a flat position. The parametric study was divided into two phases; the first phase was focused on the heat input and cooling rate parameters of the welding procedure, the second phase was focused on general parameters regarding the welding assembly. The assessment of each parameter was based on its impact on the residual stress distribution and the critical crack sizes after each welding pass for a probability of crack propagation of 5%. The main conclusions achieved from Phase A of the parametric study are summarized below:

- A low heat input that ensures full fusion of the weld and base metal is recommended. This is in agreement with the current code recommendations.
- Fast welding travel speeds result in a narrower high tensile stress area in the base metal than slow welding travel speeds, however the maximum tensile stress values are higher.
- As the welding travel speed increases the maximum tensile residual stresses decreases.
- Applying preheat/inter-pass temperature is essential for welding thick steel plates, however the improvement in the stress distribution achieved by applying temperatures greater than 110°C is not significant.

The main conclusions of Phase B of the parametric study are summarized as follows:

- The variation of material mechanical properties through the thickness of thick plate has no significant effect on the welding residual stress distribution. An assumption of uniform material mechanical properties in the simulation is adequate.

- The welding tensile transverse residual stresses increase as the thickness of the welded plates increases. Longitudinal tensile residual stresses increases as the thickness of the welded plate decreases. Thin steel plates are more susceptible to deformation from the welding procedure than thicker plates.
- The variation in the through thickness residual stresses increases as the thickness of the welded pate increases.
- Large number of welding passes results in a narrower tensile stressed area in the base metal and higher maximum tensile stresses than using a small number of welding passes.
- As the number of welding passes decreases the maximum tensile residual stresses decreases.
- The number of welding passes has no significant effect on the transverse through thickness residual stresses.

The welding travel speed, the preheat/inter-pass temperature and the number of welding passes were identified as the welding parameters with the highest impact on the developed residual stresses and the probability of crack propagation for the welding procedure of thick steel plates. Four welding procedures are recommended for butt-welding thick steel plates using an automated SAW process. Numerical analysis of the four welding procedures was performed and acceptable limits for cracks and discontinuities in the base metal before welding were provided.

Table 5.1: Values of parameters in Phases A and B of the parametric study

			Phase A[a]		
Model Number	**Welding Temperature [°C]**	**Welding Speed [mm/s]**	**Preheat/ Inter-pass [°C]**	**Base Metal Material Properties**	**Model and Studied Paths**
1[c]	1500	10	20	Avg.	Box Column Paths 1a to 14a
2	2000	10	20	Avg.	
3	2500	10	20	Avg.	
4	1500	2.5	20	Avg.	
5	1500	5	20	Avg.	
6	1500	15	20	Avg.	
7	1500	25	20	Avg.	
8	1500	10	100	Avg.	
9	1500	10	250	Avg.	
10	1500	10	400	Avg.	
			Phase B[b]		
Model Number	**Base Metal Material Properties**	**Base Metal Thickness [mm]**	**Number of Passes**	**Welding Pass size**	**Model and Studied Paths**
11	LB	75	13	Constant	Box Column Paths 1a to 14a
12	UB	75	13	Constant	
13	Avg.	12	13	Variable	Plates welded in flat position Paths 1b to 4b
14	Avg.	19	13	Variable	
15	Avg.	25	13	Variable	
16	Avg.	38	13	Variable	
17	Avg.	50	13	Variable	
18	Avg.	75	13	Variable	
19	Avg.	100	13	Variable	
20	Avg.	75	5	Variable	
21	Avg.	75	20	Variable	
22	Avg.	75	13^{+}	Variable	

[a] For all Phase A models the plate thickness is 75mm, number of welding passes is 13 and the base metal material properties are constant throughout the thickness.
[b] For all Phase B models the welding temperature is 1500°C, the welding speed is 10mm/s and the preheat/inter-pass temperature is 20°C.
[c] Model 1 is also used in the study of the base metal material parameter of Phase B

Table 5.2: Values used for the Lower bound, Average and Upper bound material properties.

	Lower bound Material	**Average Material**	**Upper bound Material**
Modulus of Elasticity (E) [MPa]	205963	217533	229103
Yield Stress (f_y) [MPa]	356	379	402
Ultimate Stress (f_u) [MPa]	579	606	633

Table 5.3: Recommendations for discontinuities in minimally restrained thick steel plates PJP butt-welded using an automated SAW procedure based on 2% probability of crack initiation.

	Minimum distance from weld groove [mm]					
			Longitudinal discontinuity			Transverse discontinuity
	Welding travel speed[a] [mm/s]	Number of passes[a]	10mm surface discontinuity	20mm surface discontinuity	20mm through thickness discontinuity	5mm surface or 10mm through-thickness discontinuities
50 < t ≤ 100mm	5	5	-	45	20	64
	15	20	25	38	18	44
	15	5	-	38	23	46
	5	20	-	44	20	58
25 < t ≤ 50mm	5	5	-	24	16	58
	15	20	18	28	12	36
	15	5	-	23	24	44
	5	20	-	30	10	50

a For all welding procedure a preheat/inter-pass temperature of 110^0C is applied.

Table 5.4: Recommendations for discontinuities in fully restrained thick steel plates PJP butt-welded using an automated SAW procedure based on 2% probability of crack initiation.

			Minimum distance from weld groove [mm]			
			Longitudinal discontinuity			Transverse discontinuity
	Welding travel speed[a] [mm/s]	Number of passes[a]	10mm surface discontinuity	20mm surface discontinuity	20mm through thickness discontinuity	5mm surface or 10mm through-thickness discontinuities
50 < t ≤ 100mm	5	5	30	60	35	67
	15	20	46	62	28	44
	15	5	38	60	30	50
	5	20	38	58	32	58
25 < t ≤ 50mm	5	5	-	34	35	65
	15	20	28	42	18	38
	15	5	23	40	32	45
	5	20	22	34	20	50

a For all welding procedure a preheat/inter-pass temperature of 110^{0}C is applied.

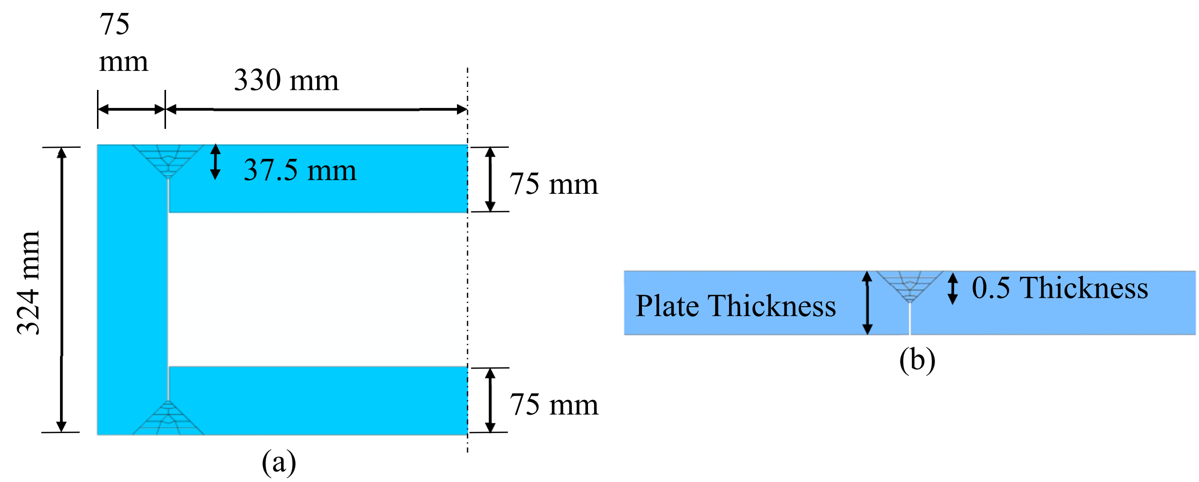

Figure 5.1: Welding procedure models. a) Built-up box column, b) 2 steel plates in the flat position

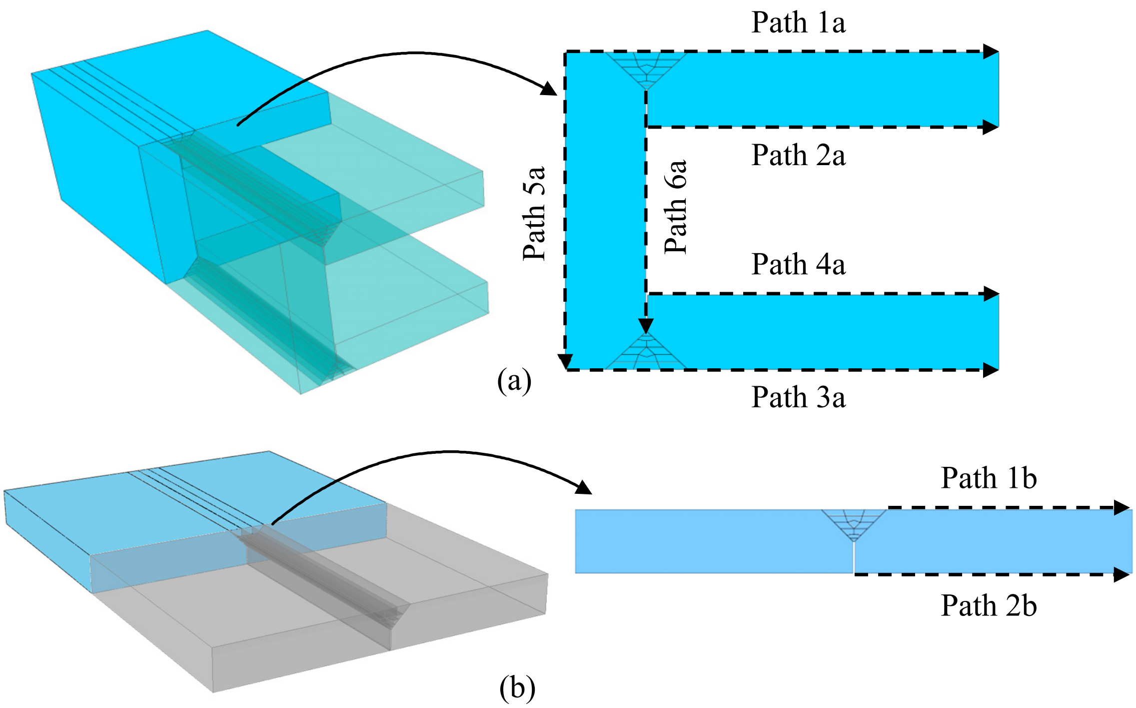

Figure 5.2: Studied paths in the transverse direction for, a) Built-up heavy box column model, b) Plates welded in flat position model.

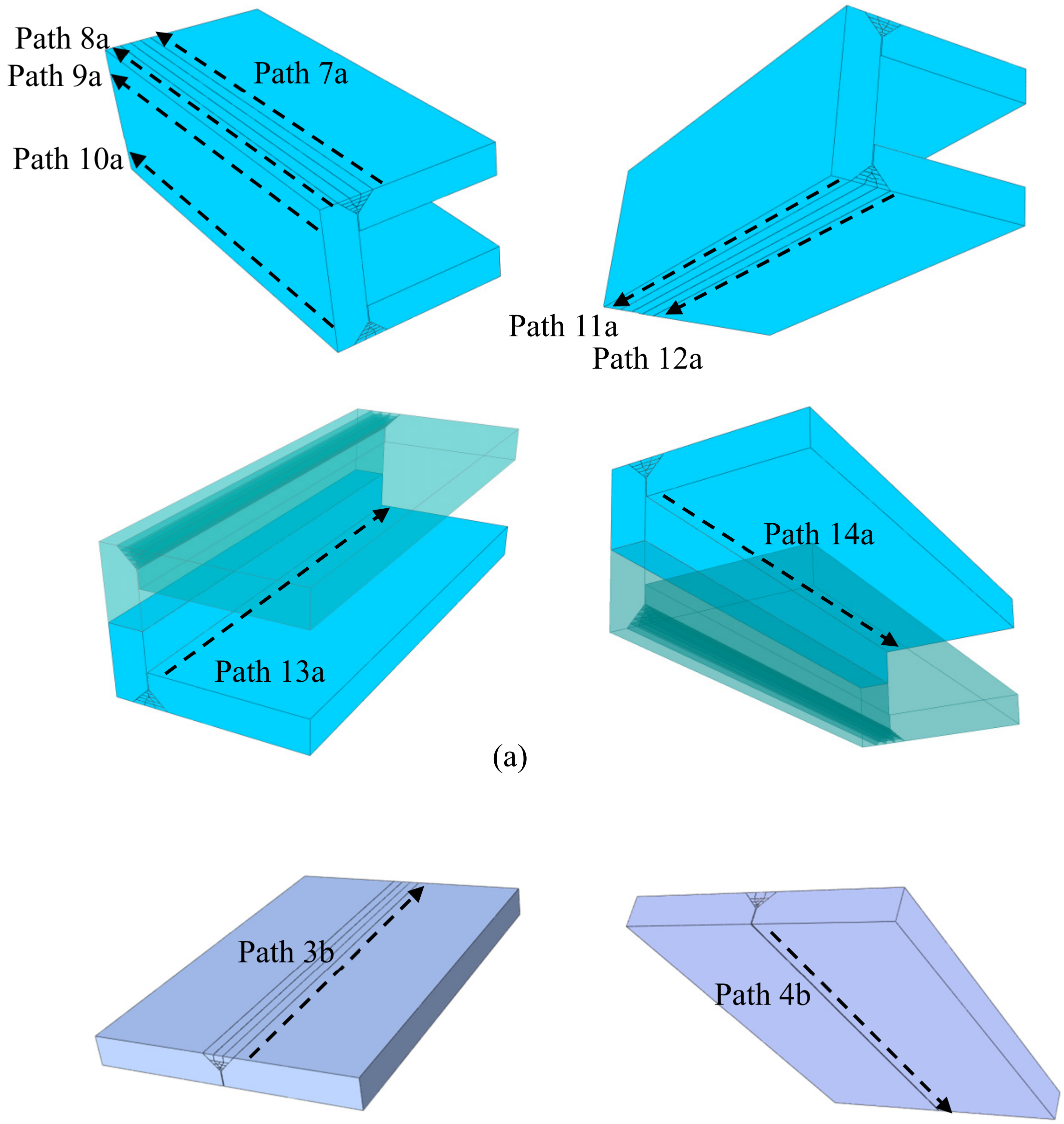

(b)

Figure 5.3: Studied paths in the longitudinal direction for, a) Built-up heavy box column model, b) Plates welded in flat position model.

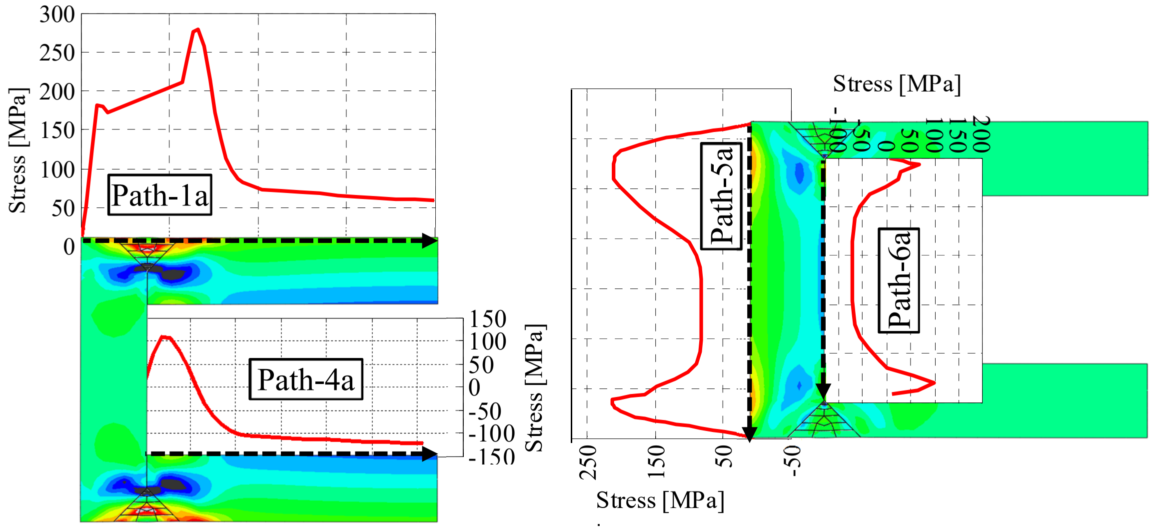

(a) (b)

Figure 5.4: An example of the welding residual stress distributions along some of the studied Paths; a) Paths 1a and 4a, b) Paths 5a and 6a

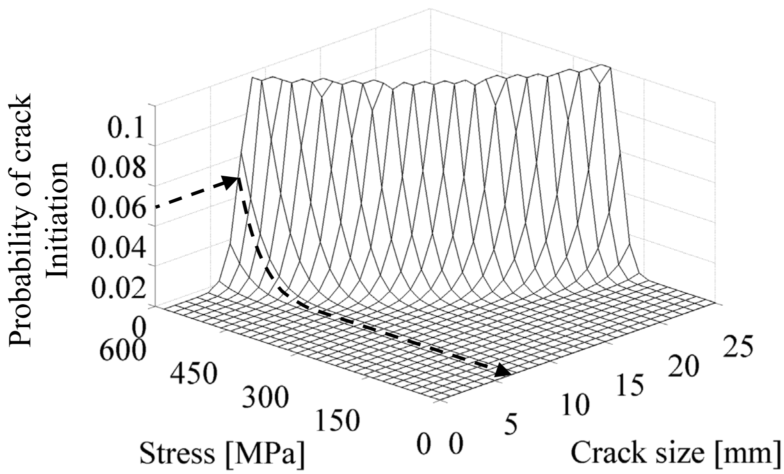

Figure 5.5: Relation between the applied stress, the crack size and the probability of the crack to initiate

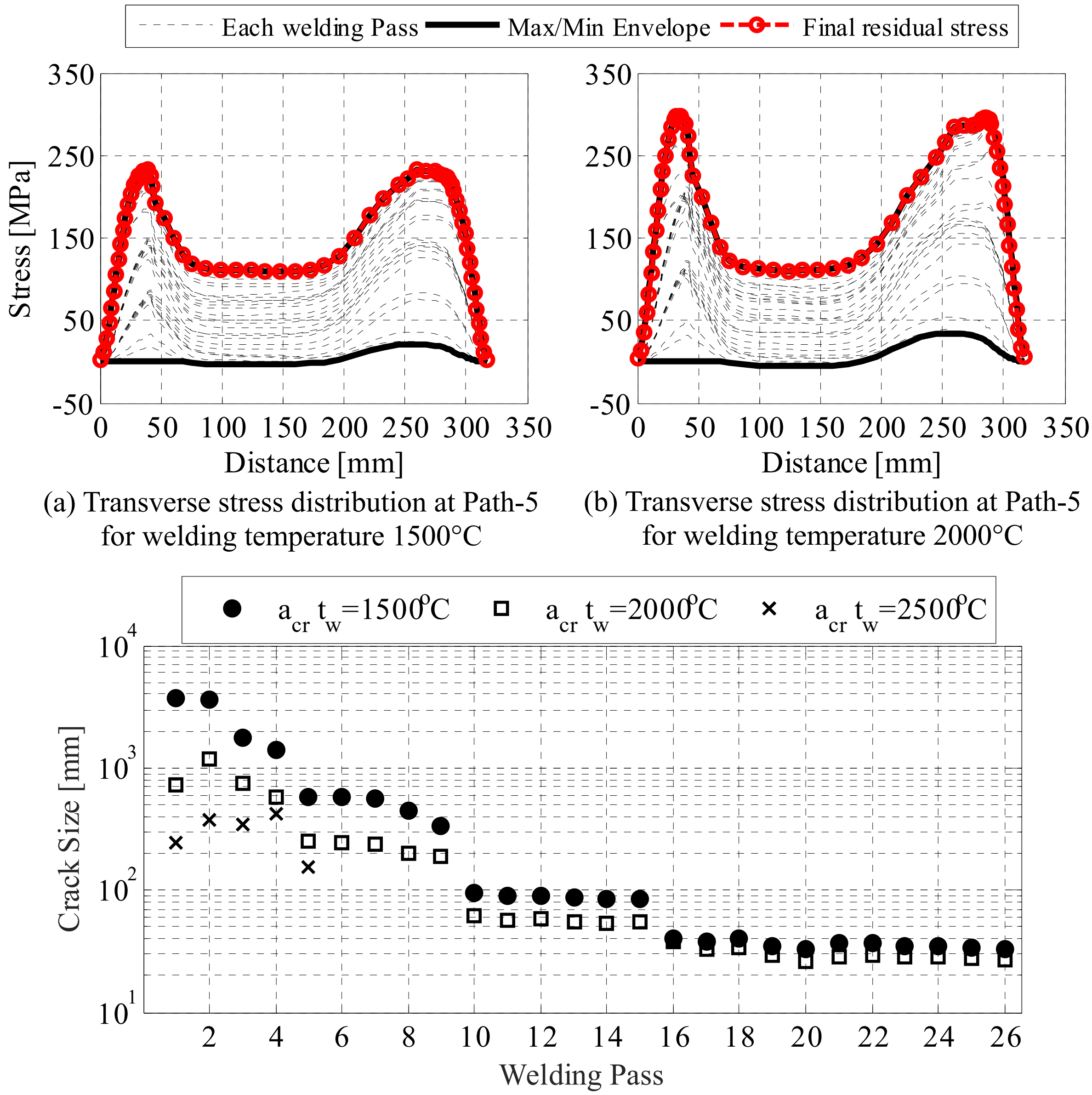

(a) Transverse stress distribution at Path-5 for welding temperature 1500°C

(b) Transverse stress distribution at Path-5 for welding temperature 2000°C

(c) Critical crack size for longitudinal crack at 5% probability of crack propagation

Figure 5.6: Effect of the welding temperature on the residual stress distribution and the critical crack size.

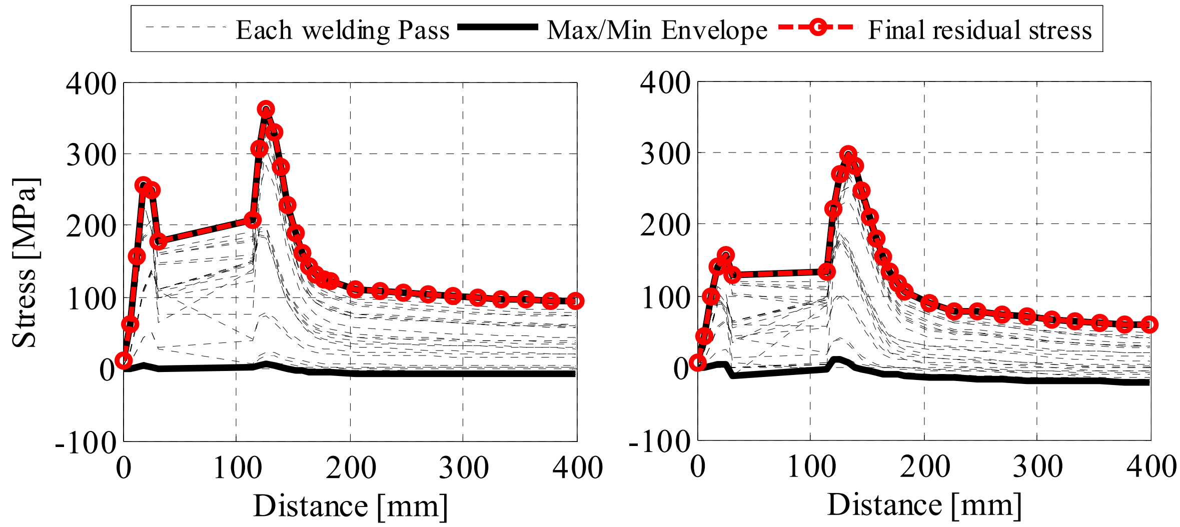

(a) Transverse stress distribution at Path-1 for welding speed 15 mm/s

(b) Transverse stress distribution at Path-1 for welding speed 5 mm/s

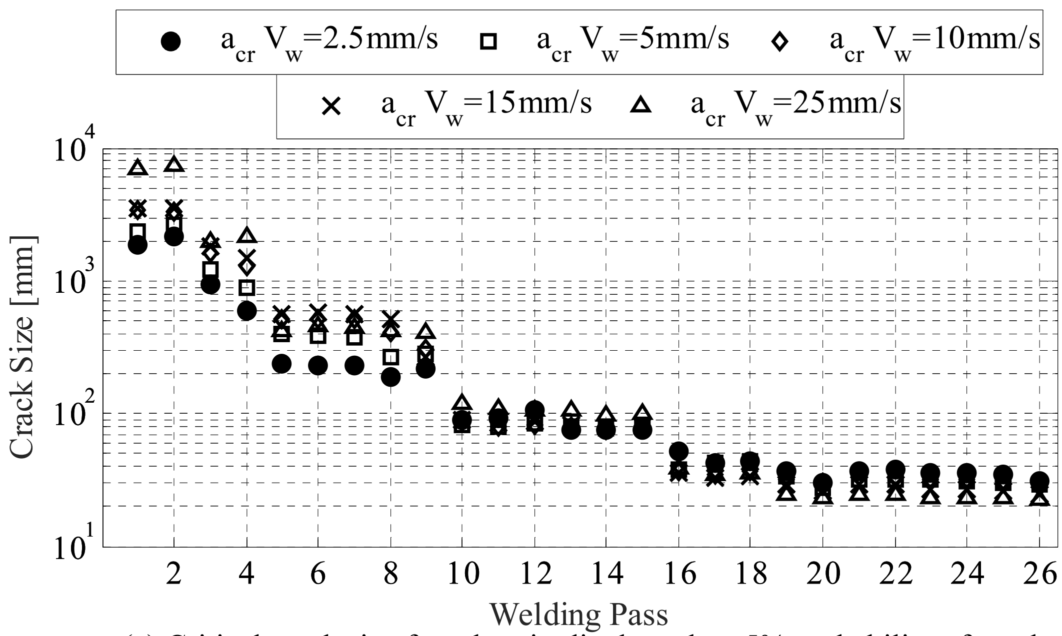

(c) Critical crack size for a longitudinal crack at 5% probability of crack propagation

Figure 5.7: Effect of the welding travel speed on the residual stress distribution and the critical crack size

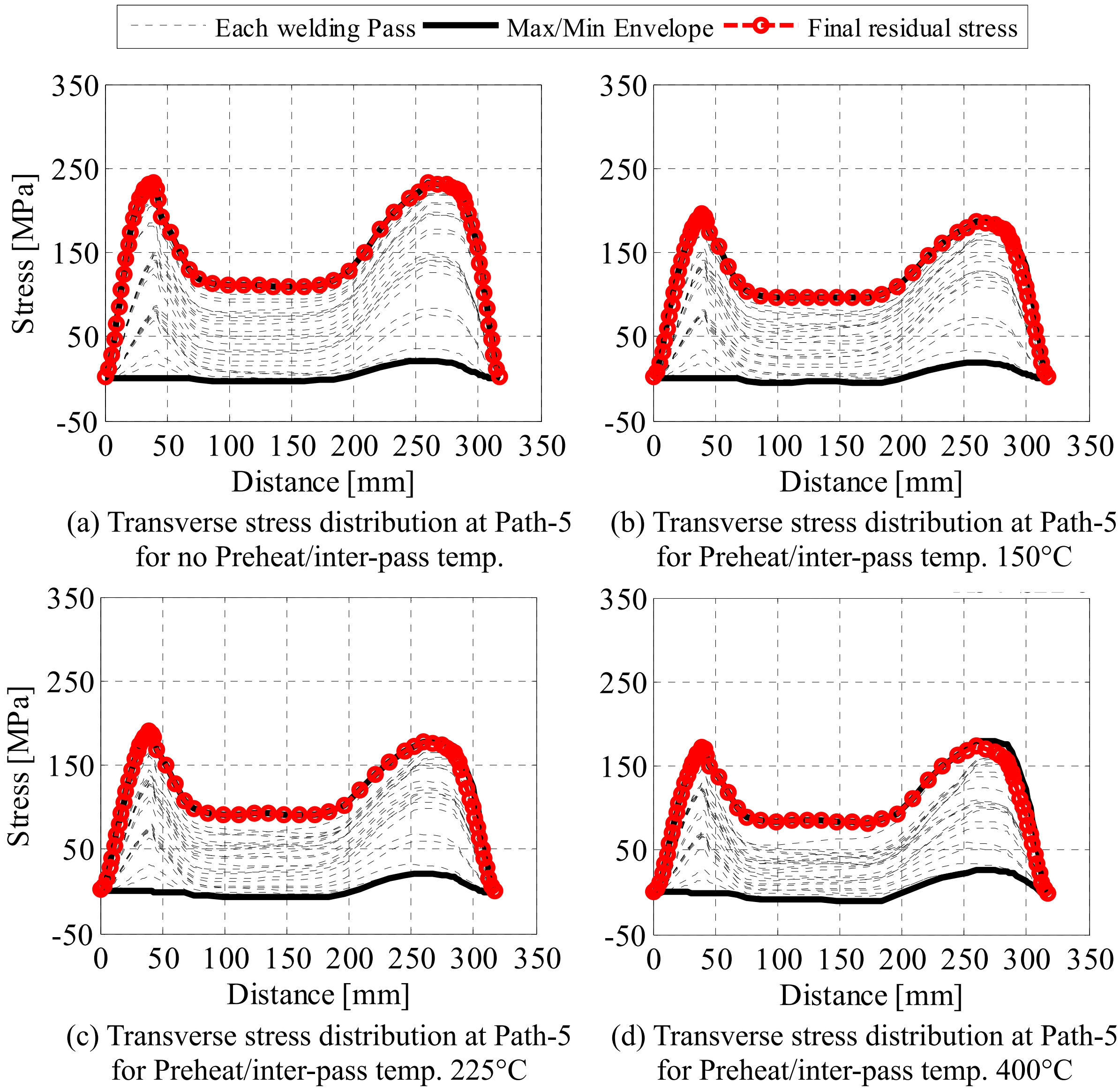

(a) Transverse stress distribution at Path-5 for no Preheat/inter-pass temp.

(b) Transverse stress distribution at Path-5 for Preheat/inter-pass temp. 150°C

(c) Transverse stress distribution at Path-5 for Preheat/inter-pass temp. 225°C

(d) Transverse stress distribution at Path-5 for Preheat/inter-pass temp. 400°C

Figure 5.8: Effect of the preheat/inter-pass temperature on the residual stress distribution.

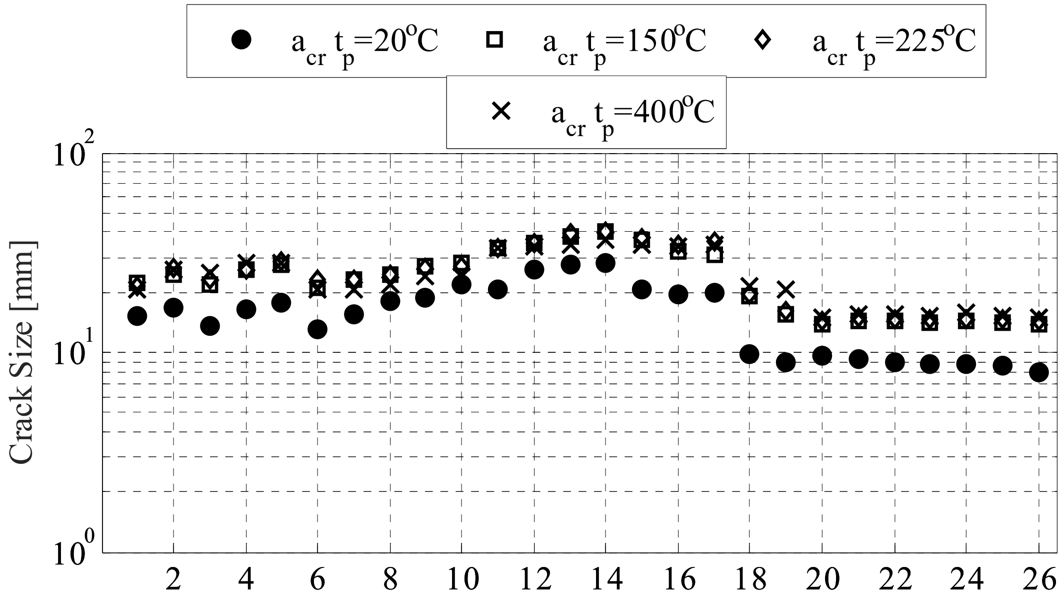

(a) Critical crack size for transverse crack at 5% probability of crack propagation

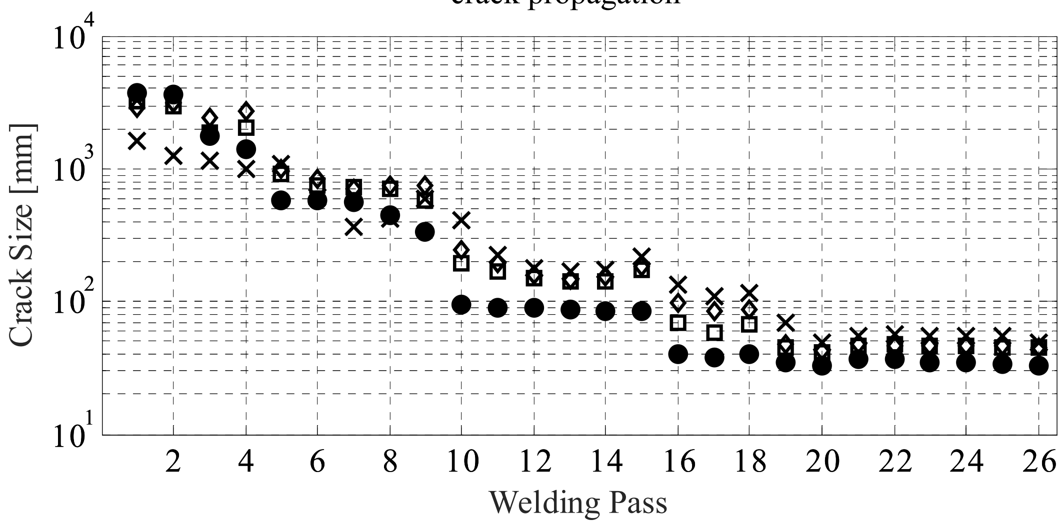

(b) Critical crack size for longitudinal crack at 5% probability of crack propagation

Figure 5.9: Effect of the preheat/inter-pass temperature on the critical crack size at 5% probability of crack initiation**.**

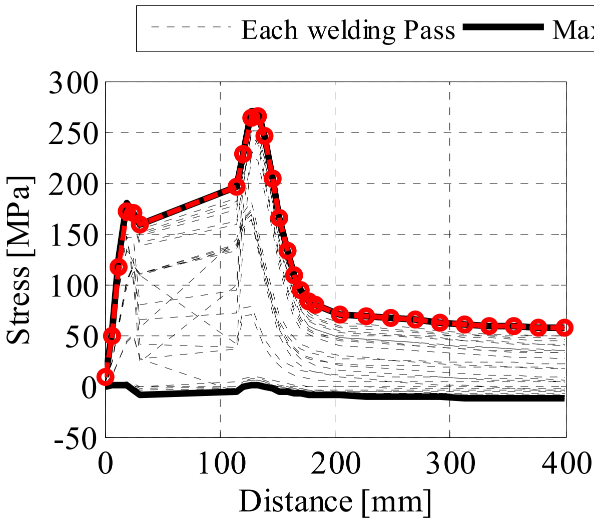

(a) Transverse stress distribution at Path-1 for lower bound material properties

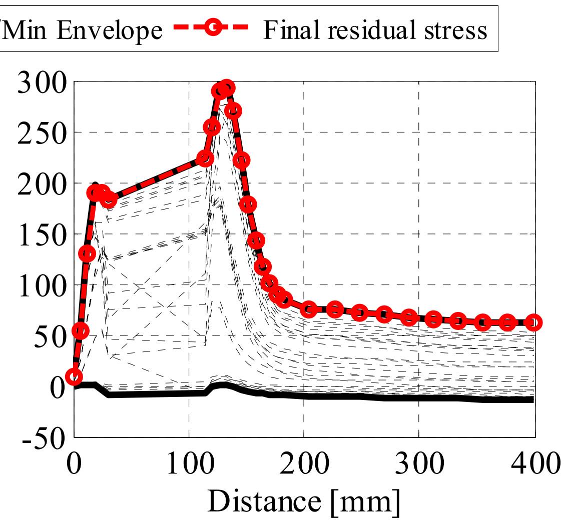

(b) Transverse stress distribution at Path-1 for upper bound material properties

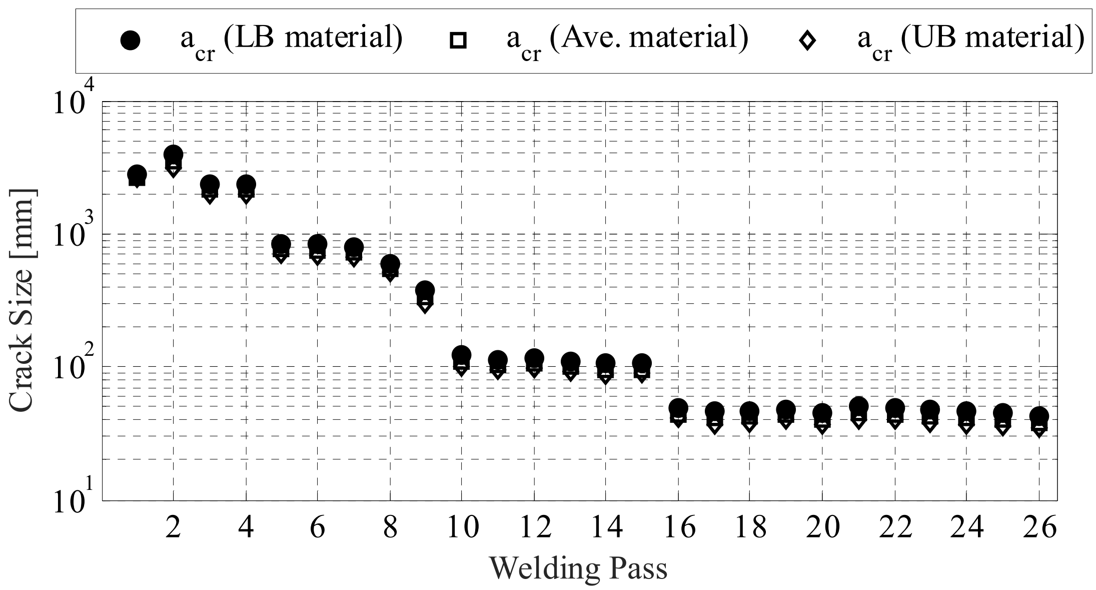

(c) Critical crack size for longitudinal crack at 5% probability of crack propagation

Figure 5.10: Effect of the base metal mechanical properties on residual stress distribution and the critical crack size.

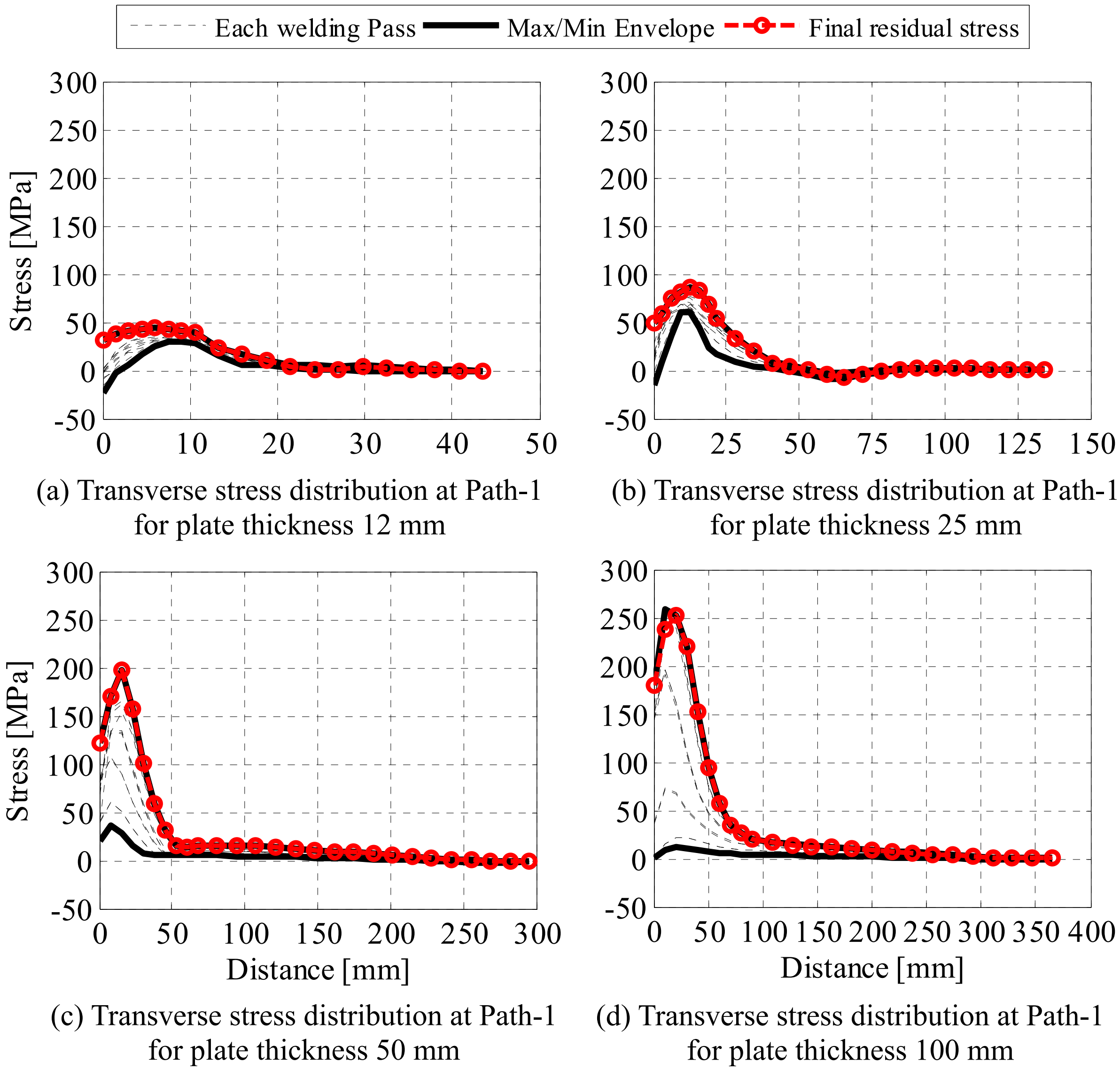

Figure 5.11: Effect of plate thickness on the transverse residual stress distribution due to welding.

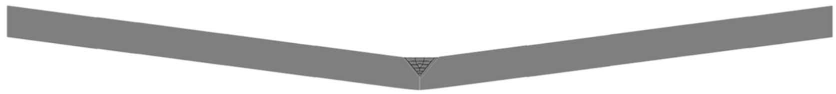

(a)

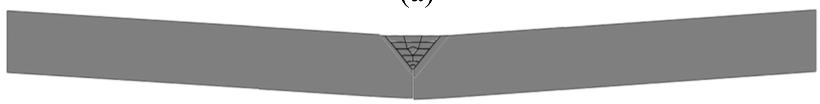

(b)

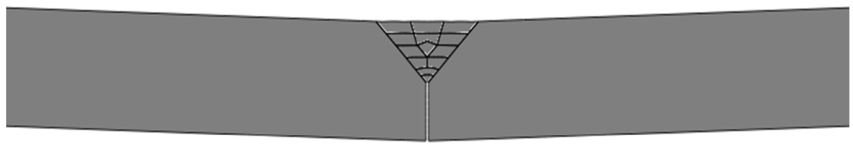

(c)

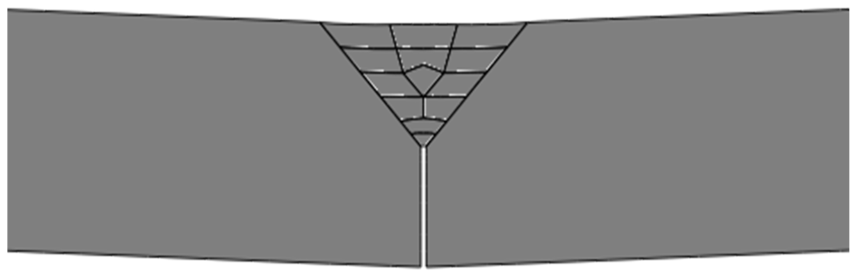

(d)

Figure 5.12: Residual deformations from the welding procedure for steel plates of thicknesses; a) 12mm, b) 25mm, c) 50mm, d) 100mm.

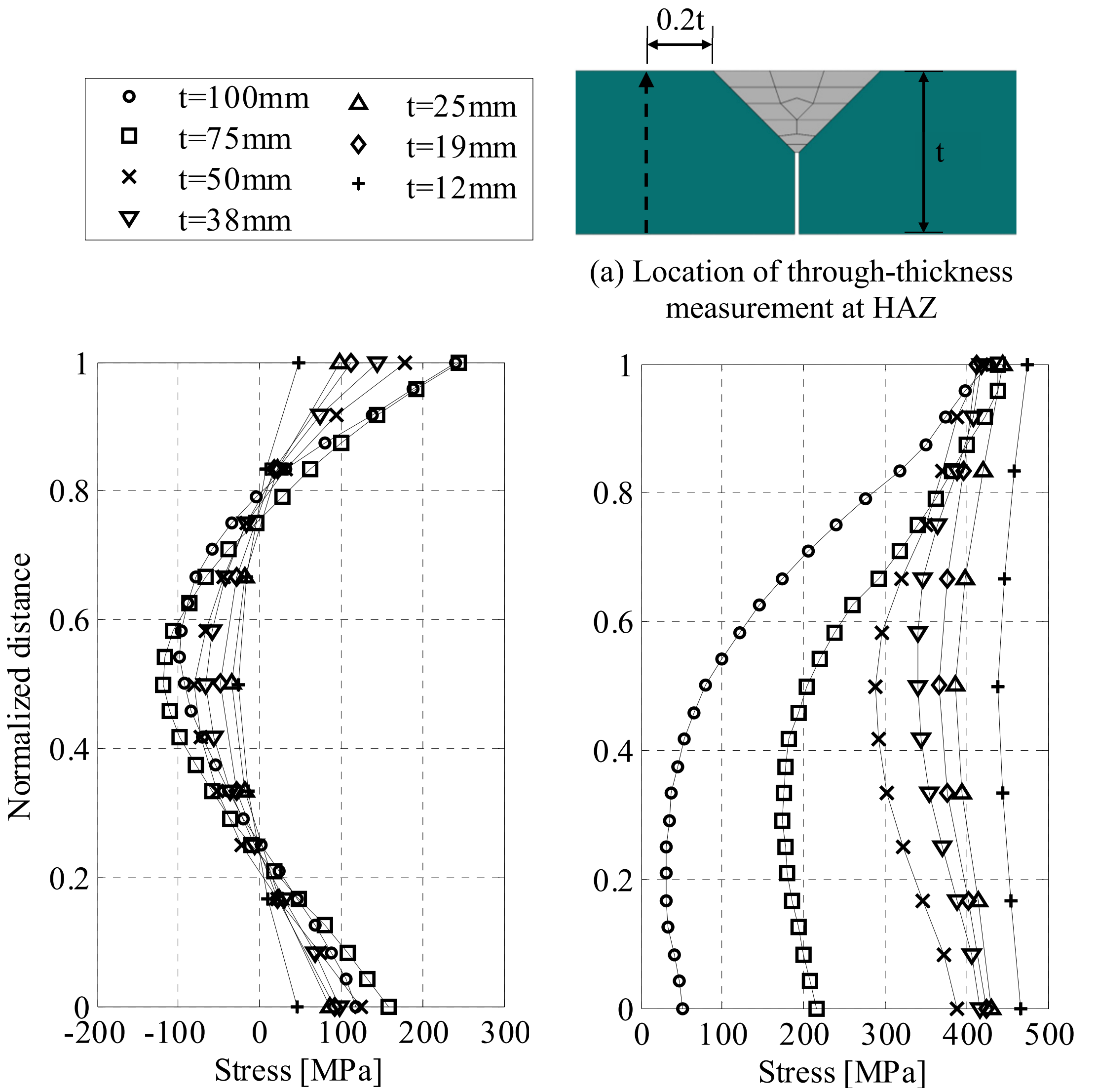

(a) Location of through-thickness measurement at HAZ

(b) Through-thickness residual transverse stress distribution at the HAZ

(c) Through-thickness residual longitudinal stress distribution at the HAZ

Figure 5.13: Transverse and longitudinal residual stresses through the plate thickness near the welding region for all plate thicknesses studied.

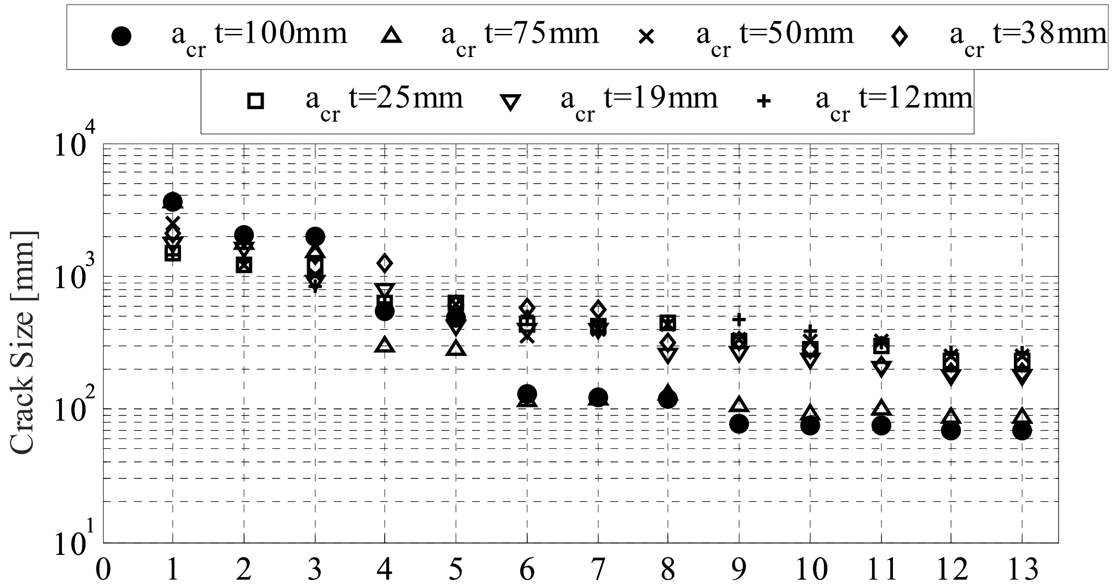

(a) Critical crack size for a longitudinal crack at 5% probability of crack propagation

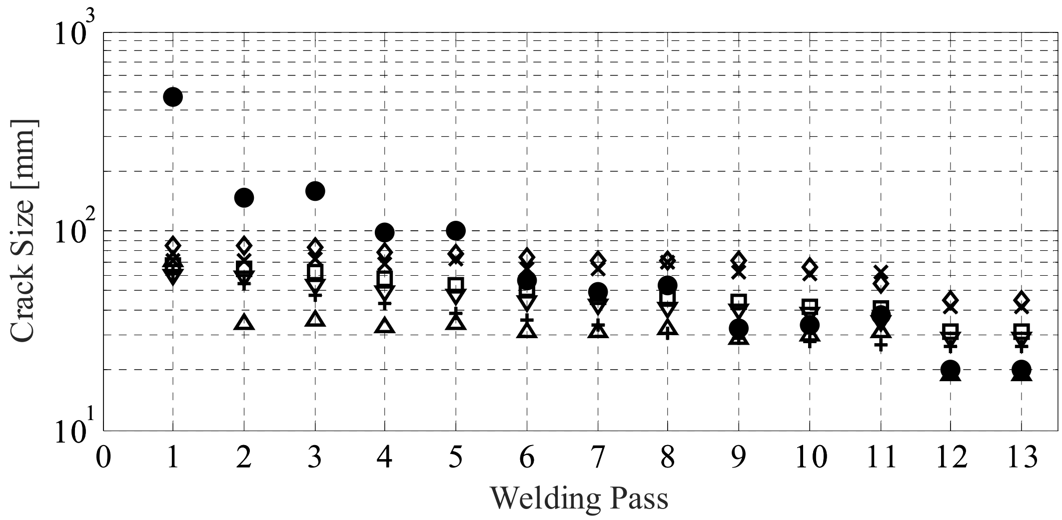

(b) Critical crack size for a transverse crack at 5% probability of crack propagation

Figure 5.14: Effect of plate thickness on the critical crack size at 5% probability of crack initiation.

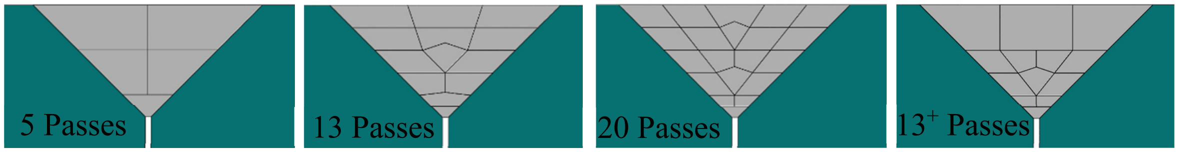

(a) Welding passes profiles for the four cases used in the study

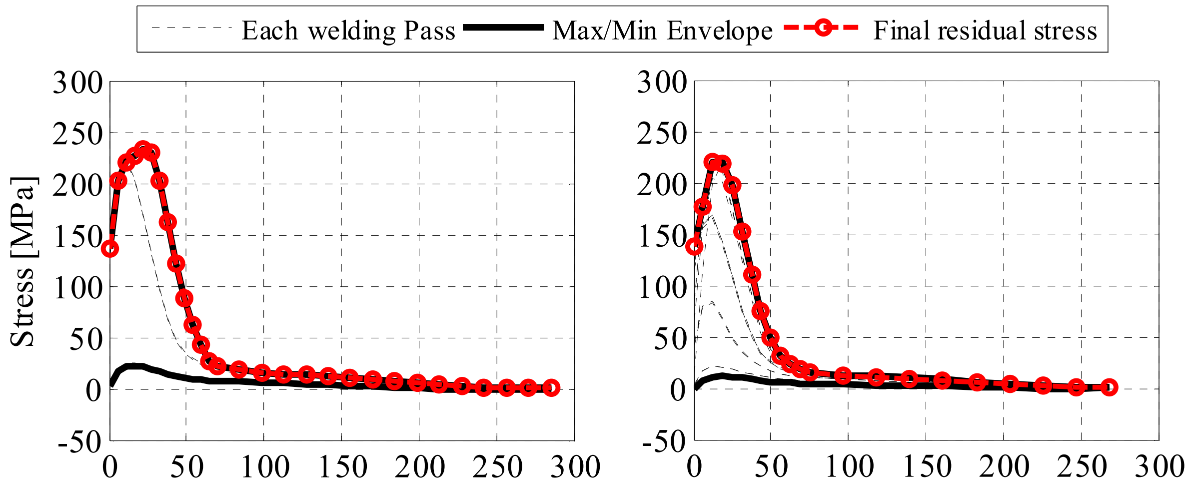

(b) Transverse stress distribution at Path-1 for 5 welding passes

(c) Transverse stress distribution at Path-1 for 13 welding passes

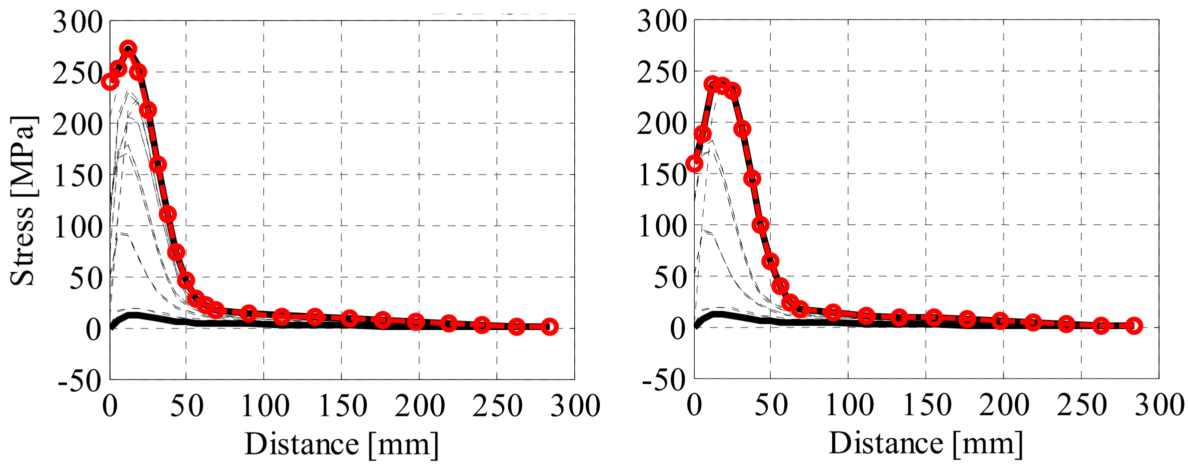

(d) Transverse stress distribution at Path-1 for 20 welding passes

(e) Transverse stress distribution at Path-1 for modified 13 welding passes

Figure 5.15: Effect of number of welding passes on the transverse residual stress.

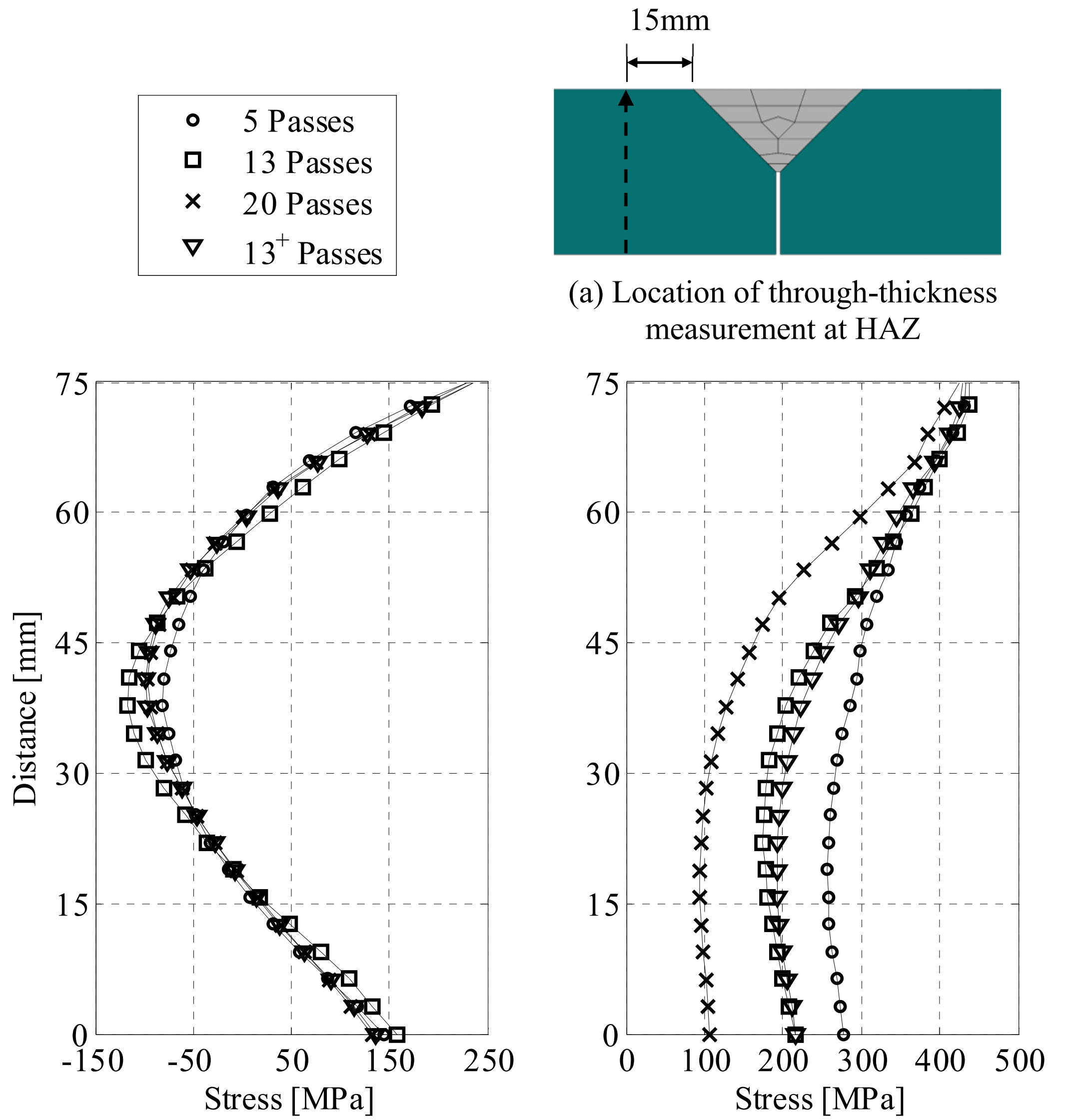

(a) Location of through-thickness measurement at HAZ

(b) Through-thickness residual transverse stress distribution at the HAZ

(c) Through-thickness residual longitudinal stress distribution at the HAZ

Figure 5.16: Transverse and longitudinal residual stresses through the plate thickness near the welding region for all cases of welding passes.

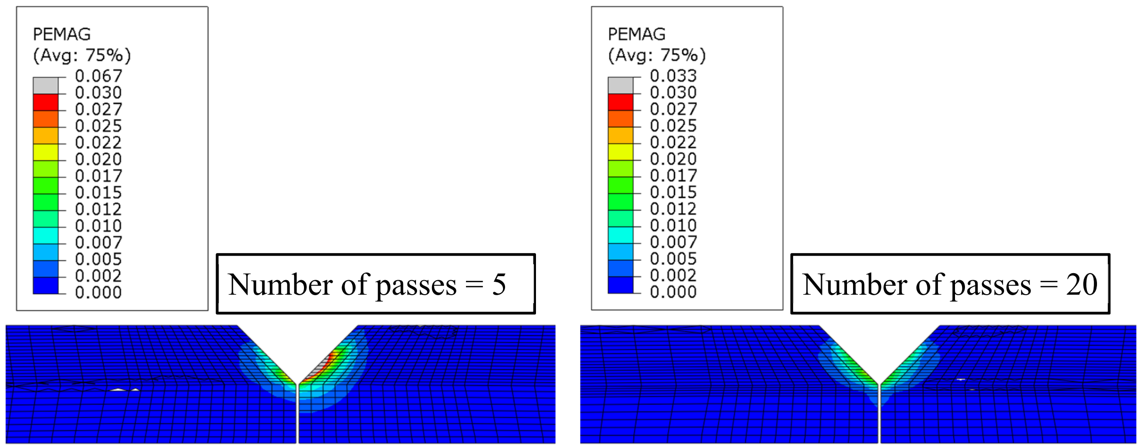

Figure 5.17: Transverse plastic strains after completion of half the welding procedure for the 5 and 20 welding passes cases.

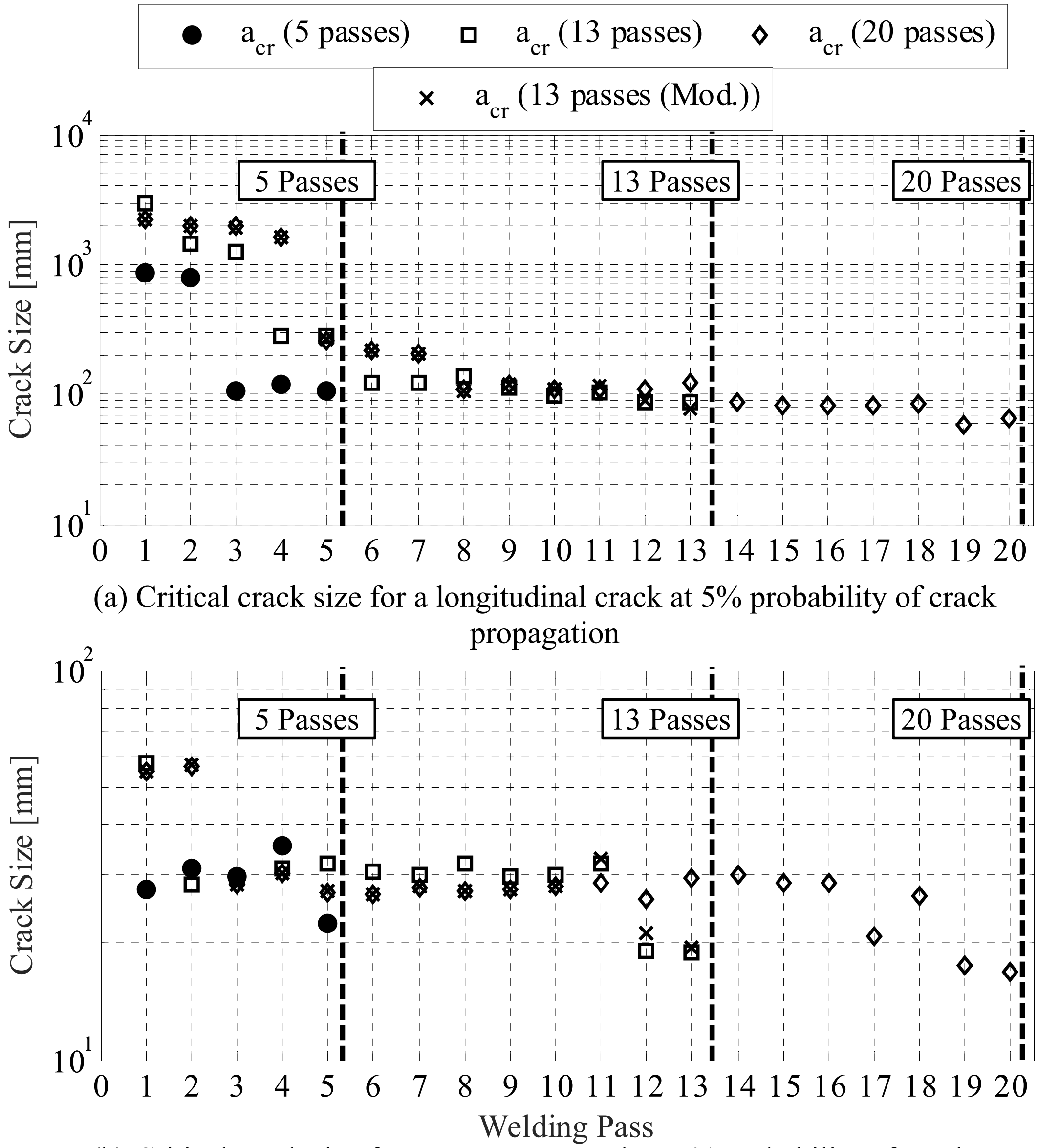

(a) Critical crack size for a longitudinal crack at 5% probability of crack propagation

(b) Critical crack size for a transverse crack at 5% probability of crack propagation

Figure 5.18: Effect of the number of welding passes on the critical crack size at 5% probability of crack initiation.

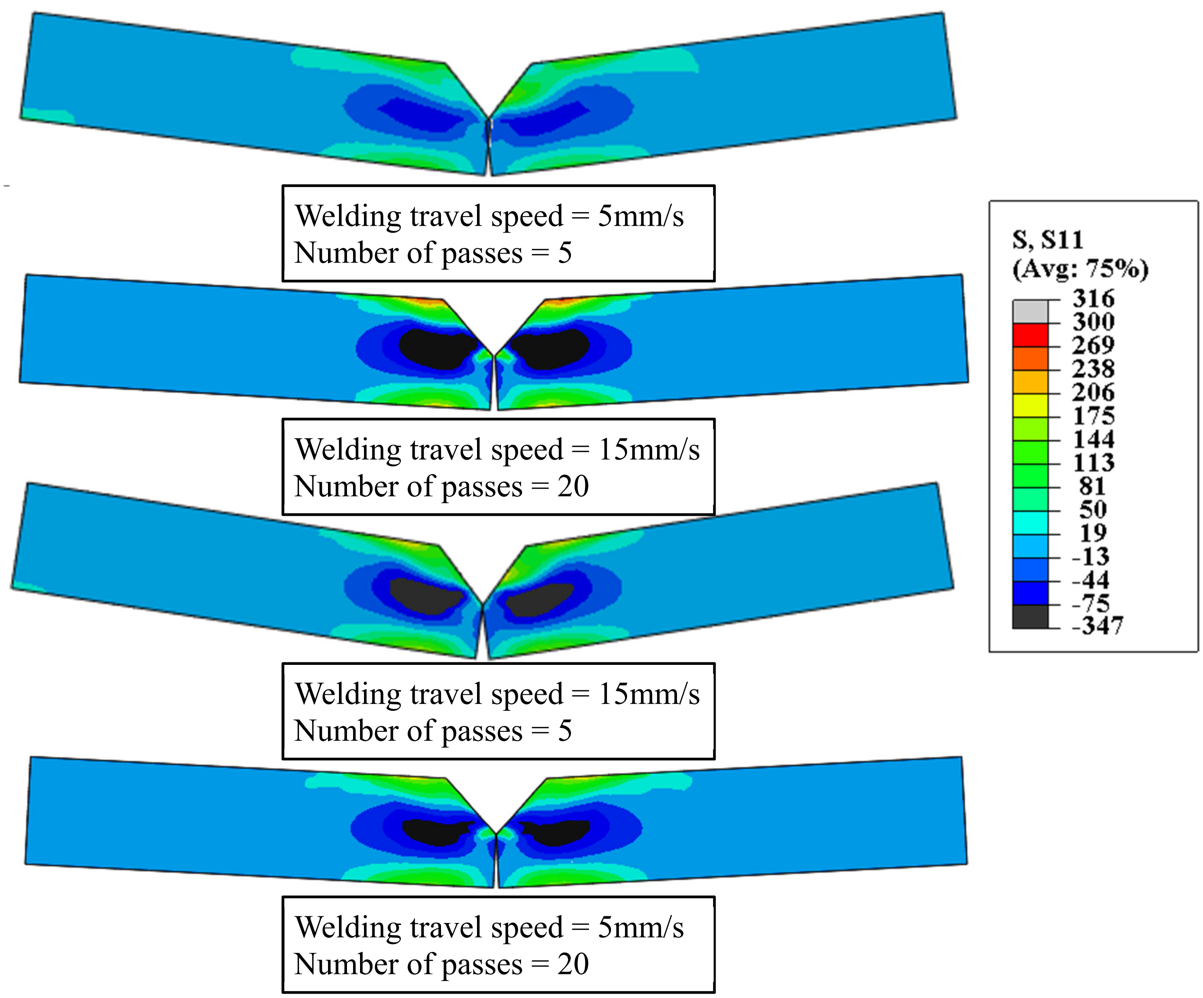

Figure 5.19: Residual transverse stress distribution and deformation (Scale factor = 5) for the four recommended welding procedures.

Chapter 6 EXPERIMENTAL INVESTIGATION OF THE EFFECT OF WELDING PROCEDURE SPECIFICATIONS FOR THICK STEEL PLATES

6.1 Introduction

Steel structures built today are required to withstand loads arising from blasts and large earthquakes, which amplify the demands to the steel structure compared to what was considered in past decades. As a result, the use of heavy steel components has become a common practice in steel construction to address these requirements; for example, heavy built-up box columns comprised of thick steel plates and heavy W-shapes are used in high rise buildings and have been recently used in the new World Trade Center building. Welded assemblies are often associated with these heavy components; such as column splices and welds in heavy built-up sections. As the thickness of welded components becomes greater, the likelihood of crack initiation in the base metal increases due to the restraint and residual stresses developed in thick plates, which are higher than those found in common 25 mm thick steel. Prequalified welding procedure specifications (WPSs) are available in current welding standards (AWS D1.1 (2010) and CAN/CSA-W59 (2013)) and can be used by fabricators for the welding of a wide range of steel assemblies. These procedures have been tested to ensure the quality of the resulting weld and the effect of the welding procedure on the surrounding base metal. If the fabricator uses a prequalified WPS he is only required to conduct non-destructive tests (NDT) to assess any resulting weld defects; whereas, if the fabricator chooses to use a welding procedure other than prequalified WPSs, this procedure has to undergo and pass qualification tests available in the welding specifications (AWS D1.1, 2010, CAN/CSA-W59, 2013). The WPSs include the permissible base metal steel grade, electrode, welding process, joint preparation geometry, base metal thickness, root opening size (for groove welds), electrode position, weld size, minimum preheat/inter-pass temperatures and tolerances. According to current welding standards (AWS D1.1 (2010) and CAN/CSA-W59 (2013)) most of the prequalified WPSs for the submerged arc welding (SAW) process are allowed to be used for plates of large thicknesses; for example, joint "B-P3-S" in AWS D1.1 [1] is a prequalified WPS where the minimum base metal plate thickness is specified as 20mm, while no maximum limit is stated. However, based on feedback from the steel industry these prequalification tests, upon which the existing WPSs were written, were conducted on steel plates no thicker than 25mm. As the demand increases for thick steel plates (i.e., thicker than 50mm) in steel buildings fabricators have been using available prequalified WPSs. In certain cases unrepairable cracks have been observed (Fisher and Pense, 1987, Blodgett and Miller, 1993). Therefore, qualification tests for welding procedures of thick plates should be conducted and developed accordingly.

Welding procedure parameters have great influence on the quality of the produced weld, as well as the heat affected zone (HAZ) of the base metal. Lee et al. (2000) performed twenty-three weld experiments to study the effect of submerged arc welding parameters on the size of the HAZ of a 38mm thick ASTM A36 (2014) steel plate. It was found that the current has the greatest effect on the HAZ size, such that a higher current results in a smaller HAZ. On the other hand, the welding voltage and electrode diameter had no significant effect on the HAZ size. In another study Yang (2008) conducted twelve welding experiments using the SAW process on ASTM A709 (2013) Grade 50 17mm thick steel plates used in wind turbines. The objective of these experiments was to study the effect of the current and the electrode travel speed on the physical and mechanical properties of the base metal. It was concluded that high electrode travel speed and current result in severe undercuts. Low heat input, achieved by low current and high travel speed, caused a lack of penetration. The toughness of the HAZ improved with an increase in the travel speed and current. Yang (2008) recommended using a moderate current of 800A and a relatively high electrode travel speed of 12.3mm/s to achieve good weld quality and productivity, as well as high HAZ fracture toughness. These studies by Lee et al. and Yang demonstrate the importance of performing material tests of welded assemblies in order to establish appropriate weld protocols. As such, experimental investigation of the effect of using different welding procedure specifications for thick steel plates, i.e. greater than 25 mm, on the weld quality and the HAZ is warranted given that relevant laboratory work has yet to be completed.

The study described herein comprises an experimental investigation of the effects of different aspects of the welding procedure on the weld quality and the material properties of the HAZ of thick steel plates. Five fully automated SAW partial joint penetration welding procedures to join two 75mm thick ASTM A572 grade 50 [8] steel plates were performed. These procedures comprised different heat input, electrode travel speed, wire feed speed and number of passes, as well as the number, size and type of electrode. Mechanical tests were then conducted for samples taken from various locations within the plates and welds. Material phase changes were identified at the HAZ using optical microscopy and micro-hardness testing. A comparison between the results of the conducted tests for the studied welding procedures is presented and recommendations are suggested for the submerged arc welding procedures for thick steel plates.

6.2 Description of the Welding Procedures Experiments

The experimental investigation of the welding procedure specifications for the SAW process included the welding of two 7000x324x75mm ASTM A572 Gr.50 (2013) grade 50 steel plates. The specified mechanical properties and chemical composition of the base metal are shown in Table 6.1. The length of the plates was divided into five segments of 1000mm each, separated by 500mm as illustrated in Figure 6.1. As such, the tested area for each welding procedure was not influenced by the welding that occurred in the neighboring segments. Each segment was welded using a welding procedure (Section 6.2.1) that was selected based on recommendations from the steel industry. For the assessment of the weld quality, specimens were extracted from the weld metal and base metal to conduct mechanical tests, as well as to carry out a visual and microscopic inspection. A discussion of the test results for each weld segment is provided in Section 6.2.2.

6.2.1 Welding procedures specifications

Five welding procedures, as recommended by industry welding engineers and steel fabricators, were utilized in this experimental program; noted as A, B, C, D and E. The WPSs varied in terms of current, number of electrodes, size of electrodes, number of passes, welding wire feed speed, electrode travel speed and heat input, and the voltage was selected according to the current (Table 6.2). Welding procedures A, B, C and D utilized solid core electrodes of diameter 2.4mm and type F7A4-EM12K (AWS A5.17/5.17M (1997 (R2007))) with suitable granular flux type (OK FLUX 10.71), while welding procedure E used metal core electrodes of diameter 3.2mm and type F7A6-EC1-H8 (AWS A5.17/5.17M (1997 (R2007))) with suitable granular flux type (Oerlikon OP139); to comply with using a high current of 1000A according to specifications (AWS D1.1, 2010, CAN/CSA-W59, 2013). The nominal mechanical properties and typical chemical composition of the electrodes are also shown in Table 6.1; the electrodes used in the experiment were tested by the providing company and they meet the requirements of the welding specifications. The welding assembly shown in Figure 6.1 is a double V groove partial joint penetration (PJP) of depth 19mm and groove angle of 60^0. A preheat/inter-pass temperature of 110^oC was maintained during all welding procedures according to AWS D1.1 (2010) and CAN/CSA-W59 (2013).

Welding procedure A is considered the common procedure used for submerged arc welding of thick plates as suggested in current welding specifications (AWS D1.1, 2010, CAN/CSA-W59, 2013). This procedure entails parallel electrode welding (Figure 6.2a), i.e. the two electrodes are both fed with a DC+ current. The procedure has a moderate average heat input of 2.4KJ/mm for eight passes on Side 1 and seven passes on Side 2, as shown in Figure 6.3. Welding procedure B comprises a low heat input compared to the common procedure by using only one electrode with DC+ current and small weld bead sizes (Figure 6.2b). The average heat input is 1.19KJ/mm for seventeen passes on Side 1 and fifteen passes on Side 2, as shown in Figure 6.3. Welding procedure C is similar to A, however the average heat input is increased to 3KJ/mm, through increasing the average current and wire feeding speed. The number of passes for Side 1 and Side 2 is six each, as shown in Figure 6.3. For the welding procedure D the average heat input is kept at moderate levels of 4KJ/mm while the weld bead size is increased. This is achieved by utilizing the SAW tandem arc welding procedure (Miller, 2006). Four electrodes are used (Figure 6.2c), such that the arc is controlled for each pair of electrodes separately. The number of passes for Side 1 and Side 2 is four passes each as shown in Figure 6.3. Furthermore, a high electrode travel speed compared to the common welding procedure A was implemented. In summary, the welding procedure D is characterized by having high weld metal deposition and low heat input, which consequently results in high productivity. The last welding procedure, E, has the highest average heat input of 8.6KJ/mm and the lowest number of passes of three on Side 1 and two on Side 2 (Figure 6.3). This procedure also utilizes four electrodes, as did welding procedure D, but of greater diameter and with a metal core that hence produced a larger deposition rate (Figure 6.2d). In addition, welding procedure E uses a high average current. It is worth mentioning that a lower heat input and higher electrode travel speed, of 6.8KJ/mm and 9mm/s respectively, was utilized for the first pass on Side 2 of this welding procedure, compared with that for Side 1 (8.6KJ/mm and 7mm/s, respectively). Furthermore, a small third welding pass was added to Side 1 of welding procedure E using only two electrodes of DC+ SAW to complete the weld profile, as illustrated in Figure 6.3. In this case, a slower wire feed speed of 230cm/s and faster electrode travel speed than for the previous passes were required.

6.2.2 Material testing program

After the completion of the welding procedures, specimens were extracted and then machined to size in order to measure the material properties and to establish a link between the welding procedure specifications, the weld quality and the fracture toughness of the HAZ. The weld quality and HAZ assessment tests were based on the qualifying tests of the welding procedure specifications as described in AWS D1.1 (2010) and CAN/CSA-W59 (2013). These tests include; side bend test, reduced section tension test, all-weld metal tension test, Charpy-V-Notch impact test and visual inspection as well as inspection by means of optical microscopy. Additional micro-hardness tests were conducted to convey the welding procedure effects on the size and hardness of the HAZ. The specimens were extracted from each welding procedure test region (Figure 6.1) and the results were compared with one another and with the requirements of the current welding specifications (AWS D1.1, 2010, CAN/CSA-W59, 2013).

A total of forty side-bend tests were conducted; four at each side for each welding procedure. The side bend test specimens (10x15x150mm) were extracted from a position perpendicular to the welding direction such that their centerline coincided with the weld centerline, as illustrated in Figure 6.4a and Figure 6.5. In these tests the specimens were bent to a U-shape, using a three point loading system, at which the load is applied using a “Simplex” hydraulic steel cylinder with a capacity of 150KN. The convex side of the bent specimen was visually inspected for discontinuities. The AWS D1.1 (2010) and CAN/CSA-W59 (2013) specify that discontinuities greater than 1mm are not acceptable. Moreover, if the sum of the discontinuities between 1mm and 3mm in size is greater than 10mm then the specimen will be rejected. A corner crack of 6mm is acceptable as long as it is not a result of a fusion defect such as slag inclusion.

A total of twenty reduced section tension tests were conducted (two at each side per welding procedure). The reduced section specimens are of length 120mm, gauge length 50mm and reduce area of 20x5mm. The tension tests were conducted using 150 KN Sintech MTS machine, which was connected to Vishay Model 5100B scanners that were used to record data using the Vishay

System 5000 StrainSmart software. The specimens were cut in a position perpendicular to the welding direction such that the weld metal is at the centre of the specimen as illustrated in Figure 6.4b and Figure 6.5. The engineering strain was measured during the test through an extensometer of a 25mm gauge length. One specimen from each side (total of 10 specimens) was equipped with 5mm strain gauges to accurately measure the Young's modulus. According to AWS D1.1 (2010) and CAN/CSA-W59 (2013) a specimen is considered acceptable if its tensile strength is not less than the minimum specified tensile range of the base metal used in the test.

Although the all-weld metal tension tests are not required for qualifying welding procedures utilizing the SAW process, this test was conducted for each welding procedure to assess the mechanical properties of the weld metal. Ten all-weld metal tension tests were performed (one at each side per welding procedure). The all-weld metal specimens are round and of length 120mm, gauge length 45mm and gauge diameter 12.5mm. This test was also conducted using a 150 KN Sintech MTS machine connected to Vishay Model 5100B scanners. Specimens were cut in a position parallel to the welding direction such that each coupon comprised only material of the weld metal, as shown in Figure 6.4c and Figure 6.5. Similar to the reduced section tension test the engineering strain was measured by an extensometer of a 25mm gauge length. According to ASTM A370 (2014) the results of this test must conform with the minimum properties specified for the weld metal (AWS D1.1, 2010) (Table 6.1).

Charpy-V-Notch (CVN) impact tests were conducted to assess the fracture toughness of the weld metal, as well as the HAZ, and to insure they meet the acceptance limits of the CAN/CSA-W59 (2013) and AWS D1.1 (2010) welding specifications. The tests were conducted using a TINIUS OLSEN impact tester Model 64 with a capacity of 256J. Another fifty CVN specimens were extracted such that the centerline of the notch is at 5mm from the edge of the weld in the direction of the base metal, as illustrated in Figure 6.4e and Figure 6.5. In order to develop the CVN-temperature relationship for weld metal, the CVN specimens for each welding procedure were divided into five sets of two such that each set is test at a different temperature. The same testing procedure was also conducted for the CVN specimens of the HAZ. The test temperatures used were -50, -25, 0, 20 and 60^{o}C.

Finally, for the visual inspection, microscopy and micro-hardness tests, three 100x25x20mm specimens from each side for each welding procedure were cut in a position perpendicular to the welding direction with the weld metal at the centerline of the specimen, as shown in Figure 6.4f and Figure 6.5. The surface of each specimen was polished and etched in a solution of 4% Nital. Figure 6.6 shows photographs of a sample specimen for each weld procedure after polishing and etching; such that the base metal HAZ and welding passes for each welding procedure are clearly identified. Specimens were assessed with a Nikon Epiphot 200 inverted metallurgical microscope with Clemex image analysis software to detect any weld defect at the weld area, fusion line, fusion lines between weld passes and HAZ. One specimen from each welding procedure was used for Vickers micro-hardness testing (ASTM E384-11e1, 2011). Clark CM-100AT manual micro-hardness tester equipped with a Vickers indenter. Measurements were taken using Clemex digital camera and software at x500 magnification. The readings were taken from a clear focused optical image. The hardness was measured based on indentation sizes of 500gf loading. Measurements were taken at small increments along a 20mm straight line that passes through the base metal, HAZ and weld metal, at 12mm from the weld surface as shown in Figure 6.7a. The indent diamond shape is shown in Figure 6.7b at 500x magnification. The micro-hardness tests were conducted in order to capture the change in hardness for the five welding procedures included in this experiment. The HAZ is expected to have higher hardness than other zones in the base metal due to the heat treatment that results in changes of the crystalline structure of steel to smaller grain sizes. Hence, the size of the HAZ can be measured through the micro-hardness test for each welding procedure.

6.3 Results and Discussion of Material Testing

6.3.1 Side bend tests

All side bend specimens were visually inspected for surface cracks. For welding procedure A two out of 8 specimens had surface cracks in the weld metal that exceeded in length the acceptance criteria for AWS D1.1 (2010) and CAN/CSA-W59 (2013). Also for welding procedure E, one specimen out of 8 exhibited a crack at the fusion line between the weld and base metal, however the crack size was less than 6mm and is considered acceptable by current specifications (AWS D1.1, 2010, CAN/CSA-W59, 2013). Figure 6.8 shows the specimens for welding procedures A and E in which cracks were observed. The welding specifications only require the completion of four side bend tests for the qualification procedure; and in case of a failed test, retests are allowed. Therefore in this case, where more than four side bend tests have passed for welding procedures A and E, according to welding specifications (AWS D1.1, 2010, CAN/CSA-W59, 2013) these welding procedure are considered to have passed the side bend test requirements. All other side bend specimens for the remaining welding procedures had no surface cracks, and as such are considered acceptable by the current weld specification criteria.

6.3.2 Reduced section tension tests

The reduced section tension specimens, which comprise the weld metal as well as the base metal, were obtained in a transverse position to the weld direction; therefore, the resulting stress-strain relationship is representative of the connection as whole, not the individual weld or base metal. A summary of the results for each welding procedure is presented in Table 6.3. The Young's modulus (E), the yield stress (f_y) and the yield strain of specimens 1 and 2 for each welding procedure were based on strain gauge (5mm gauge length) readings, while all the remaining results were based on extensometer (25mm gauge length) readings. Consequently, the tabulated values of specimens 1 and 2 in the elastic zone represent the weld metal that is located at the centre of the specimen, while specimens 3 and 4 represent that of a composite material comprising the weld metal, HAZ and base metal which results in higher elastic modulus. These E values are less accurate due to larger gauge length than specimens 1 and 2, as well as the reduced accuracy and potential slip of the extensometer. Figure 6.8b shows a sample of tested reduced section specimens from each welding procedure; the fracture of all specimens was located at the centre in the weld metal. Figure 6.9 shows the graphical representation of the engineering stress-strain curves based on the reduced section specimens shown in Figure 6.8b. It can be concluded from the results that all specimens passed the AWS and CSA (AWS D1.1, 2010, CAN/CSA-W59, 2013) specifications' requirement of having a tensile strength greater than the base metal nominal strength. Also, specimens from the welding procedure B exhibited the highest yield stress amongst the five welding procedures (Table 6.3). This is attributed to the large number of heating and cooling cycles at the welding area for this welding procedure, which hardened the steel material and increased its yield stress similar to what occurs with a quenching steel process. There was no significant difference in material yield and ultimate stress between the results of the other welding procedures.

6.3.3 All-weld metal tension tests

The all-weld metal tension test results provided the mechanical properties of the weld metal in the longitudinal direction. A sample of the all-weld metal specimens after fracture for each welding procedure is shown in Figure 6.8c; such that the fracture occurred within the gauge length of the extensometer for all specimens. A summary of the results is provided in Table 6.4; where the Young's modulus values are calculated based on the extensometer readings which resulted in higher values than that what is expected of a steel material ($2x10^5$MPa) for most specimens, this is attributed to the large gauge length as well as slipping of the extensometer during the tension test. Furthermore, graphical representations of the engineering stress-strain curves based on these specimens is shown in Figure 6.10. All specimens have met the requirements of the specifications (AWS D1.1, 2010, CAN/CSA-W59, 2013) (Table 6.1), except one specimen from the welding procedure C that did not meet the minimum elongation requirement of 0.22. This specimen experienced early brittle fracture at 0.172 strain, which occurred due to a weld defect, most likely a slag inclusion. Moreover, similar to the reduced section test results, the all-weld metal specimens from the welding procedure B had the highest yield stress due to the large number of heating and cooling cycles. Through the comparison of the results of the other four welding procedures there was no significant difference for the weld metal mechanical properties (Table 6.4).

6.3.4 Charpy-V-Notch tests

Charpy impact tests were performed for the weld metal material as well as the HAZ of the base metal. The upper and lower shelf CVN values of the weld metal and HAZ material are represented by the testing temperatures -50ºC and 60ºC respectively. The CVN absorbed energy results are shown in Table 6.5 for all welding procedures. There was no significant difference between the average lower shelf CVN values for the weld metal material of the five welding procedures, which was measured to be 13J. The average upper shelf CVN values of the weld metal for welding procedures B, A, C, D and E are 122, 111, 103, 116 and 107J. The results are found dependent on the heat input, number of passes and current; if welding procedures B, A, and C (utilizing only DC+ current) and welding procedures D and E (utilizing tandem arc welding with DC+ as well as AC current) are assessed separately as shown in Figures 6.11a, 6.11b and 6.11d. It can be concluded that using tandem arc welding with DC+ and AC results in higher upper shelf CVN value. Additionally, the weld metal upper shelf fracture toughness is inversely proportional to the heat input, current and the weld bead size (directly proportional to the number of passes). This is attributed to the cooling mechanism of a welding pass. Once a weld bead is deposited, the outer surface cools first, while the centre portion is the last to cool, resulting in tension stresses at the centre of the bead. As the size of the weld bead or the heat input and current associated with the pass increases the outer layers of the weld bead solidify faster than the inner layers, which leads to weak bond between these layers.

For the HAZ material the average lower shelf CVN values are similar for all welding procedures (13J). However, the average lower shelf CVN values for the base metal material, i.e. 31J, were unaffected by the welding procedure, based on CVN tests conducted for 75mm plates of the same material and from the same mill (Section 3.3.1.2) (Ibrahim et al., 2015). In conclusion, by comparing the CVN values of the HAZ to that of the base metal, the welding procedure results in a reduction of the material lower shelf CVN value from 31J to 13J. For upper shelf temperatures the average CVN values for the welding procedures B, A and C are 137, 127 and 122, respectively; while for welding procedures D and E 130J and 119J, respectively, were obtained. Similar to that observed for the weld metal CVN values, using tandem arc welding with DC+ and AC currents (welding procedure D and E) resulted in higher upper shelf CVN values in the HAZ compared with the welding procedure comprising DC+ alone. Despite the higher heat input utilized in welding procedure D compared with C, it produced higher CVN values in the HAZ. CVN results of both types of welding (DC and tandem arc welding) are dependent on the heat input, number of passes and current (Figures 6.11a, 6.11b and 6.11d). Moreover, by neglecting the heat input produced by the AC electrode of procedures D and E; such that the heat input becomes 2 and 4.3KJ/mm respectively, the upper shelf CVN value is found mainly dependent on the DC+ electrodes heat input as shown in Figure 6.11e. Furthermore, the average upper shelf CVN value for the base metal material, i.e. 135J, was unaffected by the welding procedure (Ibrahim et al., 2015). Welding procedures E and C (highest DC+ heat input) resulted in a reduction of the CVN value from 135J to 120J, while the other procedures had no significant effect on the CVN upper shelf value of the base metal.

The 17mm thick steel plates used in the weld experiments by Yang (2008) showed that the fracture toughness of the HAZ mainly depends on the electrode travel speed and current. Which is not the case for thick steel as shown in Figure 6.11c; the electrode travel speed had no clear correlation in the CVN values of the HAZ and the weld metal. Also welding procedures A and C had the same electrode travel speed and there was no significant change in the HAZ CVN value. However, the welding heat input incorporates the current as well as the electrode travel speed in its value. As such, it can be suggested that the toughness of the weld metal and HAZ for the 17mm thick steel plates tested by Yang are also dependent on the heat input. Moreover, all CVN values at 0°C and 21°C have achieved the AWS and CSA specifications' minimum value of 27J.

6.3.5 Visual inspection and microscopy

All specimens extracted around the weld area for each welding procedure were polished and visually inspected for defects. They were also etched and then scanned with a Nikon Epiphot 200 inverted metallurgical microscope with Clemex image analysis software to detect small defects such as porosity and slag inclusions at magnification up to 1000x. Through visual inspection, solidification cracks were detected for three specimens of welding procedure A at the first welding pass as shown in Figure 6.12a. This is attributed to the shape of the weld bead that is deep and narrow such that the solidifying grains intersect in the centre of the weld without complete fusion (Miller, 2006). Moreover, as a result of the large weld bead size for procedure E it can be seen in Figure 6.12b that an incomplete penetration took place in three specimens. These specimens were extracted from the side of the steel plate that was welded using three passes. Incomplete penetration was avoided on the other side of the plate due to the use of a lower heat input and faster electrode travel speed (Figure 6.6). No defects were detected for specimens from the other welding procedures through visual inspection. Additionally, no porosity or slag inclusion defects were observed after thoroughly examining each specimen with an optical microscope. Figure 6.13 presents captures taken by the optical microscope at 50x magnification for the weld metal – base metal fusion area for each welding procedure. Accordingly, it can be seen that for welding procedure B the transition from the HAZ to the larger grain sizes of the base metal happened at a smaller distance than the other welding procedures and the size of its HAZ is the smallest. This is attributed to the low heat input and small weld bead size associated with welding procedure B that caused only a limited region in the base to experience temperatures higher than the 723°C. This corresponds to the temperature at which the steel crystalline structure changes; when cooled, it forms a Martensite crystalline structure that is characterized by small grain size (Jefferson and Woods, 1962, CWB/Gooderham-Centre, 2005).

6.3.6 Micro-hardness test

The Vickers micro-hardness test was conducted for specimens that were used for visual inspection and microscopy (Figure 6.7a), with the results for each welding procedure shown in Figure 6.14. The welding procedure had no significant effect on the hardness of the weld metal as shown in the micro-hardness test results in Figure 6.14. The heat treatment of steel is a well-known method to achieve improved hardness and strength; therefore, the HAZ in each specimen is expected to have higher hardness than areas away from the welding region. The start and end of the HAZ at the surface of the steel plates for each welding procedure was identified by detecting the change in the material hardness, as well as by visually identifying the change in the steel crystalline structure through an optical microscope. Consequently, the size of the resulting HAZs was calculated. The welding procedure B resulted in the smallest HAZ of 1.75mm, however it had the highest hardness value of 245HV; the reason for this is the large number of heating and cooling cycles in this procedure. Welding procedure E resulted in the largest HAZ size of 5.75mm. For welding procedures A, C and D the HAZ sizes were 2.25, 2.75 and 4.25mm, respectively. Figure 6.15 illustrates the effect of each of the heat input, the number of passes, the electrode travel speed and the current on the HAZ size. From Figure 6.15a, the increase in heat input and current caused an increase in the HAZ size. The HAZ size is also correlated with the number of welding passes as shown from Figure 6.15b; in particular, no correlation can be identified between the HAZ and the electrode travel speed. A direct correlation is also achieved by dividing the number of passes by the sum of the electrode diameters used in the welding process, as shown in Figure 6.15e. In conclusion, for thick steel plates the HAZ size is mainly dependent on the ratio between the sum of the electrode diameters and the number of welding passes such that the higher the ratio the greater the HAZ size for the same weld size. This is unlike the 38mm thick steel plates that were tested by Lee et al. (2000), where the HAZ size was found to be mainly dependent on the current. However, the electrode diameter had no effect on the HAZ size in the tests conducted by Lee et al. (2000).

6.4 Summary and Conclusions

The submerged arc welding of two 75mm thick ASTM A572 Gr.50 (2013) steel plates with partial joint penetration welds using five different procedures was performed in order to develop recommendations for heavy steel assemblies. The recommendations can be applied for the welding of plates used for heavy built-up sections, as well as heavy column splices. The different welding procedure specifications varied with respect to heat input, number of passes, current, number of electrodes, size and type of electrodes, welding wire feed speed and electrode travel speed. Materials test specimens were extracted for each welding procedure with the aim to assess the quality of the weld as well as the effect of the welding parameters on the fracture toughness, hardness and size of the heat affected zone. The following welding procedure qualifying tests were conducted; side bend test, reduced section tension test, all-weld metal tension test, Charpy-V-Notch test, visual inspection and microscopy. Additionally, micro-hardness tests across the heat affected zone for each welding procedure were completed. The main observations of the SAW experiments are stated herein:

- All welding procedures passed the welding procedure qualifying tests except A (common welding procedure), which failed the visual inspection tests due to solidification cracks, and welding procedure E (side 1), which failed due to incomplete penetration of the weld bead.
- Two out of eight side bend specimens of welding procedure A showed a crack in the weld metal.
- One out of eight side bend specimens for welding procedure E had a crack at the fusion line between the weld metal and base metal.
- From the results of the reduced section and all-weld metal tension tests it is concluded that increasing the number of passes while having a low average heat input per welding pass increases the yield stress of the weld connection as well as the weld metal. This can be achieved by using a number of passes greater than 15 (welding procedure B) and a heat input less than 2KJ/mm (welding procedure D).
- The welding procedure specification had no impact on the lower shelf fracture toughness of the weld metal or that of the HAZ.
- However, each welding procedure in general, regardless of the specification, decreased the lower shelf CVN value of the base metal from 31J to 13J near the HAZ.
- Based on the results of the CVN tests conducted at the HAZ and weld metal, the fracture toughness at upper shelf temperatures of the HAZ and weld metal was affected by the

welding arc procedure; such that using tandem arc welding with DC+ and AC produced higher fracture toughness than using DC+ current alone.

- The upper fracture toughness is mainly dependent on the heat input, number of passes and current. This is in contrast to what was stated by Yang (2008) for the 17mm thick steel plates for which the fracture toughness depended on the electrode travel speed and current.
- By neglecting the heat input produced by an AC current for welding procedures D and E the fracture toughness is found to correlate to the heat input produced by a DC+ current only.
- The High heat input of welding procedure E results in incomplete penetration of the welding profile.
- Increasing the number of welding passes with low heat input per welding pass increases the hardness of the HAZ.
- Based on the results of the micro-hardness tests the size of the HAZ is mainly dependent on the heat input, number of passes used in the welding procedure and the ratio of the sum of electrode diameters to number of passes (the HAZ size increases from 2.25 to 4.25mm when the number of passes decreases from 7 to 4 and when electrode diameter-number of passes ratio increases from 0.7 to 2.4mm). This is not consistent with that observed by Lee et al. (2000) for steel plates of less thickness, for which the size of the HAZ has been shown to mainly depend on the current and is not affected by the electrode diameter.

According to the test results, for the 75 mm thick plate welding assembly utilized in the experiments, welding procedure B (largest number of passes and lowest heat input) demonstrated the highest fracture toughness of the weld metal and HAZ, narrowest HAZ size, no weld defects and passed all welding procedure qualification tests. Therefore, this welding procedure is recommended for such welding assembly of thick steel plates. However, in some cases where fabrication is required to be prompt, welding procedure B is not adequate as it requires long fabrication time due to the large number of passes. In such situation welding procedure D can be utilized due the smaller number of passes and faster electrode travel speed. Welding procedure D has also passed the welding procedure qualification tests and provides the second highest weld metal and HAZ fracture toughness. Due to the wide HAZ size compared to welding procedure B, a thorough non-destructive inspection of the base metal at this region should be established before welding to ensure the absence of any discontinuities that can propagate if subjected to welding residual stresses.

6.5 Acknowledgments

The authors sincerely thank the ADF Group Inc. and DPHV Structural Consultants for their financial and technical support and for their contribution in conducting the weld experiments and for providing the materials test specimens. The also thank Mr. Nicolas Roy for his assistance and advice with respect to weld engineering. The authors recognize the Department of Mining and Materials Engineering in the Faculty of Engineering at McGill University for providing technical support and access to the Materials and Characterization Laboratories to conduct a portion of the materials testing. The authors also acknowledge the financial support from the Natural Sciences and Engineering Research Council of Canada.

Table 6.1: Minimum mechanical properties and typical chemical composition for the base metal and weld metal according to ASTM A572 Gr.50 (2013) and AWS A5.17/5.17M (1997 (R2007))

	Mechanical Properties				Typical Chemical Composition				
	Yield Stress [MPa]	**Ultimate Stress [MPa]**	**Min. Elongation at 50mm [%]**	**Min. CVN absorbed energy [Joules]**	**C [wt.%]**	**Mn [wt.%]**	**Si [wt.%]**	**S max. [wt.%]**	**P max. [wt.%]**
A572 Gr. 50	345	450	21	27 at 21ºC	0.21	1.35	0.15-0.4	0.05	0.04
F7A4-EM12K	400	480-660	22	27 at -40ºC	0.07	1.5	0.5	0.011	0.02
F7A6-EC1-H8	400	480-660	22	27 at -50ºC	0.07	1	0.3	0.007	0.016

Table 6.2: Welding procedures specifications.

Welding procedure[a]	Average current [A]	Average voltage [V]	Electrode type	No. and diameter of electrodes [mm]	Average wire feed speed [cm/min]	Average electrode travel speed [mm/sec]	No. of passes on side 1	No. of passes on side 2	Average heat input [KJ/mm]
A	700	30	F7A4-EM12K	2x2.4 DC+	270	8.3	8	7	2.4
B	400	26	F7A4-EM12K	1x2.4 DC+	265	8.75	17	15	1.19
C	850	30	F7A4-EM12K	2x2.4 DC+	320	8.3	6	6	3
D[b]	800	31	F7A4-EM12K	2x2.4 DC+ 2x2.4 AC	340	12.5	4	4	4
E[b]	1000	31	F7A6-EC1-H8	2x3.2 DC+ 2x3.2 AC	300	7.5	3	2	8.6

[a] All welding procedures utilized a 110ºC preheat/inter-pass temperatures
[b] Tandem arc welding is utilized in these procedures

Table 6.3: Reduced section tensile test results.

Welding Procedure	Specimen No.	Young's Modulus [MPa][a]	Yield Stress [MPa][a]	Yield Strain[a]	Ultimate Stress [MPa]	Ultimate Strain	Strain at Fracture
A	**1**	266700	424	0.0017	524	0.116	0.250
	2	230445	414	0.0018	553	0.105	0.234
	3	253410	427	0.0016	570	0.111	0.257
	4	369380	411	0.0009	549	0.114	0.269
B	**1**	223105	459	0.0021	571	0.117	0.274
	2	216305	465	0.0022	565	0.114	0.265
	3	180720	470	0.0018	571	0.107	0.279
	4	346290	454	0.0010	568	0.114	0.275
C	**1**	211110	412	0.0020	552	0.119	0.232
	2	219430	415	0.0018	561	0.111	0.231
	3	193760	426	0.0018	557	0.101	0.238
	4	274870	406	0.0014	550	0.112	0.254
D	**1**	207675	433	0.0021	580	0.135	0.225
	2	210925	433	0.0020	588	0.117	0.223
	3	381400	445	0.0012	591	0.128	0.279
	4	212460	420	0.0019	566	0.144	0.328
E	**1**	218750	434	0.0020	569	0.119	0.225
	2	202355	433	0.0021	579	0.121	0.216
	3	309000	423	0.0010	558	0.113	0.332
	4	298020	418	0.0011	564	0.114	0.311

[a] Specimens 1 and 2 values, for the elastic region for each welding procedure, are based on strain gauge readings while all other values are based on extensometer readings

Table 6.4: All-weld metal tensile test results.

Welding Procedure	Specimen No.	Young's Modulus [MPa]	Yield Stress [MPa]	Yield Strain	Ultimate Stress [MPa]	Ultimate Strain	Strain at Fracture
A	**1**	350380	476	0.0014	572	0.149	0.328
	2	254040	441	0.0013	552	0.165	0.361
B	**1**	269290	496	0.0019	577	0.129	0.353
	2	366650	511	0.0012	590	0.126	0.359
C	**1**	370850	441	0.0015	550	0.154	0.359
	2	363830	456	0.0012	560	0.136	0.172
D	**1**	270530	470	0.0015	578	0.154	0.367
	2	299530	467	0.0016	582	0.153	0.454
E	**1**	234070	426	0.0014	544	0.149	0.381
	2	276980	428	0.0012	552	0.135	0.361

All values in this table are based on extensometer readings

Table 6.5: Charpy-V-Notch absorbed energy values.

Welding Procedure	Charpy-V-Notch energy values [Joules]									
	A		B		C		D		E	
Temperature	@ weld	@ 5mm	@ weld	@ 5mm	@ weld	@ 5mm	@ weld	@ 5mm	@ weld	@ 5mm
-50°C	10	9	22	11	18	16	12	24	10	17
	16	14	12	16	10	12	10	10	8	11
-25°C	48	94	62	50	25	16	37	52	37	56
	44	45	28	64	41	56	36	83	34	37
0°C	68	94	90	73	55	94	55	58	42	105
	70	76	80	102	69	102	56	90	38	120
21°C	106	122	123	111	94	85	94	57	72	76
	95	147	99	111	98	117	102	131	85	128
60°C	112	128	128	139	103	122	114	132	97	119
	110	127	115	135	103	123	117	128	118	119

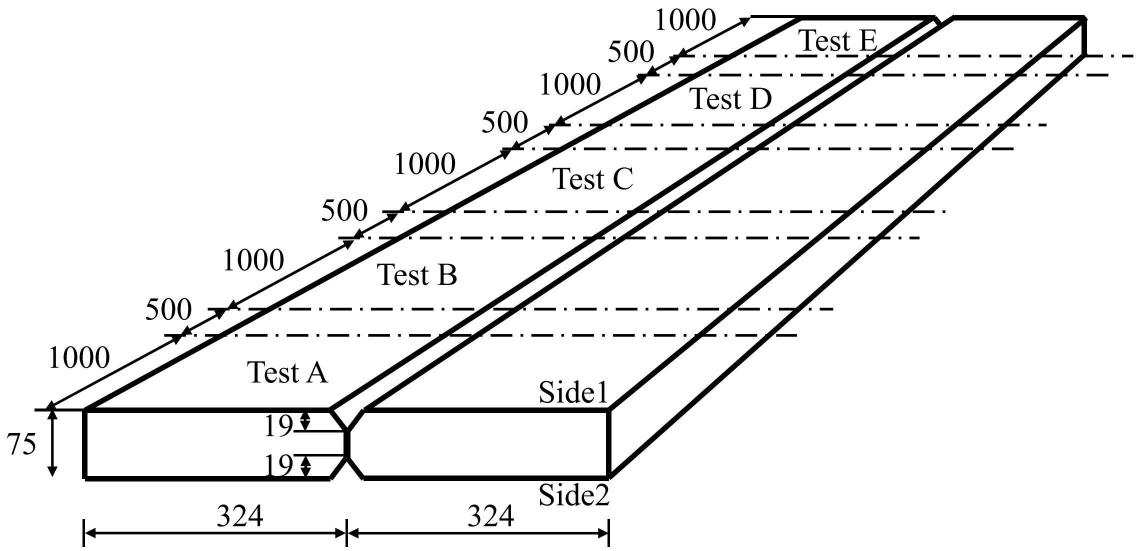

Figure 6.1: Test layout of the plate assembly (dimensions are in mm).

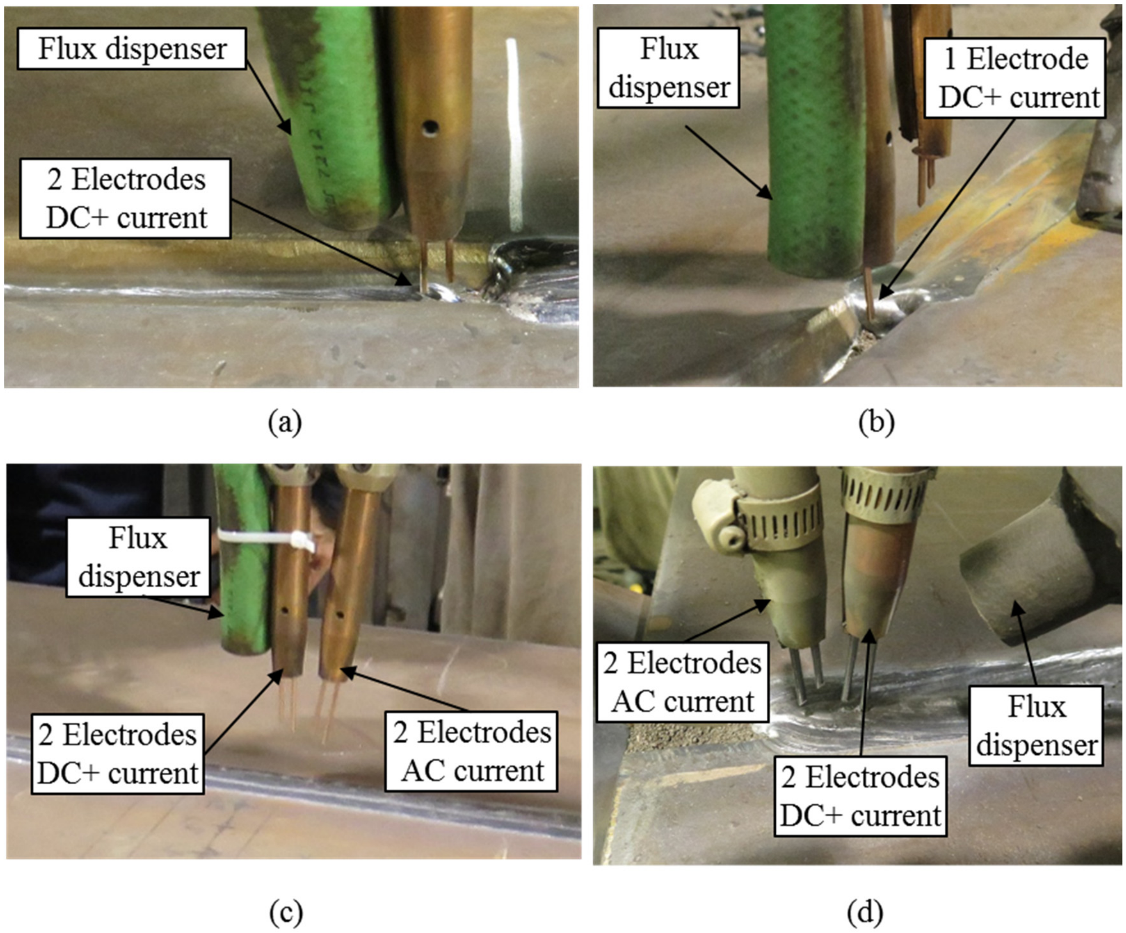

Figure 6.2: Welding electrodes set-up; a) for welding procedures A and C, b) for welding procedure B, c) for welding procedure D, d) for welding procedure E.

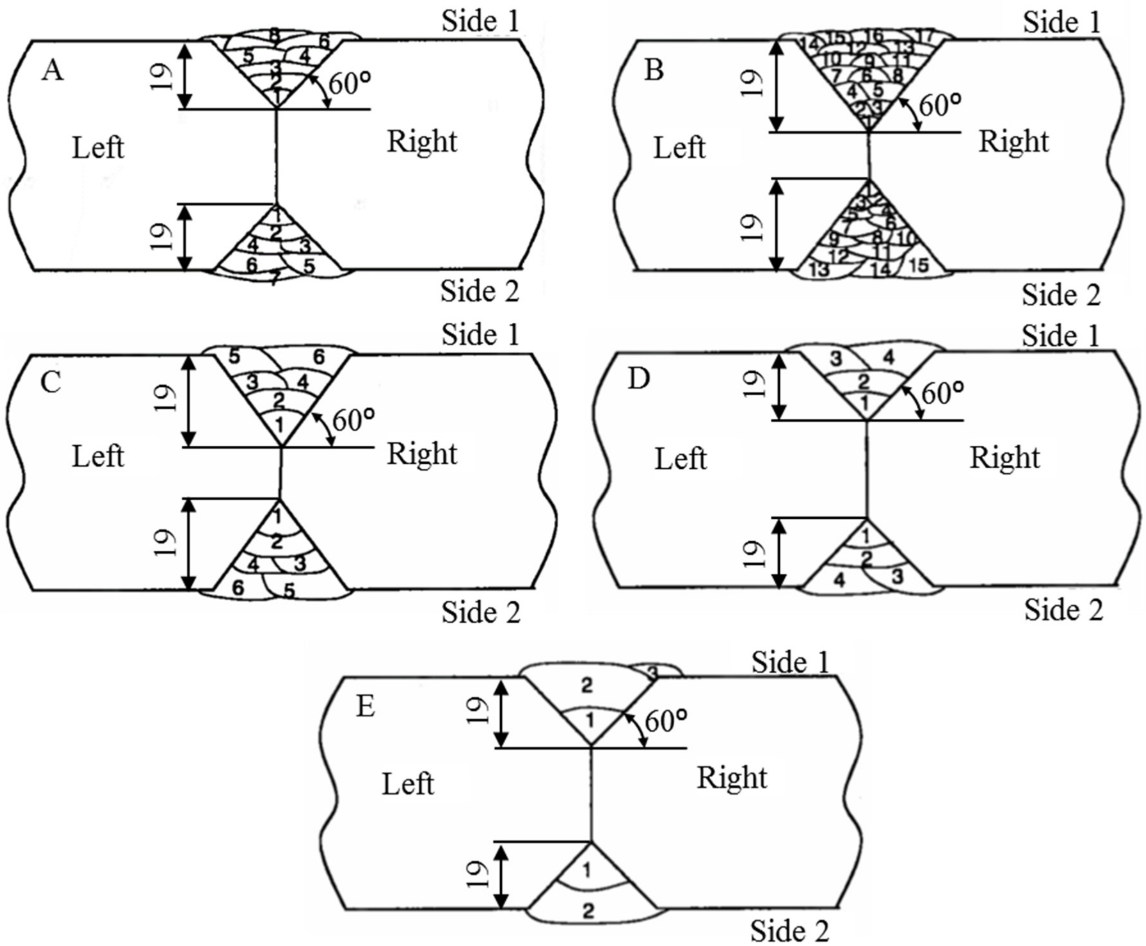

Figure 6.3: Illustration of the welding sequence for the five welding procedures (dimensions are in mm).

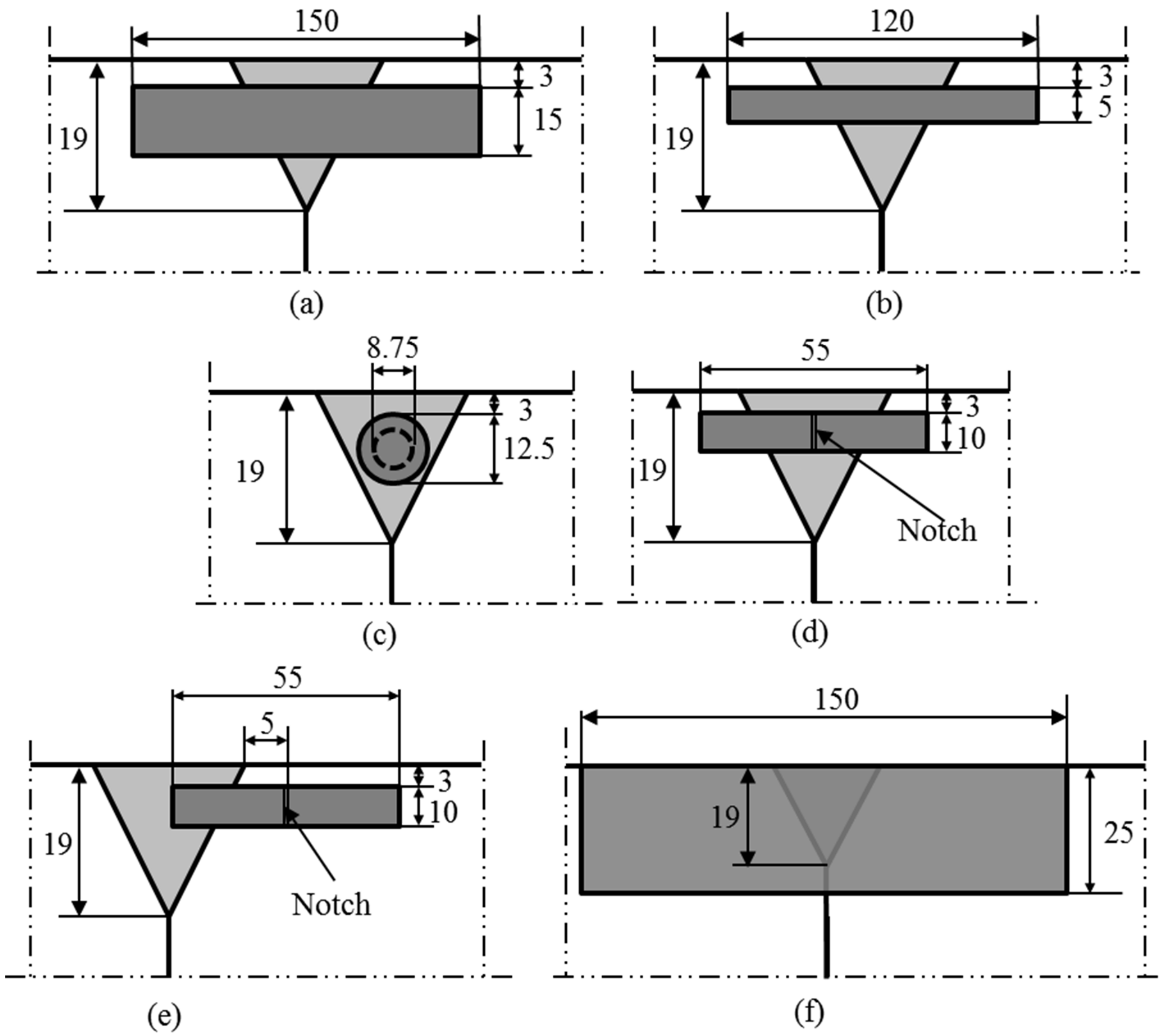

Figure 6.4: Schematic drawings for the welded assembly cross-section showing the locations and positions of specimens for; a) side bend test, b) reduced section tension test, c) All-weld metal tension test, d) CVN test at weld centerline, e) CVN test at 5mm from weld and f) Microscopy and micro-hardness tests (dimensions are in mm).

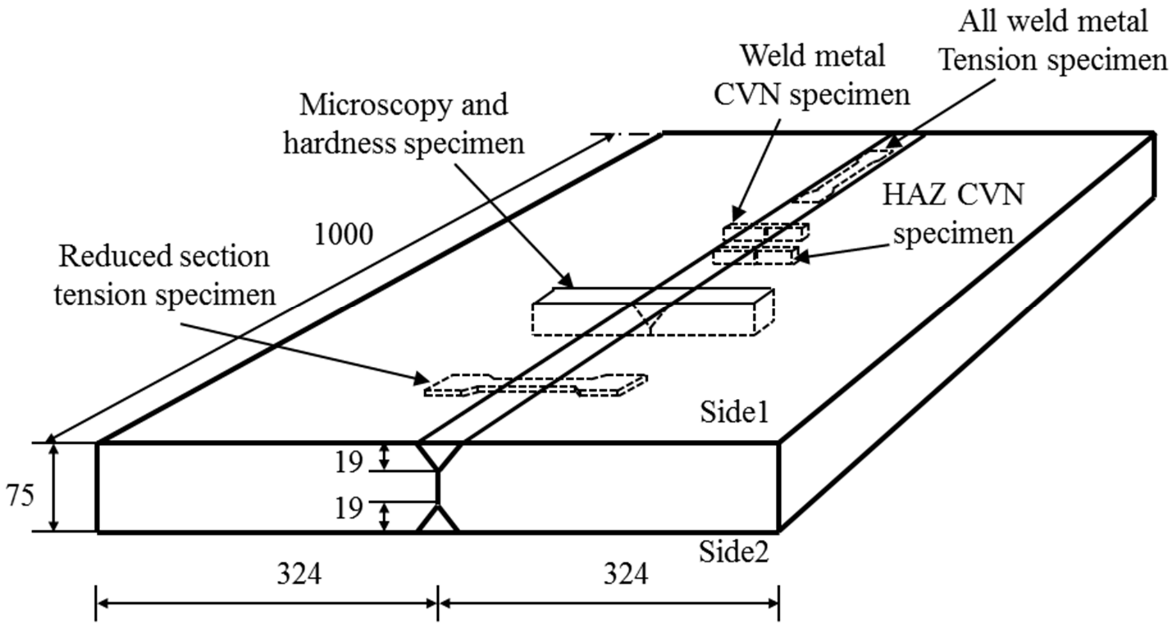

Figure 6.5: Illustration of the locations of specimens extracted for mechanical testing and microscopy for each welding procedure experiment.

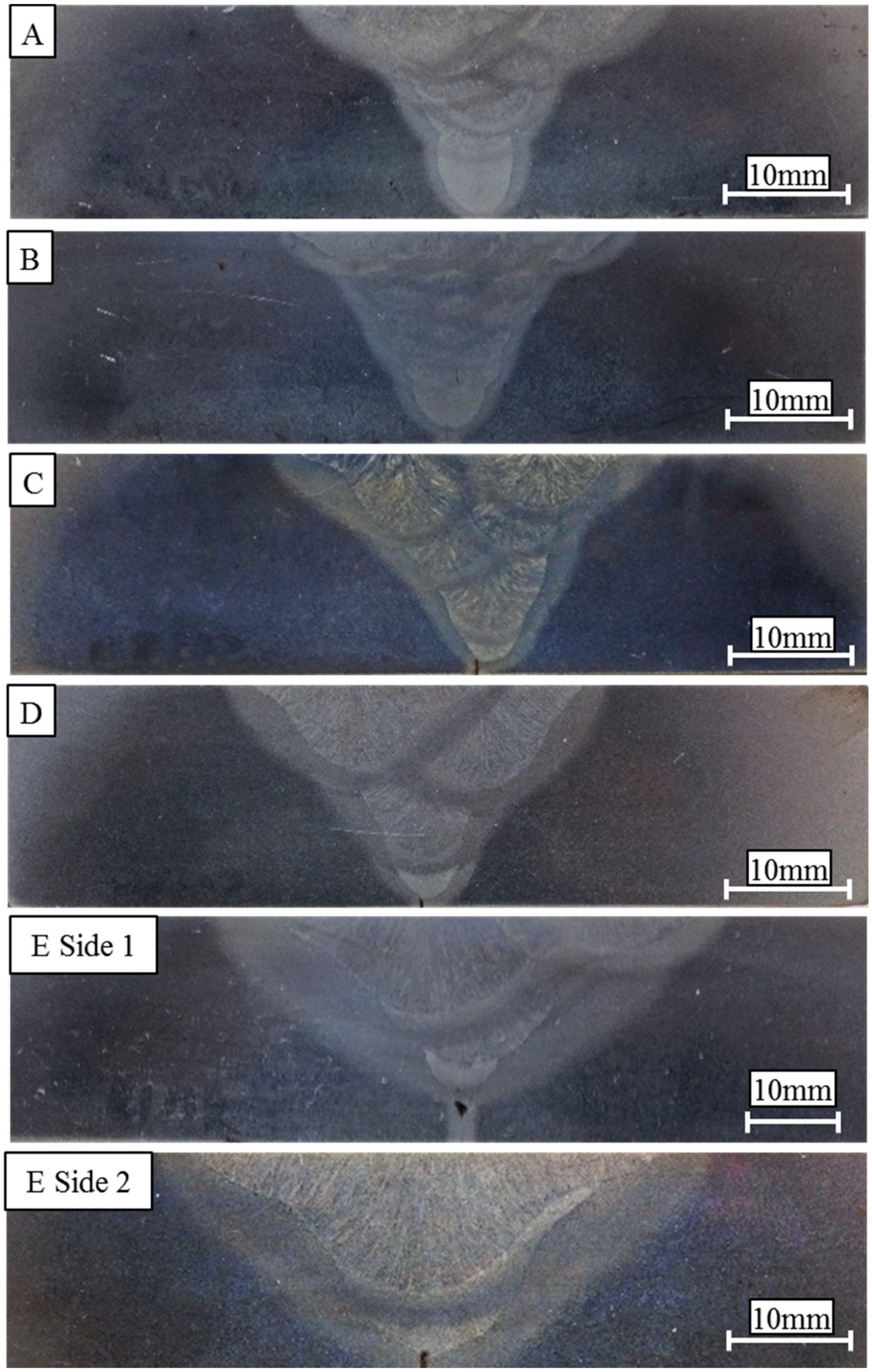

Figure 6.6: Sample of specimens used for microscopy for each welding procedure.

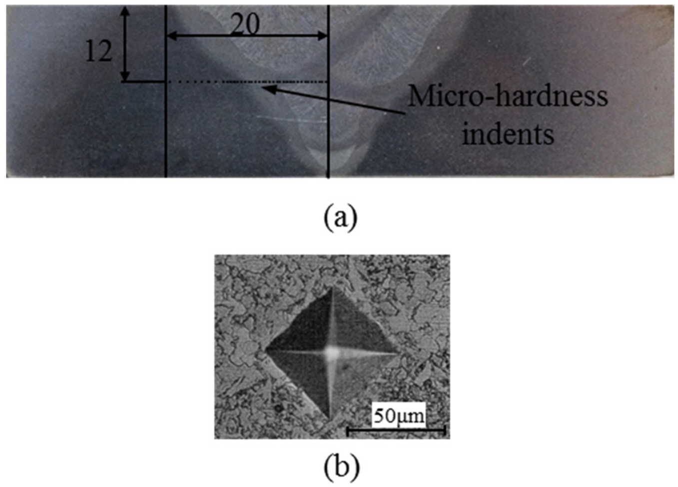

Figure 6.7: Micro-Hardness test for specimens used for microscopy; a) location of testing path on the specimen (dimensions are in mm), b) 500x magnification of an indent on the specimen.

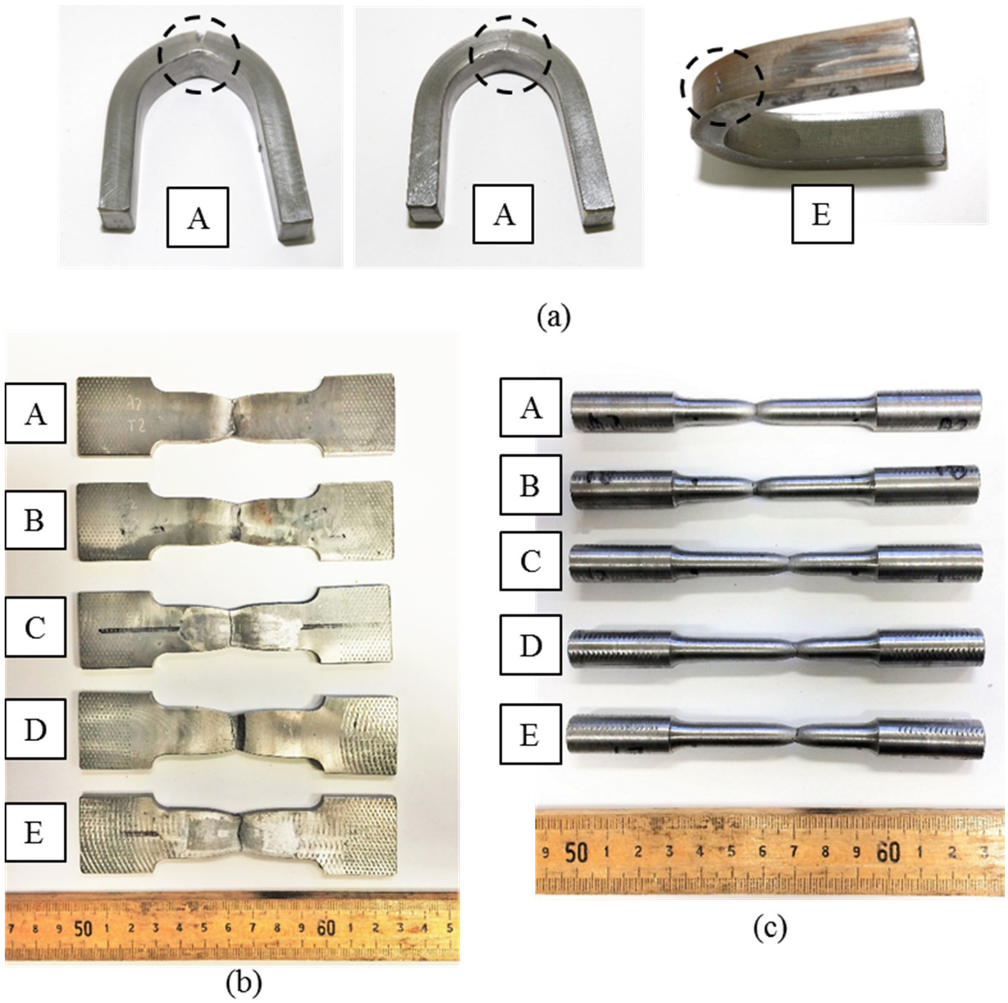

Figure 6.8: Samples of specimens after testing; a) side bend specimens b) reduced section tension specimens, b) all-weld metal tension specimens.

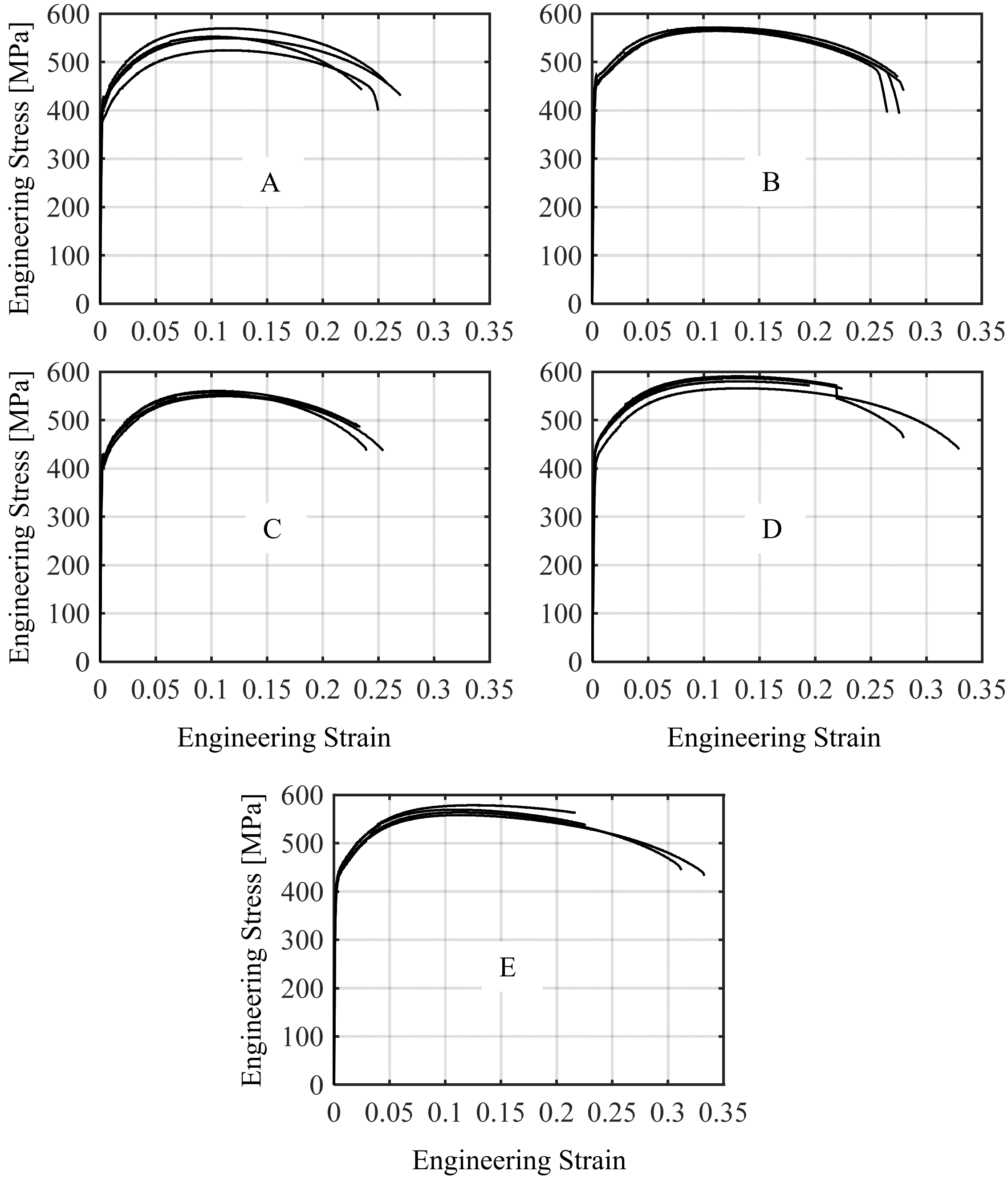

Figure 6.9: Engineering stress strain curves of the reduced section tension tests for each welding procedure.

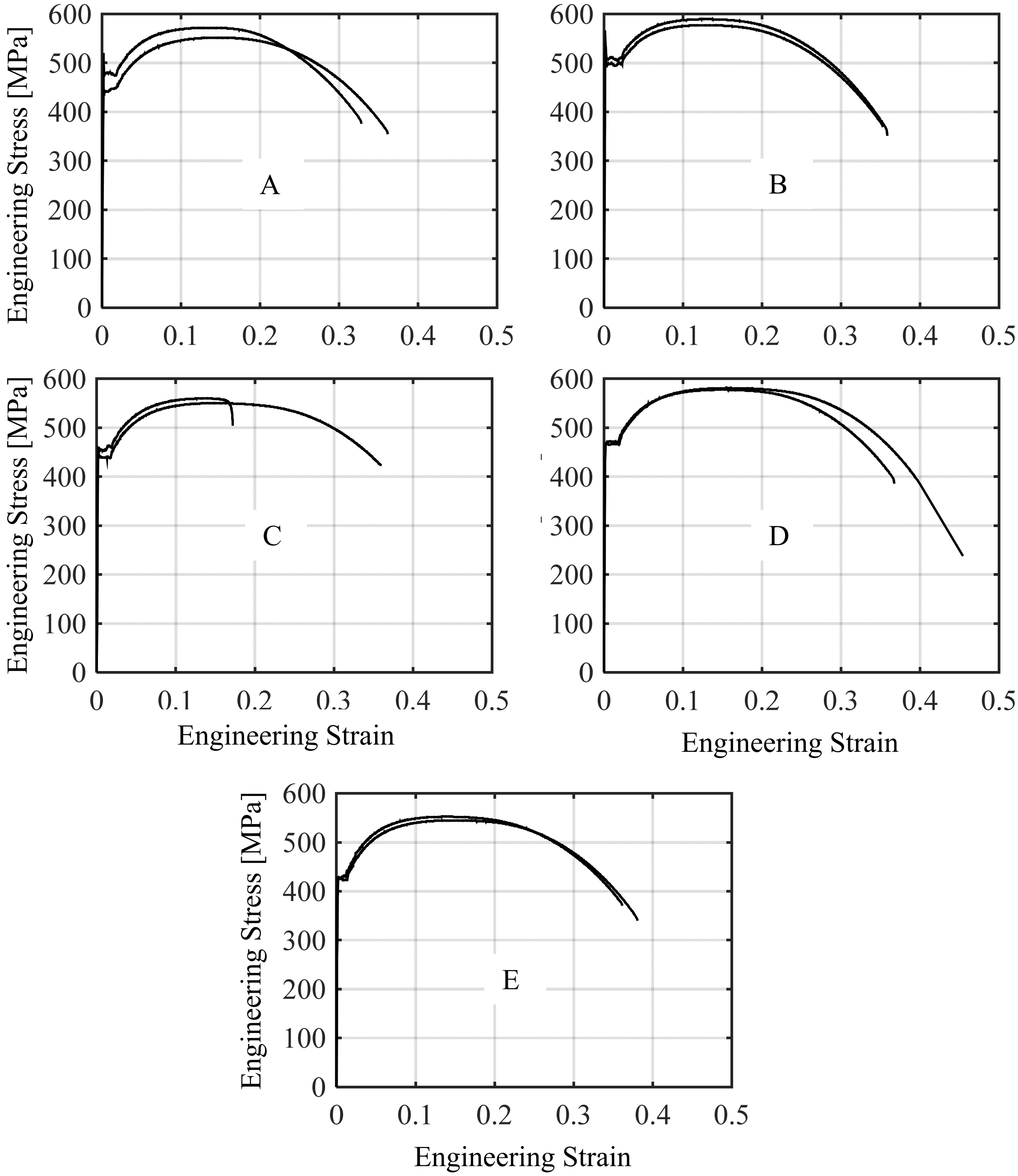

Figure 6.10: Engineering stress strain curves of the all-weld metal tension tests for each welding procedure.

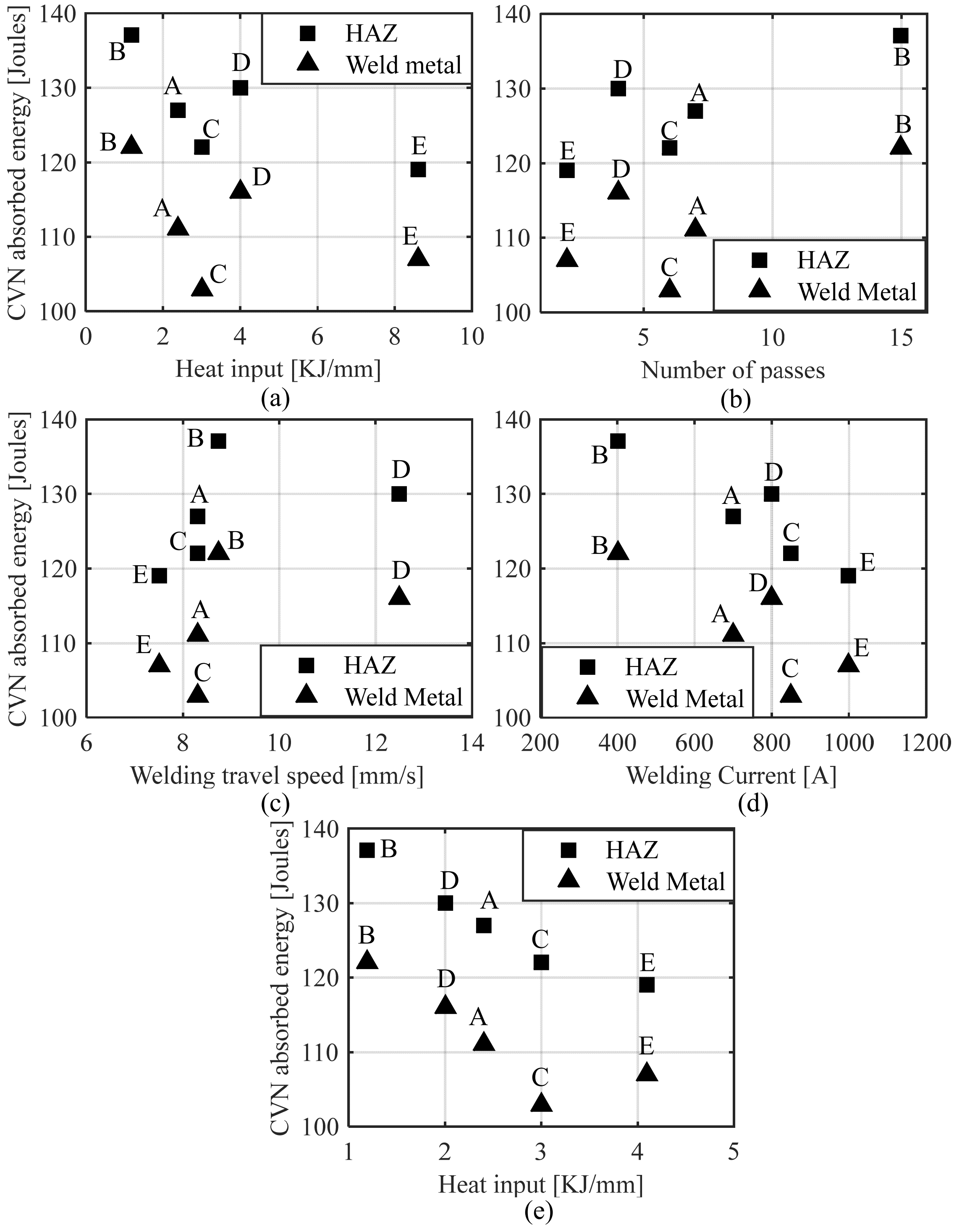

Figure 6.11: Relation between the upper shelf CVN results for the HAZ and weld metal with; a) Heat input, b) Number of passes, c) Electrode travel speed, d) Current and e) Heat input produced from DC+ arc.

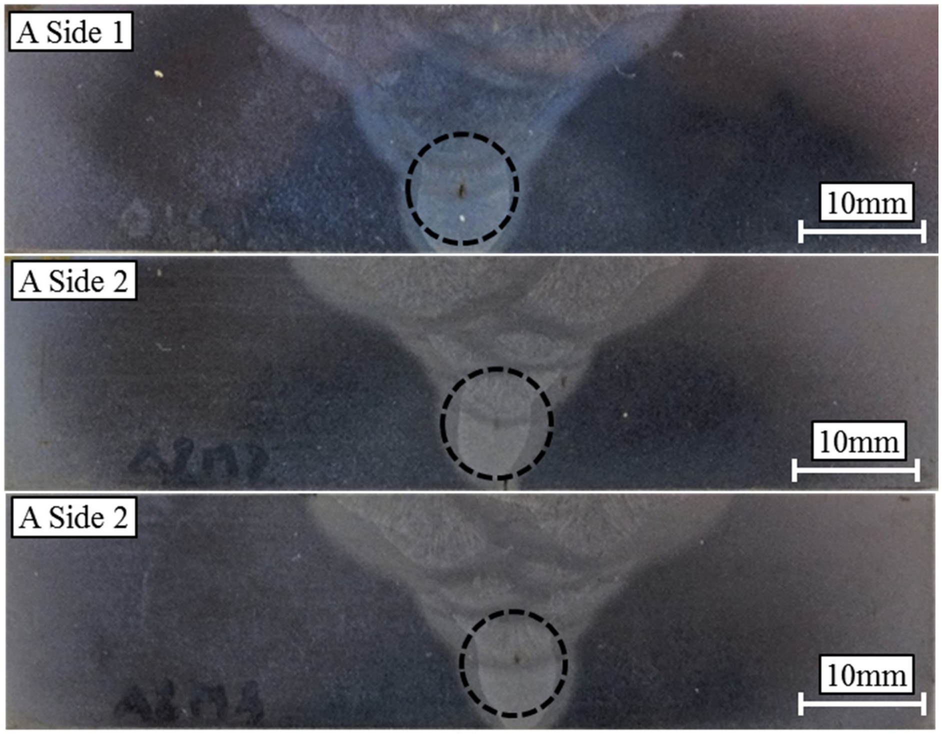

(a)

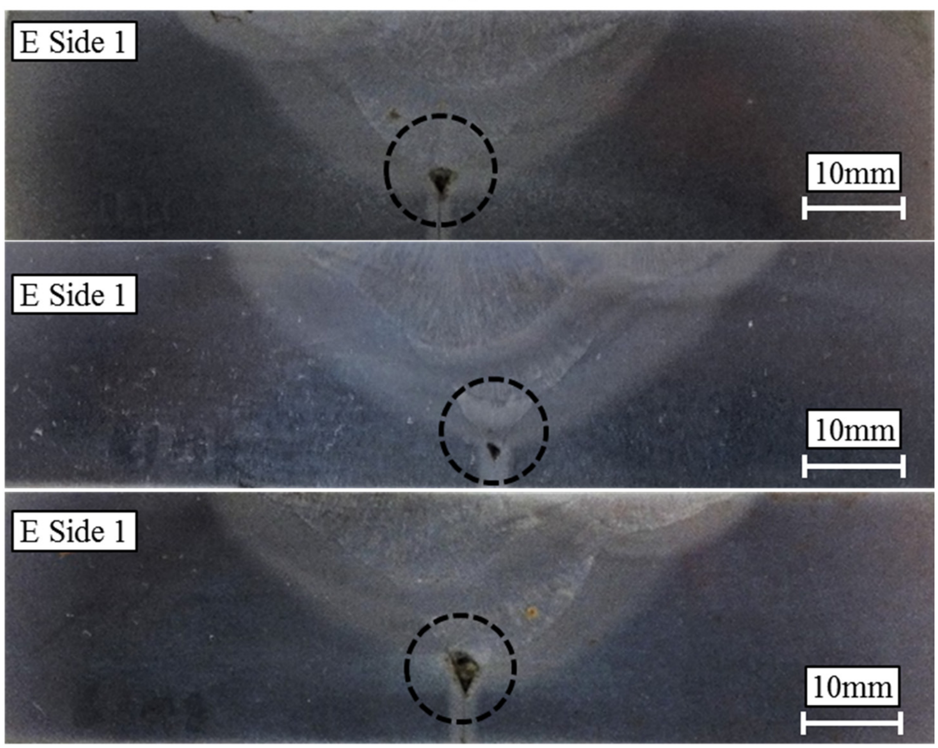

(b)

Figure 6.12: Weld defects detected through visual inspection; a) solidification cracks for welding procedure A. b) incomplete penetration for welding procedure E.

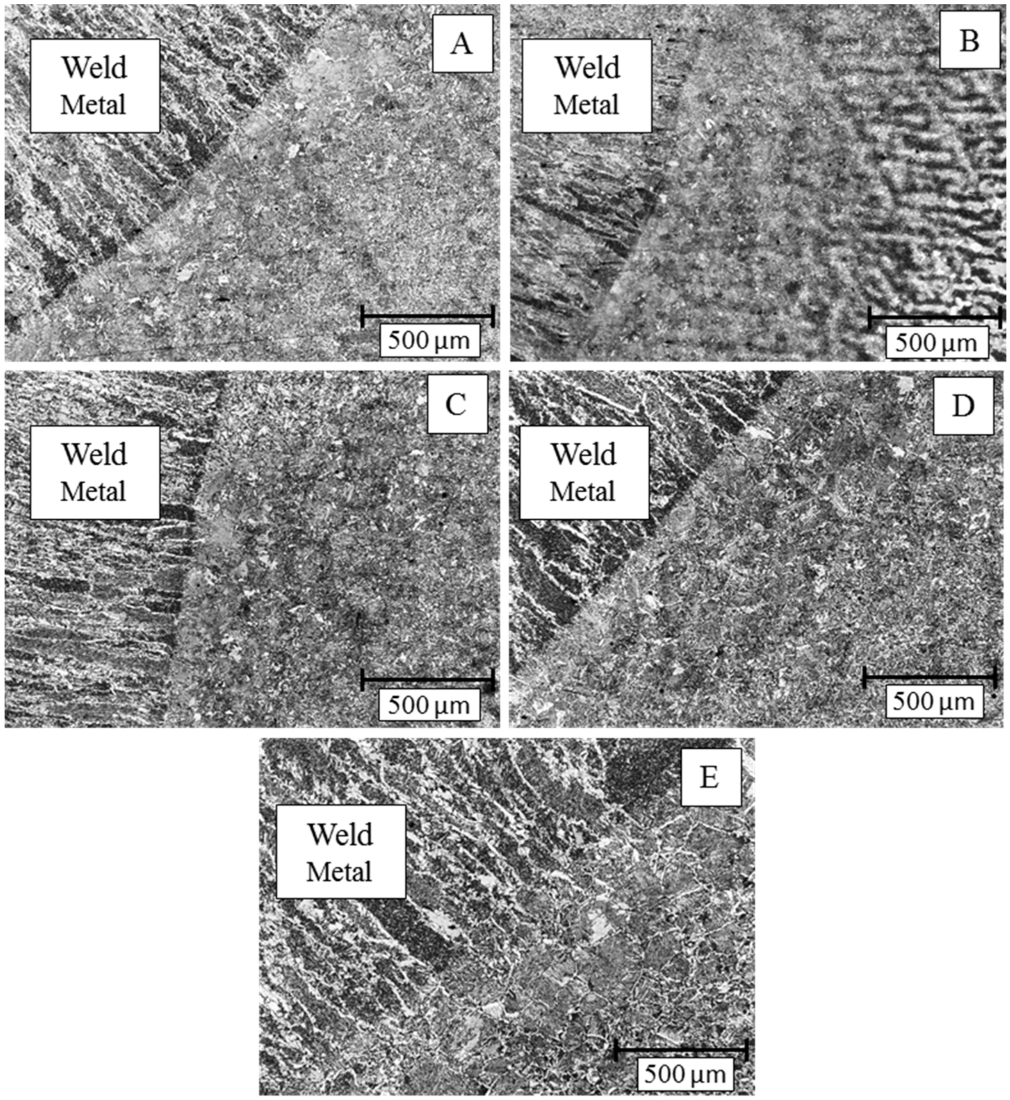

Figure 6.13: Optical microscope screen captures at fusion line for each welding procedure at 50x magnification.

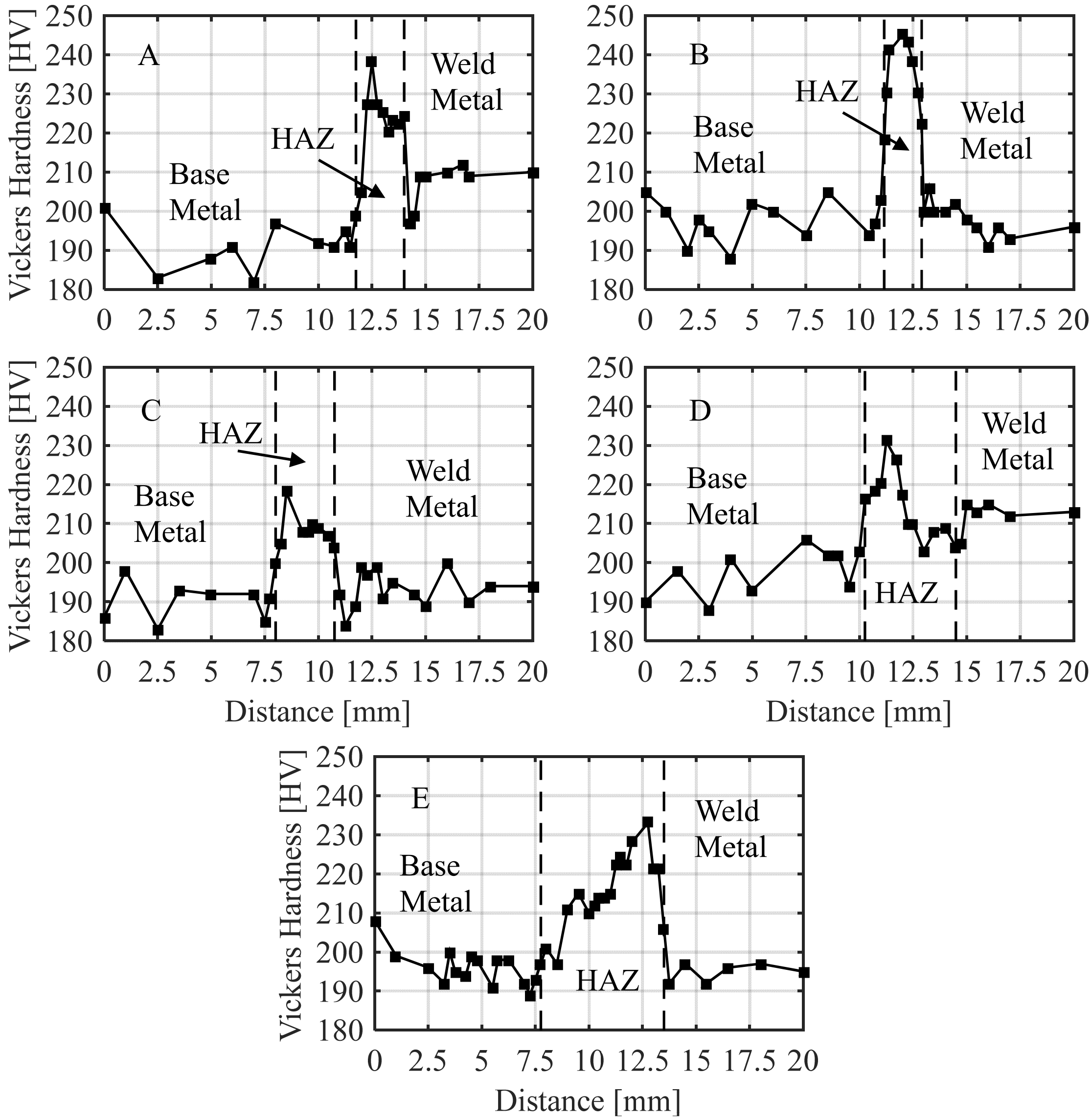

Figure 6.14: Micro-hardness test results across the base metal, HAZ and weld metal for each welding procedure.

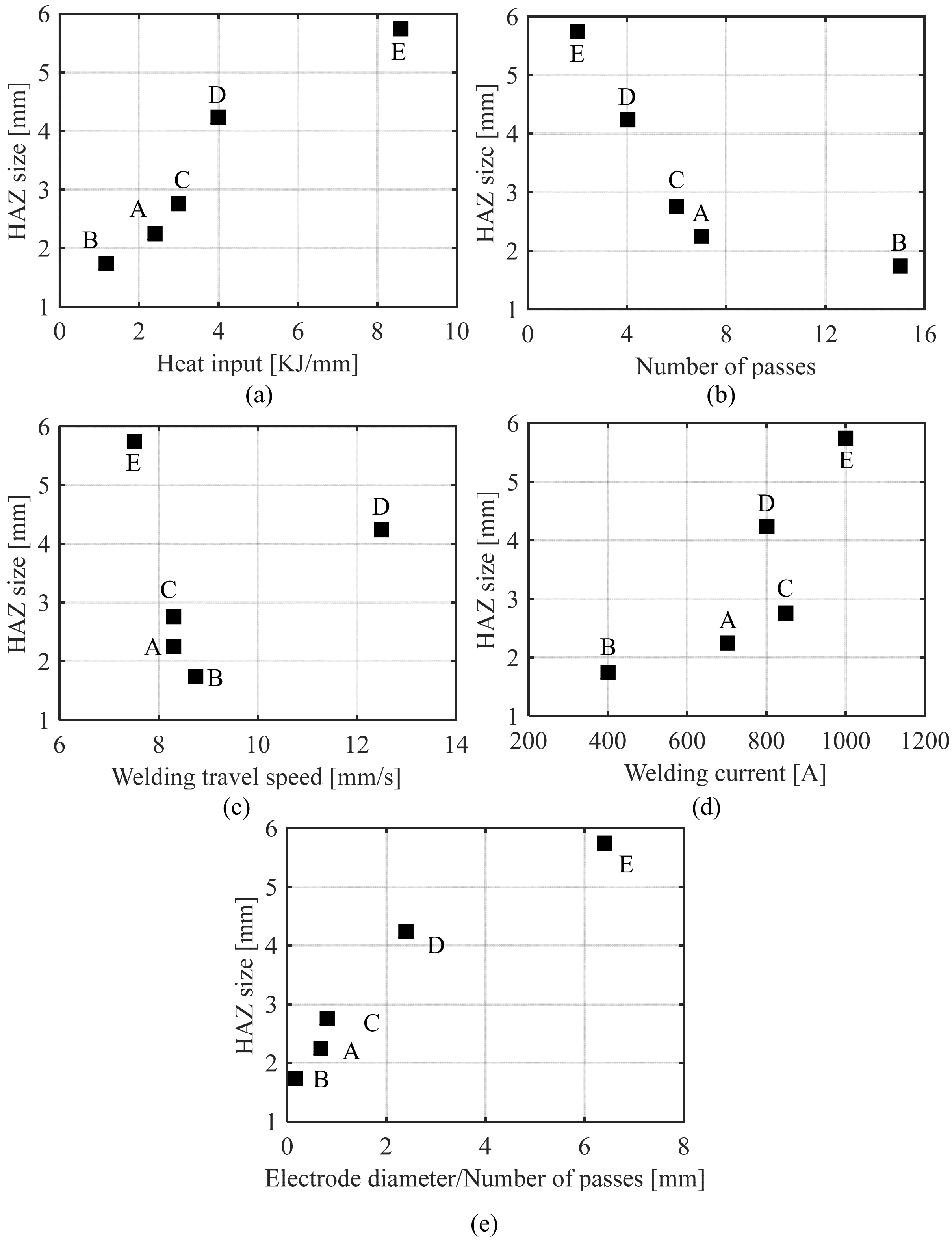

Figure 6.15: Relation between the HAZ size and; a) Heat input, b) Number of passes, c) Electrode travel speed, d) Current, e) Electrode diameter to Number of passes ratio

Chapter 7 EXPERIMENTAL INVESTIGATION IN THE EFFECT OF WELDING REPAIR ON THE HEAT AFFECTED ZONE TOUGHNESS AND SIZE

7.1 Introduction

Welding is the most common joining method in steel construction. Undesirable defects and residual stresses are often associated with the welding procedure. Welding repairs are frequently used in steel construction to remove these undesirable defects. Additionally, repairs by welding are used to retrofit existing steel components / structures that have developed cracks. The repair procedure is similar to the original welding procedure; however, it is preceded by excavation in the steel component to remove the defective region. The repair weld is subject to the same potential for undesirable defects and residual stress as found for any initial welding procedure. As a recent example, a steel fabricator was required to weld 75mm thick steel plates that developed cracks after the welding procedure due to high residual stress (Chapter 3) (Ibrahim et al., 2015). Weld repair of the developed cracks was conducted, however, additional cracks developed and the process was repeated until it was decided to scrap the plates due to the extensive cracking exacerbated by the multiple repair process. Another example of where the welding repair procedure resulted in fractures occurred for railway rails in which crack growth was influenced by the high tensile residual stresses that developed during rewelding (Jun et al., 2015). These examples illustrate how critical the influence of repairs can be on the structural integrity of the steel component and the risk of industrial losses due to scrapping. Previous experimental studies have also demonstrated the effect of repairs using welding on the structural integrity of the steel components in pressure vessels and offshore pipelines, as well as non-structural components such as cladding (Reitz, 2011, Lin et al., 2012, Jiang et al., 2013, Zeinoddini et al., 2013). However, an investigation of the effect of repairs on structural steel components for buildings has not yet been completed.

Repairs can have a considerable effect on the properties of the heat affected zone (HAZ) of the repaired material. Lin et al. (2012) executed an experimental program to investigate the effects of repeated weld repairs on the microstructure and toughness of the HAZ of 10mm thick AISI 304L stainless steel plates (ASM International Handbook Committee, 1990). Two specimens were initially fabricated using the gas tungsten arc welding (GTAW) process. This was followed by a repair involving back gouging and welding using the shielded metal arc welding (SMAW) process. The first specimen was repaired one time, and the other specimen was repaired five times, with each repair involving back gouging and welding. It was found that the orientation of the texture of the HAZ for the five times repaired specimen was different from that for the one time repaired specimen. In addition, the number of weld repairs had no effect on the boundaries of the fusion line. Moreover, the number of weld repairs had no significant effect on the fracture toughness of the HAZ. However, the failure mechanism of the five times repaired specimen was more ductile than that of the one time repaired specimen. Another experimental investigation of the effect of multiple weld repairs on the microstructure, hardness and residual stress measurements of the HAZ was conducted by Jiang et al. (2013) with 20mm thick 06Cr19Ni10 austenitic stainless steel clad plate. In this study, imperfections were removed by gouging of the stainless steel component, and then the excavated area was filled by weld metal. Four specimens were utilized in this investigation; with one, two, three and four repairs, respectively. The repair procedure was conducted such that the surface of the specimen was excavated to a depth of 4mm and then welded using a tungsten inert gas welding process. It was concluded that with the increase of the number of weld repairs the fusion line thickness increases as well as the residual stresses and hardness at the HAZ. For stainless steel clad plates, Jiang et al. (2013) recommended that no more than two weld repairs should be conducted. Likewise, experiments to measure the residual stresses caused by weld repairs in the HAZ of offshore steel pipelines were conducted by Zeinoddini et al. (2013). The results suggested that the magnitude of the developed residual stresses is equal to the yield stress of the material and that the weld repairs resulted in an increase in the size of the tensile stress field next to the weld. As weld repair is an essential part of steel fabrication, similar experimental investigations are required for structural steel components to better understand the effects of weld repairs on the properties of the HAZ.

The effect of weld repairs on the heat affected zone of structural steel plates is a challenging problem that requires to be first addressed for common thicknesses of steel plates used in regular steel structures; such that it becomes a reference point before conducting the investigation for thicker steel plates. Additionally, using thin steel plates facilitates the experimental investigation of multiple weld repairs that involves multiple excavations and welding of commonly used structural components. Presented herein is an experimental investigation of the effects of multiple weld repairs on the fracture toughness, hardness, size and microstructure of the HAZ of two 25mm thick ASTM A572 Gr.50 (2013) structural steel plates. The initial complete joint penetration weld was made by means of the submerged arc welding process. This was followed by ten weld repair experiments involving back gouging and rewelding with a semi-automated flux core with gas shield arc welding procedure. The specimens covered the range of no weld repair (control segment) to nine weld repairs. Mechanical tests were then conducted for samples taken from various locations within the plates. Material phase changes were identified at the HAZ using optical microscopy and micro-hardness testing. A comparison between the results of the conducted tests for the ten experiments is presented and recommendations are suggested for the maximum number of weld repairs that produces minimal changes to the properties of the HAZ.

7.2 Description of the Welding Repairs Experiments

The experimental investigation of the weld repairs for structural steel components involved the welding of two 9100x457x25mm ASTM A572 Gr.50 (2013) steel plates (Figure 7.1). The nominal mechanical properties and typical chemical composition of the base metal are shown in Table 7.1. The repair experiments were conducted on the same component in order to minimize the uncertainties associated with the steel material and welding setup; hence, the length of the plates was divided into ten segments of 610mm each, separated by 300mm as illustrated in Figure 7.1. One weld segment was not repaired, and thus was defined as the control segment; each of the other nine segments was repaired one time more than the previous segment. The welding and repair procedure is discussed in Section 7.2.1. For the assessment of the weld quality, specimens were extracted from the weld metal and base metal to conduct mechanical tests, as well as to carry out a visual and microscopic inspection. A discussion of the material testing program for each weld segment is provided in Section 7.2.2.

7.2.1 Welding and repair procedure specifications

The first step in the weld repair study was to weld the two 25mm thick steel plates using the submerged arc welding process (SAW). The prequalified complete joint penetration (CJP) welding procedure "B-U3c-S" was utilized according to AWS D1.1 (2010), as illustrated in Figure 7.2a. It comprised solid core electrodes of diameter 2.4mm and type F7A4-EM12K (AWS A5.17/5.17M (1997 (R2007))) with suitable granular flux type (OK FLUX 10.71). Table 7.2 shows the welding procedure specification for both sides of the joint (Figure 7.1); after completing the weld on side 1, the plates were turned over and the joint was gouged to sound metal on side 2, which was followed by the deposition of the weld metal. The next step was to grind flush the surface of both sides of the plates and to perform ultrasonic inspection (UT) to ensure the integrity of the weld and to confirm that the acceptance-rejection criteria according to "Tables 6.2 and 6.3" in AWS D1.1 (2010) were met. The weld repair segments were then marked along the length of the plates for the weld repair procedure to commence. Figure 7.3a shows the steel plates of the weld repair specimen after the SAW procedure, surface grinding and the UT inspection had been completed.

The weld repair procedure was conducted only on side 1 of the welded assembly. The procedure was divided into three steps; the first was the excavation of the welded area to a depth of 13mm using air carbon arc gouging technique at the test weld segment where the repair was to be conducted, as shown in Figures 7.3b and 7.3c (length of each repair was 610 mm). This was then followed by grinding and cleaning of the area of excavation and its surroundings (Figure 7.3d). It is worth mentioning that these steps were conducted manually by the welder. The shape of the excavation was according to prequalified flux core arc welding (FCAW) assembly "BC-P6-GF" of AWS D1.1 (2010) as illustrated in Figure 7.2b; such that a portion of the base metal is excavated as well. The following step involved welding the excavated volume using the semi-automated "BC-P6-GF" FCAW procedure specifications as described in Table 7.2, with a 1.6mm diameter E71T-9C-H4/H8 electrode (AWS A5.20/A5.20M (2005 (R2015))), 100% CO_2 shielding gas and the number of welding passes was nine. The final step was to perform UT on the repaired area to check for defects. The weld repair steps were then repeated according to the specified number of repairs at each weld segment (Figure 7.1). An illustration of the weld repair steps is given in Figures 7.3b to 7.3e through photographs taken during the fabrication process.

7.2.2 Material testing program

After the completion of the welding repairs for each segment, coupon and Charpy-V-Notch (CVN) specimens were extracted and then machined to size in order to measure the material properties and to study the impact of multiple weld repairs on the fracture toughness, microstructure, hardness and size of the HAZ. The base metal material properties were verified through tensile coupon tests. The HAZ assessment tests were based on Charpy-V-Notch impact tests and visual inspection, as well as inspection by means of optical microscopy. Additional micro-hardness tests were conducted to convey the effect of welding repairs on the size and hardness of the HAZ. The specimens were extracted from each weld repair segment as well as the control segment and the results were compared with one another and with the requirements of the current specifications (AWS D1.1, 2010, CAN/CSA-W59, 2013).

A total of four reduced section tension tests were conducted for specimens extracted from the base metal of the control segment (two in the plate longitudinal (rolling) direction and two in the transverse direction) as illustrated in Figure 7.4. The tension tests were conducted using a 150 KN Sintech MTS testing machine, which was connected to Vishay Model 5100B scanners that were used to record data using the Vishay System 5000 StrainSmart software. The reduced section coupon specimens are of length 120mm, gauge length 50mm and reduce area of 20x5mm. The strain was measured during the test through an extensometer of a 25mm gauge length, as well as 5mm strain gauges placed on each side at the center of the specimen to measure the Young's modulus. The results were compared with the requirements of ASTM A572 Gr.50 (2013) shown in Table 7.1.

Charpy-V-Notch (CVN) impact tests were conducted to assess the fracture toughness of the HAZ, and to insure it meets the acceptance limits of the CSA and AWS welding specifications (AWS D1.1, 2010, CAN/CSA-W59, 2013). The tests were conducted using a TINIUS OLSEN impact tester Model 64 with a capacity of 256J. One hundred CVN specimens were extracted (ten at the HAZ of each weld segment) in a position perpendicular to the welding direction such that the centerline of the notch is at 5mm from the edge of the weld in the direction of the base metal, as illustrated in Figure 7.4. An additional ten CVN specimens were extracted from the base metal away from the welding area of the control segment in order to compare the fracture toughness of the base metal with that of the weld repaired segments. Hence, eleven subsets of 10 CVN specimens were extracted in total. The CVN specimens of each subset were tested at temperatures of -50, -25, 0, 20 and 60^0 in order to develop the CVN-temperature relationship for the HAZ of each weld segment and the base metal. Two specimens were tested for every temperature.

Finally, for the visual inspection, microscopy and micro-hardness tests, three 100x25x20mm specimens were obtained only for the control segment and the weld segments with three, six and nine repairs in a position perpendicular to the welding direction with the weld metal at the centerline of the specimen, as shown in Figure 7.4. The surfaces of all the specimens were polished and etched in a solution of 4% Nital. Figure 7.5 shows photographs of a sample specimen, for each of the four weld segments, after polishing and etching. Specimens were assessed with a Nikon Epiphot 200 inverted metallurgical microscope with Clemex image analysis software to detect any weld defect at the weld area, fusion line, fusion lines between weld passes and HAZ. One specimen from each welding procedure was used for Vickers micro-hardness testing, which was carried out with a Clark CM-100AT manual micro-hardness tester equipped with a Vickers indenter. Measurements were taken using a Clemex digital camera and software at x500 magnification. The readings were taken from a clear focused optical image. The hardness was measured based on indentation sizes of 500gf loading. Measurements were taken at small increments along a 20mm straight line that passes through the base metal, HAZ and weld metal, at 8mm from the weld surface as shown in Figure 7.6a. The indent diamond shape is shown in Figure 7.6b at 500x magnification. The micro-hardness tests were conducted in order to capture the effect of multiple weld repairs on the hardness of the HAZ. The HAZ was expected to have higher hardness than other zones in the base metal due to the heat treatment that results in changes of the crystalline structure of steel to smaller grain sizes. Hence, the size of the HAZ could be measured through the micro-hardness test for each of the four studied specimens.

7.3 Results and Discussion of Material Testing

Based on reports provided by the fabricator, all ultrasonic inspection results after the first welding procedure as well as after each weld repair showed no unacceptable discontinuities or slag inclusions according to “Tables 6.2 and 6.3” of AWS D1.1 (2010).

7.3.1 Base metal reduced section tension tests

The reduced section tension specimens were obtained in the longitudinal direction (the direction of the plate rolling) and in the transverse direction. A summary of the results for each welding procedure is presented in Table 7.3. The Young's modulus (*E*), the yield stress (f_y) and the yield engineering strain of all specimens were based on strain gauge (5mm gauge length, 120Ω resistance) readings. The fracture of all specimens was located near the centre of the specimen and within the gauge length of the extensometer, as shown in Figure 7.7. It can be concluded from the results that all specimens met the requirements of ASTM A572 Gr.50 (2013) given in Table 7.1. The measured yield stress and ultimate stress values were between 1.04 to 1.10 of the ASTM A572 minimum values, which is within the expected range as denoted for this grade of steel in CAN/CSA-S16-14 (2014). Moreover, there was no significant difference in material yield stress and ultimate stress, as well as the engineering strain at fracture between specimens from the longitudinal and transverse directions of the plate.

7.3.2 Charpy-V-Notch tests

Charpy impact tests were performed for the base metal material as well as the HAZ. The highest and lowest testing temperatures represent the higher and lower shelf temperatures respectively, for the base metal. The CVN absorbed energy results are shown in Table 7.4 for all welding repair procedures, as well as the base metal. The CVN values for the base metal have exceeded the capacity of the testing apparatus (256J) at all testing temperatures; this indicates a high fracture toughness for the base metal material. The CVN test results at the HAZ for the specimens from all the weld segments showed high variability (Table 7.4). However, it can be concluded that in general the welding procedures have deceased the fracture toughness of the base metal at the HAZ. Furthermore, there is no clear correlation between the number of weld repairs and the value of the CVN absorbed energy. This is attributed to the variability associated with the weld repair procedure as it was a manual (gouging & grinding) - semi-automated (welding) process that depended on the dexterity of the welder; for example, this may have affected the consistency of the excavation dimensions. Moreover, all CVN values at 0°C and 21°C have attained the minimum value of 27J as given in the AWS D1.1 (2010) and CAN/CSA-W59 (2013) specifications.

7.3.3 Visual inspection and microscopy

All specimens extracted around the weld area for the four studied weld segments (control, 3, 6 and 9 repairs) were polished and visually inspected for defects. They were also etched and then scanned with the optical microscope to detect small defects such as porosity and slag inclusions at magnifications up to 1000x (Figure 7.5). Through visual inspection, no defects were detected for the specimens, regardless of the number of repairs. Additionally, no porosity or slag inclusion defects were spotted after thoroughly examining the etched surface of each specimen with the optical microscope (Figure 7.5). Figure 7.8 presents captures taken by the optical microscope at 200x magnification for the weld metal – base metal fusion area for each specimen. It can be seen that the specimen with three repairs has a similar HAZ grain size to the control specimen; however, the size of the grains in the HAZ for the specimens with six and nine repairs is smaller. This is attributed to the additional heating and cooling cycles associated with the six and nine repairs specimens, which subjects the HAZ to a similar procedure to that used when quenching steel (Jefferson and Woods, 1962, CWB/Gooderham-Centre, 2005).

7.3.4 Micro-hardness test

The Vickers micro-hardness test was conducted for visual inspection and microscopy specimens (Figure 7.5) and the results for each specimen are shown in Figure 7.9. The HAZ average Vickers hardness value for the control specimen was 200HV. For the specimens subjected to three, six and nine repairs, the HAZ Vickers hardness increased by 1.2, 1.4 and 0.5% of that of the control specimen respectively. In conclusion, the number of weld repairs had no significant effect on the hardness value of the HAZ as shown by the micro-hardness test results. The results also illustrate that the weld metal deposited through the SAW process has lower hardness than that of the weld metal deposited by the FCAW process; however, there is no significant difference in their minimum specified mechanical properties (Table 7.1). This is due to the presence of chemical compounds that increase the hardness of steel, such as Chromium, Molybdenum and Vanadium, in the welding electrode of the FCAW process (Table 7.1) (Jefferson and Woods, 1962, CWB/Gooderham-Centre, 2005). Recognizing that the HAZ is characterized by having higher hardness than other zones in the base metal due to the heating treatment (Jefferson and Woods, 1962, CWB/Gooderham-Centre, 2005), the start and end of the HAZ for each welding procedure was identified by detecting the change in the material hardness, as well as by visual identification of the change in the steel crystalline structure through an optical microscope. Consequently, the size of the resulting HAZs was calculated. The size of the HAZ for the control specimen and the specimen with three weld repairs was 1.75mm. The HAZ sizes for the specimen with six weld repairs and the specimen with nine weld repairs were 3.0 and 2.75mm, respectively. In conclusion, up to three weld repairs there is no significant change in the HAZ size, however the HAZ size increased once the number of weld repairs exceeded six by 60 to 70% of that of the control specimen. Moreover, in Figure 7.9, the transition between the hardness of HAZ to the weld metal is different in the three studied repair cases. This is attributed to the fact that the weld repair procedure is manual and therefore the width of the excavated area is not consistent for each conducted weld repair.

7.4 Summary and Conclusions

Weld repair is an essential part of any steel fabrication and retrofit process. Cases were reported of unrepairable cracks and fracture that were a result of weld repair, which resulted in changes of the properties of the heat affected zone (HAZ). In order to evaluate the effect of multiple weld repairs on the fracture toughness, microstructure and hardness of the HAZ, as well as its size, an experimental investigation was completed, involving the welding and repairing of two 25mm thick ASTM A572 Gr. 50 steel plates. The plates were first welded using an automated submerged arc welding prequalified procedure according to AWS D1.1 (2010), and then inspected for defects through ultrasonic inspection. Multiple weld repairs were subsequently conducted at each of the nine segments on the plates; one additional segment, designated as the control, was not repaired. The number of repairs ranged from one to nine. Material test specimens for the aforementioned weld repair scenarios were extracted from each segment, and tensile coupon specimens were obtained from the plates' base metal to verify its properties. The main observations of the experimental investigation are as follows:

- The ultrasonic inspection tests conducted on the welded plates after the SAW, and after each weld repair, detected no unacceptable defects according to "Tables 6.2 and 6.3" of AWS D1.1 (2010).

- The tensile tests conducted for the base metal met the requirements of ASTM A572 Gr.50 (2013). The results showed consistency of the mechanical properties of the base metal in the rolling and transverse directions.
- The variability in the weld repair procedure, due to the manual nature of gouging, grinding and flux core arc welding, resulted in high variability in the CVN values of specimens taken from each repaired weld segment.
- Based on the CVN tests conducted for the base metal of the welded plates, the CVN values of the metal were found to exceed the limit of the impact tester used (256J).
- The CVN test results showed that the CVN values at the HAZ were less than those at the base metal. However, the HAZ CVN values met the requirements of the AWS and CSA specifications.
- Based on visual inspection and microscopy, no defects were detected on the etched surface of specimens cut from the weld segment of the control, three, six and nine repairs.
- Microscopy also showed that for up to three repairs there was no change in the grain size of the HAZ, however after six repairs the grain size at the HAZ had decreased.
- Based on the hardness test the weld metal of the SAW procedure has less hardness than that of the FCAW procedure due to chemical components present in the FCAW electrode, which improve its hardness (Jefferson and Woods, 1962, CWB/Gooderham-Centre, 2005).
- There is no significant effect of the number of weld repair on the hardness of the HAZ.
- There is no significant effect of the number of weld repairs on the HAZ size up to three weld repairs. The HAZ size increased, when more than six weld repairs were carried out, by 60 to 70% of that existing after the initial welding procedure.

Based on the stated results, a recommendation of a maximum of three weld repairs for structural steel assemblies is made in order to avoid increasing the size of the HAZ. Even though the main concern of the thesis is the utilization of thick plates for welded assemblies, this experimental investigation provides guidance on the effect of multiple weld repairs on the HAZ of structural steel plate. In the future a similar study for thicker plates is required.

Acknowledgments

The authors sincerely thank the ADF Group Inc. and DPHV Structural Consultants for their financial and technical support and for their contribution in conducting the weld experiments and providing the test specimens. The authors also thank Mr. Nicolas Roy for his assistance and advice with respect to weld engineering. The authors recognize the Department of Mining and Materials Engineering in the Faculty of Engineering at McGill University for providing technical support and access to the Materials and Characterization Laboratories to conduct a portion of the materials testing. The authors also acknowledge the financial support from the Natural Sciences and Engineering Research Council of Canada.

Table 7.1: Minimum mechanical properties and typical chemical composition for the base and weld metal according to ASTM A572 Gr.50 (2013) and AWS A5.20/A5.20M (2005 (R2015))

	Mechanical Properties				Typical Chemical Composition [wt.%]									
	Yield Stress [MPa]	**Ultimate Stress [MPa]**	**Min. Elongation at 50mm [%]**	**Min. CVN absorbed energy [J]**	**C**	**Mn**	**P max.**	**S max.**	**Si**	**Cr**	**Ni**	**Mo**	**V**	**Cu**
A572 Gr.50	345	450	21	27 at 21ºC	0.21	1.35	0.04	0.05	0.15-0.4	-	-	-	-	-
F7A4-EM12K	400	480-660	22	27 at -40ºC	0.07	1.5	0.02	0.011	0.5	-	-	-	-	-
E71T-9C-H4/H8	390	490-670	22	27 at -30ºC	0.12	1.75	0.9	0.03	0.03	0.2	0.5	0.3	0.08	0.35

Table 7.2: Welding procedures specifications.

Welding Parameter	Welding Procedure		Repair Procedure
	Side1	**Side2**	
Welding Process	SAW	Gouge to sound metal + SAW	FCAW
Number of passes	4	5	9
Current [A]	500 for passes 1 and 2 750 for passes 3 and 4 DC+	500 for passes 1 and 2 750 for passes 3 and 5 DC+	260-320
Average Voltage [V]	28	28	26-30
Electrode type	F7A4-EM12K	F7A4-EM12K	E71T-9-H4/H8
No. and diameter of electrodes [mm]	1X2.4 for passes 1 and 2 2x2.4 for passes 3 and 4	1X2.4 for passes 1 and 2 2x2.4 for passes 3 to 5	1x1.6
Average Wire feed speed [cm/min]	325 for passes 1 and 2 265 for passes 3 and 4	325 for passes 1 and 2 265 for passes 3 to 5	685-800
Average Weld travel speed [mm/sec]	8	8	5-6.5
Average Heat input [KJ/mm]	1.83 for passes 1 and 2 2.7 for passes 3 and 4	1.83 for passes 1 and 2 2.7 for passes 3 to 5	1-1.85

Table 7.3: Base metal reduced section tensile test results.

Specimen direction	Specimen No.	Young's Modulus [MPa]	Yield Stress [MPa]	Yield Strain	Ultimate Stress [MPa]	Ultimate Strain	Strain at Fracture
Longitudinal	**1**	225000	372	0.0017	471	0.172	0.316
	2	241000	368	0.0015	486	0.17	0.388
Transverse	**1**	227000	361	0.0016	468	0.161	0.362
	2	216000	379	0.0018	470	0.223	0.357

Table 7.4: Charpy-V-Notch absorbed energy values for base metal and HAZ.

Temperature	CVN Values				
	-50°C	**-25°C**	**0°C**	**21°C**	**60°C**
Base Metal	256	256	256	254	247
	-	256	256	256	248
No Repairs	138	170	142	160	207
	-	127	156	193	249
1 Repair	107	147	162	207	254
	19	130	238	206	255
2 Repairs	132	151	209	190	215
	34	164	116	213	189
3 Repairs	14	132	140	197	202
	50	34	135	222	192
4 Repairs	23	54	62	174	91
	11	30	189	146	130
5 Repairs	141	134	94	172	110
	105	136	183	172	91
6 Repairs	26	57	69	98	98
	28	120	132	196	117
7 Repairs	17	46	188	134	200
	19	81	99	197	178
8 Repairs	13	22	126	126	162
	100	140	142	207	199
9 Repairs	127	149	150	125	182
	27	58	192	89	146

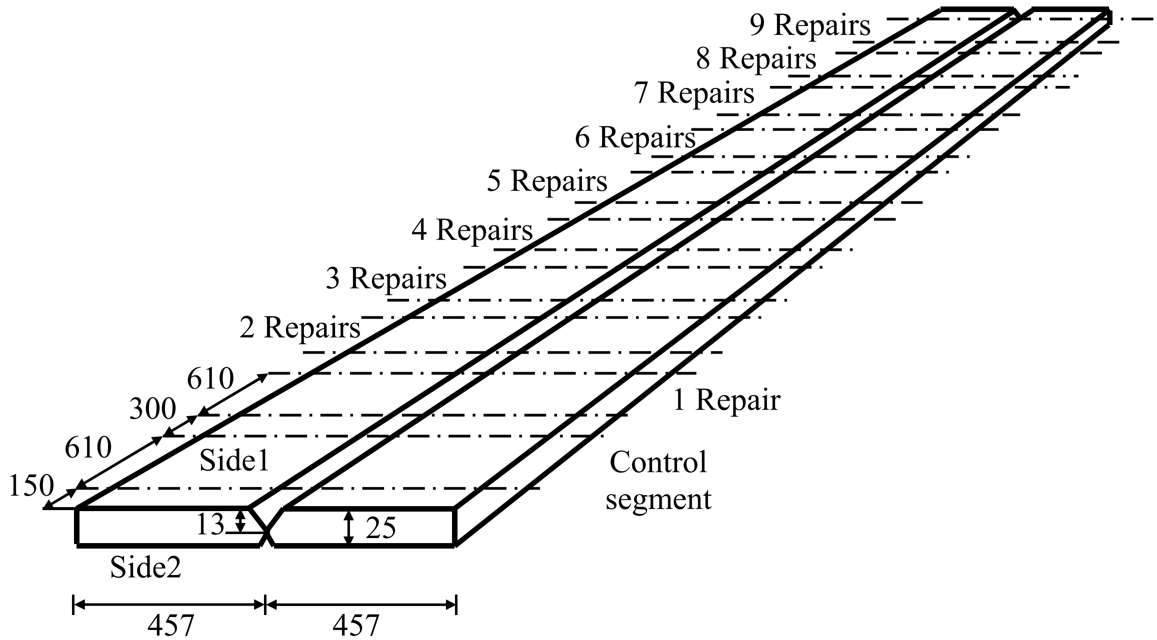

Figure 7.1: Test plate layout and the control - weld repair segments (dimensions are in mm).

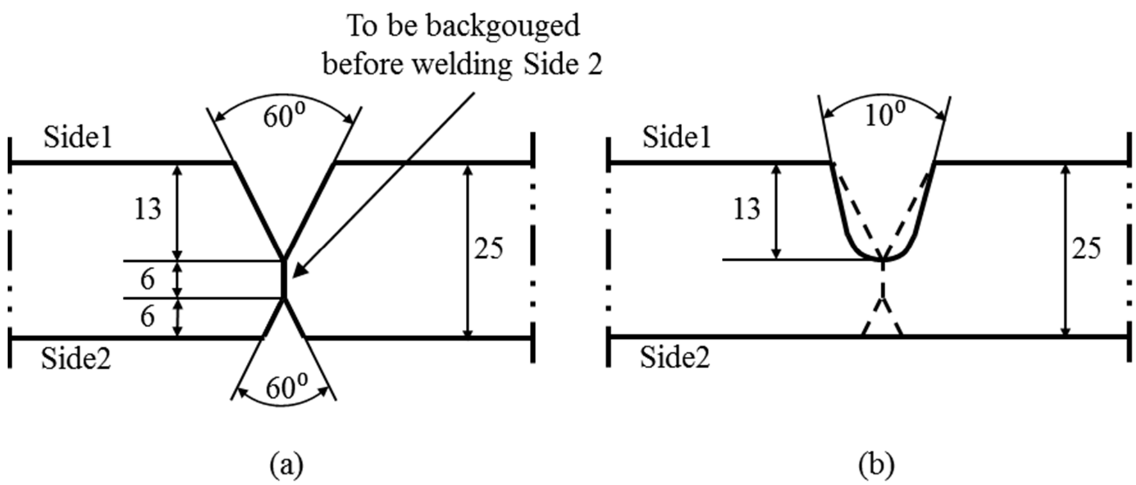

Figure 7.2: Illustration of steel plate assemblies for; a) initial SAW procedure, b) weld repair procedure (dimensions in mm).

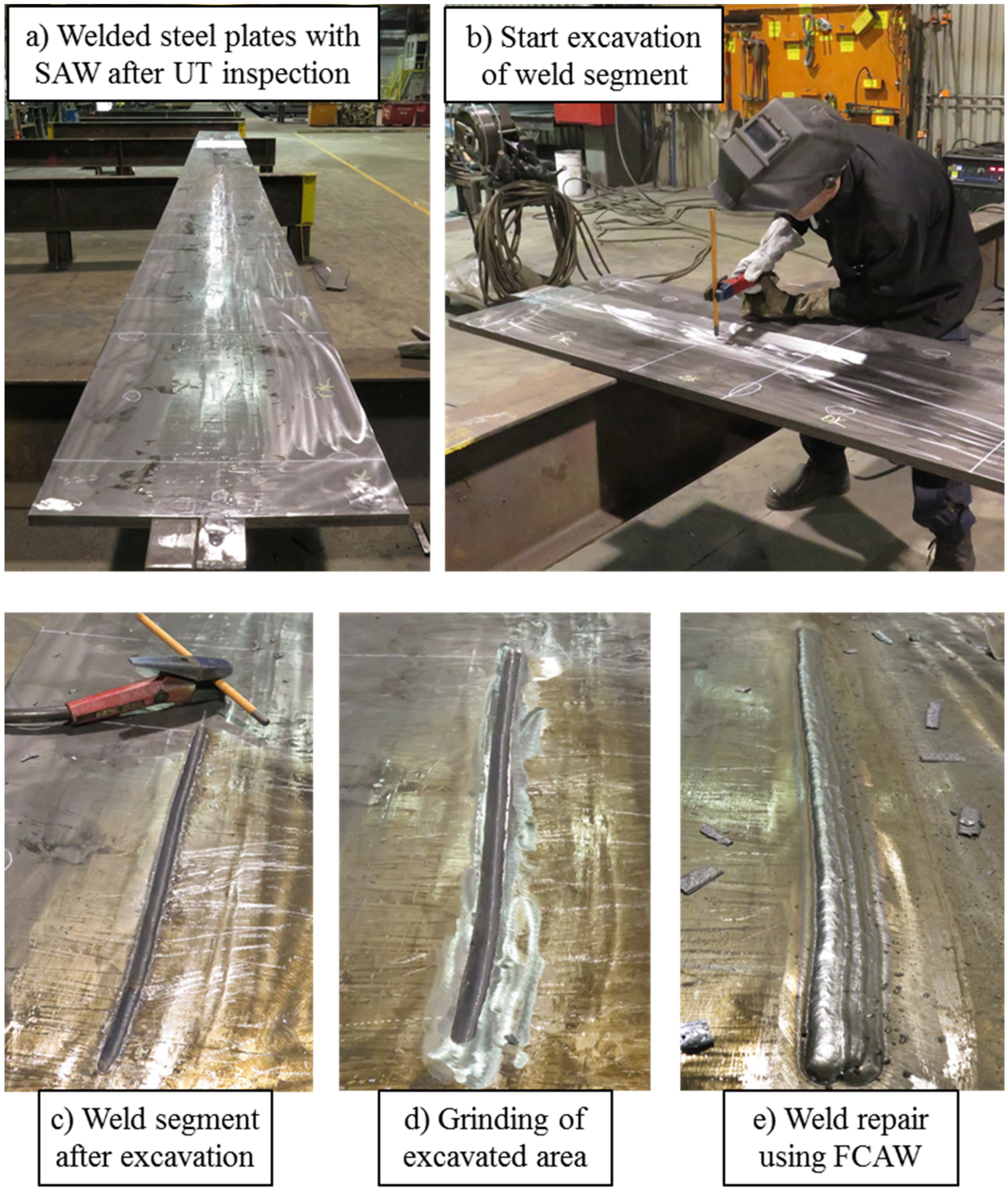

Figure 7.3: Steps of weld repair of one of the studied segments.

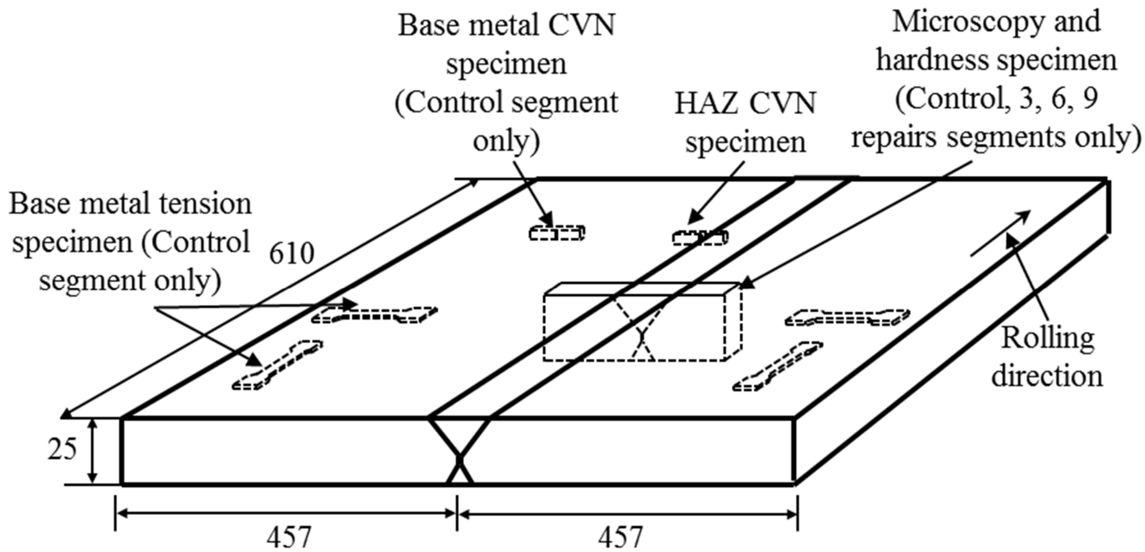

Figure 7.4: Illustration of the locations of specimens extracted for mechanical testing at each weld repair segment (dimensions in mm).

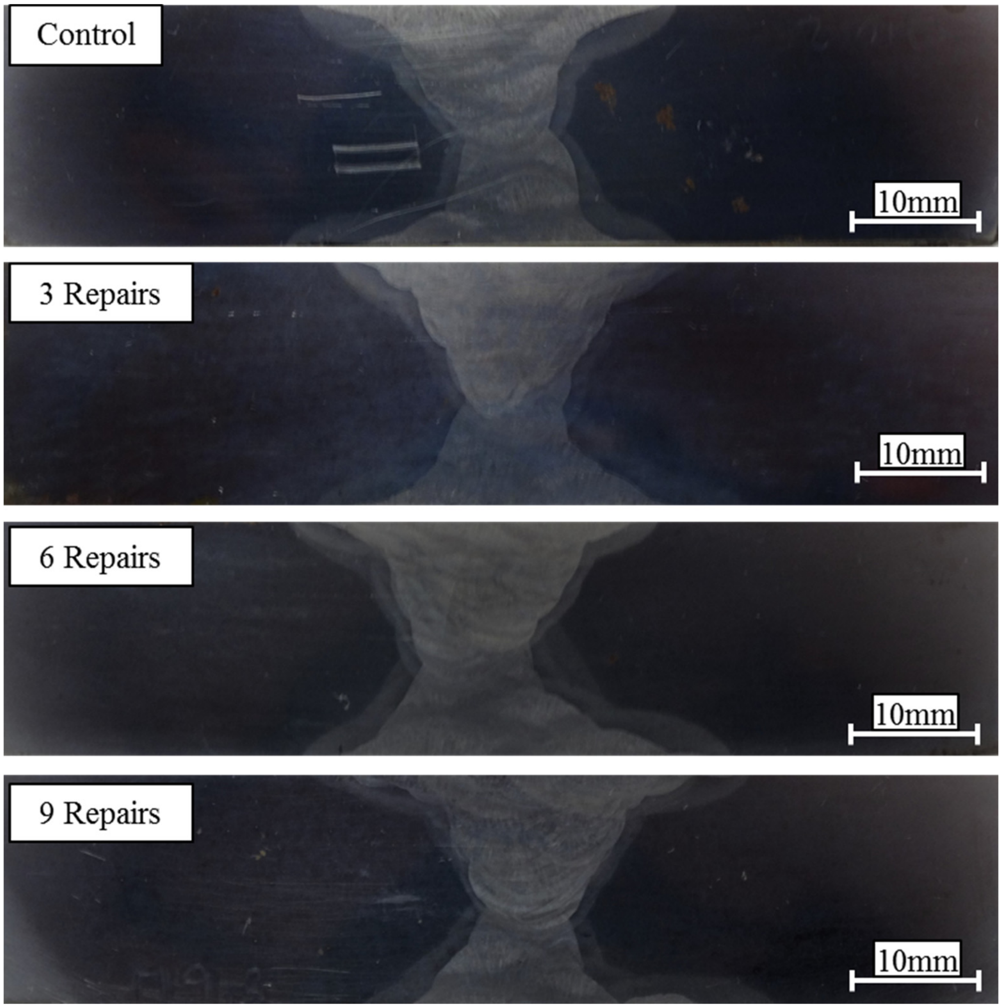

Figure 7.5: Sample of specimens used for microscopy for the studied weld repair segments.

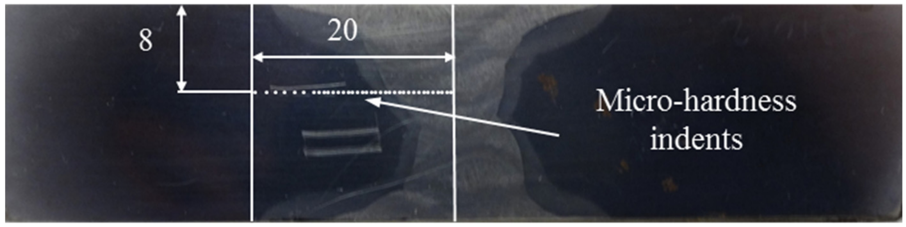

(a)

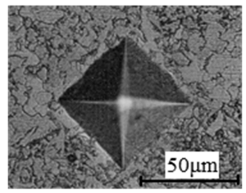

(b)

Figure 7.6: Micro-Hardness test for specimens used in microscopy; a) location of testing path on the specimen (dimensions are in mm), b) 500x magnification of an indent on the specimen.

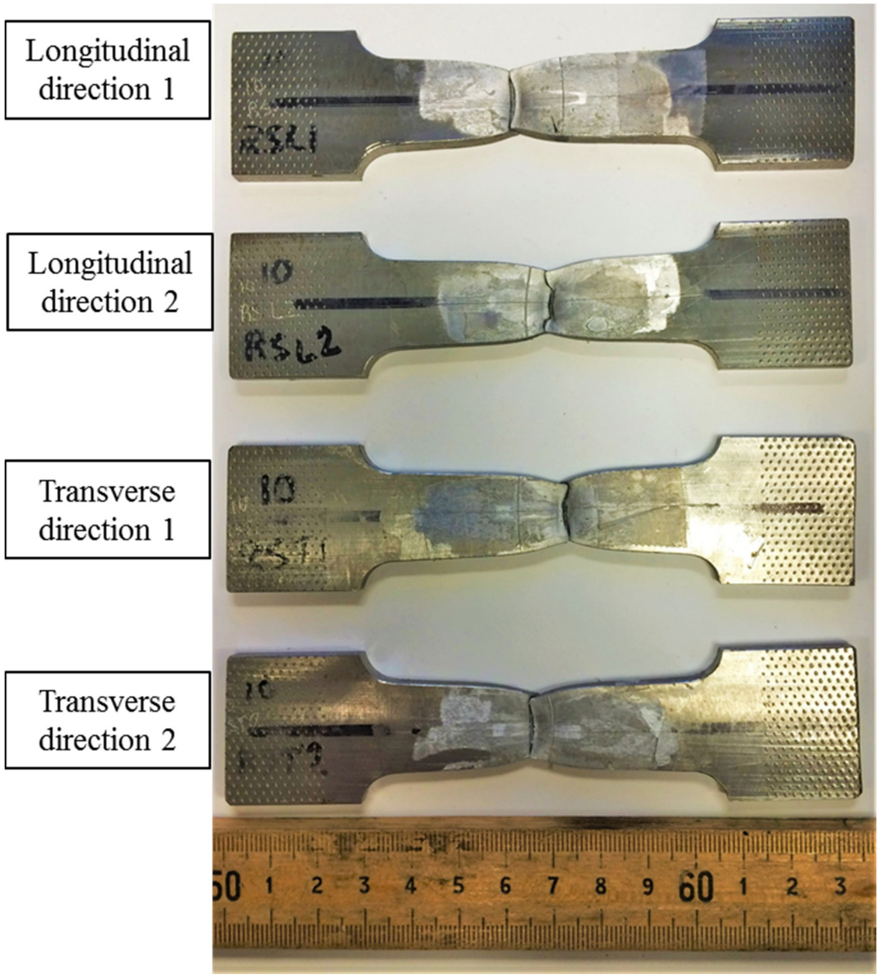

Figure 7.7: Base metal reduced section tension specimens after fracture.

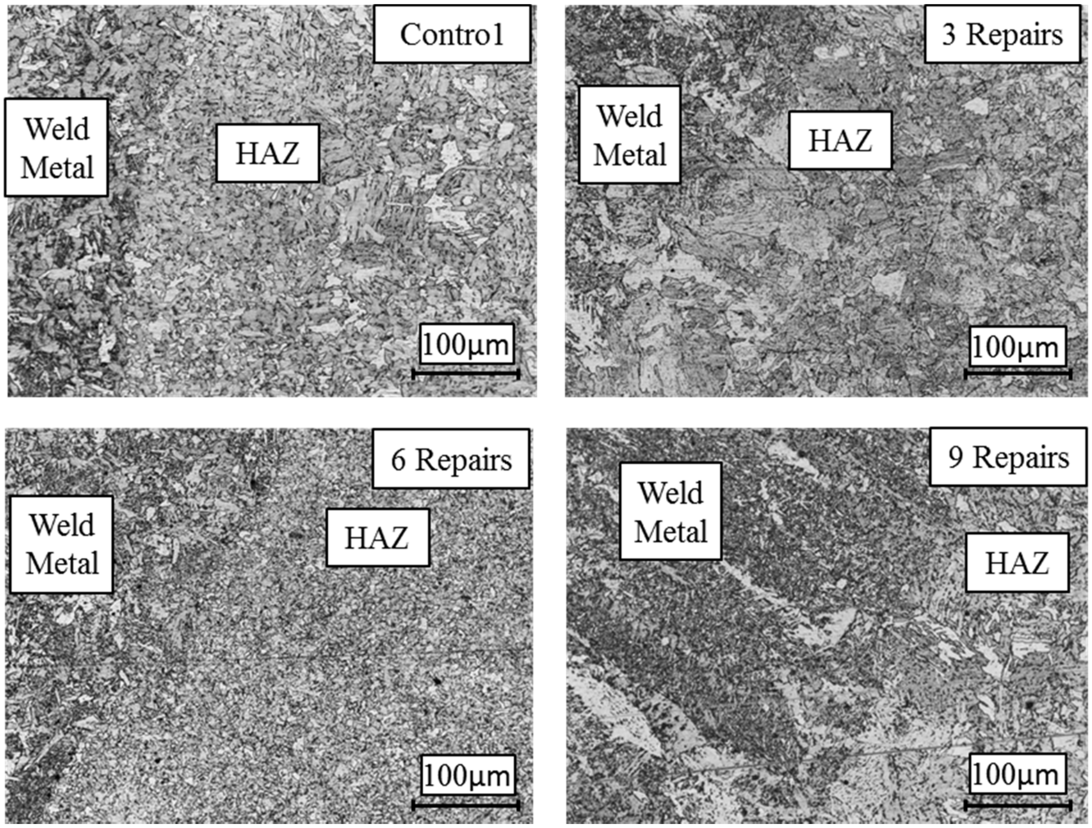

Figure 7.8: Optical microscope screen captures at fusion line for each welding procedure at 200x magnification.

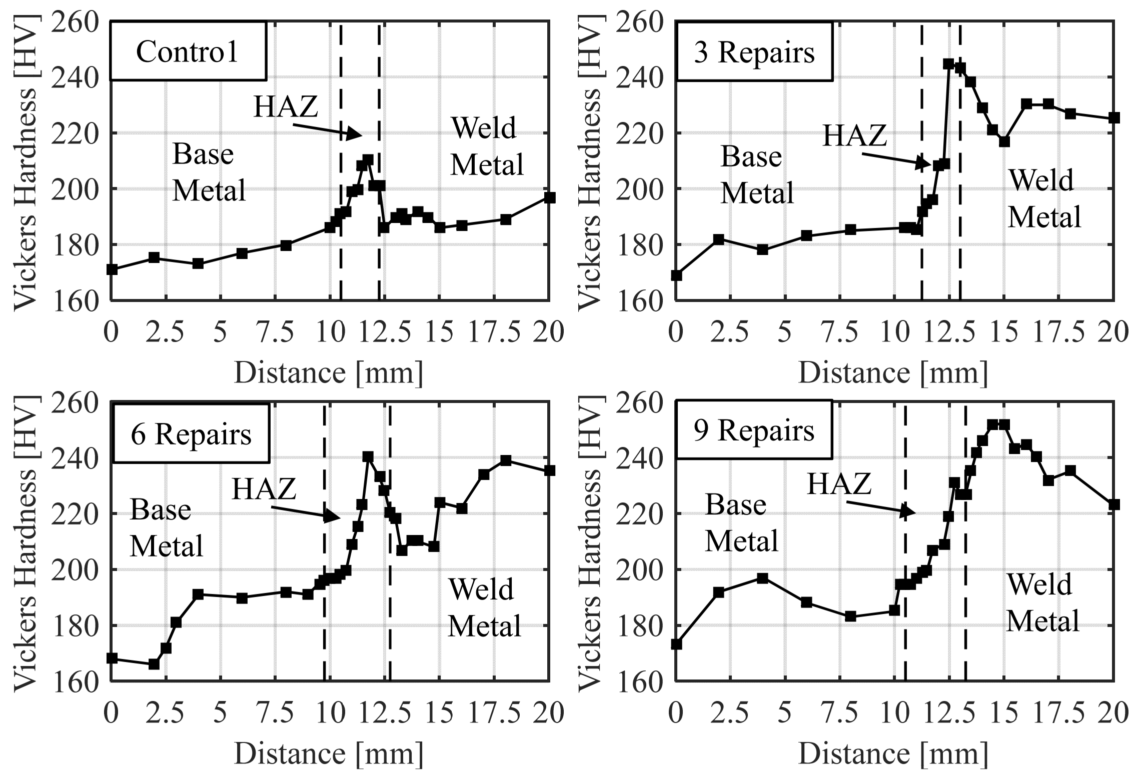

Figure 7.9: Micro-hardness test results across the base metal, HAZ and weld metal for each of the four studied samples.

Chapter 8 SUMMARY AND CONCLUSIONS

8.1 Overview

The use of heavy steel plates and built-up assemblies has become a common practice in steel construction due to design requirements that account for loads arising from blast and large earthquakes. Welding is often used in steel construction for joining components. Steel fabricators have reported unrepairable cracks because of the high residual stresses associated with the welding procedures of these heavy steel components. The main objective of this thesis was to provide quantitative guidelines for the submerged arc welding procedure and an assessment technique for discontinuities in butt-welded steel plates of thicknesses greater than 25mm. These objectives were achieved through detailed finite element analysis of the welding procedure for two case studies involving thick steel plates, which were validated with experimental results (Chapter 3). Additionally, a statistical assessment was carried out of Charpy-V-Notch impact test results of specimens extracted from different locations of a benchmark built-up box column that utilized 75mm thick steel plates. The purpose was to evaluate the fracture toughness uncertainty in the thick steel plates; thereby, providing an assessment criteria for crack initiation (Chapter 4). Using the validated finite element simulation of the welding procedure, along with crack initiation assessment criteria, a parametric study was completed for welding procedure parameters. Each parameter was assessed based on the resulting residual stresses as well as the results of the crack initiation assessment criteria. Based on the results of the parametric study quantitative recommendations were provided for the welding of thick steel plates (Chapter 5). Moreover, an experimental investigation of the effects of different welding procedures on the weld quality and heat affected zone (HAZ) was carried out; recommendations were given in addition to the parametric study results (Chapter 6). Finally, in steel fabrication it is common to repair discontinuities developed by the welding procedure as well as pre-existing discontinuities in steel components. A weld repair experiment was conducted to study the effect of multiple weld repairs on the properties of the heat affected zone. Recommendations were made regarding the maximum number of weld repairs to minimize the negative effects on the properties of the heat affected zone (Chapter 7).

8.2 Conclusions and Recommendations

This section summarizes the main conclusions as well as the recommendations developed for the welding procedure of thick steel plate. The main contributions of this research to the steel specifications are presented in Section 8.2.1. Conclusions derived from the tensile and fracture toughness tests conducted at various locations of welded thick steel plates are summarized in Section 8.2.2. The results of the study related to the effects of the parameters of the steel material on the probability of crack initiation are summarized in Section 8.2.3. Recommendations for the finite element simulation of commonly used welding procedures in heavy built-up box columns are given in Section 8.2.4. The main conclusions from the welding procedure parametric study are summarized in Section 8.2.5. The main findings from the welding procedures and weld repair experiments are summarized in Sections 8.2.6 and 8.2.7, respectively.

8.2.1 Original contributions to structural steel specifications

The main contributions to the structural steel specification are summarized herein:

- A discontinuity acceptance approach was proposed to calculate the probability of a crack to initiate through a steel component accounting for the uncertainty in its fracture toughness for different steel grades, thicknesses and at different temperatures. This methodology was developed based on rigorous statistical treatment of a large database of Charpy-V-Notch absorbed energy values that was developed for the studied steel grades.
- Based on the results of the parametric study, four welding procedures using the submerged arc welding process were recommended for butt welded thick steel plates. The post weld residual stress distributions are improved compared with those found for the commonly used welding procedure based on AWS D1.1 (2010) and CAN/CSA-W59 (2013). This was verified through welding experiments on 75mm thick plates.
- Based on the stress distribution of the four suggested welding procedures, the acceptable size and location of surface and through thickness discontinuities existing in the base metal before welding is proposed for steel plates, welded in minimal restraint conditions and

plates welded in high restraint conditions, for a probability of crack initiation of 2% (corresponding to AWS and CSA Charpy-V-Notch acceptance limit of 27J for ASTM A572 Gr.50 steel).

8.2.2 Mechanical properties and fracture toughness of thick steel plates

Based on material tests conducted on specimens from a built-up box-column that was used as a benchmark, the following conclusions were drawn:

- The regions near the welded area and regions through the plate thickness showed lower ductility (strain at fracture 0.16) than the expected nominal value for the steel grade (0.21) (ASTM A572 Gr.50, 2013).
- For tensile coupons located through the thickness of the steel plate and near the welding area the average engineering strain at fracture was lower than the specified minimum elongation for the material steel grade.
- Tensile coupons extracted from locations at the plate surface and from locations away from the weld had lower coefficient of variation for plastic strains compared to those that were extracted from the location through the plate thickness and near the weld.
- Charpy-V-Notch impact test results show a high coefficient of variation (i.e., COV ~ 60%) at lower shelf temperatures, which reveals high variability in the obtained CVN values from the same location category and correspondingly, the fracture toughness of the steel material.
- Charpy-V-Notch specimens near the weld and through the thickness showed low CVN values compared to specimens near the weld and at the plate surface at the same temperatures.

8.2.3 Properties of the finite element simulation of the welding procedure

A finite element based welding procedure simulation approach was proposed that can be used to evaluate various automated submerged arc welding procedures to determine the subsequent residual stress distributions in the steel plates. The main conclusions and recommendations are summarized as follows:

- Mesh sensitivity studies suggest that element sizes should be a minimum of 2mm and a maximum of 9mm for the development of 3-Dimensional (3-D) welding simulation models.
- The creep strain properties of the steel material had no significant impact on the stress distribution results of the finite element simulation of the welding procedure. Therefore, the creep strain properties can be excluded from the welding procedure simulation for the studied welding procedure.
- The proposed finite element modeling approach was able to predict the measured temperature values, from a welding experiment with reasonable accuracy. In particular, the maximum difference between predicted and measured temperature values were in the order of 20% or less.
- The variation of mechanical properties through the thick plate thickness did not have a significant impact on the residual stress distribution after the end of the welding procedure. An assumption of uniform material mechanical properties in the simulation is reasonable.

8.2.4 Effect of material properties on the probability of crack initiation

The proposed probabilistic approach for assessing discontinuities in steel plates was utilized to study the impact of different parameters on the probability of a crack to initiate during or after a welding process. The main findings are summarized as follows:

- An edge crack is more prone to initiate under a specified stress level than a through thickness crack, which in turn has a higher probability of initiation compared with an embedded circular crack. The proposed approach for assessing discontinuities in steel plates takes the type of discontinuity into account.
- A high strength steel material has a higher probability of crack initiation than a low strength steel material. Additionally, the uncertainty associated with the fracture toughness value increases with the steel yield stress.
- With an increase in the CVN testing temperature the probability of crack initiation decreases until the maximum fracture toughness of the steel material is reached. The difference between the probability of crack initiation in the lower and upper shelf temperatures in the direction parallel to rolling is always higher than that in the perpendicular direction.

- As the steel plate thickness becomes greater the uncertainty in the fracture toughness values of the steel component increases. This illustrates how a probabilistic approach for assessing discontinuities approach is essential for steel components that utilize thick plates.

8.2.5 Effect of welding procedure parameters on residual stresses of thick steel plates

The proposed finite element approach was utilized to conduct a comprehensive parametric study of the effect of the main parameters of the welding procedure on the residual stress distribution in welded steel plates. The main conclusions from this study are presented herein:

- A low heat input of the welding procedure develops lower residual stresses than welding procedures utilizing higher heat input values.
- Welding travel speeds greater than 10mm/s result in a narrower high tensile stress area in the base metal than slow welding travel speeds, however the maximum tensile stress values are higher.
- As the welding travel speed increases the maximum tensile residual stresses decrease.
- Applying preheat/inter-pass temperature is essential for welding thick steel plates, however the improvement in the stress distribution achieved by applying temperatures greater than 110°C is not significant.
- The welding related tensile transverse residual stresses become greater as the thickness of the welded plates is increased, whereas the longitudinal tensile residual stresses decrease. Thin steel plates are more susceptible to deformations imposed from the welding procedure than thicker steel plates.
- A narrower tensile stressed area in the base metal is created when the number of welding passes increases. The magnitude of maximum tensile stresses also increases in this case.
- As the number of welding passes decreases the maximum tensile residual stresses decreases.

8.2.6 Results of the welding procedures experimental investigation

Welding experiments involving five submerged arc welding procedures were conducted to study the effect of different parameters on the weld quality as well as the HAZ toughness and size. The parameter variation as part of the five welding procedures included: (a) the weld heat input, (b) the number of weld passes, (c) the current, (d) the number of electrodes, (e) the size and type of electrodes, (f) the welding wire feed speed and (g) electrode travel speed. Mechanical tests were conducted on specimens taken from each of the five welded plate specimens, comprising; side bend tests, reduced section tension tests, all-weld metal tension tests and Charpy-V-Notch (CVN) impact tests. Additional specimens were extracted for microscopy and micro hardness tests. The main conclusions of this experiment are summarized as follows:

- Two out of eight side bend specimens of the commonly used welding procedure per AWS D1.1 (2010) for the tested welding assembly developed a crack in the weld metal.
- One out of eight side bend specimens for the welding procedure with the highest heat input had a crack at the fusion line between the weld metal and base metal.
- From the results of the reduced section and all-weld metal tension tests it was concluded that increasing the number of passes while having a low average heat input per welding pass increases the yield stress of the weld metal.
- The welding procedure specification had no impact on the lower shelf fracture toughness of the weld metal or that of the HAZ. However, each welding procedure in general, regardless of the specification, decreased the lower shelf CVN value of the base metal from 31J to 13J near the HAZ.
- Based on the results of the CVN tests conducted at the HAZ and weld metal, the fracture toughness at upper shelf temperatures was affected by the welding arc procedure; such that using tandem arc welding with DC+ and AC produced higher fracture toughness than using DC+ current alone.
- The upper shelf fracture toughness is mainly dependent on the heat input, number of passes and current. As these parameters describe the number and amplitude of heating and cooling cycles applied in the welding procedure, which if increased, acts to increase the material yield stress while decreasing its resistance to crack initiation.
- By neglecting the heat input produced by an AC current for welding procedures D and E the fracture toughness is found to correlate to the heat input produced by a DC+ current only.
- Increasing the number of welding passes with low heat input per welding pass increases the hardness of the HAZ.

- Based on the results of the micro-hardness tests the size of the HAZ is mainly dependent on the heat input, number of passes used in the welding procedure and the ratio of the sum of electrode diameters to number of passes (the HAZ size increases from 2.25 to 4.25mm when the number of passes decreases from 7 to 4 and when the ratio of electrode diameter-to-number of passes increases from 0.7 to 2.4mm).

8.2.7 Effect of multiple weld repairs on the toughness and size of the heat affected zone

Weld repair is an essential procedure during steel fabrication and is typically done after welding thick steel plates due to high weld-related residual stresses and defects. An experimental investigation was conducted, involving the welding and repairing of two 25mm thick steel plates. Based on these tests, the effect of multiple weld repairs on the fracture toughness, microstructure and hardness of the HAZ, as well as its size was evaluated. Multiple weld repairs were conducted on nine segments on the two welded plates ranging from one to nine weld repairs; as well as one additional segment as the control specimen that was not repaired. Material test specimens for the aforementioned weld repair scenarios were extracted from each segment, and tensile coupon specimens were obtained from the plates' base metal to verify its properties. The main observations of the experimental investigation are as follows:

- The tensile tests conducted for the base metal met the requirements of ASTM A572 Gr.50 (2013) steel. Additionally, the results showed consistency of the mechanical properties of the base metal in the rolling and transverse directions.
- The variability in the weld repair procedure is fairly large. This is due to the manual nature of weld gouging, grinding and flux core arc welding. This can be seen from the high variability in the CVN values of specimens taken from each repaired weld segment. This also means that with the increase of number of weld repairs the uncertainty in the fracture toughness value of the heat affected zone increases
- Based on the CVN tests conducted for the base metal of the welded plates, the CVN values of the metal were found to exceed the limit of the impact tester (256J). All the base metal CVN results met the minimum requirements of 27J at 0^oC (AWS D1.1, 2010)

- The CVN test results showed that the CVN values at the HAZ were less than those at the base metal. However, the CVN values at the HAZ met the requirements of AWS D1.1 (2010) and CAN/CSA-W59 (2013).
- Based on Microscopy conducted for weld defects inspection it was found that for up to three repairs there was no change in the grain size of the HAZ, however after six repairs the grain size at the HAZ had decreased.
- Based on hardness tests the weld metal of the SAW procedure had less hardness than that of the FCAW procedure due to chemical components present in the FCAW electrode, which improve its hardness.
- The hardness of the HAZ seems to be more-or-less the same regardless of the number of weld repairs.
- The size of the HAZ seems to be the same if the number of weld repairs is less or equal to three. The HAZ size increased, when more than six weld repairs were carried out, by 60 to 70% of that existing after the initial welding procedure.
- A maximum of three weld repairs is recommended to avoid increasing the size of the HAZ.

8.3 Recommendations for Future Work

In this PhD thesis, quantitative recommendations for butt welded assemblies of thick steel plates were developed. Based on the findings of this research the following recommendations are suggested for future studies:

- A reliability study for the results of the proposed numerical simulation for the welding procedure to determine the accuracy and stability of the developed welding residual stress distributions.
- The welding simulation approach developed in this study can be used to conduct an investigation of the welding procedures for other weld assemblies; for instance, welded beam-to-column connections, comprising wide flange beams with thick flanges, and column splices, comprising jumbo wide-flange cross-sections that are commonly used in high-rise buildings. These subassemblies are often present in buildings subjected to seismic loads, which makes the welding tensile residual stresses more critical because they may lead to crack initiation.

- The use of high strength steel is becoming common in steel construction. Based on test results from this study, the higher the grade of the steel the lower the fracture toughness and the greater the variability of the fracture toughness. This is consistent for commonly used steel in North America. Consequently, to avoid crack initiation due to the welding procedure a similar investigation of the welding parameters on the heat affected zone in high strength steel should be conducted.
- An experimental investigation of the effect of multiple weld repairs on the tensile residual stress in the heat affected zone of the repaired assembly is required. Additionally, a numerical simulation of the welding repair procedure can be developed to study the effect of each parameter in this process; as such, improving the resultant residual stress distributions.
- A comprehensive study is required to evaluate the effect of multiple weld repairs on the fracture toughness value as well as the uncertainty in its value at the heat affected zone.
- A welding procedure simulation including the steel material phase changes during the heating and cooling process is required, as well as the explicit simulation of fracture. As a result, a more thorough study of the effect of the welding procedure on the steel microstructure and crack initiation tendencies should be conducted.

BIBLIOGRAPHY

Acevedo, C., Drezet, J. M., and Nussbaumer, A. (2013). "Numerical modelling and experimental investigation on welding residual stresses in large-scale tubular K-joints." *Fatigue Fract Eng M*, 36(2), 177-185.

American Society of Civil Engineers. (2013). *Minimum design loads for buildings and other structures*, Published by American Society of Civil Engineers, Reston, Virginia.

Andrade, E. N. (1910). *On the Viscous Flow in Metals, and Allied Phenomena*.

ANSI/AISC 341-10 (2010). "AISC 341-10." *Seismic Provisions for Structural Steel Buildings*, American Institute of Steel Construction, Chicago, Illinois.

ANSI/AISC 358-10 (2010). "AISC 358-10." *Prequalified Connections for Special and Intermediate Steel Moment Frames for Seismic Applications*, American Institute of Steel Construction, Chicago, Illinois.

ANSI/AISC 360-10 (2010). "AISC 360-10." *Specification for structural steel buildings*, American Institute of Steel Construction, Chicago, IL, USA.

ASM International Handbook Committee (1990). *ASM Handbook: Properties and selection*, ASM International.

ASTM A36 (2014). "A36 / A36M-14 Standard Specification for Carbon Structural Steel." ASTM International, West Conshohocken, PA.

ASTM A370 (2014). "A370-14 Standard Test Methods and Definitions for Mechanical Testing of Steel Products."

ASTM A516 Gr.70 (2015). "ASTM A516/516M-10(2015) Standard Specification for Pressure Vessel Plates, Carbon Steel, for Moderate- and Lower-Temperature Service."

ASTM A572 Gr.50 (2013). "A572/A572M-13a Standard Specification for High-Strength Low-Alloy Columbium-Vanadium Structural Steel."

ASTM A588 Gr.B (2010). "ASTM A588/A588M-10 Standard Specification for High-Strength Low-Alloy Structural Steel, up to 50 ksi [345 MPa] Minimum Yield Point, with Atmospheric Corrosion Resistance."

ASTM A709 (2013). "A709 / A709M-13a Standard Specification for Structural Steel for bridges." ASTM International, West Conshohocken, PA.

ASTM A913 Gr.65 (2014). "A913/A913M-14a Standard Specification for High-Strength Low-Alloy Steel Shapes of Structural Quality, Produced by Quenching and Self-Tempering Process."

ASTM A992 Gr.50 (2011). "A992 / A992M-11, Standard Specification for Structural Steel Shapes." ASTM International, West Conshohocken, PA.

ASTM E384-11e1 (2011). "Standard Test Method for Knoop and Vickers Hardness of Materials." ASTM International, West Conshohocken, PA.

AWS A5.17/5.17M (1997 (R2007)). *ANSI/AWS A5.17/A5.17M-97, Specification for Carbon Steel Electrodes and Fluxes for Submerged Arc Welding*, American Welding Society.

AWS A5.20/A5.20M (2005 (R2015)). *AWS A5.20/A5.20M-2005, Specification for Carbon Steel Electrodes for Flux Cored Arc Welding*, American Welding Society.

AWS D1.1 (2010). "AWS D1.1 2010." *Structural welding code—steel*, American Welding Society, Miami, FL, USA.

AWS D1.8 (2009). "AWS D1. 8 2009." *Structural Welding Code -- Seismic Supplement*, American Welding Society, Miami, FL, USA.

Barsom, J. M., and Rolfe, S. T. (1987). *Fracture and fatigue control in structures : applications of fracture mechanics*, Prentice-Hall, Englewood Cliffs, N.J.

Bate, S. K., Green, D., and Buttle, D. (1997). "A Review of Residual Stress Distribution in Welded Joints for the Defect Assessment of Offshore Structures." *Health and Safety Executive – Offshore Technology Report.*, Health and Safety Executive – Offshore Technology.

Benjamin, J. R., and Cornell, C. A. (1970). *Probability, statistics, and decision for civil engineers*, McGraw-Hill, New York,.

Bjorhovde, R., Brozzetti, J., Alpsten, G. A., and Tall, L. (1972). "Residual Stresses in Thick Welded Plates." *Weld J*, 51(8), S392.

Bletzacker, R. W. (1966). *Effect of Structural Restraint on the Fire Resistance of Protected Steel Beam Floor and Roof Assemblies*, Engineering Experiment Station, Ohio State University.

Blodgett, O. W., Funderburk, R. S., Miller, D. K., and Quintana, M. (1999). *Fabricators' and Erectors' Guide to Welded Steel Construction*, The James F. Lincoln Arc Welding Foundation.

Blodgett, O. W., and Miller, D. K. (1993). "The Challenge of Welding Jumbo Shapes." *Welding Innovation, James F. Lincoln Arc Welding Foundation*, X, 3-16.

Boresi, A. P., and Sidebottom, O. M. (1972). "Creep of Metals Under Multiaxial States of Stress." *Nuclear Engineering and Design*, 18(1972), 415-456.

Brickstad, B., and Josefson, B. L. (1998). "A Parametric Study of Residual Stresses in Multi-Pass Butt-Welded Stainless Steel Pipes." *Journal of Pressure Vessel and Piping*, 75, 11-25.

British Standards Institution. (2001). "Eurocode 3: Design of steel structures : Part 1.2 General rules. Structural fire design (together with United Kingdom National Application Document)." *DD ENV 1993-1-1 : 2001*, BSI, London.

Brozzetti, J., Alpsten, G. A., and Tall, L. (1971). "Welding Parameters, Thick Plates, and Column Strength." *Weld J*, 50(8), S331.

CAN/CSA-S16-14 (2014). *Design of steel structures*, Canadian Standards Association, Mississauga, ON.

CAN/CSA-W59 (2013). *CAN/CSA W59-13 Welded steel construction*, Canadian Standards Association, Mississauga, Ont.

CEN (2002). "EN 1991-1-2:2002: Actions on structures . General actions. Actions on structures exposed to fire." 62.

CEN (2005). "EN 1993-1-2:2005: Design of steel structures. General rules. Structural fire design." 84.

Chatterjee, S., and Hadi, A. S. (2006). *Regression analysis by example*, Wiley-Interscience, Hoboken, N.J.

Chen, S., and Chang, S. C. (1993). "Residual Stresses in Welded Jumbo Box Columns." *Journal of Constructional Steel Research*, 25, pp. 201-209.

Crow, E. L., Davis, F. A., and Maxfield, M. W. (1960). *Statistics manual : with examples taken from ordnance development*, Dover, New York.

CWB/Gooderham-Centre (2005). *Welding for Design Engineers*, Canadian Welding Bureau, 7250 West Credit Ave., Mississauga, ON, Canada L5N 5N1.

Dassault Systemes Simulia Corp. (2011). "ABAQUS/CAE user's manual."RI, USA.

De Garmo, E. P., Black, J. T., and Kohser, R. A. (2011). *DeGarmo's Materials and Processes in Manufacturing*, Wiley-Blackwell ltd.

Deng, D., and Kiyoshima, S. (2011). "FEM analysis of residual stress distribution near weld start/end location in thick plates." *COMMAT Computational Materials Science*, 50(8), 2459-2469.

Faruque, M. O., Zaman, M., and Hossain, M. I. (1996). "Creep constitutive modelling of an aluminium alloy under multiaxial and cyclic loading." *Internatioal Journal of Plasticity*, 12, 761-780.

Fisher, J. W., and Pense, A. W. "Procedures for Thermal Cutting and Welding Heavy Structural Shapes." *Proc., Proceedings of the National Engineering Conference and Conference of Operating Personnel*, AISC, 18-11–18-47.

Goyal, S., Laha, K., Das, C. R., Selvi, S. P., and Mathew, M. D. (2013). "Finite element analysis of uniaxial and multiaxial state of stress on creep rupture behaviour of 2.25Cr–1Mo steel." *Materials Science & Engineering A*, 563(2013), 68-77.

Graville, B. A. (1975). *The principles of cold cracking control in welds*, Dominion Bridge Co., Montreal.

Hillerborg, A., Modeer, M., and Petersson, P. E. (1976). "Analysis of Crack Formation and Crack Growth in Concrete by Means of Fracture Mechanics and Finite Elements." *Cement Concrete Res*, 6.

Hu, G., Morovat, M., Lee, J., Schell, E., and Engelhardt, M. (2009). "Elevated Temperature Properties of ASTM A992 Steel." *Structures Congress*, 1-10.

Ibrahim, O. A., Lignos, D. G., and Rogers, C. A. (2016). "Probabilistic approach for assessing discontinuities in steel components based on Charpy-V-Notch tests." *Prepared for submission to Engineering Structures Journal*.

Ibrahim, O. A., Lignos, D. G., and Rogers, C. A. (2015). "Proposed modeling approach of welding procedures for heavy steel plates (Submitted)." *Eng Struct*.

Jefferson, T. B., and Woods, G. (1962). *Metals and how to weld them*, James F. Lincoln Arc Welding Foundation, Cleveland,.

Jiang, W. C., Luo, Y., Zhang, G. D., Woo, W., and Tu, S. T. (2013). "Experimental to study the effect of multiple weld-repairs on microstructure, hardness and residual stress for a stainless steel clad plate." *Materials & Design*, 51, 1052-1059.

Johnson, A. A., and Storey, R. J. (2008). "The effect of carbon on the Charpy V-Notch ductile brittle transition curves." *ICASI & CCATM'2008 International Conference and Exhibition on Analysis & Testing of Materials*Beijing, China.

Jun, H.-K., Seo, J.-W., Jeon, I.-S., Lee, S.-H., and Chang, Y.-S. (2015). "Fracture and fatigue crack growth analyses on a weld-repaired railway rail." *Eng Fail Anal*.

Kaminetzky, D. (1991). *Design and construction failures : lessons from forensic investigations*, McGraw-Hill, New York.

Knobloch, M., Pauli, J., and Fontana, M. (2013). "Influence of the strain-rate on the mechanical properties of mild carbon steel at elevated temperatures." *Materials & Design*, 49, 553-565.

Lee, C.-H., Chang, K.-H., and Do, V. N. V. (2015). "Finite element modeling of residual stress relaxation in steel butt welds under cyclic loading." *Eng Struct*, 103, 63-71.

Lee, C. S., Chandel, R. S., and Seow, H. P. (2000). "Effect of welding parameters on the size of heat affected zone of submerged arc welding." *Mater Manuf Process*, 15(5), 649-666.

Lee, J.-Y., Kim, Y.-C., and Inose, K. (2010). "Verification of Validity and Generality of Dominant Factors in High Accuracy Prediction of Welding Distortion." *Weld World*, 54(9-10), R279-R285.

Lee, J., Morovat, M. A., Engelhardt, M. D., and Taleff, E. M. "Creep Behavior of ASTM A992 Steel at Elevated Temperatures." *Proc., 7th International Conference on Structures in Fire*, ETH Zurich, 95-104.

Lie, T. T. (1992). *Structural fire protection*, American Society of Civil Engineers, New York, N.Y.

Lienhard, J. H., and Lienhard, J. H. (2011). *A heat transfer textbook*, Dover Publications, Mineola, N.Y.

Lin, C. M., Tsai, H. L., Cheng, C. D., and Yang, C. (2012). "Effect of repeated weld-repairs on microstructure, texture, impact properties and corrosion properties of AISI 304L stainless steel." *Eng Fail Anal*, 21, 9-20.

Manigandan, K., Srivatsan, T. S., Quick, T., Sastry, S., and Schmidt, M. L. (2014). "Influence of microstructure and load ratio on cyclic fatigue and final fracture behavior of two high strength steels." *Materials & Design*, 55(0), 727-739.

Mathworks (2012). "Matlab R2012b." The MathWorks Inc.

Miller, D. K. (2006). *AISC Steel Design Guide 21 Welded Connections – A Primer for Engineers*, American Institute of Steel Construction, Chicago, IL.

Miller, D. K. (2010). "Welding heavy Structural Steel -- Successfully." *2010 NASCC: The Steel Conference*Orlando, FL, USA.

Montgomery, D. C., and Runger, G. C. (2014). *Applied Statistics and Probability for Engineers 6th Edition*, John Wiley and sons Inc.

Murakami, Y. (1987). *Stress intensity factors handbook*, Pergamon, Oxford Oxfordshire ; New York.

Nikolaidou, V., Rogers, C. A., and Lignos, D. G. (2013). "Finite element modeling of welding procedures in high strength W-Shapes." *Canadian Society of Civil Engineering, 3rd Specialty Conference on Material Engineering and Applied Mechanics*Montreal, Quebec.

Nikolaidou, V., Rogers, C. A., and Lignos, D. G. "Influence of Welding of Doubler Plates to ASTM A913 450MPa Grade Columns." *Proc., Eurosteel*.

Norton, F. H. (1929). *The Creep of Steel at High Temperatures*, McGraw-Hill Book Company, Incorporated.

Phillips, D. T. (1972). *Applied goodness of fit testing*, American Institute of Industrial Engineers.

Pilipenko, A. (2001). "Computer simulation of residual stress and distortion of thick plates in multi-electrode submerged arc welding. Their mitigation techniques." Ph.D. dissertation, Norwegian University of Science and Technology, N-7491 Trondheim, Norway.

Reitz, W. (2011). "Assessment of Weld Embrittlement in A516 Steel Due to Multiple Repair Welds." *J Fail. Anal. and Preven.*, 11(6), 618-623.

Society of Fire Protection Engineers (2008). *SFPE handbook of fire protection engineering*, National Fire Protection Association, Quincy, Mass. Bethesda, Md.

Sundaram, P., Pandey, R. K., and Kumar, A. N. (1987). "Effect of the Welding Process and Heat Input on the Fracture-Toughness of Welded-Joints in High-Strength Low-Alloy Steel." *Mater Sci Eng*, 91, 29-38.

Suwan, S. (2002). "Analysis of structural plate mechanical properties : statistical variability and implications in structural reliability." M.S. Thesis M S in Engineering, University of Texas at Austin.

Tada, H., Paris, P. C., and Irwin, G. R. (2000). *The stress analysis of cracks handbook*, ASME Press, New York.
Yang, Y. (2008). "The effect of submerged arc welding parameters on the properties of pressure vessel and wind turbine tower steels." Master of Science, University of Saskatchewan, Saskatoon.
Zehnder, A. T. (2012). *Fracture mechanics: Lecture notes in applied and computational mechanics*, Springer.
Zehnder, A. T. (2012). *Fracture Mechanics: Volume 62 of Lecture Notes in Applied and Computational Mechanics*, Springer.
Zeinoddini, M., Arnavaz, S., Zandi, A. P., and Vaghasloo, Y. A. (2013). "Repair welding influence on offshore pipelines residual stress fields: An experimental study." *Journal of Constructional Steel Research*, 86, 31-41.

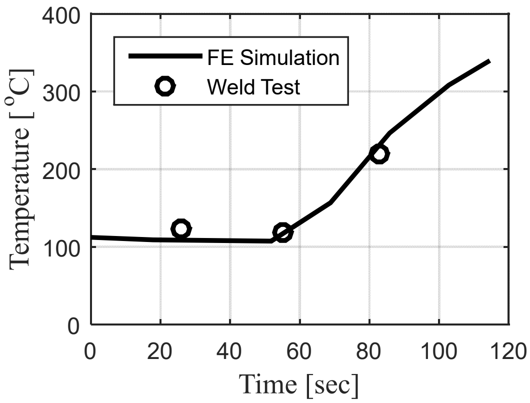

(a) Temperature at node T1 for pass number 1

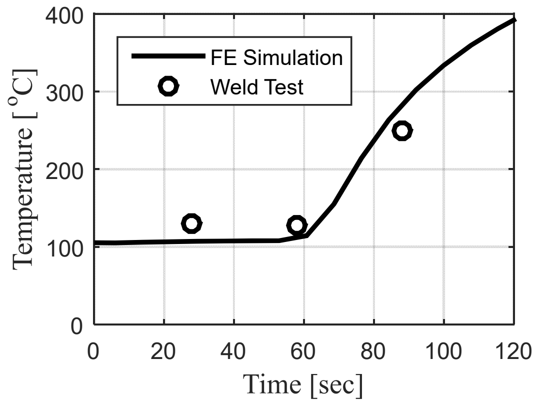

(b) Temperature at node T1 for pass number 2

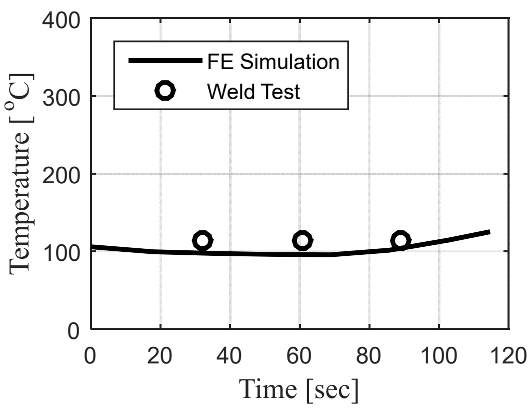

(c) Temperature at node T2 for pass number 1

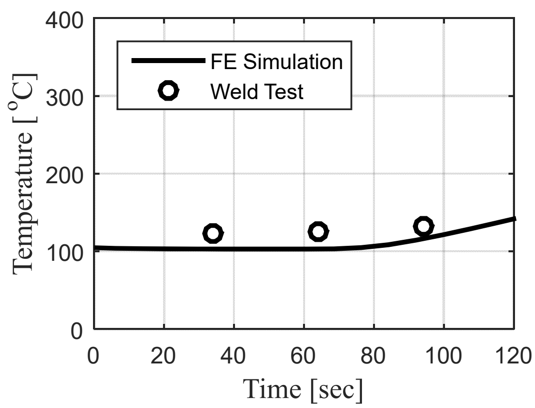

(d) Temperature at node T2 for pass number 2

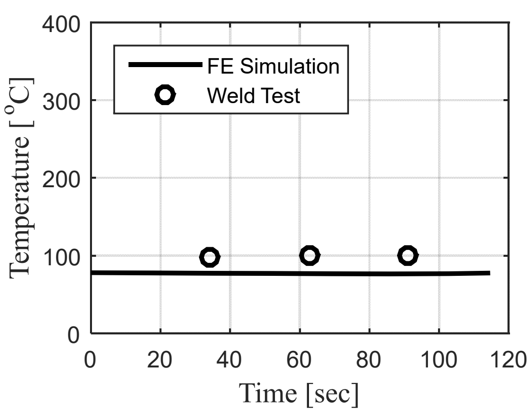

(e) Temperature at node T3 for pass number 1

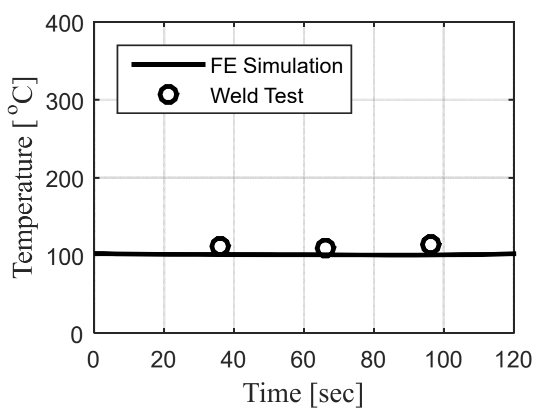

(f) Temperature at node T3 for pass number 2

Figure A.1: Comparison of temperature results from the FE simulation and the weld test results for welding passes number 1 and 2 at side 1.

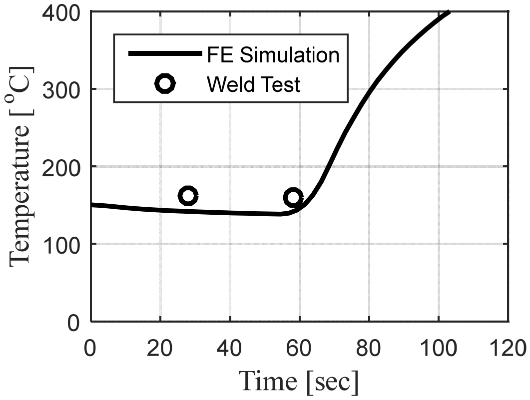

(a) Temperature at node T1 for pass number 4

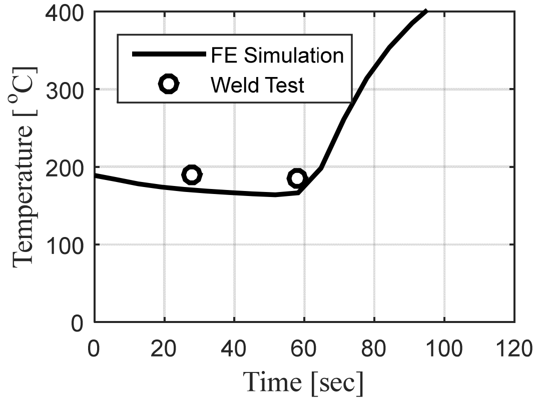

(b) Temperature at node T1 for pass number 6

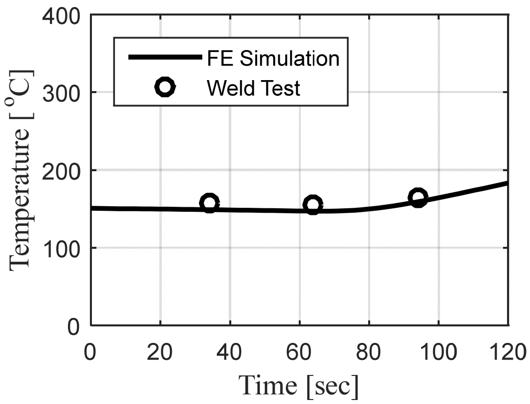

(c) Temperature at node T2 for pass number 4

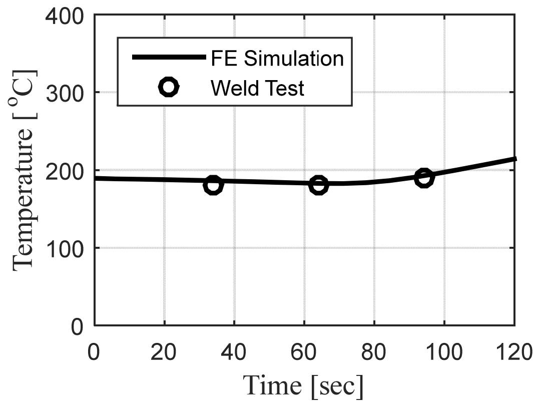

(d) Temperature at node T2 for pass number 6

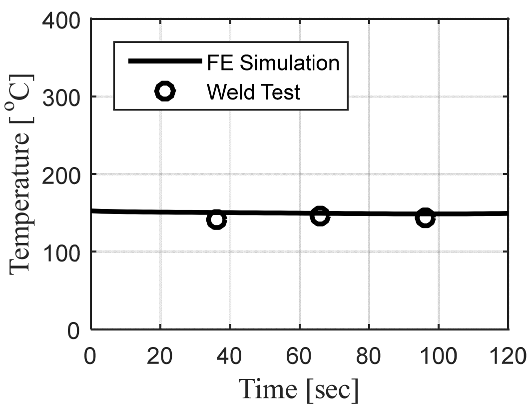

(e) Temperature at node T3 for pass number 4

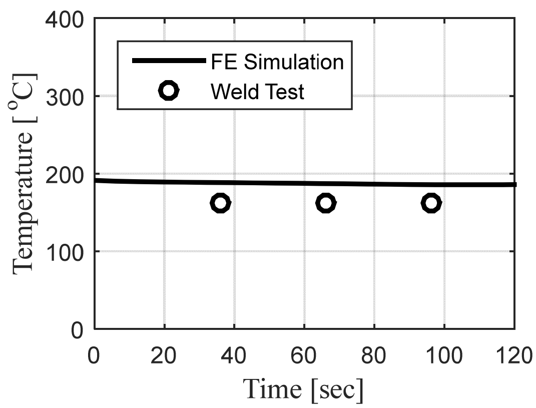

(f) Temperature at node T3 for pass number 6

Figure A.2: Comparison of temperature results from the FE simulation and the weld test results for welding passes number 4 and 6 at side 1.

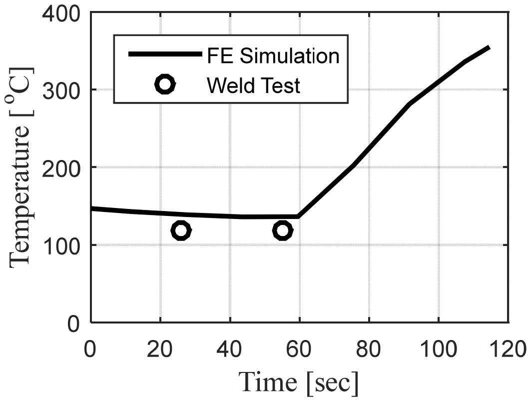

(a) Temperature at node T1 for pass number 1

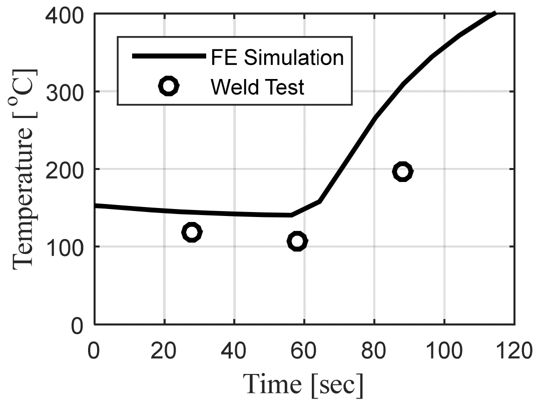

(b) Temperature at node T1 for pass number 2

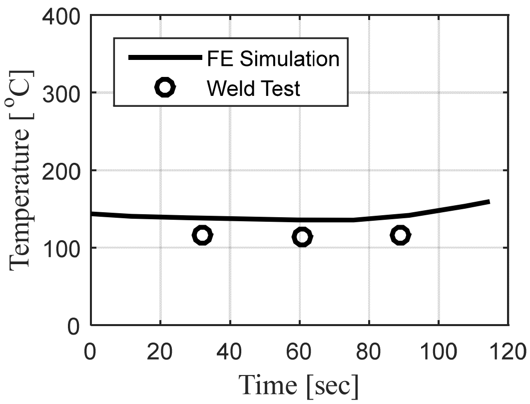

(c) Temperature at node T2 for pass number 1

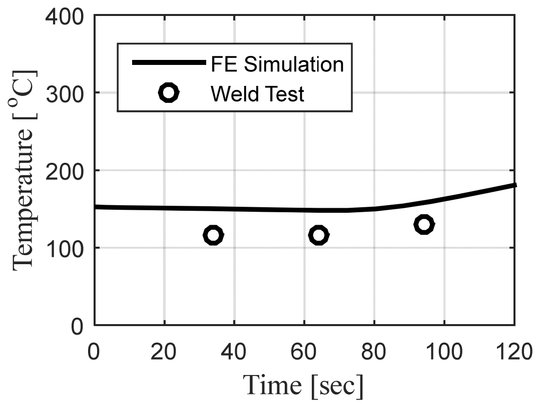

(d) Temperature at node T2 for pass number 2

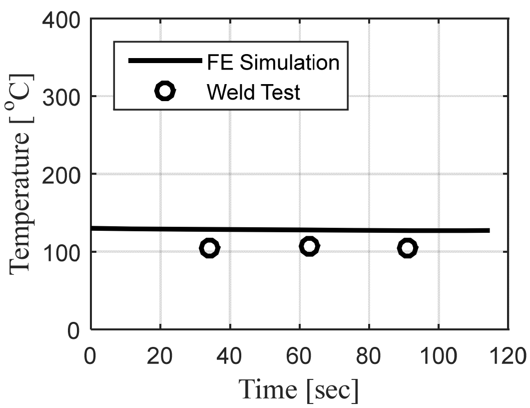

(e) Temperature at node T3 for pass number 1

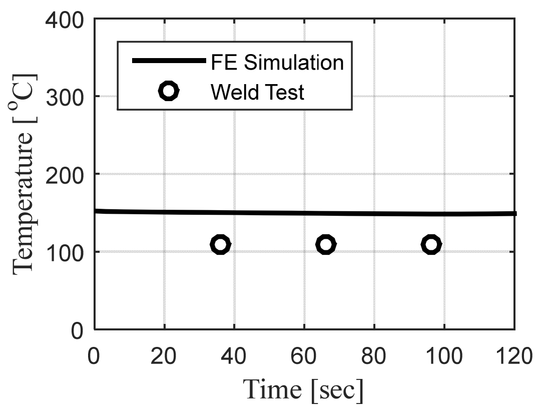

(f) Temperature at node T3 for pass number 2

Figure A.3: Comparison of temperature results from the FE simulation and the weld test results for welding passes number 1 and 2 at side 2.

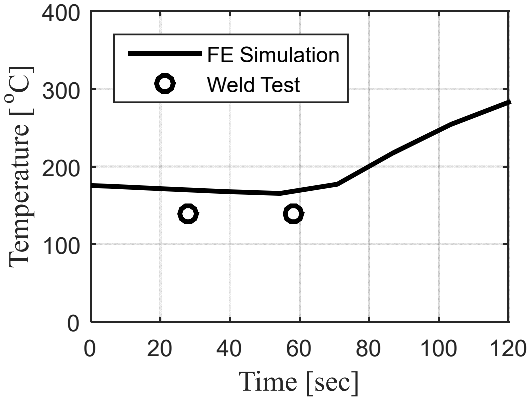

(a) Temperature at node T1 for pass number 3

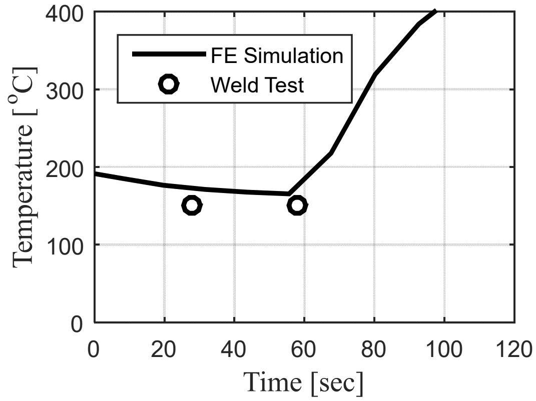

(b) Temperature at node T1 for pass number 3

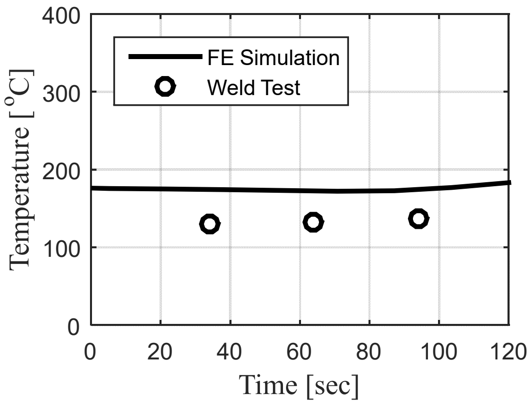

(c) Temperature at node T2 for pass number 3

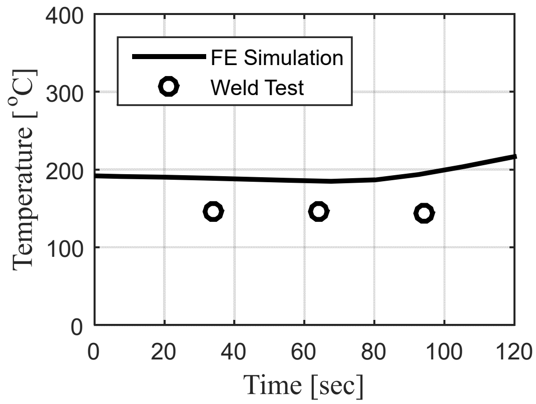

(d) Temperature at node T2 for pass number 4

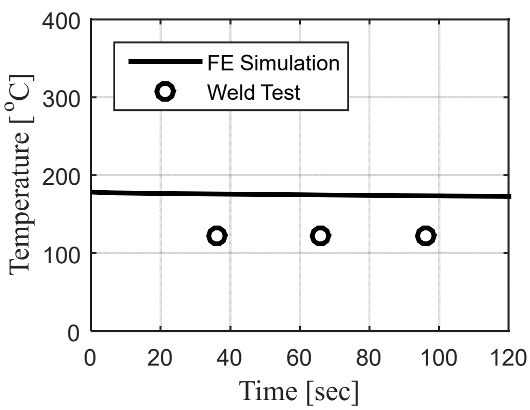

(e) Temperature at node T3 for pass number 3

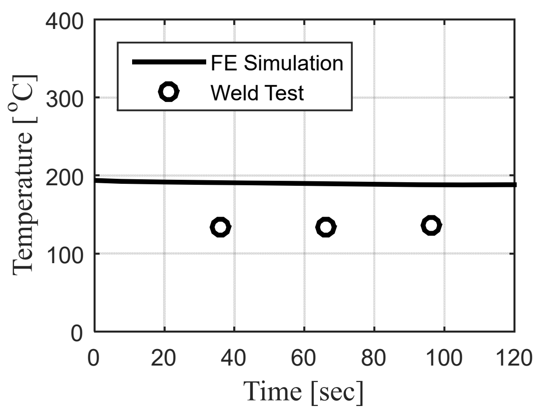

(f) Temperature at node T3 for pass number 4

Figure A.4: Comparison of temperature results from the FE simulation and the weld test results for welding passes number 3 and 4 at side 2.

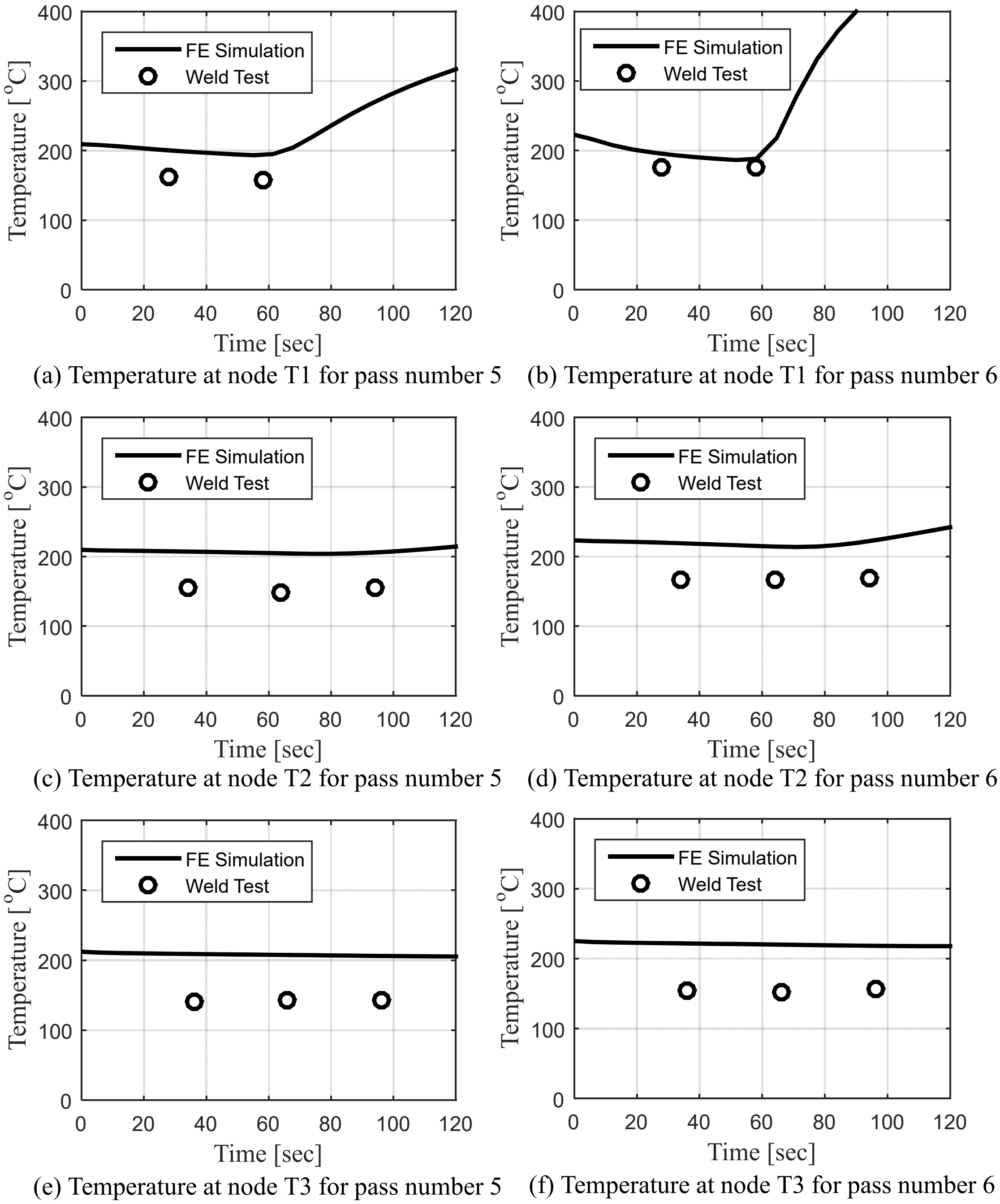

(a) Temperature at node T1 for pass number 5 (b) Temperature at node T1 for pass number 6

(c) Temperature at node T2 for pass number 5 (d) Temperature at node T2 for pass number 6

(e) Temperature at node T3 for pass number 5 (f) Temperature at node T3 for pass number 6

Figure A.5: Comparison of temperature results from the FE simulation and the weld test results for welding passes number 5 and 6 at side 2.

Appendix B: Summary of Parametric Study Results

- Phase A: Welding temperature

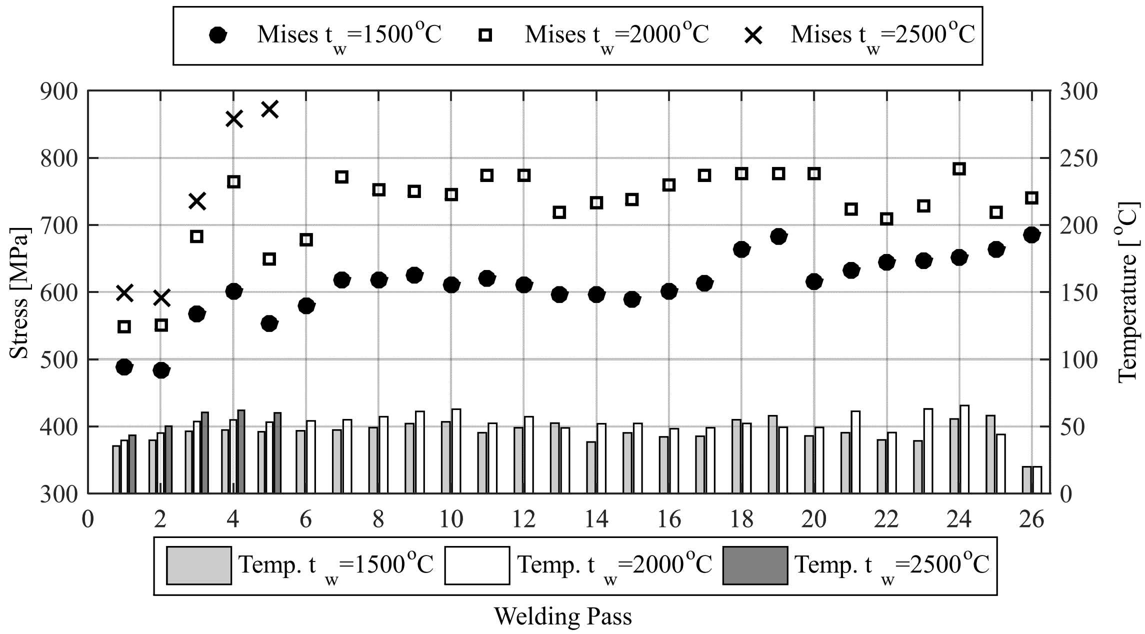

Figure B.1: Summary of maximum Mises stress values and corresponding temperatures during the welding procedure for the welding temperature parameter.

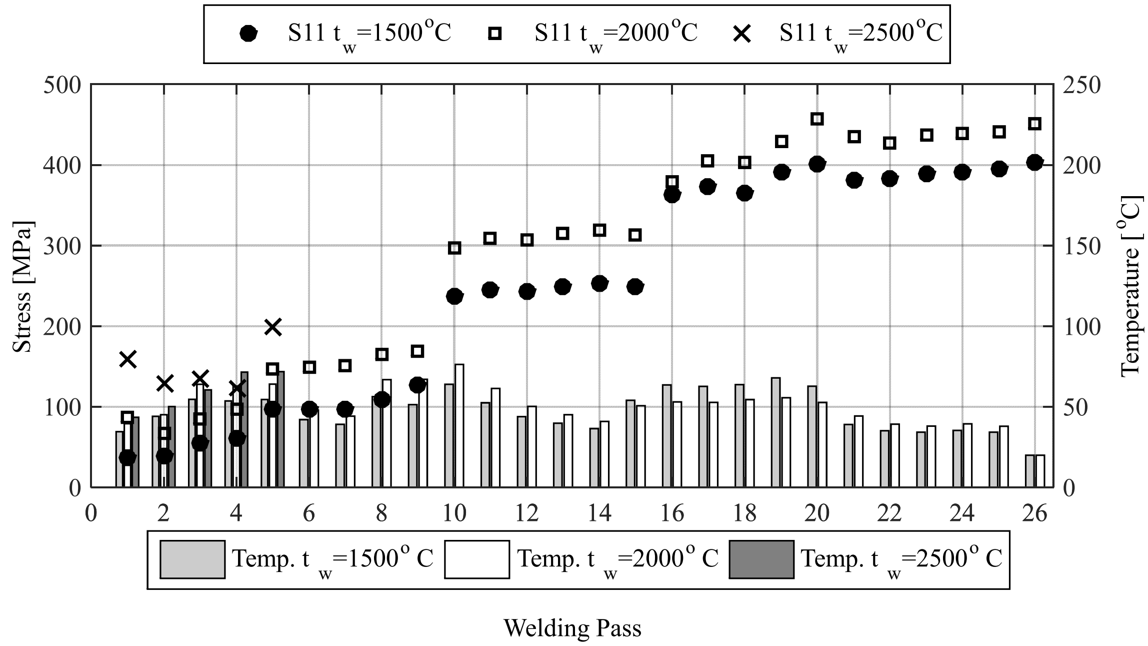

Figure B.2: Summary of maximum horizontal transverse stress values (S11) and corresponding temperatures during the welding procedure for the welding temperature parameter.

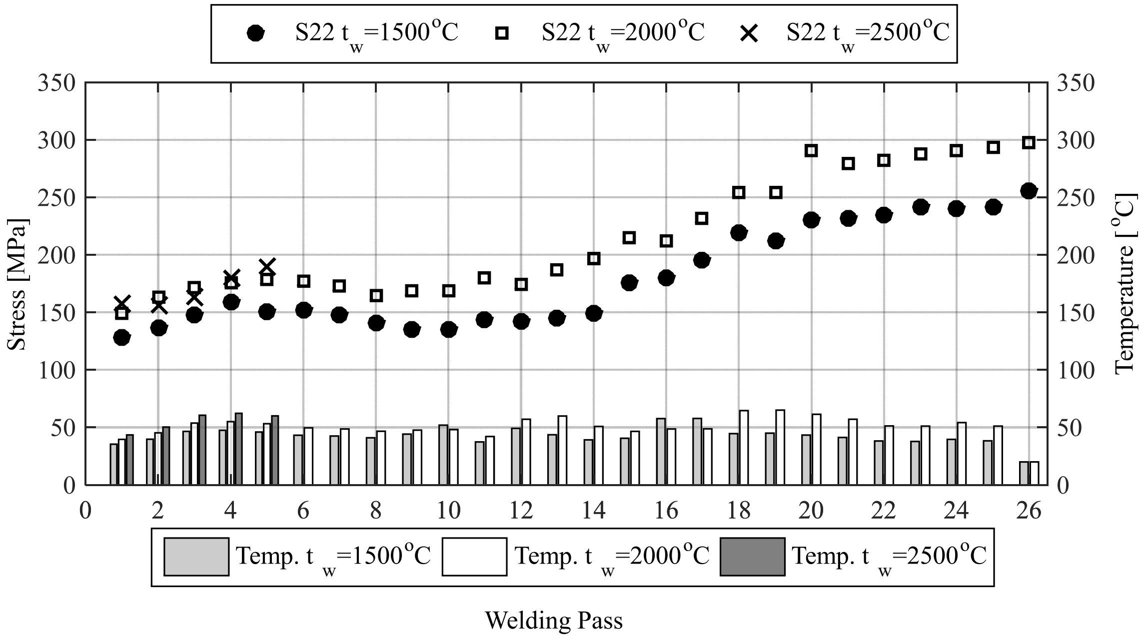

Figure B.3: Summary of maximum vertical transverse stress values (S22) and corresponding temperatures during the welding procedure for the welding temperature parameter.

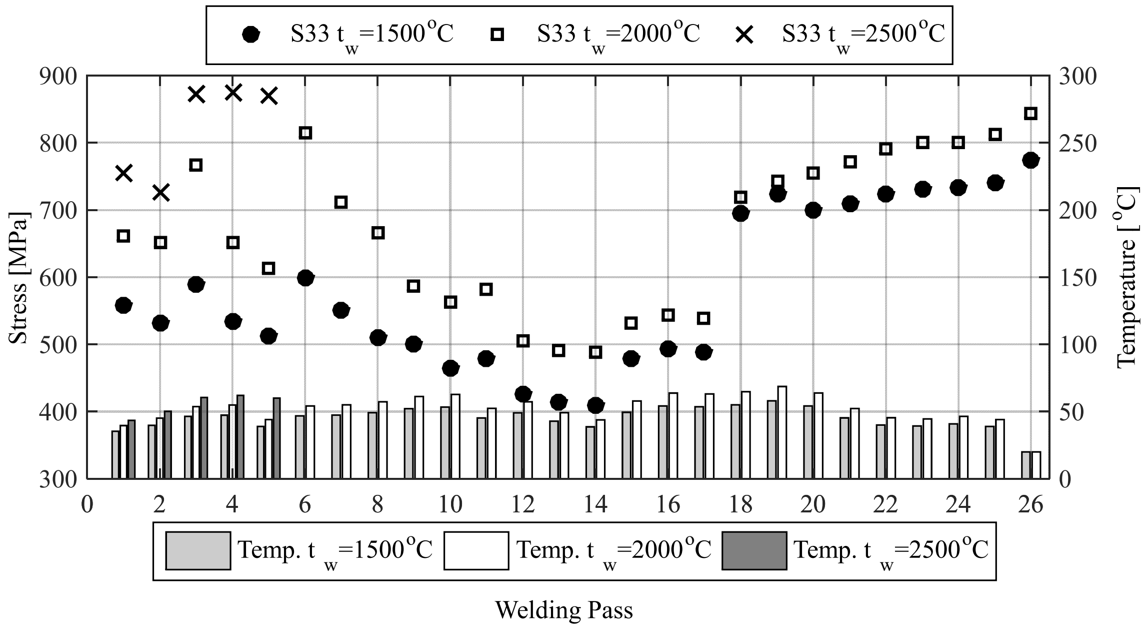

Figure B.4: Summary of maximum longitudinal stress values (S33) and corresponding temperatures during the welding procedure for the welding temperature parameter.

- Phase A: Welding travel speed

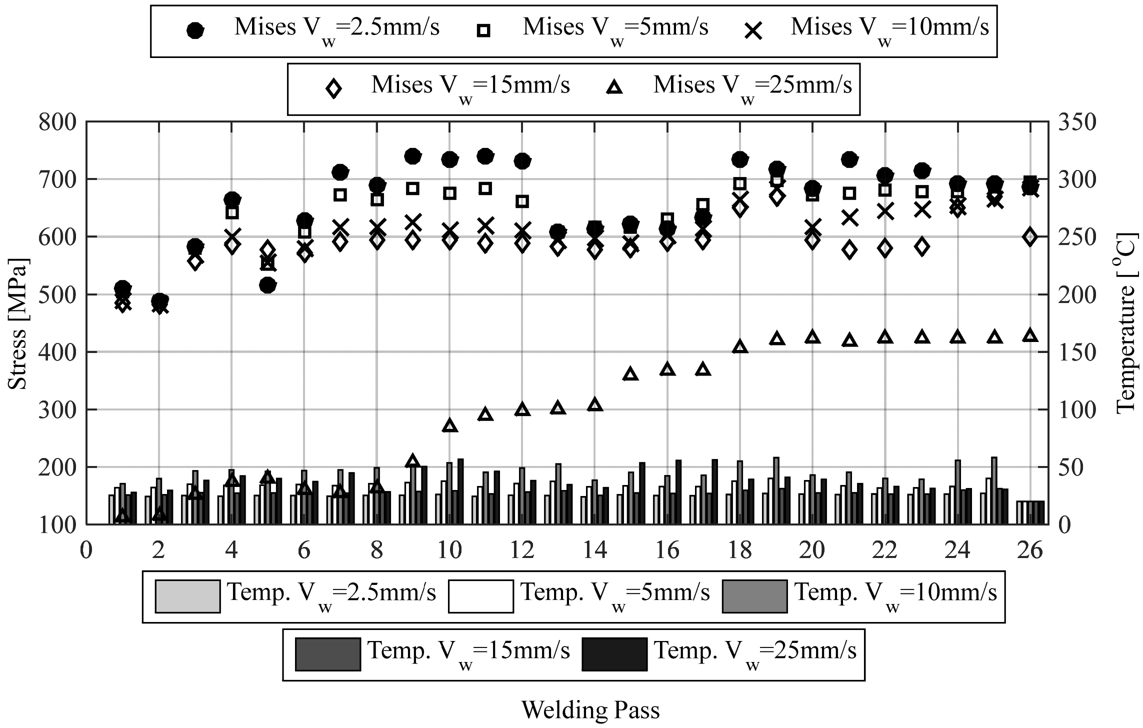

Figure B.5: Summary of maximum Mises stress values and corresponding temperatures during the welding procedure for the welding travel speed parameter.

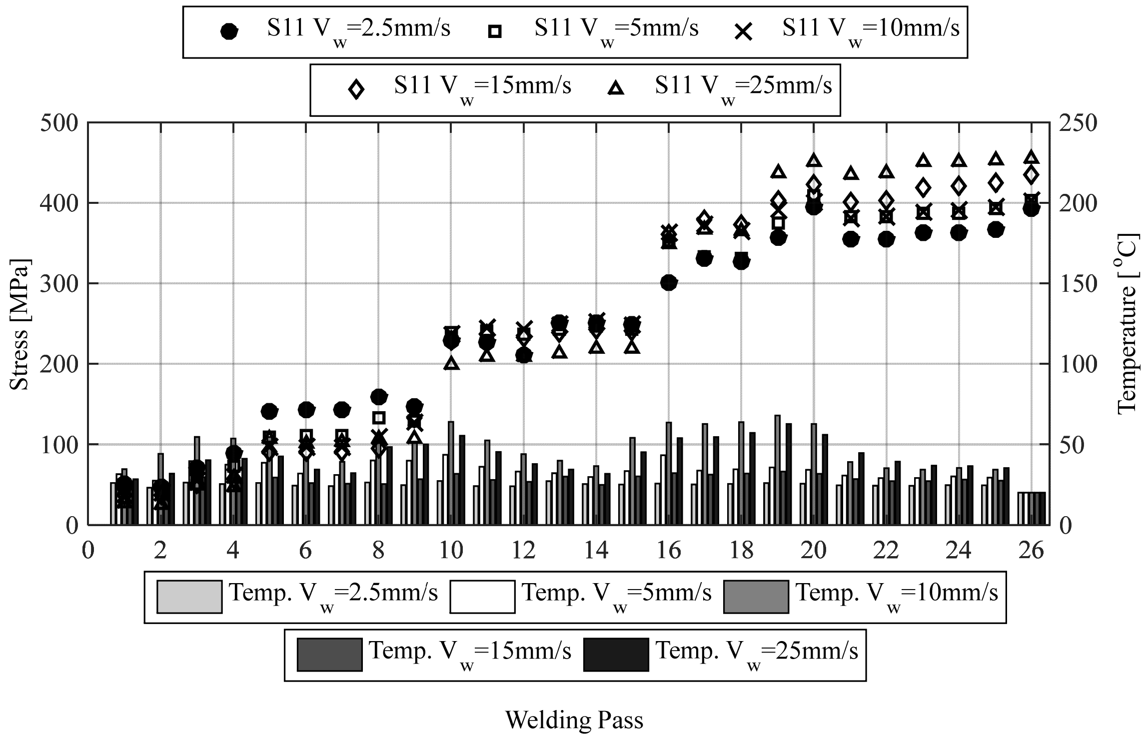

Figure B.6: Summary of maximum horizontal transverse stress values (S11) and corresponding temperatures during the welding procedure for the welding travel speed parameter.

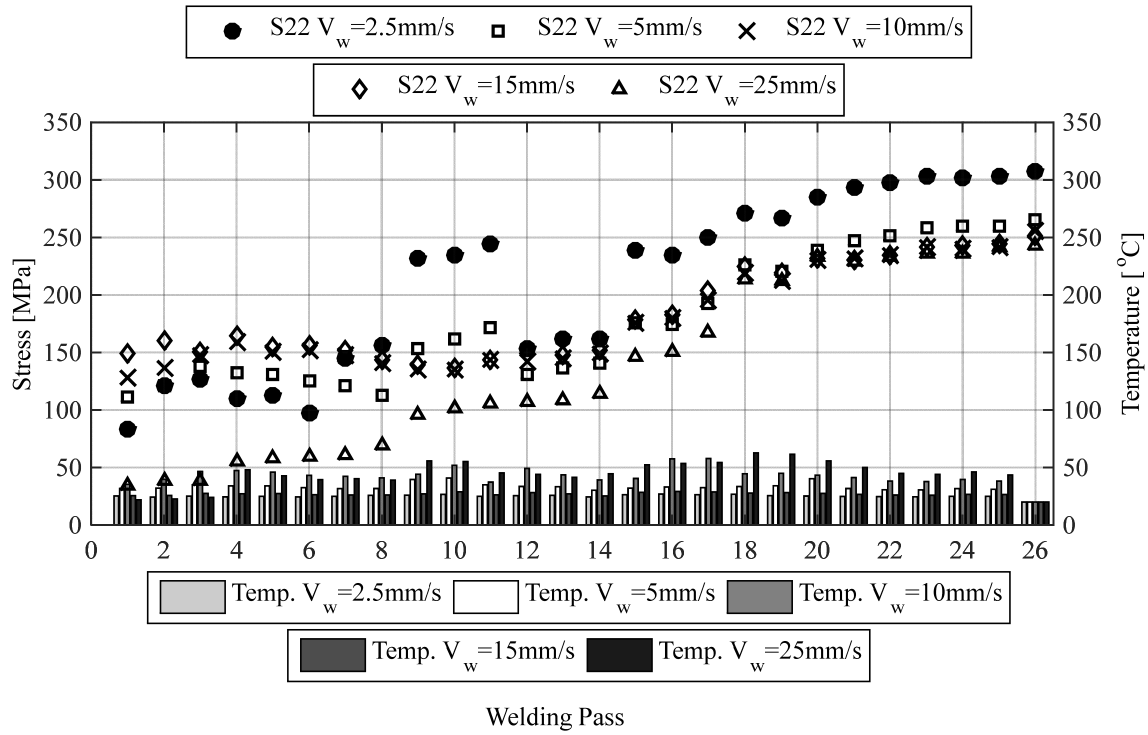

Figure B.7: Summary of maximum vertical transverse stress values (S22) and corresponding temperatures during the welding procedure for the welding travel speed parameter.

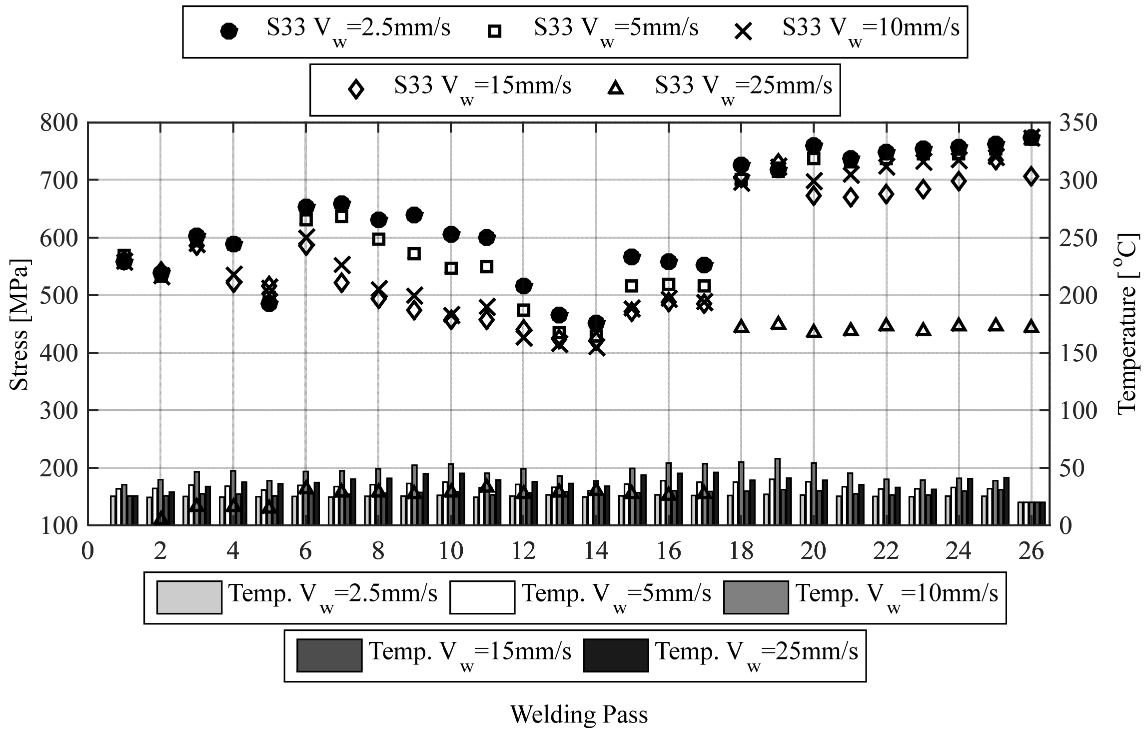

Figure B.8: Summary of maximum longitudinal stress values (S33) and corresponding temperatures during the welding procedure for the welding travel speed parameter.

- Phase A: Preheat/inter-pass temperature

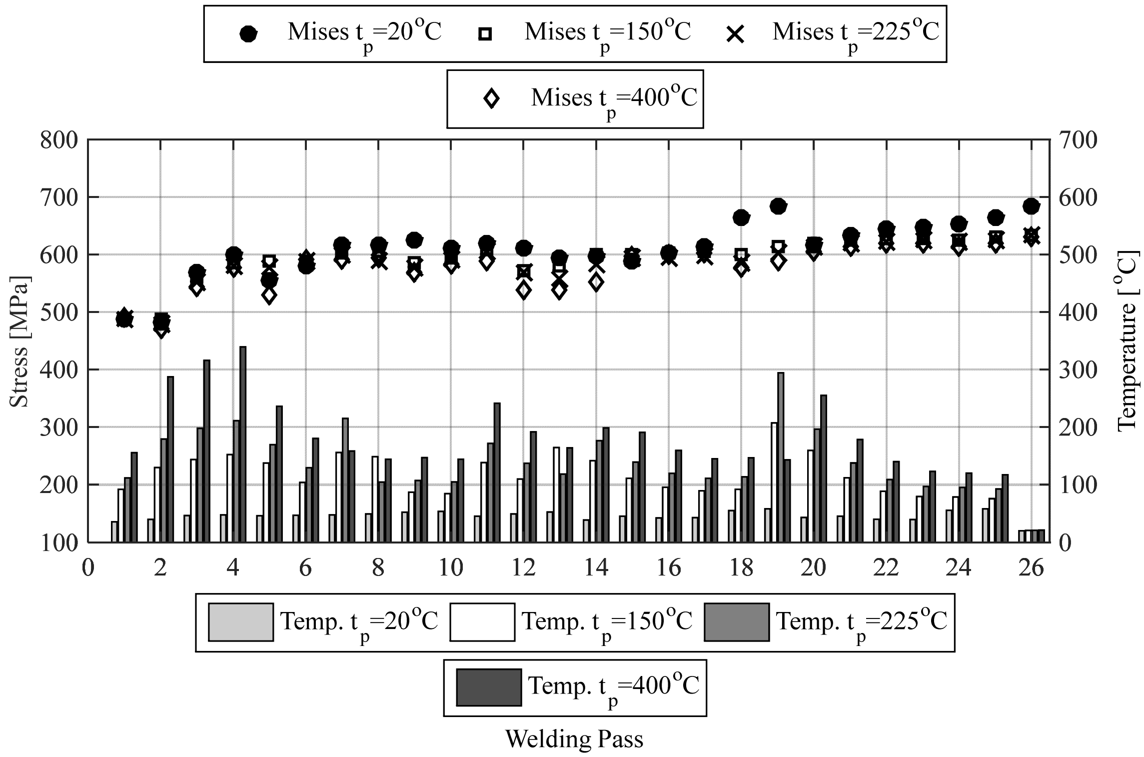

Figure B.9: Summary of maximum Mises stress values and corresponding temperatures during the welding procedure for the preheat/inter-pass temperature parameter.

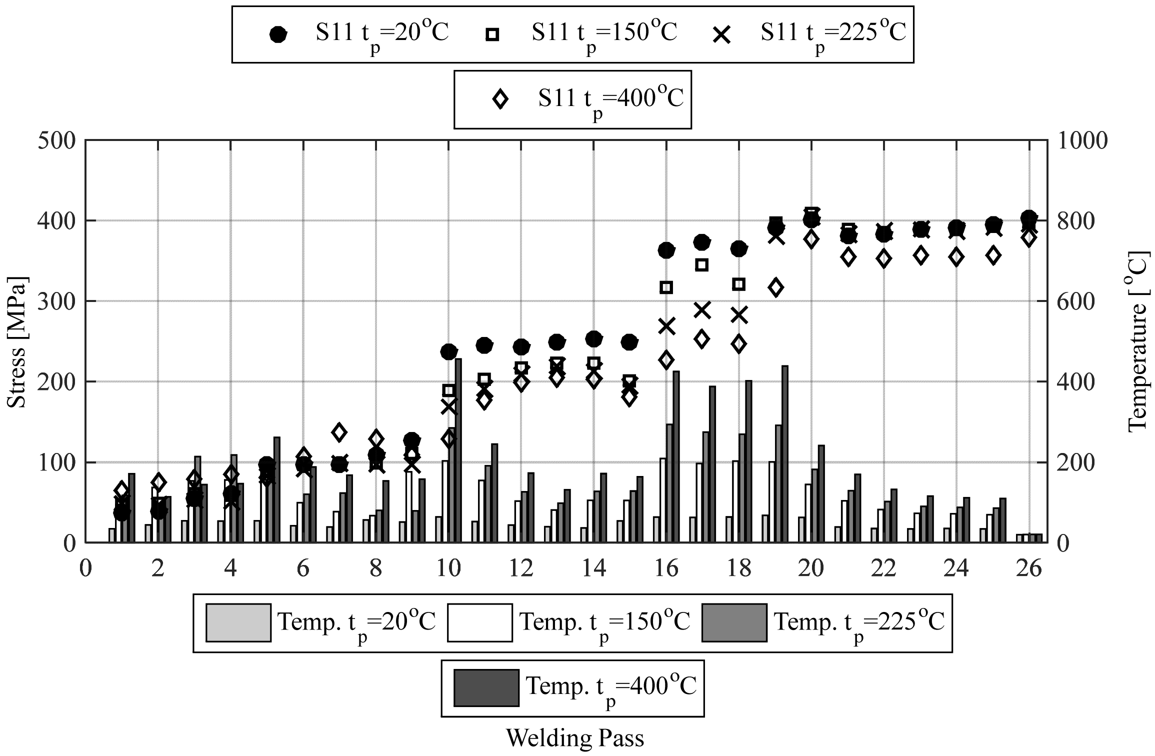

Figure B.10: Summary of maximum horizontal transverse stress values (S11) and corresponding temperatures during the welding procedure for the preheat/inter-pass temperature parameter.

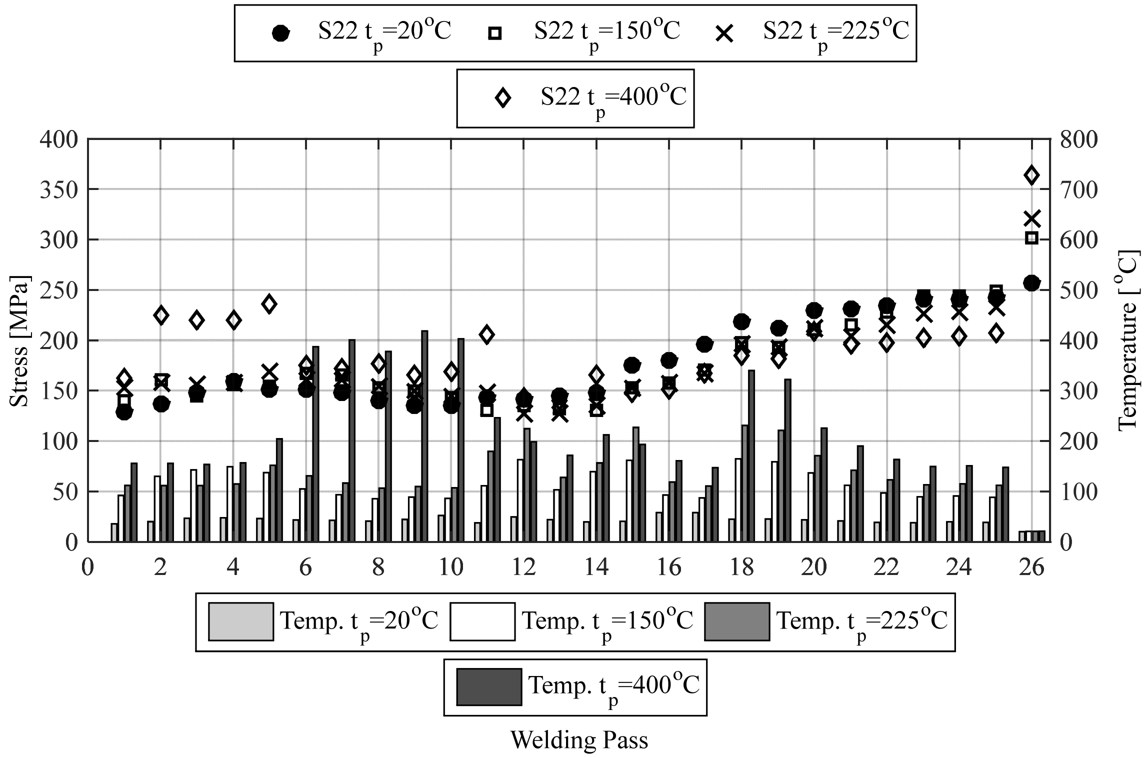

Figure B.11: Summary of maximum vertical transverse stress values (S22) and corresponding temperatures during the welding procedure for the preheat/inter-pass temperature parameter.

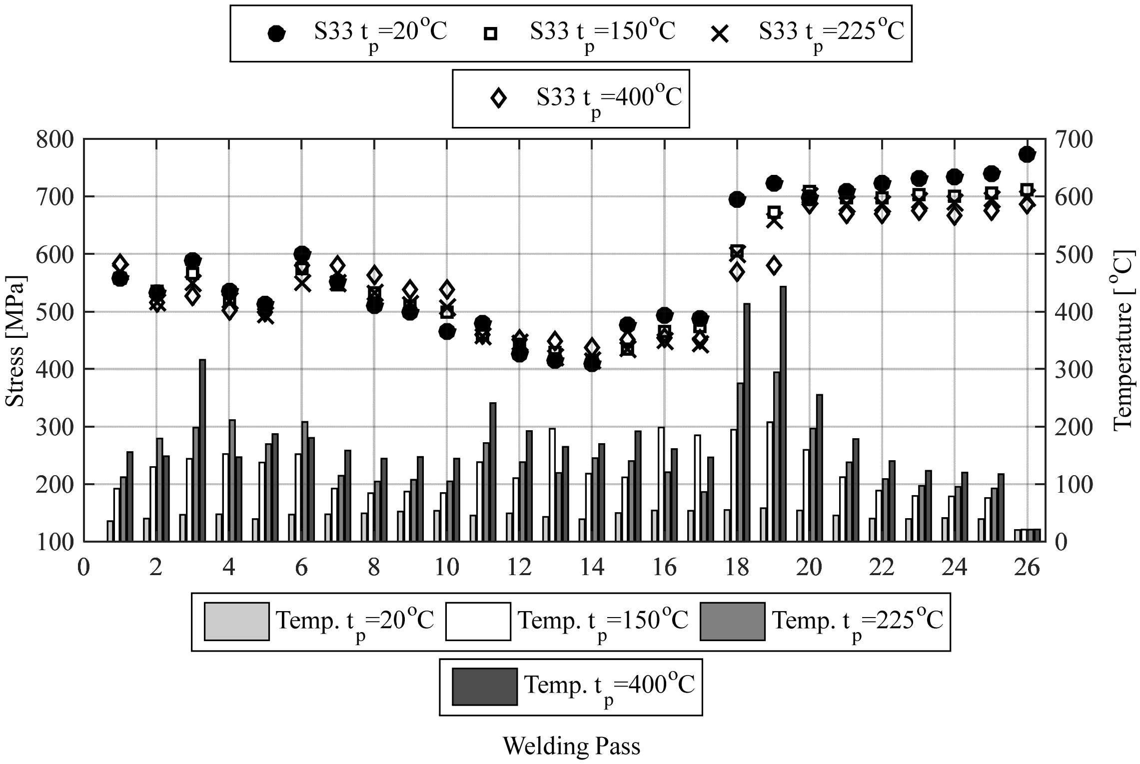

Figure B.12: Summary of maximum longitudinal stress values (S33) and corresponding temperatures during the welding procedure for the preheat/inter-pass temperature parameter.

- Phase B: Mechanical properties of the base metal

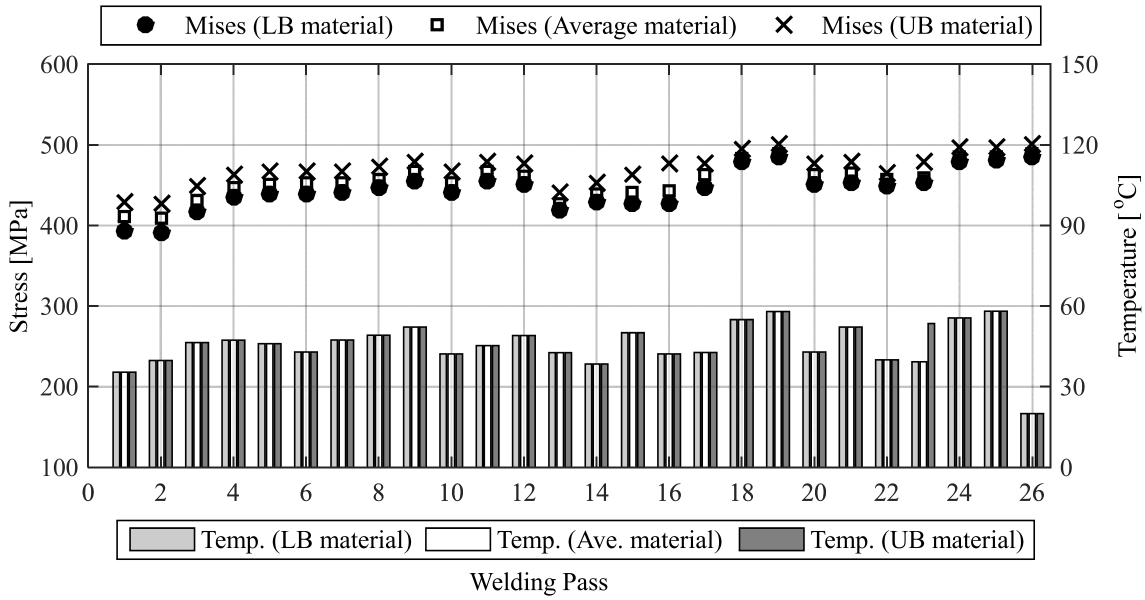

Figure B.13: Summary of maximum Mises stress values and corresponding temperatures during the welding procedure for the mechanical properties of the base metal parameter.

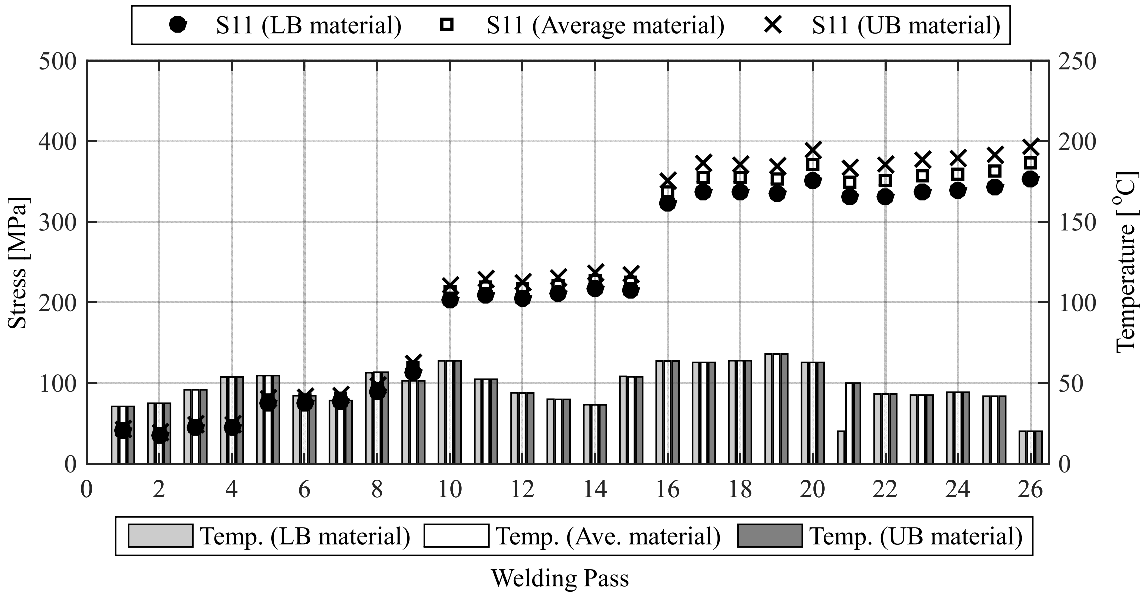

Figure B.14: Summary of maximum horizontal transverse stress values (S11) and corresponding temperatures during the welding procedure for the mechanical properties of the base metal parameter.

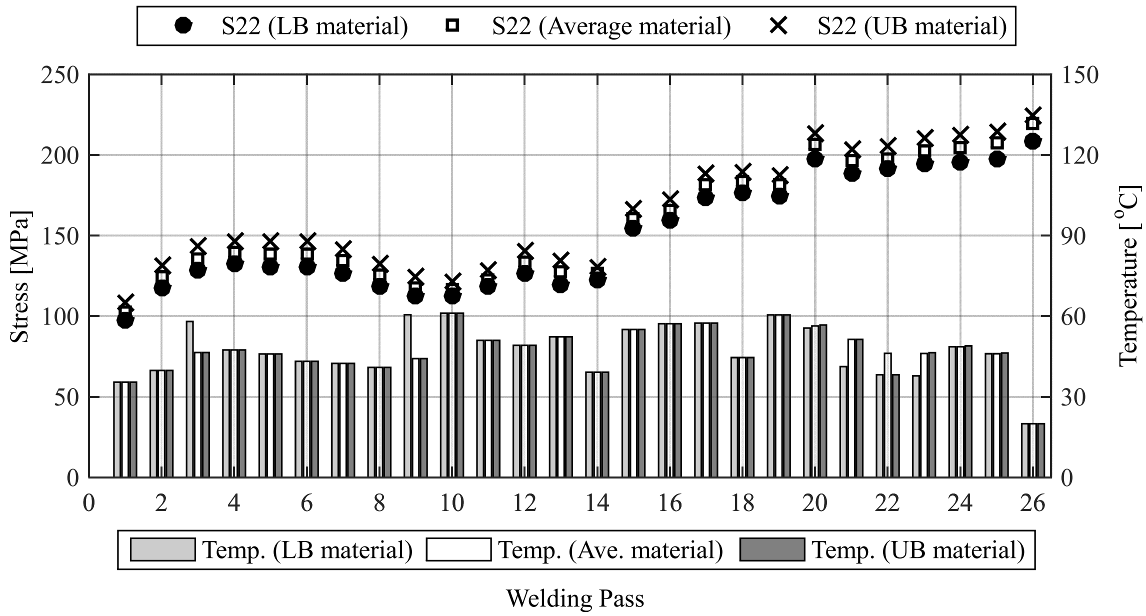

Figure B.15: Summary of maximum vertical transverse stress values (S22) and corresponding temperatures during the welding procedure for the mechanical properties of the base metal parameter.

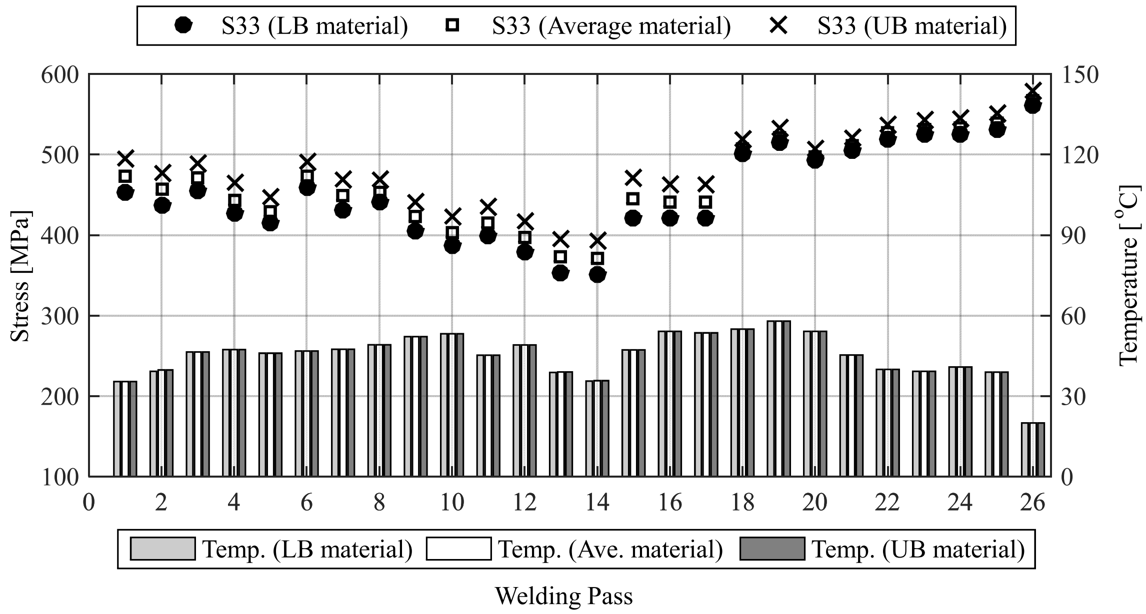

Figure B.16: Summary of maximum longitudinal stress values (S33) and corresponding temperatures during the welding procedure for the mechanical properties of the base metal parameter.

- Phase B: Base metal plate thickness

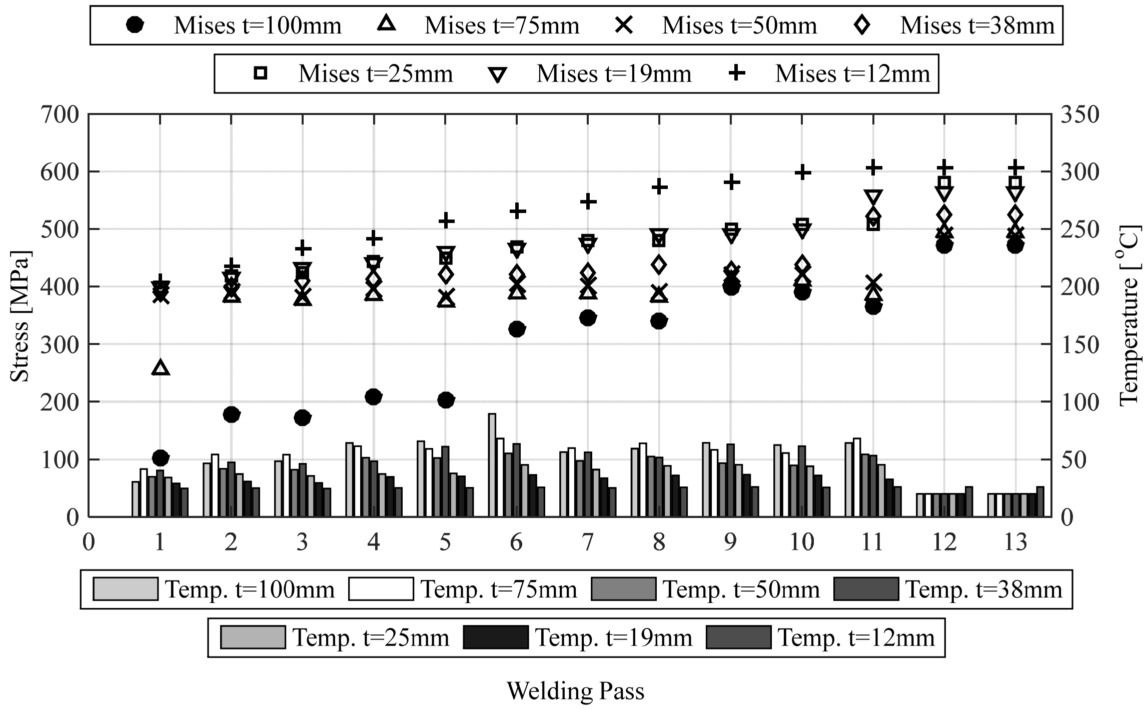

Figure B.17: Summary of maximum Mises stress values and corresponding temperatures during the welding procedure for the base metal plate thickness parameter.

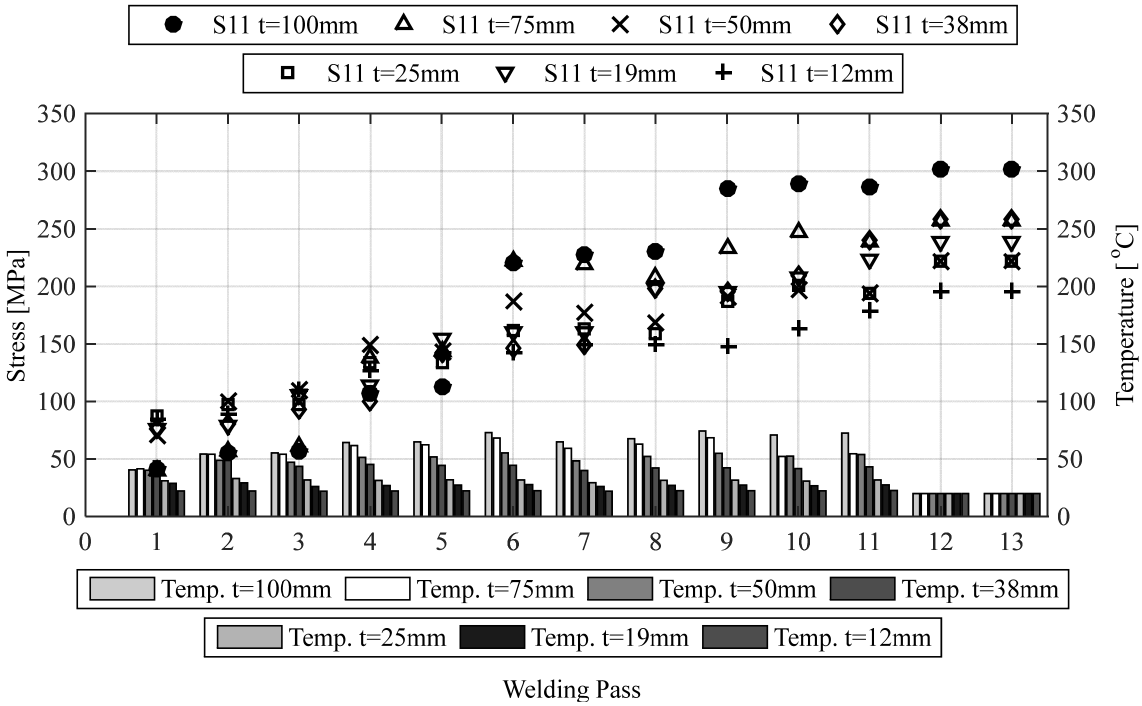

Figure B.18: Summary of maximum horizontal transverse stress values (S11) and corresponding temperatures during the welding procedure for the base metal plate thickness parameter.

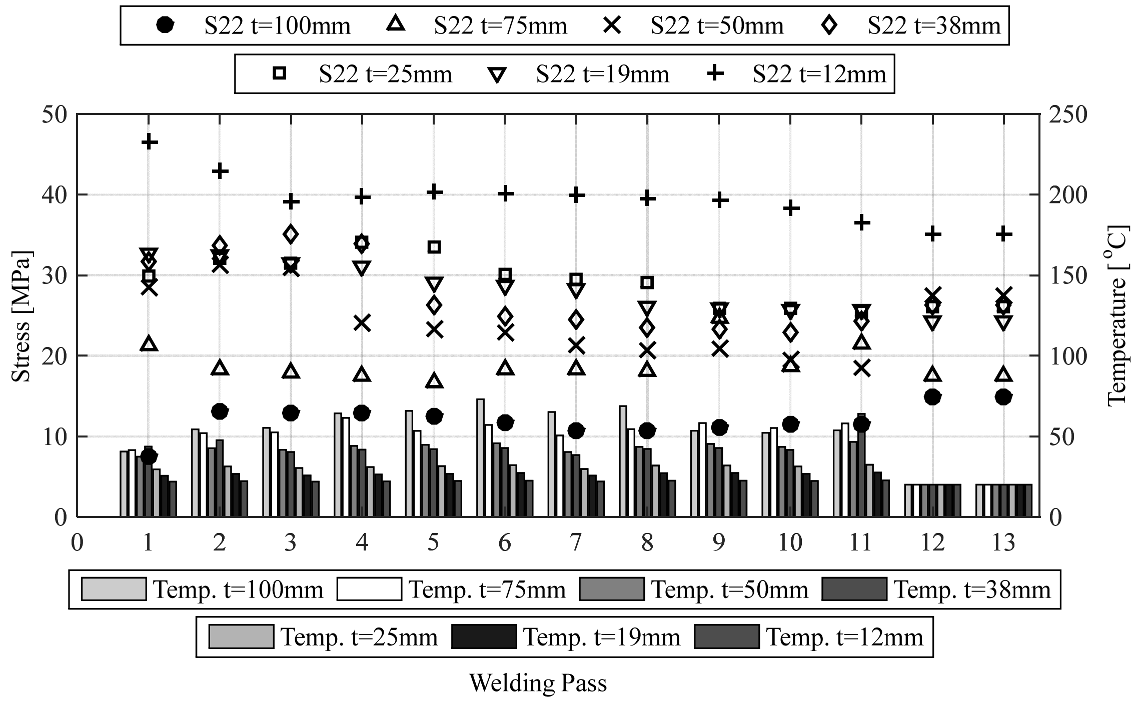

Figure B.19: Summary of maximum vertical transverse stress values (S22) and corresponding temperatures during the welding procedure for the base metal plate thickness parameter.

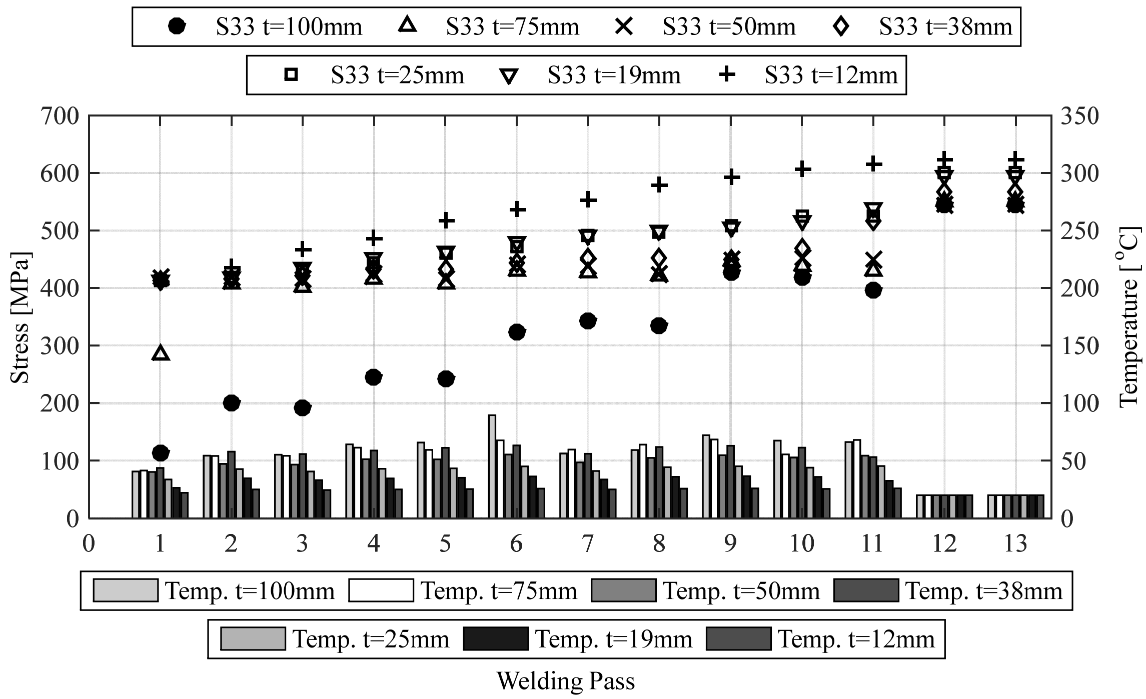

Figure B.20: Summary of maximum longitudinal stress values (S33) and corresponding temperatures during the welding procedure for the base metal plate thickness parameter.

- Phase B: Number of welding passes

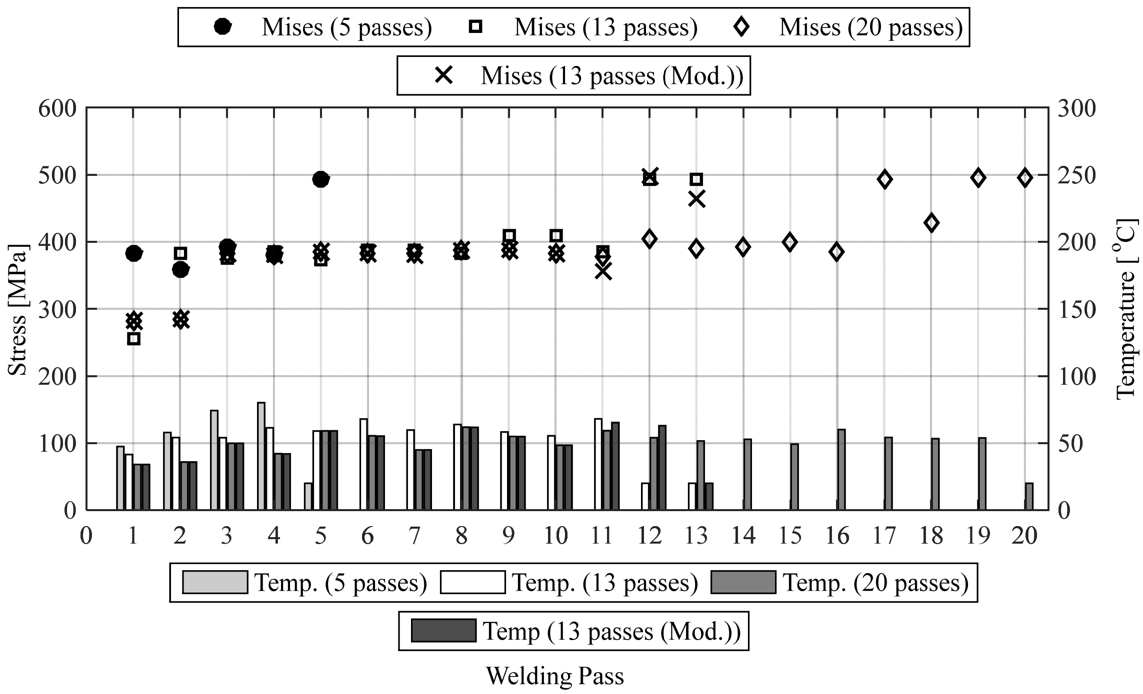

Figure B.21: Summary of maximum Mises stress values and corresponding temperatures during the welding procedure for the number of welding passes parameter.

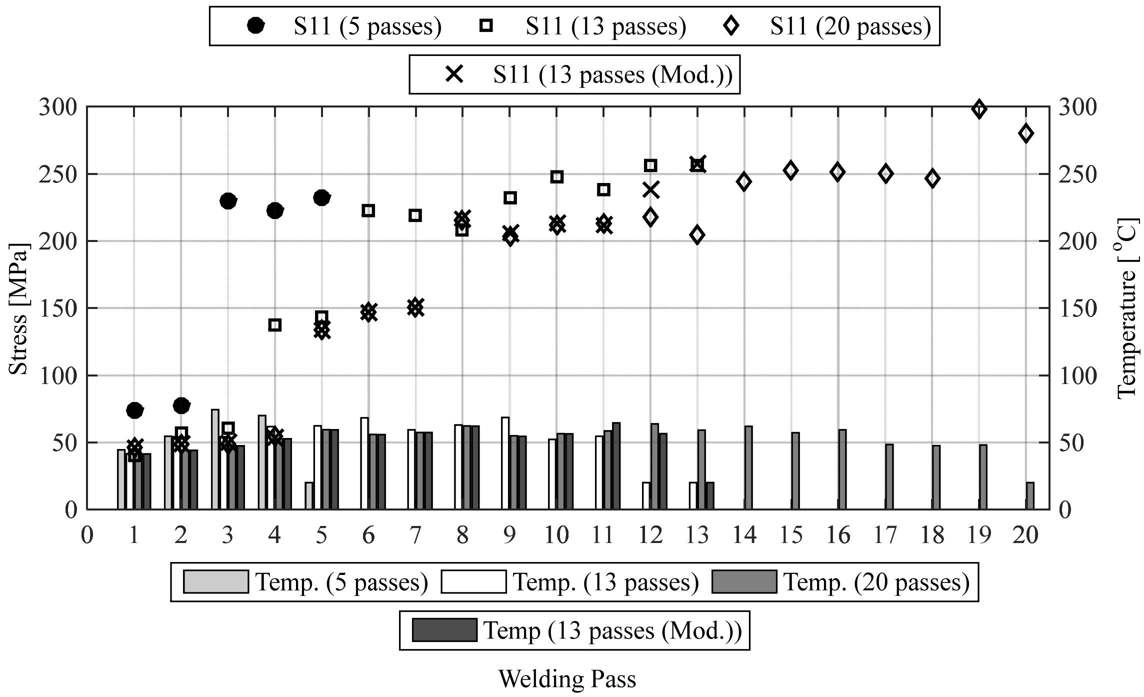

Figure B.22: Summary of maximum horizontal transverse stress values (S11) and corresponding temperatures during the welding procedure for the number of welding passes parameter.

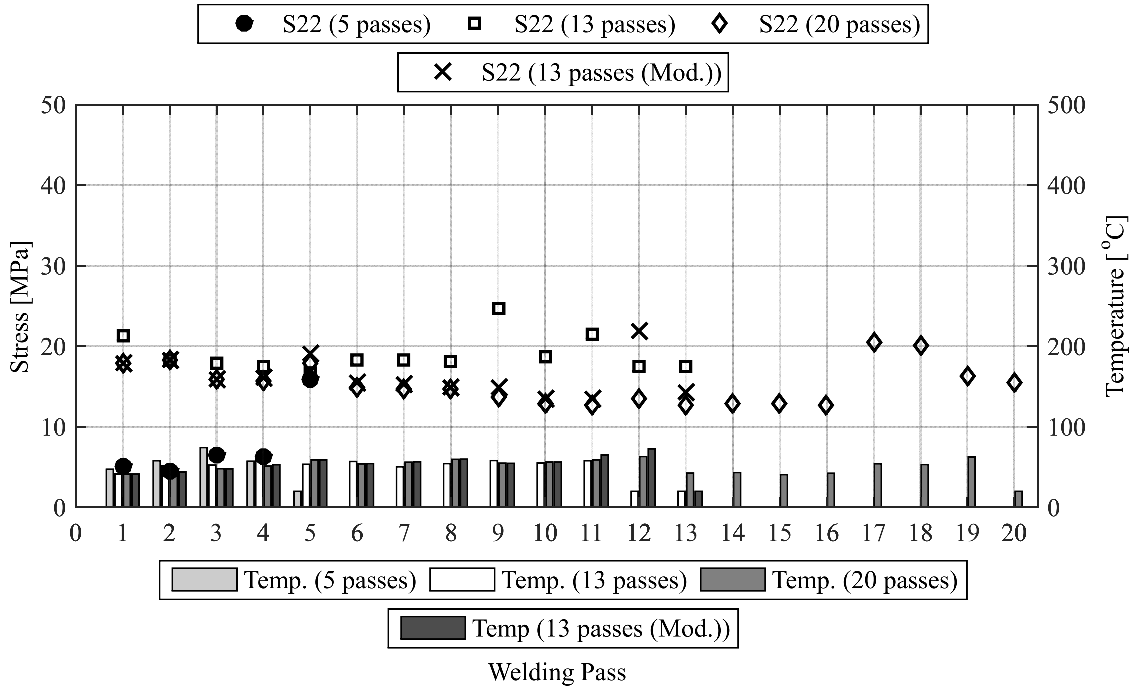

Figure B.23: Summary of maximum vertical transverse stress values (S22) and corresponding temperatures during the welding procedure for the number of welding passes parameter.

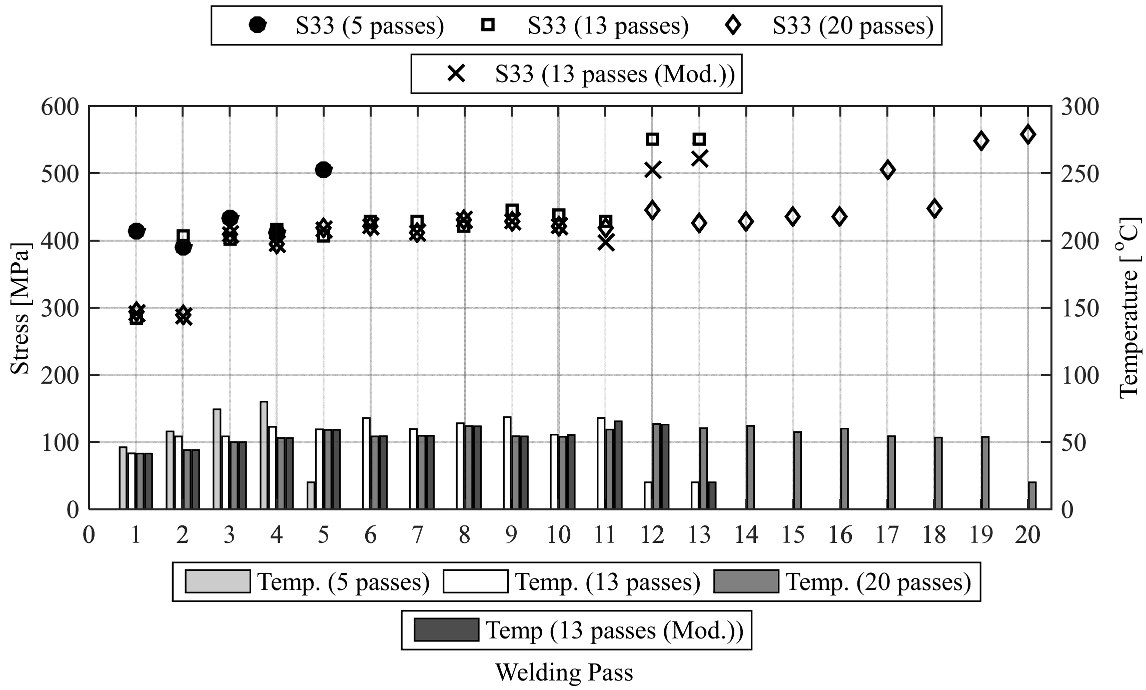

Figure B.24: Summary of maximum longitudinal stress values (S33) and corresponding temperatures during the welding procedure for the number of welding passes parameter.